

IRON AND MANGANESE REDUCTION DRIVEN BY ORGANIC MATTER AND
MIXING OF FRESH AND SALINE GROUNDWATER IN THE FRASER RIVER
DELTA AQUIFER, VANCOUVER, CANADA

by

KUN JIA

B.Sc. University of Waterloo, 2011

B.Sc. China University of Geosciences (Beijing), 2011

A THESIS SUBMITTED IN PARTIAL FULFILLMENT OF THE
REQUIREMENTS FOR THE DEGREE OF
MASTER OF SCIENCE

in

THE FACULTY OF GRADUATE AND POSTDOCTORAL STUDIES
(Geological Sciences)

THE UNIVERSITY OF BRITISH COLUMBIA
(Vancouver)

April 2015
© Kun Jia, 2015

Abstract

We present results of field investigations of the biogeochemistry of an aquifer a few km from the ocean adjacent to the Fraser River in Vancouver, Canada. At the site, a wedge of relatively dense saline ocean water enters the aquifer in the hyporheic zone at the river bottom, migrates away from the river along the base of the aquifer to a maximum distance of approximately 500m inland, where it overturns and mixes with fresh groundwater. The mixed saline - fresh water then flows back under a regional freshwater gradient and eventually discharges to the river at the top of the saline wedge. Pore waters show iron concentrations peak at over 300 mg/L (5.4 mM) and manganese at 7 mg/L (0.13 mM) at the upper mixing zone - the interface between terrestrial recharge and top of the overturned saline groundwater. The reducible concentrations on the sediment are approximately 784-2,576 mg/kg (14-46 mM/kg) iron and 110-330 mg/kg (2-6mM/kg) manganese. The dominant process is the reductive dissolution of iron and manganese oxide minerals via organic matter oxidation, although acid-volatile sulfide and methane measurements show that both sulfate reduction and methanogenesis are also occurring. Dissolved organic matter (DOM) concentrations ranged between 5 and 30 mg/L. Excitation – emission fluorescence spectroscopy is used to help identify the distinct sources of DOM, which include terrestrial from fresh recharge, detrital from sediments and from inflowing ocean water. One-dimensional kinetic reactive-transport modeling that includes primary mineral redox reactions and secondary mineral precipitation was used to: i) interpret the role of mixing of fresh and saline water, ii) to constrain reduction-rate parameters and metabolic activity levels from field data, including the oxidation rate of organic matter by iron and manganese oxides, probably accompanied with sulfate reduction and methanogenesis; iii) to understand how other secondary minerals further control aqueous ferrous iron and manganese concentrations through mineral precipitation/dissolution processes; v) to gain insight into the long-term evolution of the geochemistry at the site.

Preface

This thesis is a combination of both unpublished and published materials. Chapter 1. Figure 1.1, Chapter 2. Figure 2.2 and Figure 2.3 were modified from original sources with permissions. I was responsible for all related field and laboratory work for Chapter 1-6 with the supervision of Dr. Roger Beckie. These chapters will be modified and submitted for publication. My field work in 2012 was assisted by Dr. Roger Beckie and Dr. Uli Mayer. Dr. Uli Mayer also provided guidance with Section 5.5.

Table of Contents

Abstract	ii
Preface	iii
Table of Contents	iv
List of Tables.....	vii
List of Figures	ix
Acknowledgements	xiv
Chapter 1: Introduction	1
1.1 Background	2
1.2 Purpose and Objectives	3
Chapter 2: Fraser River Delta.....	5
2.1 Fraser River Delta.....	5
2.2 Fraser River Delta Geology.....	6
2.3 Hydrostratigraphy	6
2.4 Hydrological Properties.....	8
2.4.1 Local Groundwater Flow System	8
2.4.2 Permeability	8
2.4.3 Gradient	9
2.5 Mineralogy	9
2.6 Field Site Description	10
Chapter 3: Methodology	14
3.1 Sample Collection.....	14
3.1.1 Water Sampling.....	14
3.1.2 Gas Sampling.....	15
3.1.3 Sediment Sampling	17
3.2 Sample Analysis.....	19
3.2.1 Water Sample Analysis.....	19
3.2.1.1 Field.....	19
3.2.1.2 Laboratory	19
3.2.2 Sediment Sample Analysis	21
3.2.2.1 Kinetic Extraction	21
3.2.2.2 Sequential Extraction	25

3.2.2.3 Fe (II) and Fe (III) Speciation	28
3.2.2.4 AVS (Acid Volatile Sulfide) Determination	28
3.2.2.5 Sedimentary Organic Matter - Loss on Ignition.....	29
3.2.3 SEM/EDX Analysis	29
3.2.4 Dissolved Organic Matter Analysis	30
3.2.4.1 Florescence Analysis	30
3.2.4.2 PARAFAC Model	32
Chapter 4: Results	34
4.1 Groundwater Geochemistry	34
4.1.1 General Porewater Geochemistry	34
4.1.2 Redox Components	39
4.1.3 Iron and Manganese Reduction	42
4.1.4 Sulfate Reduction	45
4.1.5 Bicarbonate and Secondary Minerals	46
4.1.6 Methanogenesis.....	49
4.2 Isotope Analysis	50
4.2.1 Isotope Profile	50
4.2.1.1 Isotope vs. Depth	50
4.2.1.2 Isotope Composition vs. Chloride Concentration	51
4.2.1.2 $\delta D/\delta^{18}O$ Relationship.....	52
4.2.2 Mixing Ratios between Fresh Water and Ocean Water	54
4.3 Sediment Chemistry	58
4.3.1 Reactivity of Iron and Manganese Oxides	58
4.3.1.1 Kinetic Extraction	58
4.3.1.2 Parameter Comparison	64
4.3.2 Sequential Extraction	65
4.3.2.1 Fe(II) and Fe(III) Speciation	70
4.3.2.2 Reactive Fe(III) and Mn Oxides	71
4.3.2.3 Sedimentary Organic Carbon	73
4.3.2.4 Acid Volatile Sulfide (AVS) and Sulfate Reduction	74
4.3.3 SEM Analysis	75
4.4 Spectroscopic Properties of Dissolved Organic Matter	82
4.4.1 Source of Organic Matter	82
4.4.2 PARAFAC Analysis	84
4.4.3 Visual Fluorescence Peaks	87

Chapter 5: Discussion.....	93
5.1 Iron and Manganese Oxides Reduction	93
5.2 Sulfate Reduction	95
5.3 Secondary Mineral Precipitation	98
5.4 Bioavailability of Dissolved Organic Matter.....	99
5.5 PHREEQC 1-D Kinetic Reactive-Transport Modeling	103
5.5.1 Model Setup	104
5.5.1.1 Model Domain and Physical Transport	104
5.5.1.2 Geochemical Processes and Reaction Network	107
5.5.2 Model Simulation	111
5.5.2.1 Scenario 1: Iron and Manganese Reduction.....	112
5.5.2.2 Scenario 2: Secondary Mineral Precipitation ($SI_{FeCO_3}=1.5$, $SI_{MnCO_3}=0.5$).....	115
5.5.2.3 Scenario 3: Secondary Mineral Precipitation ($SI_{FeCO_3}=0$, $SI_{MnCO_3}=0$).....	118
5.5.2.4 Scenario 4: Sulfate Reduction	122
5.5.2.5 Scenario 5: Sulfate Reduction + Secondary Mineral (FeS) Precipitation	125
5.5.2.5 Scenario 6: Methanogenesis.....	129
5.5.2.7 Scenario 7: Bioavailability of Organic Matter	134
5.5.3 Long-term Evolution of the Geochemistry	140
Chapter 6: Conclusions and Recommendations	142
6.1 Conclusions	142
6.2 Recommendations	144
References.....	146
Appendices.....	152
Appendix A: Flow Time Calculation at the Kidd 2 site.....	153
Appendix B: Piezometer and Well Logs for the Kidd 2 site(L. A. Neilson-Welch 1999)	154
Appendix C: Sampling Wells and Collection Date.....	172
Appendix D: Selected Photographs	173
Appendix E: Sample Calculations for Alkalinity Titration Analysis	174
Appendix F: Sample Calculation for Methane Concentration Conversion	184
Appendix G: Sulfate Reduction Rate.....	186
Appendix H: Phreeqc Simulation Input.....	188

List of Tables

Table 2.1: Topset hydrostratigraphy of the Fraser River delta (Williams and Roberts 1989).....	8
Table 2.2: Hydraulic conductivities and gradients of four hydrostratigraphic units (L. Neilson-Welch and Smith 2001).....	9
Table 3.1: Sediment core collection.....	18
Table 3.2: Kinetic extraction solutions and mechanism	22
Table 3.3: A summary of published SEPs to differentiate iron oxides.....	26
Table 3.4: Four-step SEPs were performed in an anaerobic glove box to extract iron oxides, consisting of ion exchangeable, reactive, poorly reactive, and non-reactive iron oxides.....	27
Table 4.1: Field measured parameters in 11 standpipes, and three multilevel wells (W1, W2 and W3).....	35
Table 4.2: Concentrations of cations, anions, DOC, and HCO_3^- in 11 standpipes, and three multilevel wells (W1, W2 and W3)	36
Table 4.3: conservative tracers including Cl and isotopic compositions of four end - member water groups at the Kidd 2 site, for calculating the mixing ratio for upper and lower mixing zones.....	55
Table 4.4: Mixing results for upper mixing zone, based on Cl concentration and δD of shallow BH114 water, deep W3-9 ocean water and lower confining silt WB-11 water.	57
Table 4.5: Mixing results for lower mixing zone, based on deep ocean W3-9 water and lower confining silt WB-11 water.....	57
Table 4.6: Total iron and manganese concentrations dissolved from the Kidd 2 site sediments in the ascorbate-citrate chemical extractions after 24 h.	60
Table 4.7: Kinetic extraction was conducted under ascorbate-citrate solution buffered at pH=7.5 for 24 hours, and initial mass (m_0), kinetic rate constant (K') and reaction exponent (γ) are estimated by Matlab curve fitting.....	61
Table 4.8: Comparison of kinetic parameters, including M_0 (initial mass of extractable iron), k' (rate constant), and γ (reaction exponent).....	64
Table 4.9: solid phase sequential extractions of iron and manganese oxides at the Kidd 2 site.....	65
Table 4.10: Mineralogical analysis by SEM at the Kidd 2 site.....	77

Table 4.11: Excitation and emission wavelengths of Peak A and Peak C for water samples at different depths. Peak C is only seen at the upper mixing zone, where the iron concentration reaches its maximum.	90
Table 4.12: Summary of fluorescence PARAFAC components C1 and C2 and their corresponding peaks.	92
Table 5.1: Rates of sulfate reduction in different aquifers	96
Table 5.2: Comparison of wavelength-independent fluorescence properties (excitation maximum, emission maximum, and A:C ratio) between upper mixing zone water at the Kidd 2 site and other water types.	100
Table 5.3: Water composition of initial and boundary conditions and neighboring units in phreeqc model	105
Table 5.4: Physical parameters for the PHREEQC 1-D transport model.....	107
Table 5.5: Chemical reactions included in the PHREEQC simulations, with using database of water4q.dat.....	108
Table 5.6: Parameter values in the PHREEQC simulations.	110
Table 5.7: Rate-constant values assigned in Scenario 1-7.....	111

List of Figures

Figure 1.1: The flow system has been well characterized and modeled (L. Neilson-Welch and Smith 2001). The cross-section shows the conceptual flow convection in the Fraser River sandy aquifer. The green rectangle indicates the location of the “upper mixing zone,” where overturned saline water meets the shallow fresh groundwater. The pink rectangle indicates the location of the “lower mixing zone,” where freshwater from the lower confining silt flows up into the overlying sandy aquifer.	2
Figure 2.1: Surficial geology of the Fraser River delta (J.J. Clague 1998).	5
Figure 2.2: The Kidd 2 site is located in the Fraser River delta in south-west British Columbia.	11
Figure 2.3: Plan view of well locations at the Kidd 2 site, including three multilevel wells (W1, W2, W3), eleven standpipe piezometers (BH 101-108, 112-114), and Westbay (WB) multilevel borehole; a sediment core, represented by green dot, was collected adjacent to W3.	12
Figure 3.1: Schematic drawing of modified headspace sampler: water was pumped into the sampler through the peristaltic pump, and gas in the headspace was analyzed by the LGR gas analyzer.	17
Figure 3.2: Kinetic extraction cylindrical reactor.	23
Figure 3.3: Curve fitting for reactive iron oxides dissolution at the Kidd 2 site (depth of 12.20 m) during the ascorbate-citrate extraction for 24 hours. $M(t)$ (mmol/kg) is the residual iron oxides mass left in the extractant, and $t(s)$ is the extraction period. Y , k' and $M(0)$ were determined by Matlab statistical curve fitting.	25
Figure 3.4: Principle of fluorescence spectroscopy. As a molecule or atom absorbs energy from the light source, an electron is excited to a higher energy level. When the electron returns to its ground energy level, energy is lost as photons or fluorescence, and captured by the fluorescence detector (Fellman, Hood, and Spencer 2010).	31
Figure 4.1: Piper plot for groundwater samples from the Kidd 2 site	38
Figure 4.2: Cl^- plotted against A) Na^+ , B) Mg^{2+} , C) Ca^{2+} , D) SO_4^{2-} at the Kidd 2 site. Blue dots represent field measurements, and the red line presents the mixing line of the intruded saline water. The linear relationship of Na^+ and Mg^{2+} with Cl^- suggests dilution is the dominant control, whereas Ca and SO_4 show evidence of non-conservative reactions.	41
Figure 4.3: The non-linear relationships between Cl^- and Fe^{2+} , Mn^{2+} , HCO_3^- and DOC at the Kidd 2 site, indicating that biogeochemical processes and not mixing/dilution are their dominant controls at the Kidd 2 site.	42
Figure 4.4: Concentrations of Mn^{2+} and Fe^{2+} with depths in profile W1 at the Kidd 2 site.	42

Figure 4.5: Concentrations of Mn^{2+} and Fe^{2+} with depths in profile W3 at the Kidd 2 site.	43
Figure 4.6: Concentrations of DOC versus Fe^{2+} and Mn^{2+} at the Kidd 2 site.	44
Figure 4.8: Concentrations of HCO_3^- versus SO_4^{2-} at the Kidd 2 site. The inverse relationship is observed at both intermediate and deep water, indicating that sulfate reduction is involved in groundwater.	46
Figure 4.9: The relationship between HCO_3^- and a) Ca and b) Mg. both these two ions show positive relationship with HCO_3^- , indicating dissolution of carbonate minerals.....	47
Figure 4.10: Saturation indices calculated with the Phreeqc geochemical model, using the MINTEQ database: a) SI_Calcite, b) SI_Dolomite, c) SI_Siderite, and d) SI_Rhodochrosite.	49
Figure 4.11: dissolved methane along the depth profile in W3. The discontinuity of methane suggests inhomogeneous methane production at the Kidd 2 site.....	50
Figure 4.13: δD and $\delta^{18}\text{O}$ versus chloride (Cl) concentration in W3.	52
Figure 4.14: Shallow (< 10 m), intermediate (10-13 m), deep ocean water (13-20m) water, and deep fresh water samples are plotted as δD versus $\delta^{18}\text{O}$ to show the relationship of isotopic composition against the meteoric water line.....	53
Figure 4.15: Water sample at the upper mixing zone (W3-5) results from the mixture of the water in BH 114, W3-9 and WB-11. The water sample at the lower mixing zone (W3-12) results from the mixture of water in W3-9 and WB-11.....	56
Figure 4.16: Dissolution of iron and manganese oxides from the sediments at the Kidd 2 site as a function of time, driven by ascorbate-citrate solution buffered at pH=7.5 for 24 hours. See text for complete description and discussion.....	59
Figure 4.17: Rate constant (k') for iron and manganese oxides along the depth profile.....	62
Figure 4.18: Comparison of reactivities of iron oxide to well-defined ferrihydrite, lepidocrocite, and goethite (from Larsen & Postma 2001). The x-axis is normalized over initial mass (J/m^0), and the y-axis is the fraction (m/m^0) remaining in the solid phase.....	63
Figure 4.19: solid sediment depth profiles for a) 0.5 M HCl extractable - reactive - Fe oxide, b) 0.5 M HCl extractable - reactive Mn oxide, c) reactive Fe(II), d) reactive Fe(III), e) AVS, f) $\text{O}_2\%$	70
Figure 4.20: Comparison between aqueous Fe(II) and reactive Fe(III) along the depth profile in a) W1 and b) W3.	72
Figure 4.21: Comparison between aqueous and reactive manganese along the depth profile in a) W1 and b) W3.	72

Figure 4.22: Highly correlated relationship between reactive iron oxide and organic matter content, with $R^2 = 0.62$	74
Figure 4.23: Backscattered electron image of minerals with bright surfaces (depth=7.8m). EDS analyses of white surface indicates the presence of iron oxide.....	78
Figure 4.24: Backscattered electron image of minerals with bright agglomerates embedded into the sediment (depth=8.7m). The EDS analysis indicates the presence of iron oxide, with Al- and Si minerals, possibly quartz (SiO_2) and chlorite ($(\text{Mg},\text{Fe}^{2+})_5\text{Al}(\text{Si}_3\text{Al})\text{O}_{10}(\text{OH})_8$).....	78
Figure 4.25: Backscattered electron image of sub-angular sediment (depth=11.9m). The absence of white spot suggests little iron or manganese in sediment. The EDS analysis indicates sediment is dominantly composed of silicate minerals: including quartz (SiO_2), plagioclase ($\text{CaAlSi}_2\text{O}_8$), chlorite ($(\text{Mg},\text{Fe}^{2+})_5\text{Al}(\text{Si}_3\text{Al})\text{O}_{10}(\text{OH})_8$).....	79
Figure 4.26: Backscattered electron image of minerals with grey color, indicates the absence of iron oxide (depth=12.2m). The EDS analysis indicates the absence of iron oxide. The high Ca, P, O peaks suggest the possible mineral phases are apatite ($\text{Ca}_5(\text{PO}_4)_3(\text{OH},\text{F},\text{Cl})$), and calcite (CaCO_3).....	79
Figure 4.27: Backscattered electron image of minerals with bright agglomerates/surfaces, which embedded into the sediment (depth=13.1m). The EDS analysis indicates the presence of iron oxide as distinct “Fe” and “O” peaks.....	80
Figure 4.28: Appearance of an isolated insulating white spots ($\text{Fe}_2\text{TiO}_4 - \text{FeOx}$ inclusion) in a sediment (depth of 17.1m).	80
Figure 4.29: Backscattered electron image of sub-angular sediment (depth=20.1m). The absence of white spots suggests little iron or manganese in sediment. The EDS analysis indicates sediment is dominantly composed of silicate minerals: including quartz (SiO_2), plagioclase ($\text{CaAlSi}_2\text{O}_8$) and chlorite ($(\text{Mg},\text{Fe}^{2+})_5\text{Al}(\text{Si}_3\text{Al})\text{O}_{10}(\text{OH})_8$).....	81
Figure 4.30: Appearance of an isolated insulating white spots (FeOx inclusion) in a sediment (depth of 21.3m). EDS analysis for white spot suggest possible iron bearing mineral phases are iron oxide (FeOx) and siderite (FeCO_3).....	81
Figure 4.31: Backscattered electron image of black fragment on the mineral surface (depth of 8.7m). The EDS analysis indicates the presence of organic matter as the distinct “C” peak.....	82
Figure 4.32: Florescence index (FI) calculated for W1 and W3; the red lines indicate the saline wedge.	83
Figure 4.33: Redox index (RI) in W3, the red lines represent the upper and lower mixing zone.	85
Figure 4.34: Depth profile of quinone-like ratios of HQ/Q1, HQ/Q2, and HQ/Q3 in W3.....	86

Figure 4.35: HQ versus ferrous iron concentration in W1 and W3.	87
Figure 4.36: EEMs showing positions of the two fluorescence peaks: a) shallow groundwater zone (8.08 m), where only Peak A is seen; B) upper mixing zone (12.08 m), where both Peak A and C are seen; c) deep saline zone, where only Peak A is seen; and d) lower mixing zone, where only Peak A is seen. Note the different color scales on each plot.	89
Figure 4.37: Excitation and emission curves for the C1 and C2 components.	91
Figure 5.1: Explanation of the variation in the fluorescence index (FI) by SQ1 and SQ2.....	102
Figure 5.2: The one-dimensional reactive-transport model follows the flow line (L. Neilson-Welch and Smith 2001) indicated in red that starts at the red dot at the base of the river, flows 500 m inland, overturns and flows back to the river at the green dot.	105
Figure 5.3: Scenario 1 baseline, $T = 5,000$ years; advective flow is from left to right; distance = 0 m corresponds to saline intrusion inflow point, distance = 1,000 m corresponds to outflow point. The dots correspond to field values and the lines correspond to model simulations. a) pH; b) Aqueous concentrations of Fe(II); c) Aqueous concentrations of Mn(II); d) Saturation indices for siderite and rhodochrosite. See text for discussion.	115
Figure 5.4: Scenario 2, effect of siderite and rhodochrosite precipitation, $SI_{FeCO_3}=1.5$, $SI_{MnCO_3}=0.5$; $T = 5,000$ years; advective flow is from left to right; distance = 0 m corresponds to saline intrusion inflow point, distance = 1,000 m corresponds to outflow point. The dots correspond to field values and the lines correspond to model simulations. a) pH; b) Aqueous concentrations of Fe(II); c) Aqueous concentrations of Mn(II); d) Saturation indices for siderite and rhodochrosite. See text for discussion.	118
Figure 5.5: Scenario 3, effect of siderite and rhodochrosite precipitation, $SI_{FeCO_3}=0$, $SI_{MnCO_3}=0$; $T = 5,000$ years; advective flow is from left to right; distance = 0 m corresponds to saline intrusion inflow point, distance = 1,000 m corresponds to outflow point. The dots correspond to field values and the lines correspond to model simulations. a) pH; b) Aqueous concentrations of Fe(II); c) Aqueous concentrations of Mn(II); d) Saturation indices for siderite and rhodochrosite. See text for discussion.....	121
Figure 5.6: Scenario 4, effect of sulfate reduction; $T = 5,000$ years; advective flow is from left to right; distance = 0 m corresponds to saline intrusion inflow point, distance = 1,000 m corresponds to outflow point. The dots correspond to field values and the lines correspond to model simulations. a) pH; b) Aqueous concentrations of Fe(II); c) Aqueous concentrations of Mn(II); d) Aqueous concentrations of SO_4^{2-} . See text for discussion.....	125
Figure 5.7: Scenario 5, effect of secondary mineral (FeS) precipitation; $T = 5,000$ years; advective flow is from left to right; distance = 0 m corresponds to saline intrusion inflow point, distance = 1,000 m corresponds to outflow point. The dots correspond to field values and the lines correspond to model simulations. a) pH; b) Aqueous	

concentration of Fe(II); c) Aqueous concentration of Mn(II); d) Aqueous concentration of SO_4^{2-} ; e) Saturation index of FeS. See text for discussion..... 129

Figure 5.8: Scenario 6, effect of methanogenesis; T= 5,000 years; advective flow is from left to right; distance = 0 m corresponds to saline intrusion inflow point, distance = 1,000 m corresponds to outflow point. The dots correspond to field values and the lines correspond to model simulations. a) pH; b) Aqueous concentration of Fe(II); c) Aqueous concentration of Mn(II); d) Aqueous concentration of SO_4^{2-} ; e) Aqueous concentration of methane. See text for discussion. 133

Figure 5.9: Scenario 7, effect of bioavailability; T = 5,000 years; advective flow is from left to right; distance = 0 m corresponds to saline intrusion inflow point, distance = 1,000 m corresponds to outflow point. The dots correspond to field values and the lines correspond to model simulations. a) pH; b) Aqueous concentrations of Fe(II); c) Aqueous concentrations of Mn(II); d) Aqueous concentrations of SO_4^{2-} ; e) Aqueous concentrations of methane; f) Saturation indices for siderite, rhodochrosite and iron sulfide. See text for discussion..... 140

Acknowledgements

I would like to thank my supervisor Dr. Roger Beckie, for his guidance, advice and financial support during the completion of my thesis, as well as the opportunity for me to study such an interesting topic. Thanks also to the other members of my review committee. Dr. Uli Mayer provided great advices on the reactive transport model of the thesis, and enhanced my modeling knowledge in his course of multi-component reactive transport modelling in groundwater. Dr. Mark Johnson gave me many helpful suggestions on organic matter characterizations in my research and provided instruments for organic matter analysis.

In addition, I would like to thank the following people for their individual contributions to this thesis:

- Maureen Soon and Timothy Ma (Department of Environment Engineering, UBC), provided great assistance and references with a number of instruments and analytical procedures.
- Ashlee Jollymore, a PHD student at UBC, provided guidance on using ion chromatograph and fluorescence spectroscopy, and also developed the coding for PARAFAC model.
- Many thanks to my colleagues in the hydro group. All of you gave me extensive help and assistance in the past three years. Your kindness and companionship let me feel like we are a big family and I will always treasure all those special memories.

Finally, I want to thank my parents for love, support, and encouragement. Special thanks to Mr. Cui for such unforgettable dishes and memories you made for me.

Chapter 1: Introduction

This thesis examines the biogeochemistry of iron, manganese, and organic matter in an anaerobic deltaic aquifer a few kilometers from the ocean, adjacent to the Fraser River in Vancouver, Canada. At the site, a wedge of relatively dense saline ocean water from the base of the Fraser River enters the aquifer in the hyporheic zone at the river bottom, and migrates away from the river along the base of the aquifer to a maximum distance of approximately 500 m inland where it overturns and mixes with fresh groundwater. The mixed saline-freshwater then flows back under a regional freshwater gradient and eventually discharges to the river at the top of the saline wedge. Two saline-groundwater mixing zones are located along the saline wedge: freshwater from the lower confining silt flows up into the overlying sandy aquifer (the “lower mixing zone”) and terrestrial recharge from inland rides up on top of the intruded saline water (the “upper mixing zone”) (Figure 1.1). Astonishingly high concentrations of Fe(II) and Mn(II) are observed along the intrusive seawater circulation flowpath, especially at the upper mixing zone, where pore waters show Fe(II) concentrations that peak above 300 mg/L (5.4 mM) and Mn(II) peaking at 7 mg/L (0.13 mM).

Although both groundwater flow and biogeochemical redox processes are critical for understanding iron and manganese biogeochemistry, the role of the mixing of saline and non-saline water and the bioavailability of organic matter in aquifer sediments is still poorly understood. Few studies have examined the biogeochemical redox process under saline intrusion conditions in aquifers, and even fewer have looked at the relationship between sediment properties and organic matter reactivity. Hence, our studies are aimed at the following research questions: 1) What are the solid-phase sources of Fe(II) and Mn(II) and how reactive are they? 2) What is the releasing mechanism for Fe(II) and Mn(II)? 3) What are the sources of organic matter that drive reduction from fresh recharge, from inflowing marine water, or detrital from sediments?

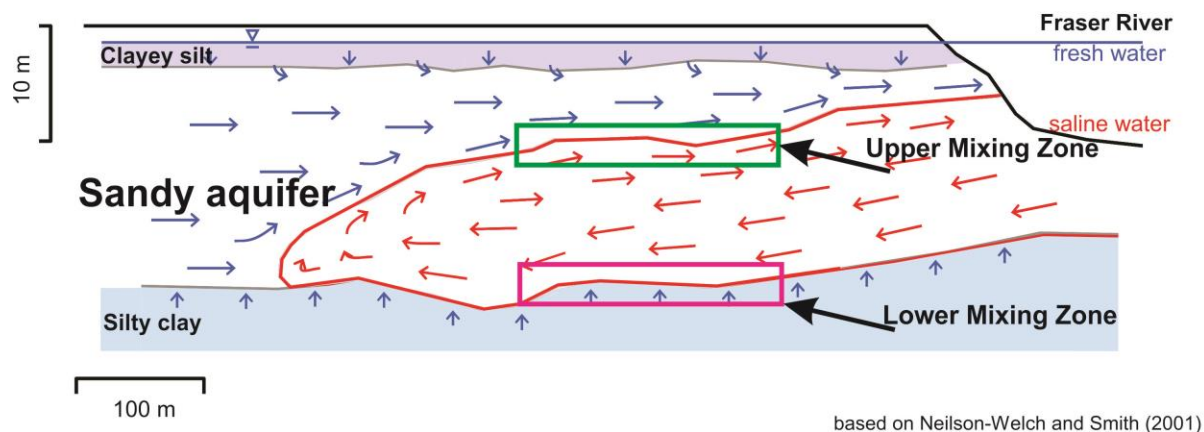


Figure 1.1: The flow system has been well characterized and modeled (L. Neilson-Welch and Smith 2001). The cross-section shows the conceptual flow convection in the Fraser River sandy aquifer. The green rectangle indicates the location of the “upper mixing zone,” where overturned saline water meets the shallow fresh groundwater. The pink rectangle indicates the location of the “lower mixing zone,” where freshwater from the lower confining silt flows up into the overlying sandy aquifer.

1.1 Background

In the past decade, increasing interest has been shown in the biogeochemical redox reactions between metals and organic carbon in groundwater. In natural groundwater and sediments, organic matter is usually the ultimate source of electrons that microorganisms transfer to terminal electron acceptors, such as oxygen (O_2), nitrate (NO_3^-), Mn(IV), Fe(III), sulfate (SO_4^{2-}) and carbon dioxide (CO_2), through what are known as the terminal electron-accepting processes (TEAPs) (Lovley and Chapelle 1995). In natural groundwater, soil, and sediments, microbial reduction of Fe(III) or Mn(IV), which is accompanied with oxidation of organic matter, is considered as one of the most important biogeochemical reactions. The reduction of Fe and Mn not only plays a critical role in controlling the carbon cycle, but also has environmental significance in the release and fate of metals in aquatic systems.

In natural groundwater, as oxygen is depleted during the oxidation of organic matter, bacteria turn to Mn(IV) and Fe(III) for respiration. Both iron and manganese oxides tend to reduce under anaerobic conditions, and release aqueous Fe(II) and Mn(II) into solution. Therefore, microbial-driven degradation processes exert a major control on aqueous Fe(II) and Mn(II) concentrations in

groundwater. In addition to iron and manganese reduction, under anaerobic conditions, sulfate reduction should also be evaluated since it is difficult to segregate different terminal electron-accepting reactions into separate zones, at least for Fe(III)/Mn(IV) and sulfate reduction (Jakobsen 1999). Moreover, to characterize iron and manganese cycling and zonation, anaerobic biogeochemical electron flow and groundwater transport pathways must be jointly assessed since dissolved solutes are also controlled by advective flow in aquifer systems.

Groundwater flow affects biogeochemical reactions by establishing and sustaining redox and nutrient gradients. The classic example is that of a reduced dissolved organic contaminant penetrating into an aerobic aquifer. Redox reactions occur principally along the outer fringes of the plume where redox and nutrient gradients are established (Prommer, Barry, and Davis 2002). The reactions, in this case, are strongly controlled by the upstream source of organic matter and the mixing between the organic-rich and aerobic waters.

1.2 Purpose and Objectives

The purpose of this thesis is to investigate the cycling of Fe(II) and Mn(II) associated with organic matter in the reduced, circumneutral groundwater in the Fraser River delta. After reviewing the sediment depositional sequences and methodologies that were applied in this research, we used aqueous geochemistry data collected at multiple wells to investigate the primary and secondary redox reactions in the aquifer system. Then, we used kinetic and sequential extractions to determine iron and manganese oxide reactivities, and differentiate their fractions in sediments. Excitation-emission fluorescence spectroscopy was then applied to identify the distinct sources of dissolved organic matter and characterize the organic matter complex. Lastly, we developed a one-dimensional kinetic reactive-transport model that includes primary mineral redox reactions and secondary mineral precipitation to: i) interpret the role of mixing of fresh and saline water, ii) to constrain the reduction rate parameters and metabolic activity levels from field data, including oxidation rate of organic matter by iron and manganese oxides, probably accompanied with sulfate reduction and methanogenesis, and iii) to examine the future evolution of the aquifer

system and explain why high concentrations of Fe(II) and Mn(II) are only observed in the upper mixing zone.

Chapter 2: Fraser River Delta

2.1 Fraser River Delta

The delta of the Fraser River, which discharges into the Strait of Georgia, is the largest and most important on the west coast of British Columbia, Canada (J.J. Clague et al. 1991). The Fraser River delta consists of upper and lower delta plains. The upper delta plain is found along the Fraser River in the greater Vancouver area and includes the diked section of the delta (Figure 2.1). The lower plain extends approximately 10 to 15 km to the west and is mainly comprised of tidal flats (J.J. Clague 1998).

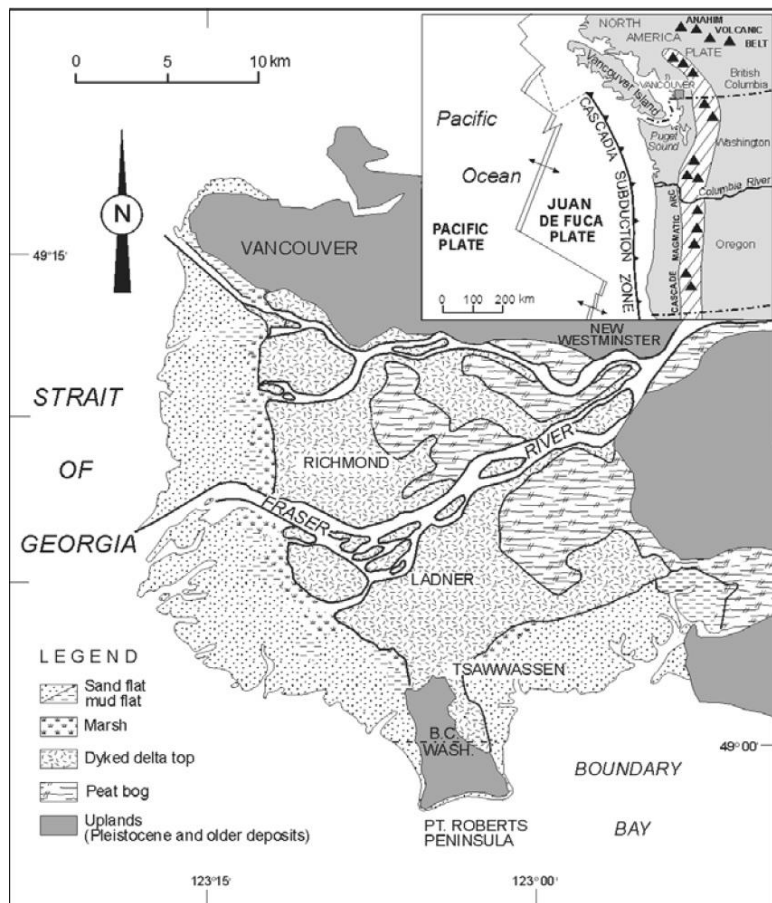


Figure 2.1: Surficial geology of the Fraser River delta (J.J. Clague 1998).

2.2 Fraser River Delta Geology

The Fraser River delta lies on granite rocks overlain by thick Quaternary sequences of glacial deposits that, in turn, are overlain by surficial deltaic sediments, deposited when the sea level rose during approximately the last 9,000 to 10,000 years (J.J. Clague et al. 1991). The Fraser River delta is geologically young and began forming in the late Pleistocene by vertical deglacial deposition and lateral progradational when the Cordilleran Ice Sheet began to retreat (J.J. Clague 1998).

As rapid deglaciation occurred during the Holocene, a series of heterogeneous glacial successions, with thicknesses of up to several hundred meters, were accreted over the basement rock. These sequences included proglacial, marine, and fluvial sediments (J.J. Clague et al. 1991).

Accompanying the rapid vertical accretion was the lateral progradation of the floodplain, due to the advance of the lower arm of the Fraser River, which had rapid sedimentation rates. As the Fraser River prograded, its floodplain extended into the Strait of Georgia and towards the west and southwest of New Westminster (J.J. Clague et al. 1991).

2.3 Hydrostratigraphy

With the disappearance of the Cordilleran Ice Sheet and progradation of the Fraser River delta, up to 300 m of postglacial deltaic sediment sequences were deposited in the Fraser River delta. Even though sea level has risen approximately 12 m from its lowest level over the past 9,000 years, the lateral progradational rate (1 m/a to 6.5 m/a) was sufficient to keep pace with the vertical accretion, resulting in continuous progradation of the delta (Williams and Roberts 1989). As a result, alluvial sediments were deposited most extensively over the lower portions of the Fraser River delta, rather than low-energy depositional sediments such as clayey layers, tidal marshes and lagoons. The postglacial deltaic deposits consisted of a deep marine silt and mud bottomset unit, a thick interbedded sand, a silt foreset unit up to 150 m thick, and a much thinner intertidal, fluvial silt and sand topset unit (J.J. Clague et al. 1991). These three separate units were controlled by the interaction of tidal and fluvial processes and are distinguished by seismic reflection and lithological stratigraphy (J.J. Clague et al. 1991).

Our research focuses on local groundwater flow and its geochemistry in the topset unit, consisting of flat-lying silt and sand material. Overall, the topset unit is characterized by fining upward sequences, indicating that the rate of sea level rise continuously slowed. The topset unit is further divided into four major sub-units; the top-most unit consisting of 1-4 m surficial peat bog and clayey silt. The second unit is composed of interbedded silt and sand, 2-6 m in thickness, which overlies the third unit of fine to coarse-grained homogenous sand down to a depth of 20 m. The deepest unit is a fine-grained delta slope deposit extending from depths of 20 m to 150 m (Williams and Roberts 1989).

AMS radiocarbon ages of wood and shells at depth from various locations of cores showed that the topset unit started accumulating approximately 5,000-6,000 years ago (J.J. Clague et al. 1991). The bottom silt-clay delta slope deposit with organic sedimentation indicates that the sea level remained comparatively stable and it allowed deposition of fine-grained materials. The overlying alluvial coarse to medium homogenous sand extended at least 18-19 m below the mean sea level (bmsl) (Williams and Roberts 1989). Organics, such as wood fragments and vegetation, suggest a relatively high-energy depositional environment during that period of deposition. The overlying interbedded silt and sands represent laterally migrating distributary channel deposition, which is characterized by scattered wood fragments and fining upward sequences. Lastly, most of delta surface is capped with organic-rich clayey silt and peat bog deposits, indicating that these floodplain facies were accumulated in salt marshes to fresh fluvial water.

Table 2.1 summarizes these four hydrostratigraphic units. Since both the topmost and bottommost units are low permeability fine-grained materials, they formed the upper and lower confining boundaries for the internal sand units (Williams and Roberts 1989).

Table 2.1: Topset hydrostratigraphy of the Fraser River delta (Williams and Roberts 1989)

Unit	Depth (m)	Confined aquifer classification	Description
1	1-4	Upper aquitard	Surficial clayey silt and peat bog
2	4-9	Sand aquifer	Interbedded silt and sand
3	9-20	Sand aquifer	Coarse to medium homogenous sand
4	>20	Lower aquitard	Silty clay

2.4 Hydrological Properties

2.4.1 Local Groundwater Flow System

A three-dimensional numerical model has been developed to simulate the groundwater flow in the Fraser River delta (Ricketts 1998). Since the base of the main channel and the north arm of the Fraser River penetrate into the internal sandy aquifer, the confined sandy aquifer is hydraulically connected to the hyporheic zone of the Fraser River, and groundwater flow is mainly controlled by the drainage system. The recharge in the sandy aquifer mainly relies on direct precipitation. The result of the model (Ricketts 1998) suggests that approximately 10% of rainfall (130 mm/a) directly recharges into the sandy aquifer, and most of the precipitation is lost by surface runoff and evaporation.

2.4.2 Permeability

Neilson-Welch and Smith (2001) estimated the hydraulic conductivities (K) of the four hydrostratigraphic layers (summarized in Table 2.2). Based on aquifer tests conducted by Neilson-Welch and Smith (2001), the internal sandy aquifer is quite reproducible and nearly isotropic, with the exception of some interbedded silts in Unit 2. The fine-grained materials of Units 1 and 4 have relatively low permeabilities that are 3 to 6 orders of magnitude smaller than the internal sand. The steady-state hydraulic conductivity through the upper aquitard is two orders of magnitude higher than the lower silty aquitard, indicating that more frequent interaction occurs between infiltrating precipitation and the groundwater.

Table 2.2: Hydraulic conductivities and gradients of four hydrostratigraphic units (L. Neilson-Welch and Smith 2001).

Unit	Depth (m)	Hydraulic conductivity (m/s)	Gradient (m/m)
1	1-4	5×10^{-8}	NA
2	4-9	6×10^{-5}	10^{-4} to 10^{-5}
3	9-20	4×10^{-4}	10^{-4} to 10^{-5}
4	>20	1×10^{-10}	NA

2.4.3 Gradient

The local topography of the lower Fraser River delta is essentially flat, sloping 1-3° to the west (J.J. Clague 1998). The ground surface is approximately 1.5 m above the mean sea level, and the water table is about 1.5 m below the ground surface (L. Neilson-Welch and Smith 2001). The hydraulic gradient (i) in the sandy aquifer is low as expected, ranging from 10^{-4} to 10^{-5} (L. Neilson-Welch and Smith 2001).

2.5 Mineralogy

Simpson and Hutcheon (1995) documented and detailed the topset sediments and mineralogy down to a depth of 54 m at various locations on the Fraser River delta and off-shore areas adjacent to Sea Island. Simpson and Hutcheon (1995) classified the sediment into two categories, consisting of sand-rich and clay-rich sediments. This classification is consistent with previous seismic and stratigraphic investigations conducted on the Fraser River delta, which characterized fining upward sequences from bottom sand to the surficial clayey-silt (Williams and Roberts 1989; J.J. Clague et al. 1991).

The immature sandy sediment is made up of (by weight) 50-60% quartz, 30-40% feldspar, up to 15% mica or illite, and less than 2% chlorite, amphibole, and pyrite. The clay-sized sediment, in 0.2 to 2 μm size ranges, consists of 45% illite, 5-10% smectite and chlorite, 0-12% kaolinite, and 10% quartz

and feldspar fragments. In the $<0.2\ \mu\text{m}$ clay sized fraction, most of the sediment contains clay minerals, quartz, and even feldspar in trace amounts (G. Simpson and Hutcheon 1995).

Calcite has been detected in many of the sand samples, up to a maximum of 11% (by weight) (G. Simpson and Hutcheon 1995). Moreover, calcite cemented concretions and calcite concretions were found in the ancient buried channels and present day distributary tidal channels, respectively. These concretions suggest that the carbon is probably derived from the mechanism of methanogenesis in the mixing zone of seawater-meteoric water, which could provide the constantly renewed source of Ca^{2+} and HCO_3^- (G. Simpson and Hutcheon 1995).

Pyrite framboids were found in both sand and clay samples, suggesting precipitation of the iron monosulphides (FeS) and pyrite (FeS_2) in sediments. These sulfide minerals possibly precipitated as the dissolved Fe^{2+} reacted with the HS^- from bacterial mediated SO_4^{2-} reduction, since the dissolved Fe^{2+} has also been detected in groundwater in concentrations up to 70 mg/L (G. Simpson and Hutcheon 1995). Sulfate reduction is further supported by sulfur isotope differentiation, which shows the enrichment of ^{34}S in SO_4^{2-} in deep pore water samples at depths up to 8 m below ground surface. The enrichment of ^{34}S in residual SO_4^{2-} indicates the reduction of sulfate to sulfide by anaerobic bacteria that incorporates ^{32}S into solid sediments. Nevertheless, depletion of ^{34}S in residual SO_4^{2-} in some of the deepest samples is probably due to the preferential incorporation of ^{34}S into the mineral aggregation (G. Simpson and Hutcheon 1995).

Siliceous diatoms have also been noticed in both sand and clay sediments (G. Simpson and Hutcheon 1995), indicating that the groundwater is saturated with respect to silica (SiO_2). Quartz and clay minerals are probably the source of silica in sand and clay-rich sediments, respectively.

2.6 Field Site Description

The field study area, known as the Kidd 2 site, is approximately 380 m to the south of the north arm of the Fraser River, on LuLu Island (Figure 2.2), a deltaic island located in the lower mainland of the Fraser River delta. The site is owned by BC Hydro (the provincial power utility company),

and an active substation (Kidd 2 Substation) is installed on the western side of the property (Figure 2.3).

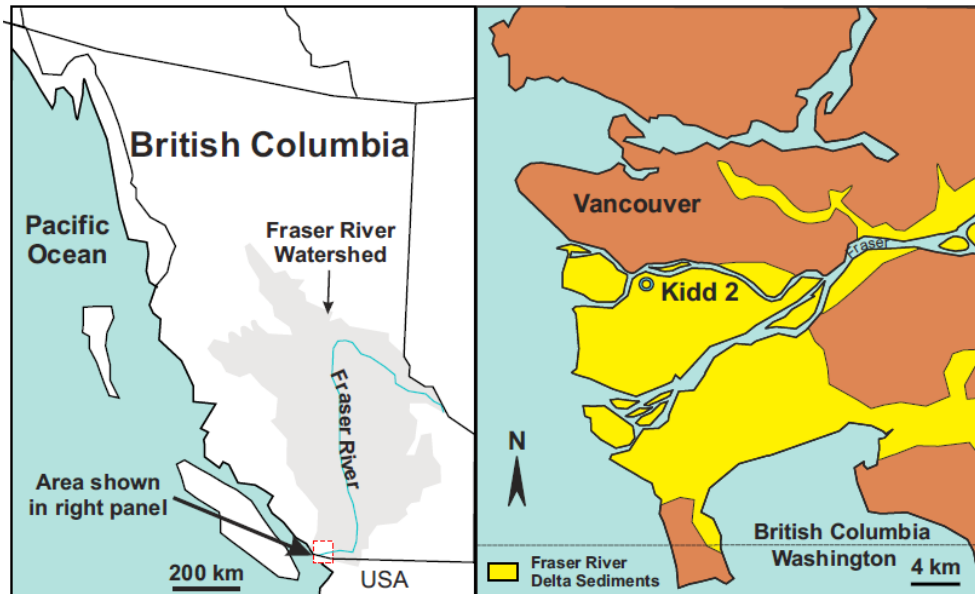


Figure 2.2: The Kidd 2 site is located in the Fraser River delta in south-west British Columbia.

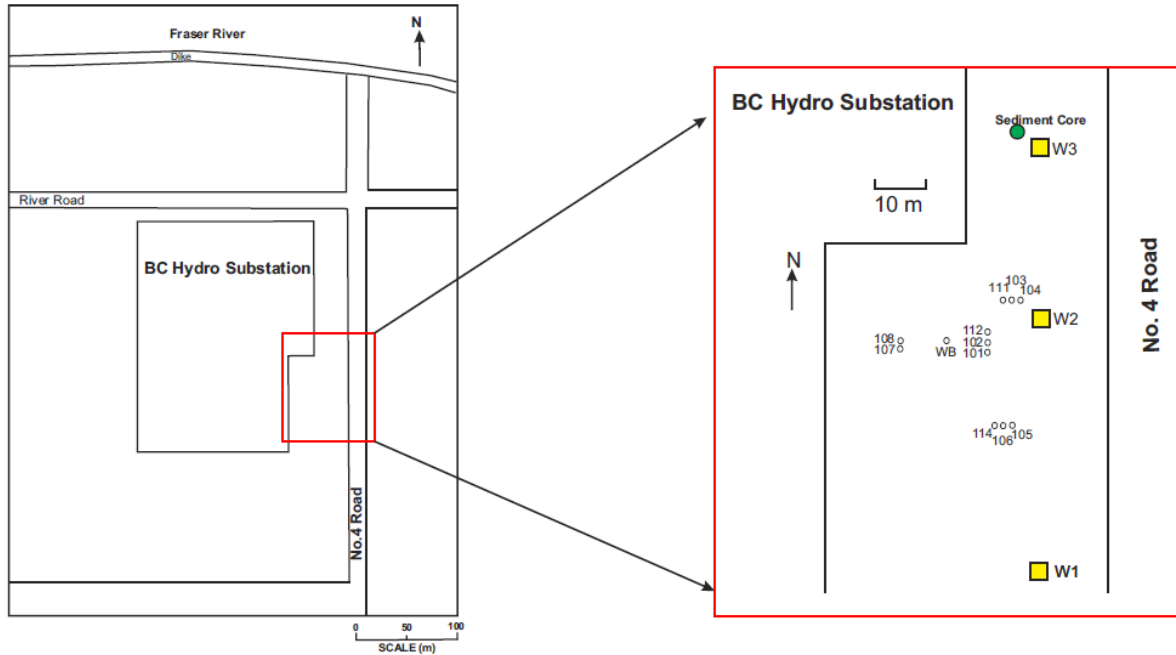


Figure 2.3: Plan view of well locations at the Kidd 2 site, including three multilevel wells (W1, W2, W3), eleven standpipe piezometers (BH 101-108, 112-114), and Westbay (WB) multilevel borehole; a sediment core, represented by green dot, was collected adjacent to W3.

Hydrostratigraphy and groundwater flow at the Kidd 2 site is well understood based on previous field investigations conducted by UBC's hydrogeology group. The local hydrostratigraphy and hydrological properties are similar to the Holocene topset sediment sequences discussed above (Table 2.1 and Table 2.2) (L. Neilson-Welch and Smith 2001). Nevertheless, no peat bog is found at the top of the Kidd 2 site.

Sea water from Georgia Strait migrates as far as 10 km inland along the Fraser River (J. A. Hunter 1994), leading to saline water intrusion in adjacent aquifers. Neilson-Welch and Smith (2001) developed a density-dependent groundwater flow model of the lower Fraser River sandy aquifer at the Kidd 2 site. Based on the estimated hydraulic conductivity and gradient in the sandy aquifer (L. Neilson-Welch and Smith 2001), and assuming a porosity of 0.3, the total travel time along the 1000 m saline wedge is approximately 240 years (See detailed calculation in Appendix A).

A plan view of the installed standpipe piezometers and multilevel wells at the Kidd 2 site is shown in Figure 2.3. The installations include three multi-level sampling wells (W1, W2, W3), eleven piezometers (101 to 108 and 111 to 114), and one West Bay multilevel sampling borehole (WB).

Each multilevel well has 15 sampling ports distributed at approximately 1 m intervals at depths from 8 to 22 m, though several ports from W1 and W2 were either damaged during installation or clogged and not operational (L. Neilson-Welch and Smith 2001). Until 2013, W1 and W2 had 12 and 6 functional sampling ports, respectively. A continuous sediment core was retrieved adjacent to W3 (Figure 2.3) to compare sediment properties with corresponding pore water geochemistry. The detailed description of core collection and information is discussed in Section 3.3.

The eleven standpipe piezometers are further categorized into three groups by their screen depth: shallow wells with screen depths of 3.5-5 m (111, 112, and 114), intermediate wells with screen depths of 11-13 m (102, 104, 106, and 108), and deep wells with screen depths of 16-18 m (101, 103, 105, and 107). Both intermediate and deep wells have screen lengths of 0.75 m, while shallow wells have screen lengths of 1.5 m (L. Neilson-Welch and Smith 2001). The Westbay multilevel borehole (L. Neilson-Welch and Smith 2001) consists of 12 sampling ports, covering depths of 2.5 m to 35.5 m. The deepest three sampling ports (23.5 m, 31 m, and 35.5 m) are within the bottom silty clay unit, and the rest of the sampling tubes span the internal sandy layer. Detailed well log information is in Appendix B. Regrettably the wells were destroyed in 2013 when the Kidd II substation was expanded.

Chapter 3: Methodology

3.1 Sample Collection

3.1.1 Water Sampling

A total of 51 water samples were collected from three multilevel wells (W1, W2, W3), eleven standpipe piezometers (BH 101-108, 112-114), and one Westbay (WB) multilevel borehole in April 2012 and another 33 samples, from W1, W2 and W3, were collected in September 2012.

Groundwater samples were gathered from all geological formations except for the surficial clayey silt. Details of the sampling wells and collected data are listed in Appendix C.

Low-flow peristaltic and Tornado pumps (Proactive Environmental Products Ltd) were used to draw groundwater from the ports of the multilevel monitoring wells and from mid-screen of the standpipe piezometers, respectively. Prior to the collection of water samples in the piezometers, Tornado pumps were placed approximately in the middle of the screened intervals and at least three volumes of water were purged. To collect the water that represents the formation pore water immediately in the vicinity of a well screen without significant disturbance, purging rates were controlled within 0.6 L/min. For multilevel wells, three tubing volumes of water were purged by peristaltic pump prior to the collection of representative groundwater samples. Groundwater sample collection began at the ports closest to the surface and moved progressively downwards to ports at greater depths.

Prior to collecting water samples, pH and temperature were measured and monitored in a sealed flow-through cell with an OAKTON™ pH/mV/°C 11 meter and probe, and conductivity was measured using a Hanna HI8733 electrical conductivity (EC) meter and probe. The pH meter was calibrated prior to measurements using standard calibration solutions of pH 4 and pH 7. Both pH and EC meters were temperature-correlated, and the calibrated slopes (%) for pH measurements were greater than 95%.

After the readings stabilized, flow-through parameters were recorded and groundwater samples were then collected in 80 ml high-density polyethylene (HDPE) bottles. For each sample location, three bottles of groundwater were collected. The samples were filtered through 30 mm diameter 0.45 μm cellulose filters using 60 ml syringes. Each bottle was filled completely and sealed with duct tape to inhibit oxidation and evaporation. The first bottle was used for anion analysis therefore no acid was added. The second sample was for cation analysis and was preserved with 1 ml of 50% HNO_3 to approximately pH 2. The third sample was collected for alkalinity, dissolved oxygen (DO) (for shallow samples only), and ammonia (NH_4^+) (described below) which were analyzed in the field immediately after collection.

In September 2012, 33 water samples were collected from the three multilevel wells W1, W2, and W3 at the Kidd 2 site for organic chemistry analysis. For each sampling port, two bottles of groundwater were collected. These samples were filtered with 30 mm 0.45 μm filters, and then stored in amber glass bottles with Teflon-lined caps. The first bottle was acidified with concentrated sulfuric acid (H_2SO_4) to approximately pH 2, and analyzed for dissolved organic matter (DOC). The second bottle of groundwater was collected for fluorescence spectroscopy analysis and contained no preservative agents. All samples were preserved at 4°C.

3.1.2 Gas Sampling

Methane (CH_4) was measured in multilevel well W3 and analyzed directly in situ by an LGR ultraportable greenhouse gas analyzer. The LGR gas analyzer could measure methane, carbon dioxide and water vapor simultaneously. The measurement range for CH_4 was 0.01-1,000mg/L¹. The measured vapor concentration was converted to its equilibrated dissolved aqueous concentration using Henry's law:

$$P = H \cdot S$$

¹ <http://www.lgrinc.com/analyzers/ultraportable-greenhouse-gas-analyzer/>

Where P is the vapor pressure (atm) trapped in the headspace, S is the solubility of the particular gas in solution, expressed as mole fraction (mol gas/mol solution), and H is Henry's law constant at a particular temperature (atm).

In this method, a headspace of gas in equilibrium with the solution is created by the partitioning of a volatile gas from its aqueous phase (Kampbell and McInnes 2003). Usually, the vapor is collected from the headspace in gas sampling bottles and delivered to a GC (Gas Chromatograph) for analysis. We modified a traditional headspace sampler so that it could directly connect to the LGR gas analyzer in the field and CH_4 concentrations could be analyzed simultaneously. At equilibrium, the concentration of the gas within the trapped volume is related to the dissolved aqueous concentration by Henry's law.

A plastic column capped with a two-hole silicone rubber stopper was used as a modified headspace sampler (Figure 3.1). Two glass tubes of different lengths were inserted into these two holes. The "gas out" tube was connected to the LGR gas analyzer while the "water in" tube was connected to a peristaltic pump. The "gas out" tube was shorter than the "water in" tube, in case water flowed back to the LGR gas analyzer.

A laboratory bracket held up the sampler column as the water sample was pumped through. As the water was moved through the column, the dissolved gas slowly diffused into the column's headspace until an equilibrium state was reached between the aqueous and vapor phases. A 2.5 L PYREX® beaker was placed underneath the column to collect the water sample. Since the "gas out" glass tube was connected to the LGR gas analyzer, the concentration of CH_4 trapped in the headspace could be directly analyzed and recorded. As the exchange between aqueous and vapor phases approached equilibrium, the concentration readings were expected to stabilize.

Groundwater samples were analyzed starting at the sample port closest to the ground surface and sampling progressed downwards in 1 m intervals. At each sampling port, pumping was continued for 30 minutes to maintain similar conditions at each sampling depth. For most ports; however, equilibrium was not established within the 30-minute period. One possible explanation is that the

headspace was not small enough and therefore most of the CH_4 remained dissolved in the water and did not diffuse into the headspace. Accordingly, the dissolved methane concentrations are qualitative, but as the same procedure was used to collect every measurement, the relative concentrations should be intercomparable.

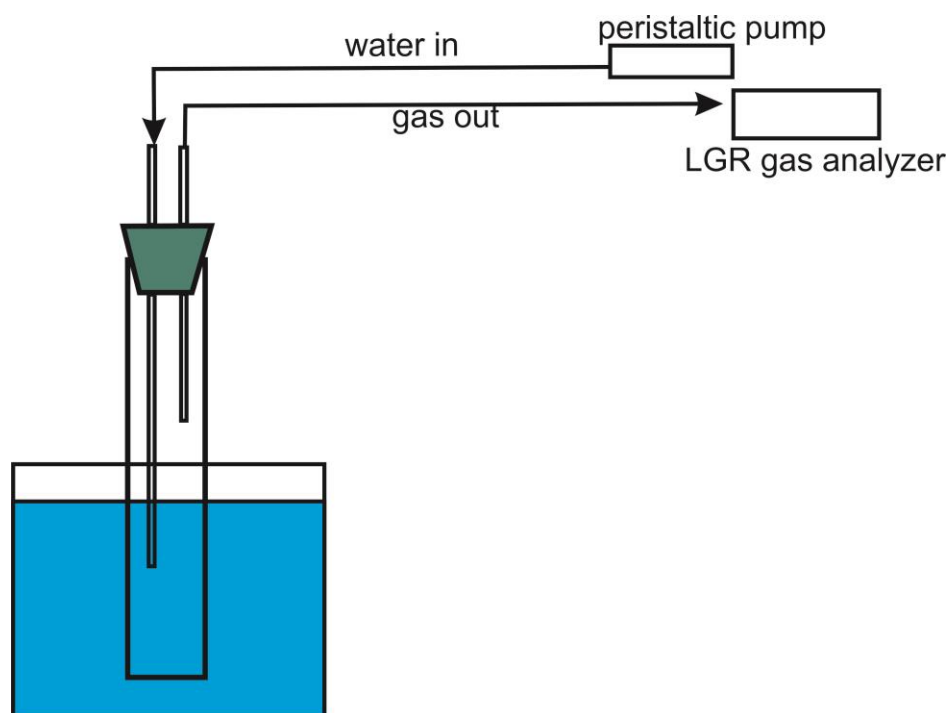


Figure 3.1: Schematic drawing of modified headspace sampler: water was pumped into the sampler through the peristaltic pump, and gas in the headspace was analyzed by the LGR gas analyzer.

3.1.3 Sediment Sampling

On January 21, 2013, a continuous sediment core was collected adjacent to multilevel well W3 (Figure 2.3) using a sonic drill rig operated by Sonic Drilling Ltd. An approximately 15 cm diameter core barrel of approximately 3.0 m length was first used to advance from the surface. As the core barrel was retrieved to the surface, the water and fine material typically drained from the sample. The core samples were then inserted into clear plastic sleeves. During the drilling process, the drill bit was sometimes pushed up and down, leading to core samples that were either compressed or

stretched under the intense vibration. Therefore, sample depths needed to be corrected according to the actual length of the core.

The sediment core was retrieved in 7, 10-foot sections from the ground surface to a depth of 21.3 m (70 ft), and the detailed core information is provided in Table 3.1.

Table 3.1: Sediment core collection

No.	Depth (m.b.g.s)	Interval (m)	Recovery %	Description
1	0.0 - 3.0	NA	60	Poor recovery, sediment was only collected at depth of 3.0 m (10 ft)
2	3.0 - 6.1	NA	22	Poor recovery, sediment was collected in the middle of the core as average
3	6.1 - 9.1	0.3	70	The topmost sediment from 6.1-6.5 m is compressed due to the clayey silty intervals with high water content
4	9.1 - 12.2	0.3	100	Medium sand, good recovery
5	12.2 - 15.2	0.3	100	Medium sand, good recovery
6	15.2 - 18.3	0.3	100	Medium sand, good recovery
7	18.3 - 21.3	0.3	90	The bottommost sediment at 21.3 m (70 ft) and below could not be collected since the drill intersected the lower silt layer

To avoid oxidation of the sediment samples at the Kidd 2 site the plastic sleeves were kept sealed until they were sub-sampled. For every sediment core, samples were collected in 0.3 m intervals from the core and placed in zip-lock bags. Each 0.3 m interval resulted in approximately 1 L of sample. The sediment bags were then immediately passed to the working area that was set up on a flat surface and equipped with an N₂ gas cylinder. Samples were purged with N₂ for at least 3 minutes to expel O₂. After purging, the zip-lock bag was closed, sealed with duct tape, and then frozen immediately in a cooler containing dry ice. Within 4 hours of collection, the core samples were transported back to the laboratory and stored in a freezer at -30°C.

To compare the effectiveness of the preservation process, a barrel of unpreserved sample was collected. The barrel of sediment was untreated and directly exposed to air. Unpreserved samples were then air-dried and homogenized using an agate mortar and pestle. The color of the unpreserved samples turned red, which was accredited to the oxidation of ferrous iron. In contrast, the treated sediment samples remained gray and black.

3.2 Sample Analysis

3.2.1 Water Sample Analysis

3.2.1.1 Field

Alkalinity was measured by Gran analysis on 25 ml of sample using 0.1872 N sulfuric acid (H_2SO_4), titrated with a Gilmont GS-1200A microburet. Dissolved oxygen (DO) was measured with CHEMets®K-7501 kits. Potential contamination from atmospheric O_2 and abundant ferrous iron indicates that DO is probably overestimated. Ammonia N-NH_4^+ concentrations were determined by a HACH DR/2010 spectrophotometer with the Nessler method (method 8038).

3.2.1.2 Laboratory

Groundwater samples from the Kidd 2 site were analyzed in the laboratory for concentrations of dissolved anions, dissolved cations, dissolved organic carbon (DOC), and water isotopes ($\delta^{18}\text{O}$ and $\delta^2\text{H}$).

Dissolved anions were analyzed with a Metrohm™ 861-Advanced Compact Ion Chromatograph (IC) at UBC's Ecohydro Laboratory. Fluoride (F^-), bromide (Br^-), chloride (Cl^-), nitrate (NO_3^-), nitrite (NO_2^-), phosphate (PO_4^{3-}), and sulfate (SO_4^{2-}), were analyzed with a detection limit of 0.01 mg/L. Saline groundwater samples with high concentrations of Cl^- and SO_4^{2-} , as indicated by electrical conductivity, required dilution before analysis. The anions were identified as peaks in a chromatogram, and quantification was done by measuring the peak areas. The analysis showed that F^- , Br^- , NO_3^- and NO_2^- were absent in all of the water samples; only Cl^- and SO_4^{2-} were detectable. Since some samples with high conductivity were diluted over 100 times, to meet the

requirements for the standard solutions, dilution may have caused considerable uncertainties. A “known addition” test was done to resolve the overlapping peaks and dilution uncertainties. Results showed that the error of Cl^- was within 1%. Nevertheless, the disagreement in measurements of SO_4^{2-} ranged from 10 to 15%, which suggests that the precision and bias of SO_4^{2-} must be considered. One possible reason for the large margin of error for SO_4^{2-} is the observed cap between the SO_4^{2-} signal curve and the baseline for some samples. The downward quadratic curve had a long tail on the right side, producing a non-negligible area under the curve. Since the instrument did not recognize this area, the measured SO_4^{2-} concentrations would be expected to be underestimated.

Concentrations of dissolved cations were analyzed with a Varian™ 725ES Inductively Coupled Plasma (ICP)-Atomic Emissions Spectrometer (AES), also known as an ICP-Optical Emissions Spectrometer (ICP-OES) at UBC’s Department of Earth, Ocean and Atmospheric Sciences. Nine elements were selected for analysis: calcium (Ca), sodium (Na), magnesium (Mg), potassium (K), iron (Fe), manganese (Mn), phosphate (P), sulfur (S), and silica (Si).

Concentrations of dissolved organic carbon (DOC) were analyzed with high temperature HACH™ IL 550 TOC-TN analyzers at the Environmental Engineering Laboratory in UBC’s Department of Civil Engineering. IL 550 TOC-TN analyzers are used to analyze the total organic carbon (TOC), which measures all carbon atoms covalently bonded in organic molecules. For this project, since water samples had already passed through 0.45 μm filters to remove particles, measured TOC values represented dissolved organic carbon (DOC). IL550 TOC-TN analyzers use a high-temperature combustion method to measure organic carbon in water, with a detection limit of 1 mg/l.

Oxygen isotopic composition ($\delta^{18}\text{O}$ and $\delta^2\text{H}$) for eleven selected water samples (BH112, W3-1, W3-2, W3-3, W3-4, W3-5, W3-7, W3-9, W3-11, W3-13, and W3-15) in a vertical profile were measured by the laser spectroscopic DLT-100 Liquid-Water Isotope Analyzer, developed by Los Gatos Research Inc. Water isotope ratios of oxygen ($^{18}\text{O}/^{16}\text{O}$) and hydrogen ($^2\text{H}/^1\text{H}$) are applied to determine the water provenance as well as the amount of mixing between two or more differing water sources. A comprehensive isotope analysis had been performed earlier at the Kidd 2 site

(Douglas 2011). The accuracy of the DLT-100 for clean or freshwater samples is within approximately $\pm 1\text{‰}$ for δD and $\pm 0.1\text{‰}$ for $\delta^{18}\text{O}$. For saline waters, the accuracy decreases to $\pm 2\text{‰}$ for δD and $\pm 0.25\text{‰}$ for $\delta^{18}\text{O}$, due to the optical interference from high salinity or other turbidity in saline water².

3.2.2 Sediment Sample Analysis

Sediment samples were analysed by kinetic extraction, sequential extraction, Fe(II) and Fe(III) speciation, acid volatile sulfide (AVS) determination, and solid organic matter quantification.

3.2.2.1 Kinetic Extraction

The chemical composition and reactivity of iron oxides in the sediments was analyzed using kinetic extractions (Postma 1993; Hyacinthe 2006; Larsen and Postma 2001). Postma (1993) used ascorbate at pH=3.0 to extract the iron oxide. Hyacinthe (2006) used three solutions to extract iron oxide, including: i) buffered ascorbate-citrate at pH=7.5, ii) ascorbate at pH=2, and iii) 1M HCl. The results show that the rate constants increase in order of: buffered ascorbate (pH 7.5) < ascorbate (pH 2) < 1M HCl. Hyacinthe (2006) argued that an ascorbate-citrate solution is the most appropriate method to quantify the reactive Fe(III) pool in estuarine sediments and that the time-dependent release of iron can be fitted quite well to a reactive-continuum model. The dissolution mechanism of the buffered ascorbate-citrate solution is ligand-enhanced reductive dissolution (Hyacinthe 2006). Ferric iron, Fe(III), is expected to be reduced to ferrous iron, Fe(II), and the amount of iron Fe(II) leached by the ascorbate-citrate solution can be easily measured and recorded. Dissolution-rate parameters can then be estimated by the least-squares fitting method.

Rate constants determined by ascorbate solution were usually found to be 1.1-2.4 times faster than those buffered ascorbate - citrate solution (Hyacinthe 2006). Therefore, the kinetic rates determined by these two extractions are similar, and can be used for comparisons between and within sediments. In Section 4.3.1.2, the kinetic parameters k' and γ for the selected six samples at the Kidd 2 site were compared to the extraction results from Postma (1993) and Hyacinthe (2006).

² <http://www.lgrinc.com/analyzers/isotope/>

Eight sample intervals (7.83 m, 10.97 m, 12.20 m, 15.54 m, 15.84 m, 19.30 m, and 21.33 m) were selected for kinetic extractions (Table 3.2). The extractions were performed in a vinyl glove box (Coy Laboratory Products) under an anaerobic condition. To create the anaerobic condition, the glove box was purged with a mixture of pure N₂ and N₂/H₂ until O₂ in the chamber was below 2%. A photograph of the anaerobic glove box is shown in Appendix D, photo 1. Distilled deionized water (DIW) was first bubbled with N₂ for at least half an hour to eliminate O₂ before transfer into the glove box.

Table 3.2: Kinetic extraction solutions and mechanism

Extractant	Extractant preparation	Extraction mechanism	References
Buffered ascorbate (10 g/l)	Sodium citrate (50 g/L) + sodium bicarbonate (50 g/L)	ligand-enhanced reductive dissolution	(Hyacinthe and Van Cappellen 2004), (Hyacinthe 2006)

Prior to extraction, frozen samples were transferred into the glove box and thawed. In the glove box, 1 L of ascorbate-citrate extractant solution was prepared, and continuously stirred by a suspended stir bar. Sediment kinetic extraction experiments were conducted in a 2 L cylindrical reactor at room temperature (Figure 3.2). At the bottom of the reactor, a 37 µm pore-size nylon mesh and a 10 µm-sized filter paper were attached to prevent any loss of sample and clogging of the sampling tubing. 1 L of anoxic pH=7.5 ascorbic-citrate solution was then added into the reactor. A mass of freshly thawed sediment was weighed and added to the reactor at time t=0. The reactor was then placed on a mechanical shaker to suspend the sediments in solution. During the 24 hours of the experiment, filtered samples (0.45 µm pore size) were periodically collected with a syringe through the tubing situated at the bottom of the reactor. These filtered samples were immediately acidified with a few drops of 50% HCl to a pH of approximately 2. Fe(II) and Mn(II) concentrations were later analyzed by a HACH DR2010 spectrophotometer, with the Ferrozine

method (method 8147) and the 1-(2-Pyridylazo)-2-Naphthol Pan method (method 8149), respectively.

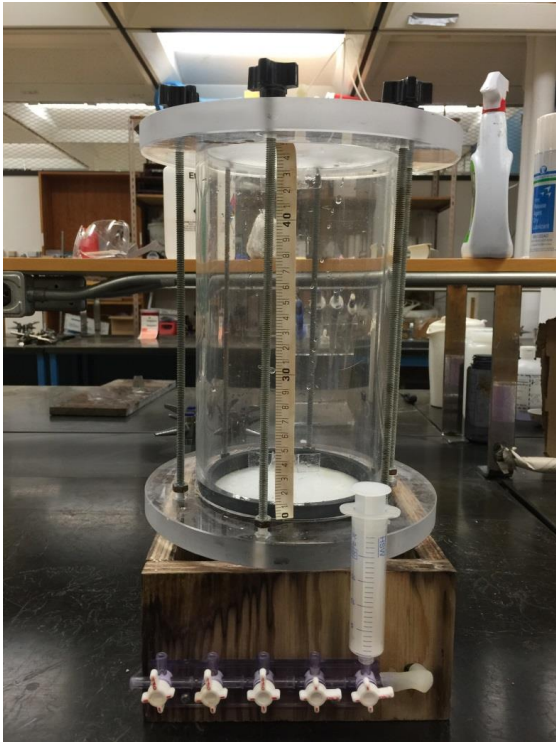


Figure 3.2: Kinetic extraction cylindrical reactor.

A reactive continuum model has been used to successfully fit iron/manganese dissolution curves of the dissolved metals to the total mass of reactive iron/manganese oxides over time (Hyacinthe and Van Cappellen 2004; Hyacinthe 2006). The dissolution curves $\left(\frac{M(t)}{M(0)}\right)$ are fitted with a simple Gamma-type reactive continuum distribution approach (Boudreau and Ruddick 1991) (Equation 3.1).

$$M(t) = M(0) \left(\frac{a}{a+t} \right)^v \quad \text{Equation 3.1}$$

where $M(0)$ is the initial mass (mol) of extractable iron/manganese present in the sediment sample, and $M(t)$ is the corresponding mass (mol) remaining at time t , and a and v are curve-fitting parameters. Equation 1 can be rearranged in the form of the general rate law for dissolution of

minerals under constant solution composition (Christoffersen and Christoffersen 1976), as shown in Equation. 3.2.

$$\frac{J}{M(0)} = k' \cdot \left(\frac{M(t)}{M(0)} \right)^Y \quad \text{Equation 3.2}$$

where k' is an initial rate constant at $\left(\frac{M(t)}{M(0)} \right) = 1$. J is the rate of dissolution (mol/s), and Y is the exponent that represents crystal geometry, the particle size distribution and the reactive site density (Larsen and Postma 2001). Postma (1993) found that $Y=1.1$ for ferrihydrite reduction by ascorbic acid at pH=3. Equation 3.2 can be integrated to give equations 3.3 and 3.4 (Larsen and Postma 2001).

$$\text{For } Y=1: \frac{M(t)}{M(0)} = e^{-k't} \quad \text{Equation 3.3}$$

$$\text{For } Y \neq 1: \frac{M(t)}{M(0)} = [-k'(1 - Y)t + 1]^{\frac{1}{1-Y}} \quad \text{Equation 3.4}$$

Equation 3.4 was fitted to the time-dependent mineral dissolution data to determine optimized parameters Y , k' and $M(0)$, using Matlab statistical curve fitting. The lower and upper limits for parameters were constrained for 95% confidence intervals. Figure 3.3 shows an example of the Matlab curve fitting for time-dependent mineral dissolution.

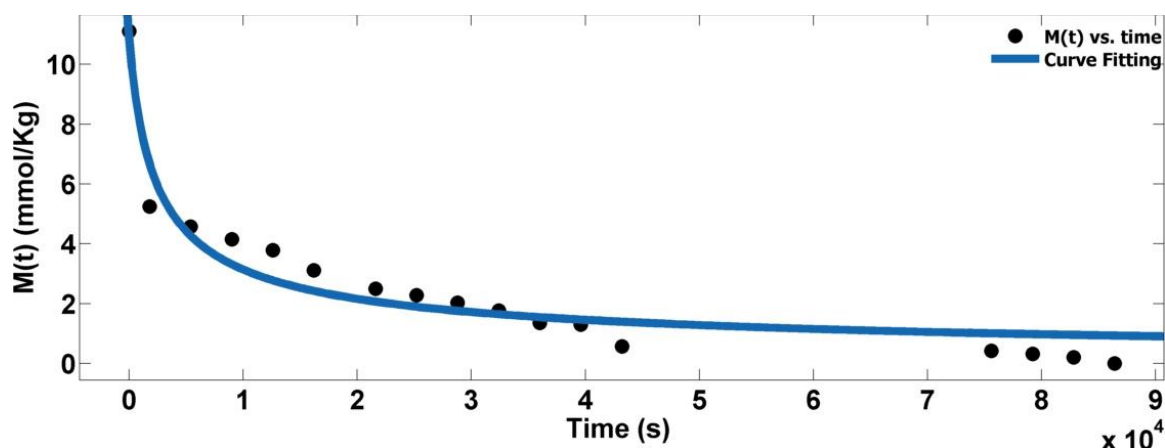


Figure 3.3: Curve fitting for reactive iron oxides dissolution at the Kidd 2 site (depth of 12.20 m) during the ascorbate-citrate extraction for 24 hours. $M(t)$ (mmol/kg) is the residual iron oxides mass left in the extractant, and $t(s)$ is the extraction period. Y , k' and $M(0)$ were determined by Matlab statistical curve fitting.

3.2.2.2 Sequential Extraction

Sequential extraction procedures (SEPs) were used to differentiate pools of iron and manganese oxides and their contributions to the soluble species. Manganese (Mn) has similar chemical properties and ionic radii to iron (Fe), and both of them form mixed oxides. Mn and Fe were grouped together in our sequential extractions.

Although SEPs have been widely used in research and the mining industry to characterize the partitioning of heavy metals or mineral phases in buried deposits, no well-accepted standard procedure is associated with each specific phase. Moreover, a series of successive chemical extractants usually has different dissolution mechanisms and intensities. Therefore, the order and type of chemical treatments must be carefully selected to meet the specific objectives (Hall et al. 1996). The amorphous iron oxides have been shown to be chemically more reactive or susceptible than the crystalline forms, and can therefore be separated on this basis. Table 3.3 summarizes the published SEPs for different iron oxides, depending on their crystallinity.

Our research objective is to characterize Fe and Mn pools. Based on sample types and compositions at the Kidd 2 site, in combination with our research objective, a specific 4-step SEPs

scheme (Table 3.4) was developed. The evaluated pools were ion-exchangeable iron oxides (1M CaCl_2), reactive iron oxides (0.5M HCl), crystalline iron oxides (1.0 M $\text{NH}_2\text{OH}\cdot\text{HCl}$ in 25% CH_3COOH), and non-reactive iron oxides (1:1 full strength HCl- HNO_3 Aqua Regia solution).

Table 3.3: A summary of published SEPs to differentiate iron oxides

Target phase	Extractant	Extraction procedures	Reference
Absorbed/ exchangeable fraction	1.0 M CaCl_2	pH=7, 24 h, room temperature	(Heron et al. 1994), (Tessier, Campbell, and Bisson 1979)
	1.0 M HOAc	pH=5, 6 h, room temperature	(Hall et al. 1996; Tessier, Campbell, and Bisson 1979)
Reactive iron oxides	0.25 M $\text{NH}_2\text{OH}\cdot\text{HCl}$ -0.25 M HCl	at 50°C, 30 min extract amorphous Fe oxide, degree of dissolution of the crystalline Fe oxides below 1% total Fe.	(Chao and Zhou 1983)
	Ascorbate-citrate acid	pH=8, 24 h, room temperature	(Hyacinthe and Van Cappellen 2004; Hyacinthe 2006)
	0.5 M HCl	24 h, room temperature, Best for only amorphous Fe oxides	(Heron et al. 1994),(Lovley and Phillips 1986a)
Crystalline iron oxides	0.175 M Ammonium Oxalate $(\text{NH}_4)_2\text{C}_2\text{O}_4$ in 0.1 M Oxalic Acid $\text{H}_2\text{C}_2\text{O}_4$,	pH=3, 4 h, room temperature, in dark Extract amorphous Fe oxides in the absence of magnetite and organic complexes	(Sondag 1981),(Chao and Zhou 1983)
	Dithionite-citrate $(\text{Na}_2\text{S}_2\text{O}_4)$ buffer("DCB") in 0.2 M sodium acetic acid	pH=4.8, 30 min, at 50°C The degree of dissolution of hematite and goethite possibly over 100% if grinding is not applied.	(Coffin 1963),(Chao and Theobald 1976)
	1.0 M $\text{NH}_2\text{OH}\cdot\text{HCl}$ in 25% HOAc	pH=4.8, 3 h, at 90°C	(Hall et al. 1996)
	0.005 M Ti(III) - citrate- EDTA-bicarbonate	pH=7, 2 h, room temperature	(N.E.Keon 2001)

Target phase	Extractant	Extraction procedures	Reference
Residual non-reactive iron oxides	HF - HClO ₄	Total digestion	(Tessier, Campbell, and Bisson 1979)
	HCl - HNO ₃	For 5 h at 80°C Aqua Regia (1:1 full strength HCl-HNO ₃ acid solution)	(Horneman, van Geen, et al. 2004)

Table 3.4: Four-step SEPs were performed in an anaerobic glove box to extract iron oxides, consisting of ion exchangeable, reactive, poorly reactive, and non-reactive iron oxides.

Step	Target Phase	Procedures	SSR ^a (g:ml)	Extraction mechanism
1	Ion exchangeable ions	1 M CaCl ₂ , room temperature, 24 h rotation, 2 DIW rinse at end	0.4:40	cation exchange for replacing exchangeable metals
2	ferrihyrite and partly akagenite (βFeOOH), best for amorphous Fe oxyhydroxides	0.5 M HCl, room temperature, 24 h rotation, 2 DIW rinse at end	0.4:40	Proton dissolution Fe-Cl complexation
3	Intermediate in crystallinity between amorphous iron oxides and crystalline iron oxides	1.0 M NH ₂ OH.HCl in 25% CH ₃ COOH, water bath at 90°C for 3 h, 2 times with 25% CH ₃ COOH rinse at end, 1-1.5 h repetition	0.4:40	Reduction of Fe(III) to Fe(II)
4	Total extractable iron oxides	Aqua Regia (1:1 full strength HCl-nitric acid solution, water bath at 80°C for 5h)	0.4:40	Proton dissolution Total digestion

Note: ^a solid – solution ratio

The extractant reagents that were used in the SEPs were “analyzed reagent” grade and all extractant solutions were made in the glove box to avoid contact with oxygen. All glassware was soaked with 10% (v/v) HNO₃ and rinsed with DIW to avoid metal contamination. All leaches were performed in high density polypropylene HDPE centrifuge tubes. The water content was determined for distinct samples by the oven-drying method. For sequential extractions, freshly thawed samples were used and the results were converted to dry mass concentrations using the measured water content.

A total of 42 sediment samples were analyzed from depths of 6.10 m to 21.34 m, in intervals of 0.30 m. For each sample, approximately 1 g of wet sediment was transferred into a 50 ml HDPE centrifuge tube, and the sample mass was determined. To track mass loss during extractions, the mass of each centrifuge tube was recorded before and after each new extractant addition. Once a certain amount of each extractant was added to moisten the sediments in the centrifuge tubes, the tubes were sealed, moved into a test-tube holder, and put on a mechanical shaker for the required extraction time. The first two steps were performed in the glove box. Steps 3 and 4 were completed in a water bath outside of the glove bag. After completing each extraction step, the samples were centrifuged at 2,500 rpm for 30 minutes. The samples were then transferred back into the glove box and the supernatants were decanted into 60 ml syringes and filtered with 30 mm 0.45 μ m cellulose-acetate filters. The extractant solutions were then stored in plastic sample bottles and preserved with HNO_3 to a pH of approximately 2. Before adding the next extractant into the HDPE centrifuge tubes, the sediments were rinsed twice with 5 ml DIW followed by 10 minutes of centrifugation, in case any residual extractant solution remained in the tubes that might result in impurities in the next extraction. The SEP extractant solutions were analyzed by ICP-OES for concentration of metals, including Fe, Mn, As, S, Si, Mg, K, Na, P, and Al.

3.2.2.3 Fe (II) and Fe (III) Speciation

The second 0.5 M HCl step preserves the oxidation state of iron. Both Fe(III) from amorphous hydrous iron oxides and Fe(II) from other secondary minerals were released into the extractant solution. Total Fe was analyzed by ICP-OES. Iron speciation was measured immediately after the HCl extraction by the ferrizone method with an HACHTM DR/2010 spectrophotometer (method 8147). Samples were diluted 10 to 50 times to bring iron concentrations below 1.4 mg/L (the maximum analyzed concentration).

3.2.2.4 AVS (Acid Volatile Sulfide) Determination

In parallel to the sequential extractions, a separate one-step acid volatile sulfide (AVS) extraction was performed to quantify iron monosulfides, FeS, in the sediments under the assumption that AVS is equal to FeS. 1M HCl was used as the extractant as it attacks amorphous sulfides in the

sediments but does not dissolve crystalline sulfides (Keon et al. 2001). Released H₂S gas is trapped by a zinc acetate solution to form ZnS precipitates, which were quantified by the methylene blue method (Cline, 1969).

3.2.2.5 Sedimentary Organic Matter - Loss on Ignition

Solid organic matter content (%OM) was determined by Loss on Ignition (LOI) analysis at the Environmental Engineering Laboratory in UBC's Department of Civil Engineering. %OM is represented by the weight loss on ignition at 550° C.

In preparation for the LOI analysis, frozen samples were transferred into the glove box, and approximately 5 g of wet soil samples were passed into heavy-duty sample bags. These soil samples were then characterized by two analyses: water content determination and loss on ignition analysis. First, well-mixed moist samples were placed in a weighed aluminum boat and dried to a constant weight in an oven at 103-105°C overnight. The percentage moisture was calculated from the difference between the pre- and post-oven weights of the aluminum boats. For the second analysis, the dry samples were weighed again and baked at 550° C for another 3 hours. After completing the ignition, samples were re-weighed and the final weights were recorded. Organic matter contents were determined by the difference between dry weight and final weight.

3.2.3 SEM/EDX Analysis

In an attempt to characterize iron and manganese minerals and their secondary phases, eight sediment samples were collected at the Kidd2 site at various depths (7.84 m, 8.71 m, 11.89 m, 12.19 m, 13.11 m, 17.06 m, 20.11 m, and 21.33 m) and coated with evaporated carbon (Edwards Vacuum Coater Auto 306) before being analyzed by the Philips XL30 scanning electron microscope (SEM), equipped with a Bruker Quantax 200 energy-dispersive X-ray spectrometer (EDX) and light element XFLASH® 4010 Silicon Drift Detector (SDD).

During the SEM process, a focused electron beam with small spot size was used to scan the mineral surfaces, producing sharp images of high resolution. Backscattered electrons (BSE) are also generated by the scanning beam and these signals were collected by detectors for qualitative analysis. Approximately 60 spots of interest (white color spots) from the 8 samples were observed by BSE images to identify iron- and manganese-bearing minerals. The chemical compositions of the selected spots were obtained by EDX microanalysis. This approach, combined with previous macroscopic observations made by Mark Bolton (2004) provided a more complete picture of the processes involved in iron and manganese reduction, and in organic matter oxidation.

3.2.4 Dissolved Organic Matter Analysis

Dissolved organic matter (DOM) has been recognized for its biogeochemical significance in the cycling between metals and organic matter in anoxic environments since it is the major source for bacteria metabolism. To better characterize biogeochemical characteristics of DOM and trace their compositional changes in a highly dynamic ecosystem, fluorescence spectroscopic techniques and the PARAFAC model has been used in this study.

3.2.4.1 Florescence Analysis

All Fluorescence spectra were obtained by using a Horiba Aqualog® (Horiba Scientific, Edison, NJ, USA) spectrofluorometer, equipped with subtractive double excitation monochromators. A 150 W ozone-free vertically mounted xenon arc lamp was used as the excitation source. Figure 3.4 illustrates the principle of the fluorescence spectroscopy. Fluorescence is a photoluminescence process in which molecules are excited to higher energy levels by absorption of energy from the excitation light source. As the excited molecules return to their ground states, energy is lost as photons or fluorescence, and captured by the fluorescence detector (Fellman, Hood, and Spencer 2010). The fluorescence emission is measured at a right angle to the light source, to avoid measuring incident radiation. As molecules with specific structures would be excited and would re-emit at certain wavelengths, the excitation and emission wavelengths of fluorescence occur with a specific relation to the organic compounds. A spectrofluorometer measures molecular

fluorescence as three-dimensional excitation-emission matrices (EEMs) (Coble et al. 1990), where a series of emission spectra are continuously collected over a range of excitation wavelengths.

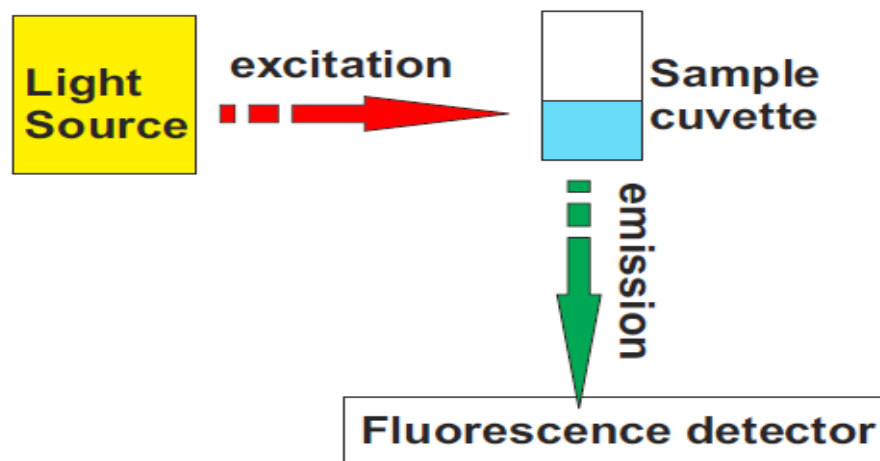


Figure 3.4: Principle of fluorescence spectroscopy. As a molecule or atom absorbs energy from the light source, an electron is excited to a higher energy level. When the electron returns to its ground energy level, energy is lost as photons or fluorescence, and captured by the fluorescence detector (Fellman, Hood, and Spencer 2010).

In this study, fluorescence EEMs were created for a total of 32 water samples that had been collected from multilevel wells (W1, W2, and W3) at the Kidd2 site. Both excitation and emission were set up with a bandpass at 5 nm. Fluorescence intensities are a function of the excitation and emission wavelengths, measured across excitation wavelengths ranging from 240 to 600 nm in 3 nm increments and emission wavelengths ranging from 212 to 621 nm over an integration time of 0.5 s. The excitation spectra and the emission spectra are parallel to the x-axis and y-axis, respectively. Therefore, every EEM consists of 121 excitation and 125 emission spectra, resulting in discrete measurements at 15,125 excitation/emission wavelength pairs.

To eliminate the Rayleigh scatter and the water Ramen peak, organic-free DI water was used as the “blank” and the fluorescence EEM spectra for each sample was obtained by subtracting the DI water (blank) spectra automatically. Water samples were analyzed in 1 cm quartz cuvette (10 ml). Between each sample, the quartz cuvette was rinsed 3-times with DI water, followed by 3-times

with the sample to reduce possible cross-contamination. To minimize the inner filter effects (IFE), as described by Spencer, Bolton, and Baker (2007), water samples were diluted with DI water if necessary until the UV absorbance was below 0.2 units at 254 nm. Finally, all EEMs were normalized to the integrated area under the maximum fluorescence intensity at excitation 350 nm (Lawaetz and Stedmon 2009). In this way, the fluorescence intensities were presented in Raman Units (R.U.). In addition, two water samples (W103 and W314) were analyzed in duplicate, to check the reliability of results.

3.2.4.2 PARAFAC Model

The parallel factor analysis (PARAFAC) model is a statistical tool that uses EEM datasets, and decomposes the dataset into different fluorescent groups (components), based on their unique spectra shapes. Therefore, each component gives rise to a unique excitation and emission spectrum, and can be considered as a single fluorophore or as a group of similar fluorophores (Cory and McKnight 2005). In this study, the corrected EEMs of 32 groundwater samples were subsequently entered into MATLAB (Mathworks, Natick, MA) and the EEM datasets were resolved into 13 components in the PARAFAC model (Cory and McKnight 2005). Each component was presented as its relative distribution (% of total) for a given sample. No obvious residues were found after adapting the EEM dataset into the PARAFAC model, indicating that the 13-component model was suitable for decomposing the groundwater DOM at the Kidd 2 site.

Of the 13 components, 7 were identified as quinone moieties, which have been shown to attribute to the electron-shuttling ability of humic and fulvic acids (Lawaetz and Stedmon 2009). Based on their redox state and shifts in fluorescence spectra, two sub-groups have been further classified, including three oxidized quinones (Q1, Q2, and Q3) and four reduced quinones (SQ1, SQ2, SQ3, and HQ) (Cory and McKnight 2005). To quantify the redox state of the quinone moieties, Miller et al. (2006) defined a Redox Index (RI), which is determined by the ratio of the sum of reduced quinone-like inputs to total quinone-like inputs. Besides the quinone-like components, two components resemble amino acids (C8 tryptophan and C13 tyrosine), and the four remaining

components are unknown (C1, C3, C6, and C10) and also included in the PARAFAC model (Cory and McKnight 2005).

Chapter 4: Results

4.1 Groundwater Geochemistry

4.1.1 General Porewater Geochemistry

Table 4.1 presents the field measured parameters including pH, temperature, electrical conductivity, dissolved oxygen (DO) and flow rate, and Table 4.2 presents the concentrations of dissolved cations, anions, dissolved organic carbon (DOC), and bicarbonate (HCO_3^-). A sample calculation for the alkalinity titration and associated data are presented in Appendix E.

Table 4.1: Field measured parameters in 11 standpipes, and three multilevel wells (W1, W2 and W3)

Sample ID	Depth (m)	pH ^a	Electrical conductivity ^b ($\mu\text{S}/\text{cm}$)	Temperature($^{\circ}\text{C}$) ^c	DO (mg/l) ^d	Flow rate ^e (L/min)
BH101	17.25	7.04	2220	12.1	0	0.54
BH102	11.33	6.64	17250	13.7	0.05	0.11
BH103	17.30	7.14	42000	NA	0	0.27
BH104	12.09	6.82	20160	12.2	0	0.15
BH105	17.36	6.73	27210	11.38	0	0.60
BH106	11.99	6.36	22800	NA	0	0.10
BH107	17.24	7.01	19250	12.9	0	0.11
BH108	12.24	6.28	12920	16.2	0	0.42
BH111	4.50	6.46	1064	12.3	0.09	0.58
BH112	4.50	7.40	682	NA	0.08	0.63
BH114	4.72	6.39	628	NA	0.11	0.44
W1-1	8.08	6.56	2420	12.2	0.1	0.60
W1-3	10.08	6.43	15890	12.1	0	0.37
W1-6	13.07	6.72	24800	11.8	0	0.58
W1-7	14.08	6.90	23500	11.5	0	0.10
W1-8	15.08	6.90	23900	11.6	0	0.10
W1-9	16.17	6.79	NA	NA	0	0.10
W1-10	17.08	6.80	24100	NA	0	0.10
W1-11	18.08	6.87	24200	NA	0	0.08
W1-12	19.08	6.98	23900	11.5	0	0.08
W1-13	20.06	7.02	24000	11.6	0	0.10
W1-14	21.07	7.09	24000	11.4	0	0.10
W1-15	22.03	7.17	23900	11.4	0	0.09
W2-1	8.04	6.49	899	11.6	1.05	0.07
W2-3	10.05	6.46	39700	NA	0	0.47
W2-10	17.09	6.98	24700	11.8	0	0.50
W2-11	18.09	7.03	24900	11.7	0	0.47
W2-13	20.09	7.06	24900	11.9	0	0.46
W2-14	21.09	7.14	23600	11.6	0	0.30
W3-1	8.08	6.70	1041	12.2	0.13	0.46
W3-2	9.07	6.60	828	13.1	0.01	0.45
W3-3	10.08	6.55	848	11.6	0	0.43
W3-4	11.08	6.55	1013	11.3	0	0.52
W3-5	12.08	6.43	12310	11.8	0	0.37
W3-6	13.07	6.82	19080	11.4	0	0.10
W3-7	14.08	6.46	22400	11.2	0	0.23
W3-8	15.08	6.78	22300	11.7	0	0.44
W3-9	16.17	6.78	24100	11.3	0	0.23
W3-10	17.08	6.82	24100	12.1	0	0.56
W3-11	18.08	6.86	22500	11.5	0	0.45
W3-12	19.08	6.98	17890	11.4	0	0.32
W3-13	20.06	7.27	11220	11.8	0	0.45
W3-14	21.07	7.44	4890	10.9	0	0.48
W3-15	22.03	7.57	3790	10.5	0	0.41

Note: ^{a, c}: measured with OAKTON™ pH/mV/°C meter in a flow-through cell

^b: measured with Orion™ model 115 conductivity meter in a flow-through cell

^d: measured with Geotech™ peristaltic pump, running with medium to full speed

^e: measured with CHEMets®K-7501 k

Table 4.2: Concentrations of cations, anions, DOC, and HCO_3^- in 11 standpipes, and three multilevel wells (W1, W2 and W3)

	Cation ^a								Anion ^b		Alkalinity ^c	Organic carbon ^d	Methane ^e
Sample	Na^+	Mg^{2+}	Ca^{2+}	K^+	Mn^{2+}	Fe^{2+}	Si	S	Cl^-	SO_4^{2-}	HCO_3^-	DOC	CH ₄
ID	(mg/L)	(mg/l)	(mg/L)	(mg/L)	(mg/L)	(mg/L)	(mg/L)	(mg/L)	(mg/L)	(mg/L)	(mg/L)	(mg/L)	(mg/L)
BH101	4235	691	62.1	5.7	2.8	62.1	39.1	409	8725	498	331	NA	NA
BH102	2901	494	265	5.6	1.1	265	47.6	195	7317	257	622	NA	NA
BH103	4316	714	62.6	5.8	3.6	62.6	38.0	431	9610	564	170	NA	NA
BH104	3113	543	172	5.4	3.3	172	45.0	137	7443	218	872	NA	NA
BH105	4265	704	37.1	6.1	3.4	37.1	36.9	412	9420	505	361	NA	NA
BH106	3717	607	98.2	6.5	4.2	98.2	44.0	229	8609	304	616	NA	NA
BH107	4128	706	60.4	6.1	4.8	60.4	40.3	216	9057	267	664	NA	NA
BH108	1721	360	436	4.0	0.9	435	51.9	252	4045	401	259	NA	NA
BH111	107	56.9	67.2	3.0	1.0	67.2	69.0	26.3	97.8	54.2	539	NA	NA
BH112	94.0	56.0	85.6	0.3	1.1	85.6	68.5	9.2	93.0	36.3	569	NA	NA
BH114	23.1	48.7	26.2	0.3	1.7	26.2	77.0	3.6	51.8	32.3	272	NA	NA
W1-1	139	39.8	63.2	4.4	0.9	63.2	23.7	436	8535	539	36.0	28.9	NA
W1-3	2296	479	311	5.4	4.5	311	33.8	21.9	121	33.4	469	7.1	NA
W1-6	4019	664	60.3	7.0	1.9	60.3	23.3	270	5845	504	212	6.3	NA
W1-7	3821	699	61.9	6.8	1.5	61.9	34.3	299	9054	408	546	7.5	NA
W1-8	4040	697	61.3	6.8	1.4	61.3	33.7	296	9018	419	614	7.0	NA
W1-9	4107	686	69.2	6.7	1.5	69.2	33.6	303	8702	400	627	7.4	NA
W1-10	4304	685	66.3	7.0	1.6	66.3	32.2	295	8400	393	637	7.7	NA
W1-11	4173	703	61.8	7.1	1.8	61.8	31.8	299	8800	398	633	6.9	NA
W1-12	4095	734	82.7	6.9	1.8	82.7	32.3	299	8701	395	536	6.6	NA
W1-13	4010	620	65.1	6.8	2.0	65.1	31.1	311	9577	410	527	6.6	NA
W1-14	3933	673	71.1	7.6	2.2	71.1	15.7	288	8698	365	550	6.0	NA
W1-15	4094	698	66.5	7.8	2.8	66.5	29.7	294	8836	425	389	6.7	NA
W2-1	59.4	50.5	63.9	2.3	1.1	63.9	28.1	310	8519	411	550	26.3	NA
W2-3	580	141	250	1.9	3.6	250	33.2	6.3	56.0	13.1	514	13.4	NA
W2-10	4237	729	59.9	5.3	3.3	59.9	57.7	95.1	1577	187	315	6.4	NA
W2-11	4201	754	63.6	5.7	3.4	63.6	38.3	439	9032	604	302	6.1	NA
W2-13	4452	694	57.5	6.5	4.2	57.5	35.3	448	8879	563	289	5.8	NA
W2-14	4181	677	50.7	7.2	4.8	50.7	31.0	400	8921	556	286	4.4	NA

Sample	Na ⁺	Mg ²⁺	Ca ²⁺	K ⁺	Mn ²⁺	Fe ²⁺	Si	S	Cl ⁻	SO ₄ ²⁻	HCO ₃ ⁻	DOC	CH ₄
ID	(mg/L)	(mg/L)	(mg/L)	(mg/L)	(mg/L)	(mg/L)	(mg/L)	(mg/L)	(mg/L)	(mg/L)	(mg/L)	(mg/L)	(mg/L)
W3-1	53.2	44.7	43.0	0.3	0.9	43.0	29.7	398	9166	503	212	26.0	NA
W3-2	51.1	44.8	44.0	0.3	1.0	44.0	68.6	11.3	50.3	37.3	437	22.7	2.3
W3-3	52.2	49.0	53.3	2.3	1.1	53.3	69.8	10.4	42.2	35.1	495	23.0	7.9
W3-4	131.4	58.6	123	0.5	1.7	123	30.8	8.9	54.1	39.6	427	22.9	6.1
W3-5	1756	347	307	33.9	3.5	301	65.4	21.1	252	46.7	423	11.9	6.2
W3-6	3154	590	108	54.1	1.4	108	51.6	136	4128	367	498	11.0	4.9
W3-7	3850	604	90.0	53.6	1.9	90.0	44.6	295	7411	377	587	8.4	4.6
W3-8	4053	575	49.7	50.3	4.4	49.7	45.9	405	8702	507	192	5.4	6.8
W3-9	4451	600	44.1	47.7	6.7	44.1	20.4	390	7678	495	132	6.0	8.8
W3-10	4281	610	45.8	53.2	6.2	45.8	18.5	396	9349	521	213	5.0	14.1
W3-11	3956	578	39.4	63.5	5.7	39.4	17.3	393	8736	469	212	6.0	18.3
W3-12	2966	450	22.4	65.1	3.9	22.4	16.1	331	8465	404	440	7.5	25.1
W3-13	1905	402	10.5	70.8	3.0	10.5	13.9	226	6424	260	424	9.4	2.3
W3-14	786	43.8	1.3	36.2	0.2	1.3	12.1	177	4480	250	534	10.7	7.9
W3-15	723	29.1	9.4	2.9	0.0	9.4	11.4	0.9	1669	71.4	707	11.1	6.1

Note: ^a: concentration of cations determined by ICP-OES

^b: concentration of anions determined by IC

^c: concentration of bicarbonate determined by Gran titration method

^d: concentration of DOC determined by IL-550 TOC-TN analyzer, using high temperature combustion method

^e: concentration of CH₄ determined by LGR gas analyzer, which measured vapor concentration

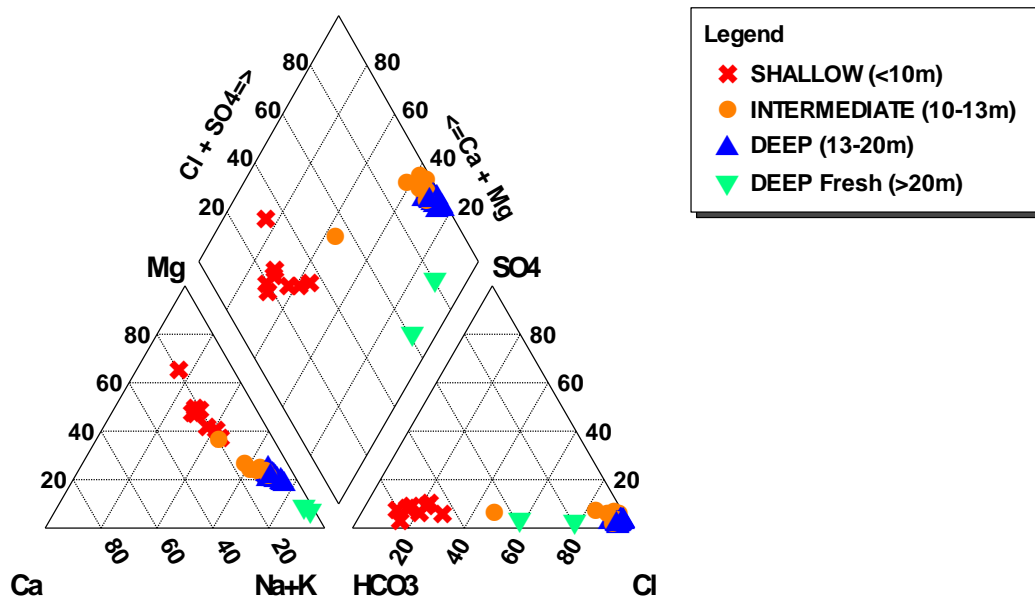


Figure 4.1: Piper plot for groundwater samples from the Kidd 2 site

We assume that the groundwater geochemistry is not changing significantly over the timescale of this study (12 – 18 months), and that the results here represent a relatively steady snapshot in time. This assumption is acceptable because the saline circulation formed thousands of years ago, and transit time for the saline circulation is approximately 250 years. Variations due to seasonal changes and daily tidal fluctuations are not significant. Charge-balance errors for all water samples were within 5%, and considered acceptable. Whereas missing organic acids would normally provide for excess positive charge (Oliver, Thurman, and Malcolm 1983), most charge-balance errors are negative, indicate missing cations.

The major-species groundwater geochemistry for all the monitoring wells at the Kidd 2 site is plotted in Figure.4.1 on a Piper plot. Based on water depth, four different groundwater types have

been recognized, including shallow fresh groundwater (<10m), intermediate water at the upper mixing zone (10-13m), deep saline water (13-20m) and deep fresh groundwater from the lower confining silt layer (>20m). It is observed that the shallow fresh groundwater, intermediate water and the deep ocean water lay on an approximate mixing line (Figure.4.1). As ocean water infiltrates into the sandy aquifer, the water type changes from ocean dominant (Na-Mg-Cl) to carbonate dominant (Ca-Mg-HCO₃⁻). Moreover, it clearly shows that the deep freshwater does not follow the mixing line, and therefore has relatively minor impact on the major-element chemistry of the aquifer.

The DO for most of groundwater samples was below the detection limits, except for the shallowest wells. The dissolved Fe(II) and Mn(II) concentrations in groundwater were estimated to be 10 to 350 mg/L, and 0.01 to 6.7 mg/L, respectively. The absence of oxygen and presence of dissolved Fe(II) and Mn(II) indicates that the groundwater is anaerobic and reduced. It is expected that Fe(II) and Mn(II) are derived from the reduction of iron and manganese oxides through biogeochemical pathways. SO₄²⁻ is principally introduced by ocean intrusion. However, the linear mixing line in the Piper plot suggests that sulfate is for the most part conservative, and that sulfate reduction is relatively minor at the Kidd 2 site (Bolton and Beckie 2011), compared to iron and manganese reduction. Methanogenesis is also suspected at the site because methane (CH₄) has been detected in groundwater. However, it is likely the methanogenesis is only significant at the lower mixing zone where at the boundary of the sandy aquifer and lower silty clay layer.

4.1.2 Redox Components

Concentrations of different ions or elements measured at given depths are the result of both mixing of groundwater and ocean water and chemical reactions. The role of mixing and dilution can be investigated by assuming Cl⁻ to be a conservative species and comparing it to other species through cross plots (Figure.4.2). Na⁺ and Mg²⁺ have linear relationships with Cl⁻, indicating that the mixing of fresh groundwater and ocean water is the main process controlling the concentrations of the two ions, which is consistent with the Piper plot (Figure.4.1). SO₄²⁻ and Ca²⁺ are linearly correlated with Cl⁻ when Cl⁻ concentrations are below 5,000mg/L. Nevertheless, when Cl⁻

concentrations are above 5,000 mg/L, both SO_4^{2-} and Ca^{2+} begin to show deviations, suggesting that the two ions are dominantly controlled by mixing process, with diagenetic reactions at high salinities.

The deviation of Ca^{2+} can be largely explained by the cation exchange. As ocean water intrudes into the aquifer with an amount of Na^+ , the introduced Na^+ replaces Ca^{2+} and Mg^{2+} ions, which were originally adsorbed onto the exchangeable sites of the sediments, especially sites enriched in organic carbon. Therefore, Ca^{2+} and Mg^{2+} tend to be released into the groundwater. Since Ca^{2+} has stronger exchange affinity than Mg^{2+} (Appelo and Postma 2005 p. 242), the deviation of Ca^{2+} along Cl^- is expected to be greater, especially in high Cl^- zones. However, the greatest deviation along the mixing line is probably due to the measurement error and minor heterogeneity rather than cation exchange.

The deviation of SO_4^{2-} at high salinities can be explained by the sulfate reduction. Simpson and Hutcheon (1995) used sulfur isotopes to demonstrate the presence of sulfate reduction in most of the groundwater samples that were collected along the coastal line of the Fraser River delta. Although most of Simpson's water samples for sulfur isotope analysis were collected at shallow depth, the enrichment of ^{34}S in SO_4^{2-} in high salinity water (Graham Simpson and Hutcheon 1995) provides support for sulfate reduction at the Kidd 2 site. The depletion of SO_4^{2-} in the high Cl^- zone suggests the presence of sulfate reduction. Acid volatile sulfur sediment analyses (presented later) also support the notion of sulfate reduction.

Fe^{2+} , Mn^{2+} , and HCO_3^- do not correlate with Cl^- at all (Figure 4.3), which suggests that their concentrations are strongly controlled by diagenetic reactions. Since Fe^{2+} , Mn^{2+} , and HCO_3^- are all involved in bacterial-mediated redox reactions, the non-linear relationships support the hypothesis that Fe(II) and Mn(II) are derived from iron and manganese reduction.

The concentration of DOC ranges from 4 to 29 mg/L, with the tendency to decrease with Cl^- . However, an inverse relationship between DOC and Cl^- does not exist. DOC reached 26-28 mg/L in the shallow freshwater zone and it remained relatively constant at low values (4-6mg/L) in the

deep saline water, suggesting that DOC may be released from the surficial clayey silt layer rather than being introduced by ocean water. The dramatic decrease in DOC in the deep saline water may be explained either by the mixing process or the faster consumption rate of DOC in the deep saline water, or by a combination of both.

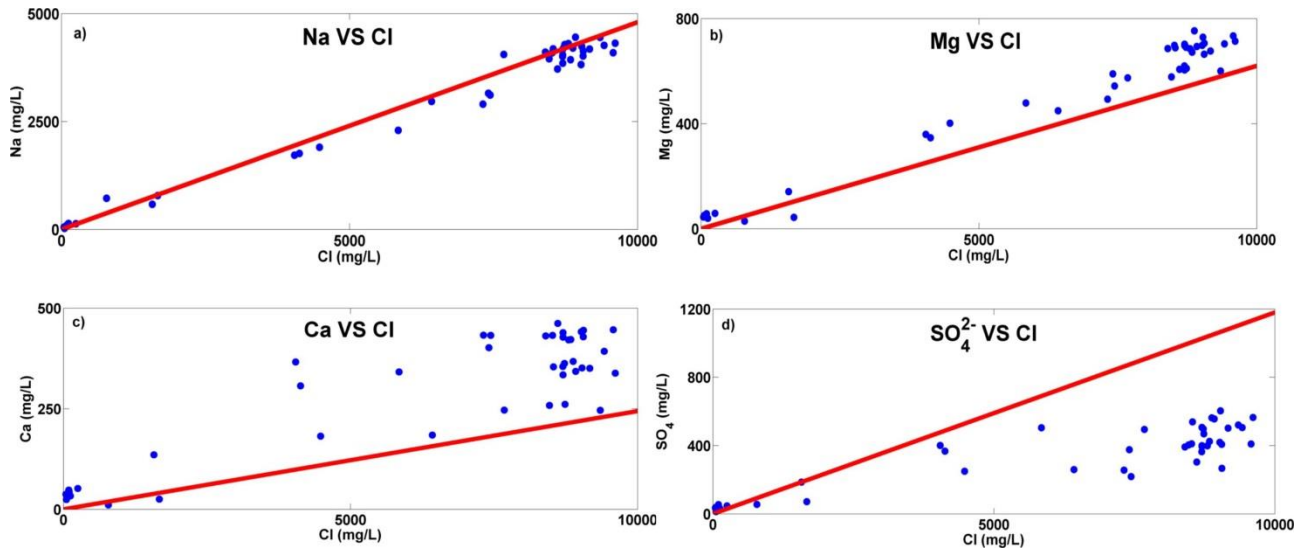


Figure 4.2: Cl^- plotted against A) Na^+ , B) Mg^{2+} , C) Ca^{2+} , D) SO_4^{2-} at the Kidd 2 site. Blue dots represent field measurements, and the red line presents the mixing line of the intruded saline water. The linear relationship of Na^+ and Mg^{2+} with Cl^- suggests dilution is the dominant control, whereas Ca and SO_4 show evidence of non-conservative reactions.

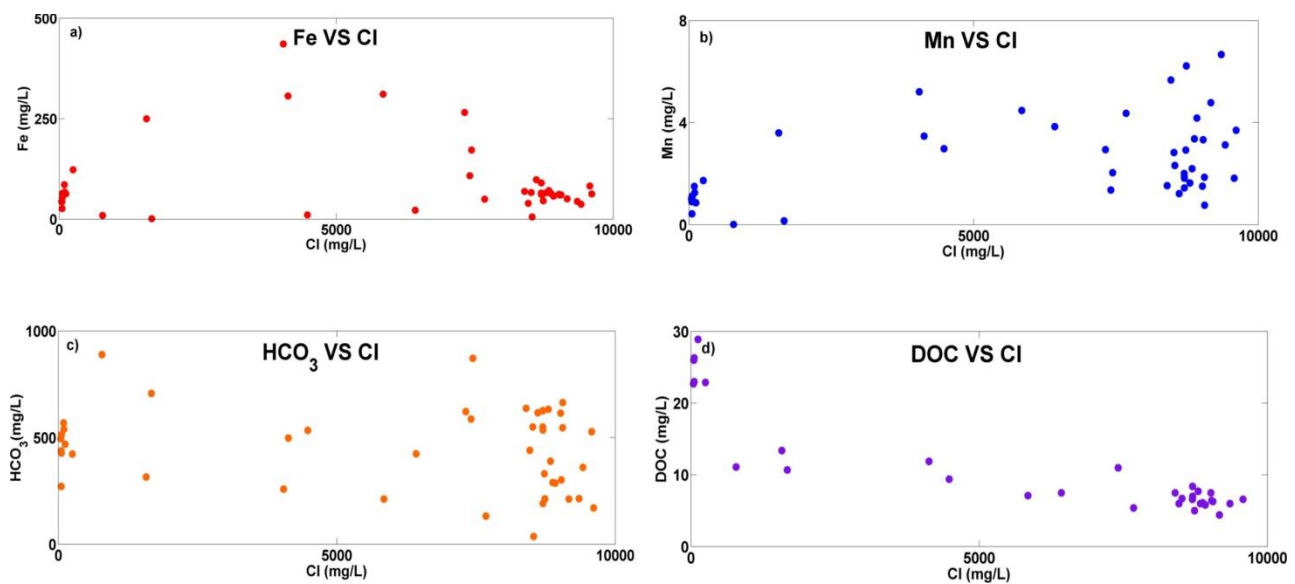


Figure 4.3: The non-linear relationships between Cl^- and Fe^{2+} , Mn^{2+} , HCO_3^- and DOC at the Kidd 2 site, indicating that biogeochemical processes and not mixing/dilution are their dominant controls at the Kidd 2 site.

4.1.3 Iron and Manganese Reduction

Figure 4.4 and 4.5 present Fe and Mn concentration depth profiles in W1 and W3, respectively. The concentration profile in W2 is excluded since there are only a few sampling ports. In W1 (Figure. 4.4), there were coincident peaks of Fe and Mn at a depth of 10.08 m, where their concentrations reached 311.1 mg/L and 4.5 mg/L, respectively. Below 13.08 m, the Fe concentrations sharply decreased to 50 mg/L and remained constant. The dissolved Mn concentrations increased above a depth of 16 m, from 1.5 to 2.8 mg/L. Unlike the single and concomitant peak pattern of Fe and Mn in W1, Mn in W3 (Figure. 4.5) had double peaks at depths of 12.08 m and 16.17 m. The first coincident peak of Fe and Mn was at the upper mixing zone (12.08 m), where Fe reached its highest concentration. Between 12.08 m and 22.08 m, Fe continuously decreased, from 306.5 mg/L to 9.4 mg/L. Nevertheless, Mn began increasing at 14.08 m depth and reached its maximum value (6.67 mg/L) 16.17 m depth in the center of the deep saline water, then decreased to 0.01 mg/L at the bottom of the aquifer.

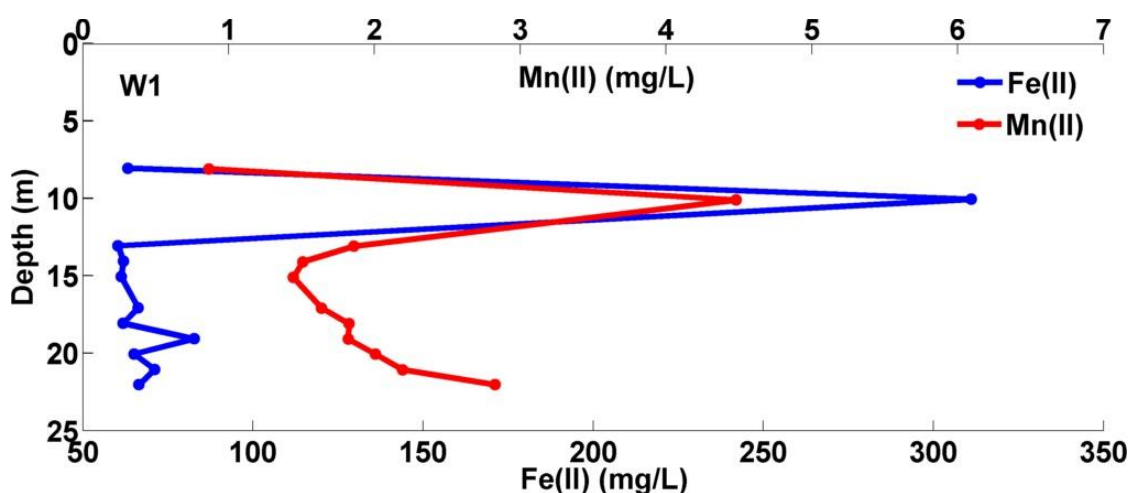


Figure 4.4: Concentrations of Mn^{2+} and Fe^{2+} with depths in profile W1 at the Kidd 2 site.

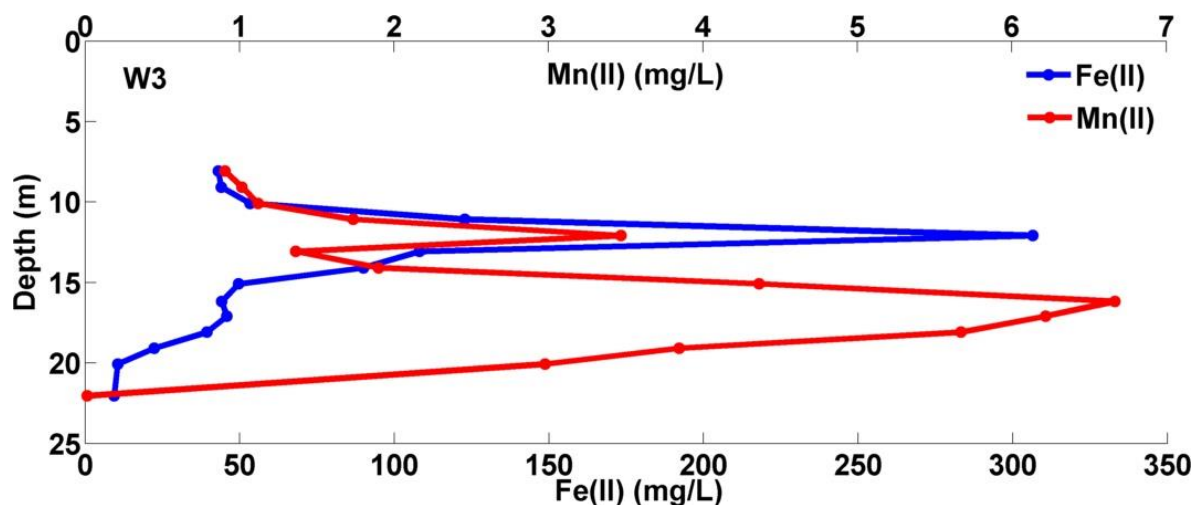


Figure 4.5: Concentrations of Mn^{2+} and Fe^{2+} with depths in profile W3 at the Kidd 2 site.

It is observed that in both W1 and W3, Fe was relatively low and constant in the shallow groundwater zone, ranging from 40 mg/L to 60 mg/L. It increased rapidly at 10-12m depth in the upper mixing zone, where it reached its highest concentrations in both wells, 300-311 mg/L. Below the upper mixing zone Fe in W1 dropped from 311 mg/L to 60 mg/L over 1 m, and remained at approximately 60-80 mg/L at depths of 11 m to 20 m. In W3, the peak in Fe was detected at a depth of 12.08 m, and Fe dropped from the peak value of 306 mg/L to 108 mg/L over 1 m depth. It then decreased continuously to 10 mg/L from a depth of 13 m to 22 m.

DOC and HCO_3^- can be used as tracers of the iron and manganese reduction pathways, since anaerobic respiration consumes DOC and increases HCO_3^- . Figure 4.6 shows that the DOC is negatively correlated with the Fe^{2+} and Mn^{2+} only at intermediate depths from 10 m to 12 m, which further suggests that the most intensive iron and manganese reduction is occurring at the upper mixing zone, accompanied with the oxidation of organic matter. At other depths, the relationship cannot be clearly defined as DOC concentrations remain relatively low and constant. The constant DOC values in these zones suggests that iron and manganese reduction is not preferred at shallow or deep water zones, and only takes place intensively at intermediate depths. However, the relationship between DOC and metals will be obscured if the fermentation of detrital organic matter is the source of DOC.

No well-defined relationship is seen between Fe/Mn and HCO_3^- (Figure. 4.7). Fe and HCO_3^- are observed to have a poor relationship through the depth profile, and Mn and HCO_3^- show an inverse correlation, especially in intermediate and deep water zones. These inconsistent relationships suggest that iron and manganese redox reactions are not the main process control of HCO_3^- in groundwater or that Fe and Mn concentrations are affected by other processes (Horneman, Van Geen, et al. 2004). Phreeqc simulation reveals that groundwater is supersaturated with respect to siderite (FeCO_3) and rhodochrosite (MnCO_3); thus, some Fe, Mn, and HCO_3^- would precipitate out of the solution. Moreover, HCO_3^- may be affected by carbonate mineral precipitation and dissolution. The effect of secondary reactions will be shown in the bicarbonate section (4.1.5). Finally, the relationship may be obscured by the insufficient sampling points in the upper mixing zone, where iron and manganese reduction occurs intensively.

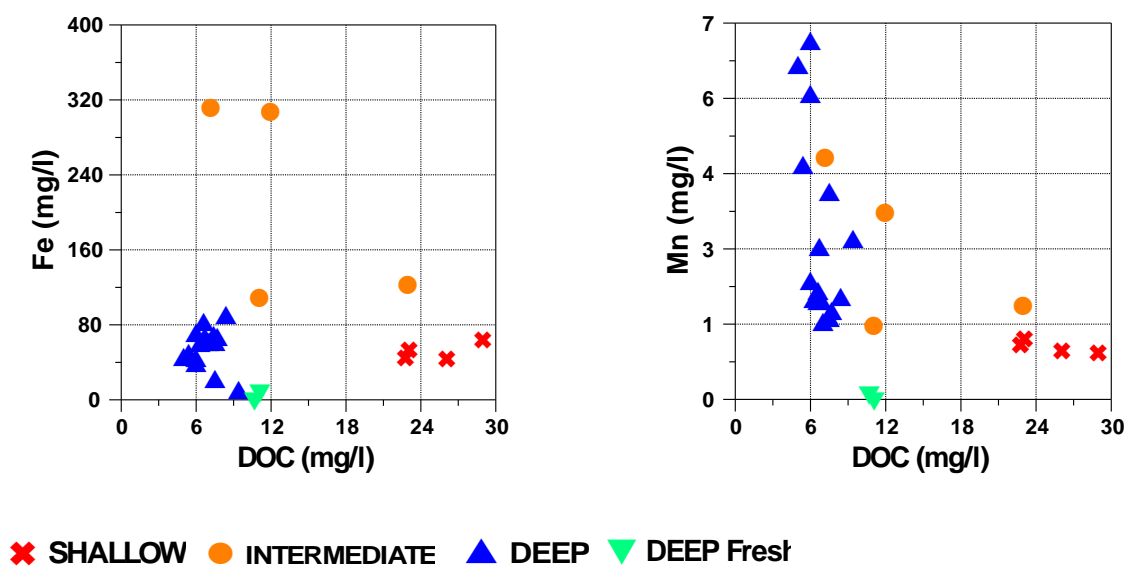


Figure 4.6: Concentrations of DOC versus Fe^{2+} and Mn^{2+} at the Kidd 2 site.

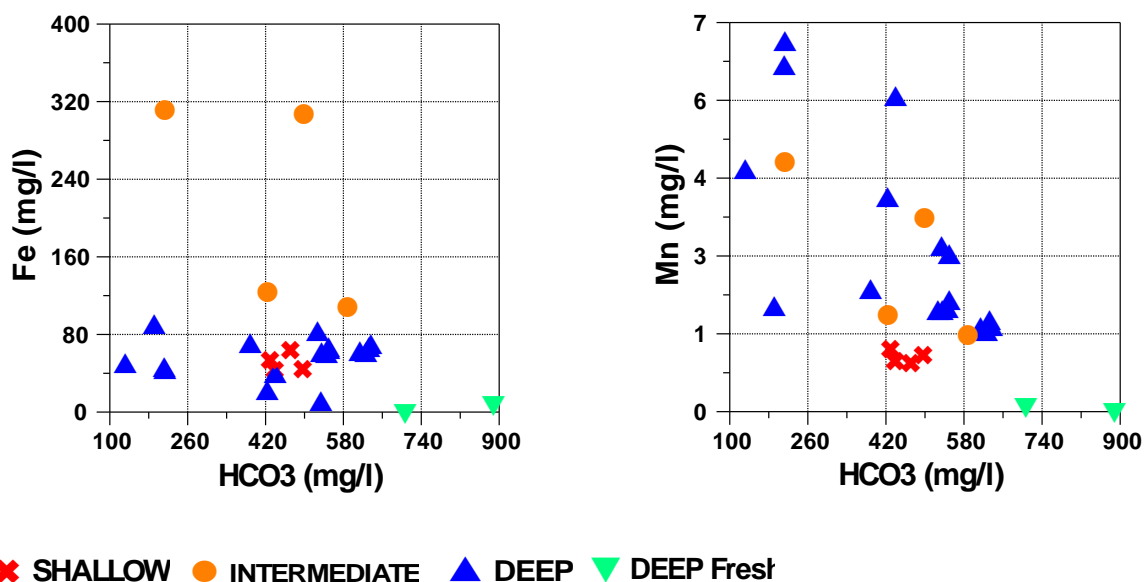
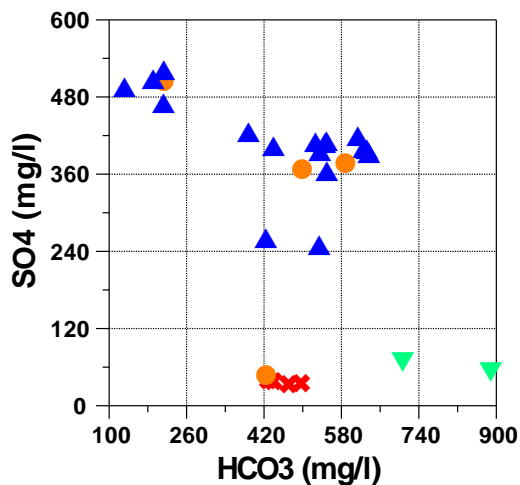


Figure 4.7: Concentrations of HCO₃⁻ versus Fe²⁺ and Mn²⁺ at the Kidd 2 site.

4.1.4 Sulfate Reduction

As sulfate is reduced, HCO₃⁻ is released into groundwater. The inverse correlation between SO₄²⁻ and HCO₃⁻ (Figure. 4.8) is consistent with sulfate reduction in the intermediate and deep saline water. This result is consistent with the plot of Cl⁻ of SO₄²⁻ (Figure 4.2), which deviation of SO₄²⁻ is associated with high Cl⁻ concentration. In the intermediate water, one sample point (yellow dot) was seen to fall outside of the range. The point is located at the uppermost region of the ocean wedge, where mixing occurs with the least amount of ocean water. The extent of sulfate reduction cannot be inferred from the inverse correlation between SO₄²⁻ and HCO₃⁻ (Figure. 4.8).



✖ SHALLOW ● INTERMEDIATE ▲ DEEP ▼ DEEP Fresh

Figure 4.8: Concentrations of HCO_3^- versus SO_4^{2-} at the Kidd 2 site. The inverse relationship is observed at both intermediate and deep water, indicating that sulfate reduction is involved in groundwater.

4.1.5 Bicarbonate and Secondary Minerals

The plot of HCO_3^- versus Cl^- (Figure. 4.2) shows a non-linear relationship, suggesting that HCO_3^- is intensively involved in diagenetic reactions, rather than in the mixing process.

Fe and Mn released into groundwater by reduction can be incorporated with HCO_3^- to form siderite (FeCO_3) and rhodochrosite (MnCO_3), respectively. SI calculations show that pore water at all depths is supersaturated with respect to siderite (Figure. 4.10). The highest SI value in W3 was found at a depth of 12.08 m (Figure. 4.10), concomitant with the Fe peak. SI values reached 1.5-2 at the upper mixing zone, but only 0.5-1.2 at the deep saline water, indicating siderite is more likely to precipitate at upper mixing zone than at other depths.

SI values with respect to rhodochrosite were supersaturated in most groundwater samples. The highest SI value (0.92), was found at a depth of 20.06 m. SI values decreased to negative values at

depth. Unlike SI distributions of siderite, the SI of rhodochrosite tends to be greater than zero at depths from 16-20 m.

Besides bacterial-mediated iron, manganese and sulfate reduction, secondary reactions like carbonate mineral dissolution and precipitation also play a significant role in the HCO_3^- concentrations in solution. HCO_3^- is seen to have a positive relationship with Ca and Mg, especially in intermediate and deep water zones (Figure. 4.9), suggesting that carbonate mineral dissolution is linked with the HCO_3^- in these zones. The SI's show that most groundwater samples are undersaturated with respect to calcite (CaCO_3) and dolomite [$\text{MgCa}(\text{CO}_3)_2$] (Figure. 4.10), indicating the dissolution of these two minerals is favored. The plot of SI versus depth in W3 (Figure. 4.10) shows that only two of fifteen groundwater samples are supersaturated with respect to calcite. Unlike calcite, dolomite has a stronger tendency to precipitate at depths of 18-22 m, where the SI values range from 0.4 to 0.6. As the result, the relatively poor correlation relationship between Mg^{2+} and HCO_3^- is observed (Figure 4.9) and indicates the dissolution of dolomite is less dominant than that of calcite.

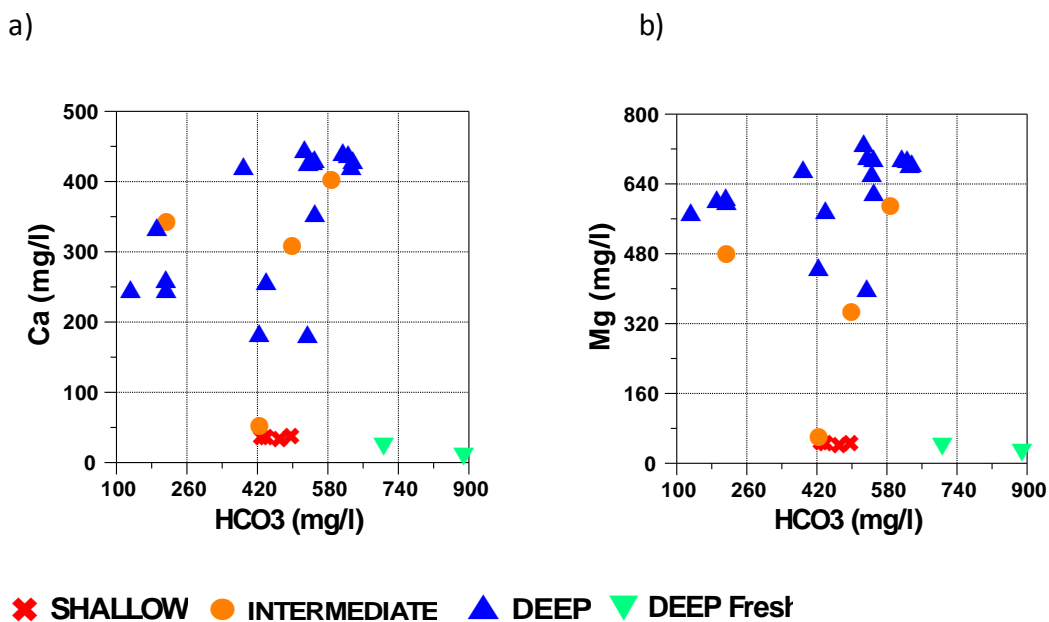
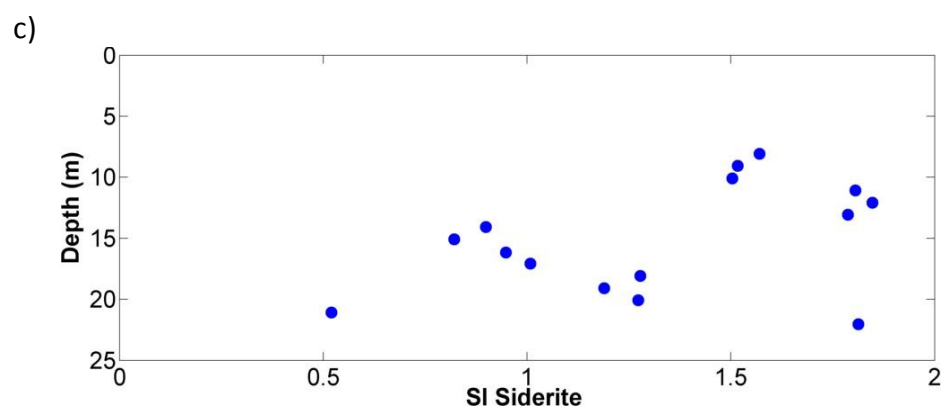
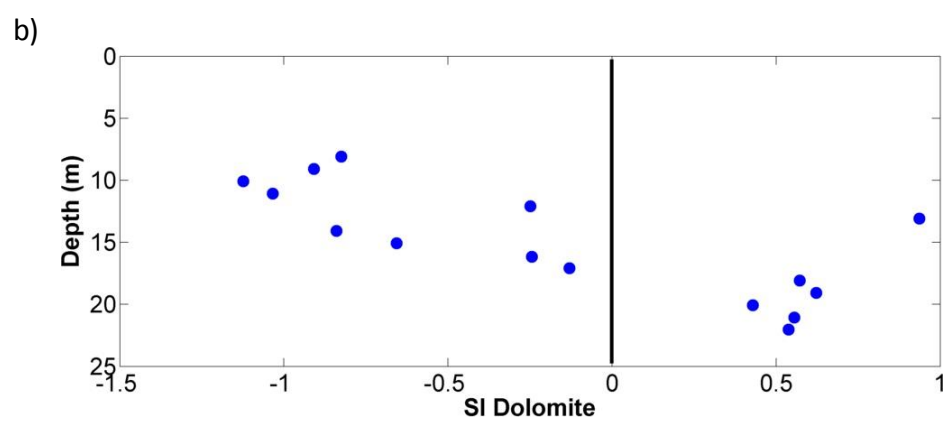
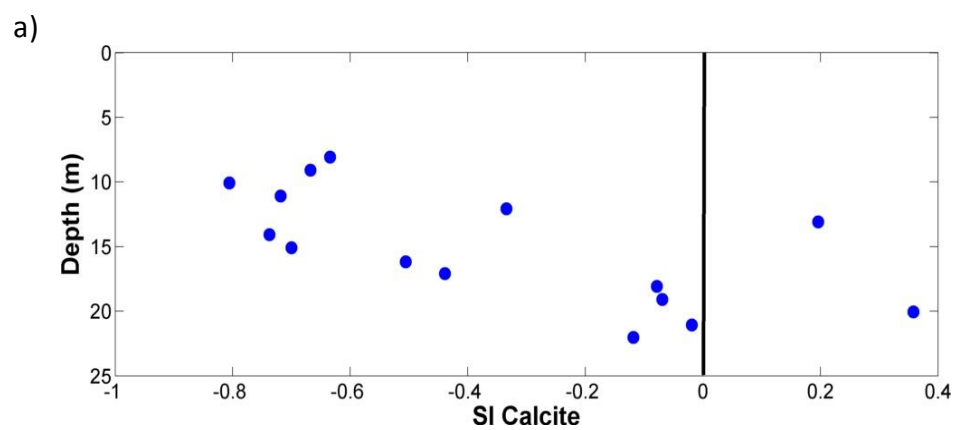


Figure 4.9: The relationship between HCO_3^- and a) Ca and b) Mg. both these two ions show positive relationship with HCO_3^- , indicating dissolution of carbonate minerals.



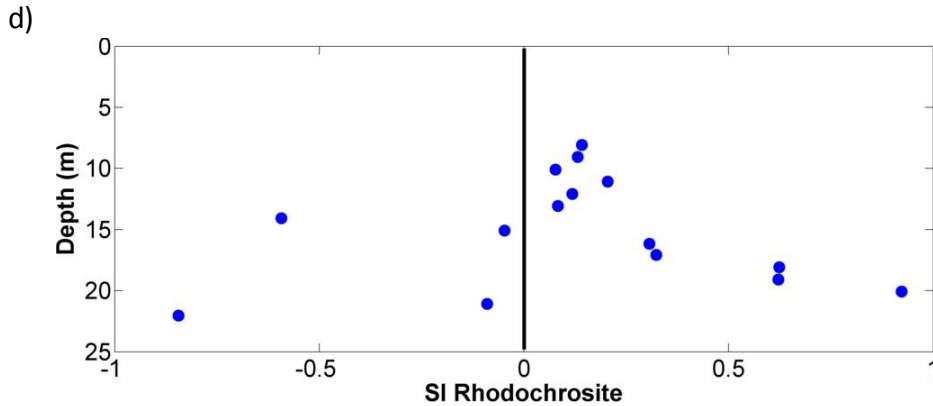


Figure 4.10: Saturation indices calculated with the Phreeqc geochemical model, using the MINTEQA2 database: a) SI_Calcite, b) SI_Dolomite, c) SI_Siderite, and d) SI_Rhodochrosite.

4.1.6 Methanogenesis

Qualitative methane concentrations have been measured along depth profile in W3, and Henry's law has been applied to convert CH_4 in the headspace to that in solution. Please see the Appendix F for a sample calculation.

Dissolved methane (Figure. 4.11) decreases between 10.08 m and 14.08 m, and then increases steadily with depth at 14.08m, reaching a maximum concentration of 25.1 mg/L at 19.08 m. Below 19.08 m, methane exceeds the instrument measurement limit. The high production of methane in the deep groundwater suggests that methanogenesis mainly plays a role in the lower confining silt layer. In shallow groundwater, the presence of methane is probably due to groundwater transport processes rather than methane production, given the abundant iron and sulfate. As methane formation rate is characterized by high spatial variation (Hansen, Jakobsen, and Postma 2001), the increase in methane at depth of 10m is not necessary for high methanogenesis, but could be related to the upward transport of methane from the lower silts.

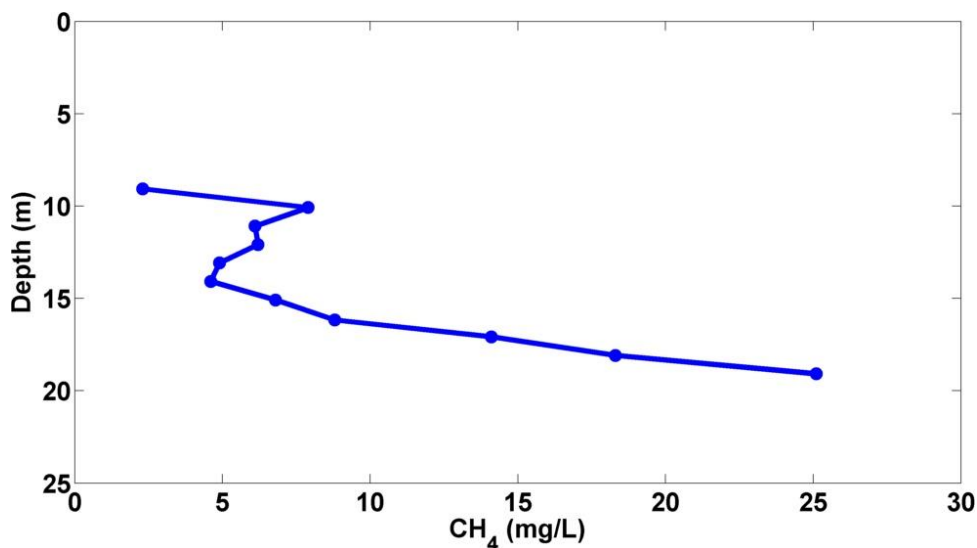


Figure 4.11: dissolved methane along the depth profile in W3. The discontinuity of methane suggests inhomogeneous methane production at the Kidd 2 site.

4.2 Isotope Analysis

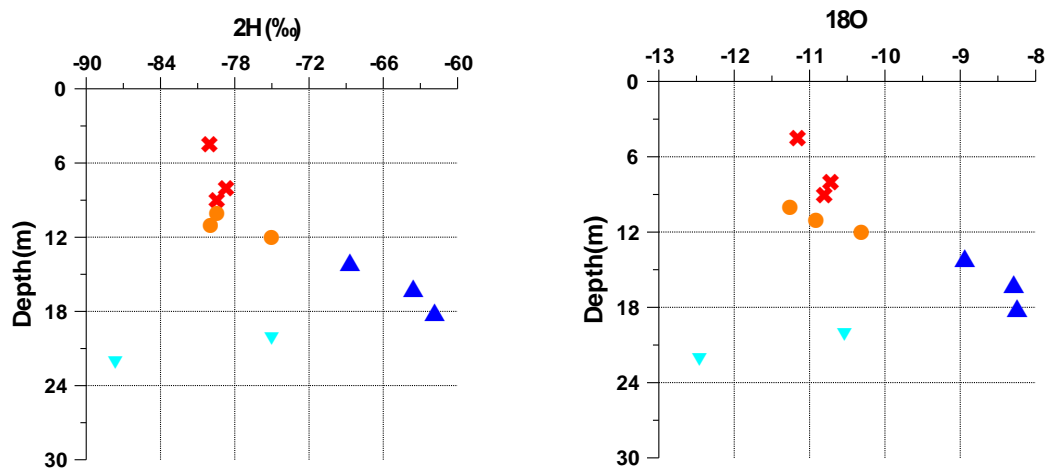
4.2.1 Isotope Profile

4.2.1.1 Isotope vs. Depth

Water isotopes of ^{18}O and ^2H for selected water samples in W3 were analysed. Based on the isotope analysis, four water types were classified, including shallow groundwater from meteoric recharge, mixing of Fraser River sandy aquifer groundwater and the saline water, pure saline water and the deep fresh water from the lower confining silt layer. Both δD and $\delta^{18}\text{O}$ show consistent relationships with depth (Figure. 4.12). Overall the result agrees well with the previous isotope analysis at the Kidd 2 site (Douglas 2011), which supports the conceptual model of saline intrusion. Douglas demonstrated the presence of a mixing process at transition zones and mapped mixing ratios in cross section.

The isotope composition in the shallow groundwater zone is close to the accepted composition of local precipitation, which is supported by the conceptual model. Between depths of 10m and 13 m, the trend is for less depleted isotopic compositions in both δD and $\delta^{18}\text{O}$, consistent with ocean water mixing with the aquifer groundwater. In the upper mixing zone and the deep saline zone,

water becomes even more enriched in both δD and $\delta^{18}O$. Below 20 m the trend reverses sharply and both δD and $\delta^{18}O$ become more depleted, even more than what was observed at shallow depths above 10.08 m. The reverse trend indicates that most of the depleted upward flowing groundwater from the lower confining silt layer is mixed with the ocean-sandy aquifer groundwater.



✕ SHALLOW ● INTERMEDIATE ▲ DEEP ▼ DEEP Fresh

Figure 4.12: δD and $\delta^{18}O$ over depths in W3.

4.2.1.2 Isotope Composition vs. Chloride Concentration

Cl concentrations in shallow groundwater above 10 m were found to be lower than 100 mg/L. Below this depth, Cl concentration increases as more portions of ocean water mix with the groundwater. The Cl concentration in pure sea water is approximately 18,000 mg/L. The maximum measured Cl concentration in W3 reached 9,348 mg/L, indicating that sea water makes up roughly 52% of the groundwater there.

Since seawater is more enriched in both δD and $\delta^{18}O$, the mixing of ocean water with fresh groundwater should result in a straight line if one assumes conservative mixing. The strong

positively correlation ($R^2 > 0.80$) of δD and $\delta^{18}O$, along with the Cl data (Figure. 4.13), is indicative of seawater intrusion and the process of mixing with fresh groundwater. The largest deviation for both δD and $\delta^{18}O$ was seen at a depth of 22.03 m, where water mixes with the water coming from the lower confining silt layer, which dilutes Cl to 781 mg/L. The deviation suggests that water in the lower silt is even more depleted than groundwater in the aquifer and represents a distinct source of water.

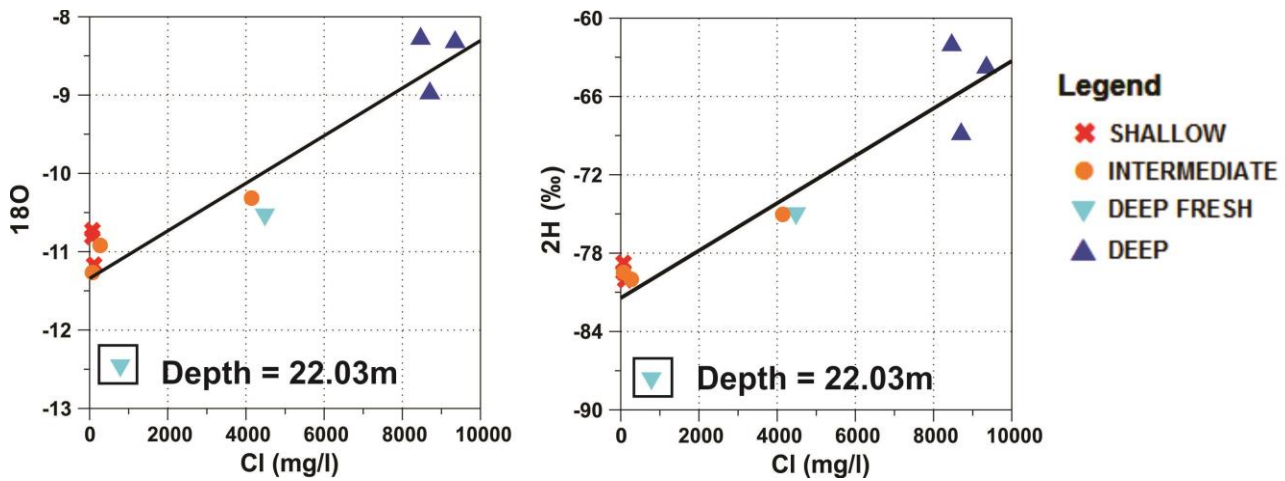


Figure 4.13: δD and $\delta^{18}O$ versus chloride (Cl) concentration in W3.

4.2.1.2 $\delta D/\delta^{18}O$ Relationship

The δD versus $\delta^{18}O$ plot (Figure. 4.14) shows changes in the water isotope composition with water groups along the meteoric water line, giving an overall sense of water isotope composition within the regional water sources over the vertical profile. The plot also acts as a good method to identify any potential non-conservative mixing process due to water-rock reactions.

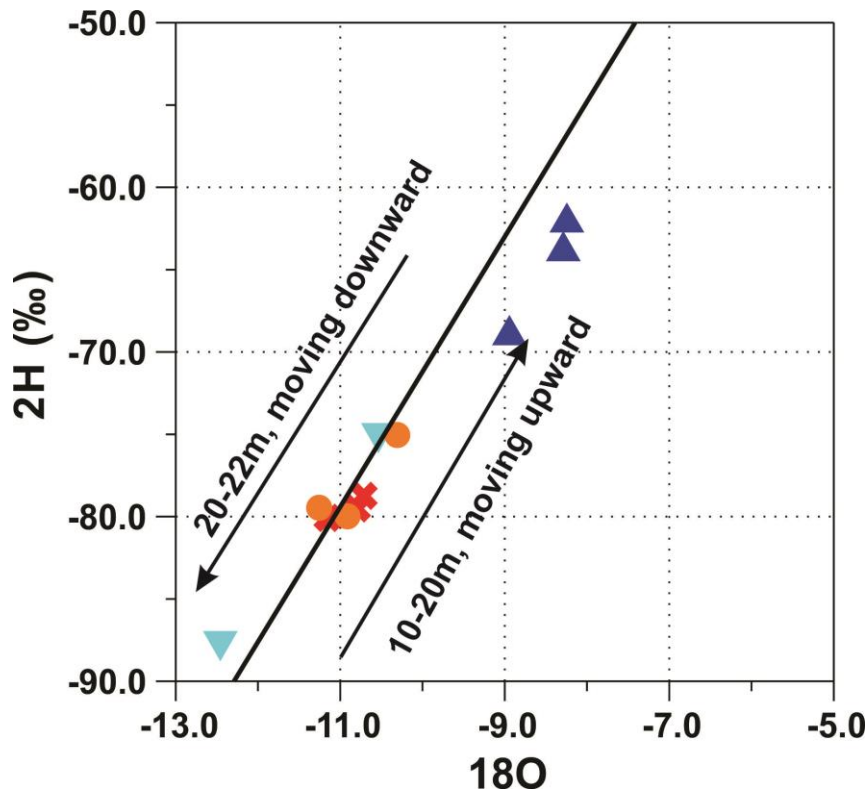


Figure 4.14: Shallow (< 10 m), intermediate (10-13 m), deep ocean water (13-20m) water, and deep fresh water samples are plotted as δD versus $\delta^{18}\text{O}$ to show the relationship of isotopic composition against the meteoric water line.

The solid black line represents the meteoric water line. Shallow water samples have a uniform isotopic composition, whereas water samples collected from deeper water zones (>10m) become heavier with depth. Moving upward along the meteoric line, water samples from 10-20 m are less depleted in both δD and $\delta^{18}\text{O}$, indicating more intensive mixing with sea water. Approaching the contact between the medium sand and lower confining silt, however, at a depth of 20 m, isotope composition begins decreasing and becomes more depleted, since water in the silt layer is mostly depleted. The data points at the intermediate depth and deep ocean zone do not agree with the meteoric water line, suggesting that considerable geochemical non-conservative reactions may have accompanied the mixing process.

4.2.2 Mixing Ratios between Fresh Water and Ocean Water

The linear relationship between isotope composition and Cl concentration is indicative of the mixing of seawater and groundwater. δD and $\delta^{18}O$ can be considered to mix conservatively and the mixing of two distinct waters can be easily quantified using simple linear algebra. The proportion of mixing of two different water types in a particular water sample can be defined by Equation 4.1 below:

$$C_{\text{mixing}} = x \cdot C_A + (1-x) \cdot C_B \quad (\text{Equation 4.1})$$

Where C_A and C_B represent concentrations of different water types and x represents the mixing ratio in a particular water sample.

Based on the interpretation of isotope compositions at the Kidd 2 site (Douglas 2011), water could be interpreted as a mixture of four sources of water: meteoric recharge water (R), aquifer groundwater (Gw), deep confining silt groundwater (S), and ocean water (O). Table 4.3 lists the four end members at the Kidd 2 site. Based on the Piper plot (Fig. 4.1) and the isotope profile (Fig. 4.12), we used the shallowest water (BH114) at depth of 4.5m as meteoric recharge water and the deepest water (WB-11) at depth of 31m as the deep confining silt groundwater. Before ocean water enters into the aquifer, it has been diluted at the hyporheic zone of the Fraser River bottom, where Cl concentration was 10,100 mg/L (Bianchin, 2001). Due to the lack of the isotope data in the hyporheic zone, we selected water (W3-9) in the center of ocean circulation which has the peak of Cl concentration (9,348 mg/L) to represent the ocean water geochemistry.

Both isotope compositions and Cl concentrations are used to estimate the mixing ratio from various water sources. Here, we focus on calculating mixing at both the “upper mixing zone” and the “lower mixing zone” of the ocean wedge. As the ocean circulation formed thousands of years ago, it is expected that the original aquifer groundwater in the mixing zones has been largely flushed and is negligible. The water at the upper mixing zone is actually a three-way mixture of meteoric recharge water, ocean water, and deep confining silt water. This three-way mixing relationship can be resolved using two conservative tracers (Cl and δD or Cl and $\delta^{18}O$) at upper

mixing zone. Water at the lower mixing zone is basically a mixture of ocean water and the confining silt water. In doing so, we essentially determine an approximate proportion of water type that occurs at lower mixing zone using any one of the three conservative tracers.

Table 4.3: conservative tracers including Cl and isotopic compositions of four end - member water groups at the Kidd 2 site, for calculating the mixing ratio for upper and lower mixing zones.

Group	Depth (m)	Sample ID	Cl (mg/l)	δD	$\delta^{18}O$
Meteoric Recharge	4.50	BH114	51.8	-77.0	-10.1
Ocean Water	16.17	W3-9	9348	-63.6	-8.3
Deep Confining Silt Groundwater	31.00	WB-11	92.6	-95.0	-13.5

Based on the isotope data and Cl concentration, the mixing equations can be re-written as:

$$Cl_{\text{mixing}} = a Cl_{\text{group1}} + b Cl_{\text{group2}} + c Cl_{\text{group3}} \quad (\text{Equation 4.2})$$

$$\delta D_{\text{mixing}} = a \delta D_{\text{group1}} + b \delta D_{\text{group2}} + c \delta D_{\text{group3}} \text{ or} \quad (\text{Equation 4.3})$$

$$\delta^{18}O_{\text{mixing}} = a \delta^{18}O_{\text{group1}} + b \delta^{18}O_{\text{group2}} + c \delta^{18}O_{\text{group3}} \quad (\text{Equation 4.4})$$

$$a + b + c = 1 \quad (\text{Equation 4.5})$$

As shown in Fig. 4.15, water samples collected at W3-5 (12.08 m) and W3-12 (19.08 m) represent the upper and lower mixing zone, respectively, on the ocean wedge. Water composition at W3-5 results from mixing of the shallowest meteoric recharge water (BH 114), the ocean water (W3-9)

and the deep confining silt water (WB-11). The water composition at W3-12 results from mixing of the W3-9 and WB-11.

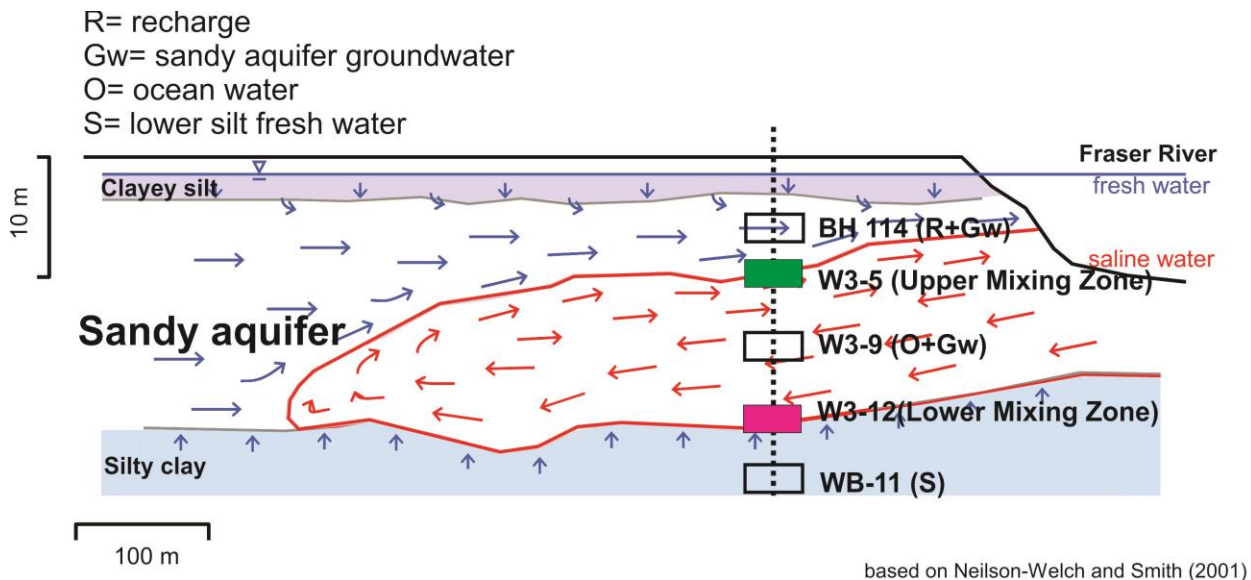


Figure 4.15: Water sample at the upper mixing zone (W3-5) results from the mixture of the water in BH 114, W3-9 and WB-11. The water sample at the lower mixing zone (W3-12) results from the mixture of water in W3-9 and WB-11.

Based on the Cl and δD in Table 4.3, water at the upper mixing zone (W3-5) is approximately 48% BH114 shallow water, 40% W3-9 ocean water and 12% of the confining silt water (Equation 4.2, 4.3 and 4.5). Mixing results calculated by Cl and the $\delta^{18}O$ are similar, which the water is 44% BH114 water, 46% W3-9 ocean water and 10% of the confining silt water (Equation 4.2, 4.4 and 4.5). The average mixing ratio therefore is 46% shallow meteoric recharge water, 43% deep ocean water and 11% lower confining silt water (Table 4.4).

Table 4.4: Mixing results for upper mixing zone, based on Cl concentration and δD of shallow BH114 water, deep W3-9 ocean water and lower confining silt WB-11 water.

Group	Ratio	δD and Cl	$\delta^{18}O$ and Cl	Average
Meteoric Recharge water	BH114	48%	44%	46%
Deep ocean water	W3-9	40%	46%	43%
Lower confining silt water	WB-11	12%	10%	11%

As water at lower mixing zone is basically a two - part mixture, mixing ratios can be calculated using either three conservative traces independently. Isotopes indicate that the lower mixing zone water is 80% W3-9 deep ocean water and 20% WB-11 deep water while, Cl indicates 68% W3-9 water and 32% WB-31 water. The average mixing ratio therefore is 76% ocean-groundwater mixing water and 24% adjacent deep water from the lower confining silt layer (Table 4.5).

Table 4.5: Mixing results for lower mixing zone, based on deep ocean W3-9 water and lower confining silt WB-11 water.

Group	Ratio	δD	$\delta^{18}O$	Cl	Average
Deep ocean water	W3-9	80%	79%	68%	76%
Lower confining silt water	WB-11	20%	21%	32%	24%

The results show that the mixing ratios calculated from Cl and isotopes are consistent with each other. The water compositions at the upper and lower portions of the ocean wedge are different, even though they are on the same flow line. Since the ocean wedge has existed for thousands of years and is essentially at steady-state, the water composition calculated here can be considered as the annual average composition.

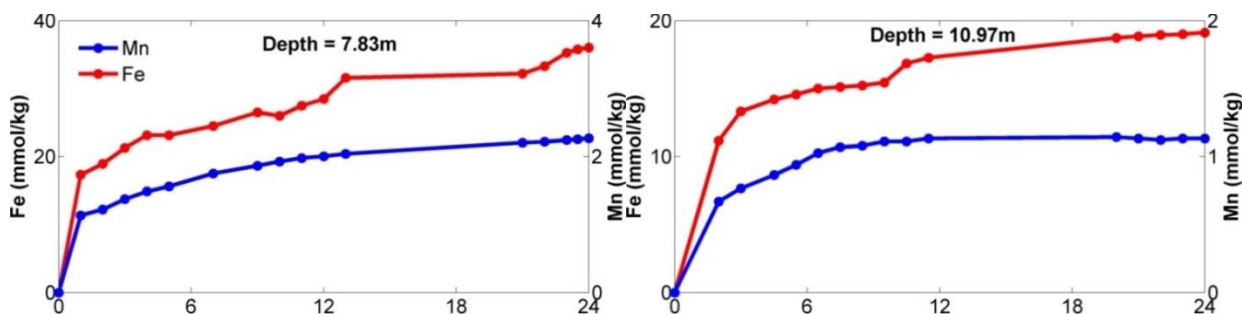
4.3 Sediment Chemistry

4.3.1 Reactivity of Iron and Manganese Oxides

Sediment cores were collected adjacent to W3 at the Kidd 2 site. Sediments from six specific depths (7.83 m, 10.97 m, 12.20 m, 15.54 m, 19.30 m, and 21.33 m) were analyzed by kinetic extractions to characterize the pools of iron and manganese oxides and determine their reactivities along the depth profile. Reactive iron and manganese oxides were extracted with an ascorbate-citrate solution, buffered at pH=7.5, and the released iron and manganese were continuously monitored as a function of time. The graph of released iron and manganese with time was then interpreted with a reactive continuum approach (Hyacinthe 2006), which allows for calculating the reactivity (k') and the reaction exponent (γ).

4.3.1.1 Kinetic Extraction

Iron and manganese dissolution curves for sediments at selected depths in the buffered ascorbate-citrate extraction solution are plotted in Figure 4.16. A rapid release of iron and manganese occurs from the sediments in the first hour, followed by a decelerating production rate. Both iron and manganese show similar dissolution trends, suggesting that their reactivities are comparable. Moreover, the amount of extracted manganese is one order of magnitude smaller than the extracted iron, which is consistent with their aqueous concentrations. For most of the samples, the iron and manganese concentrations approached constant values at the end of the extraction period, indicating the complete dissolution of the ascorbate-citrate reactive iron and manganese pools. One exception is seen at the shallowest sediment (depth of 7.83 m), where the iron and manganese tend to increase after 24 hours of extraction.



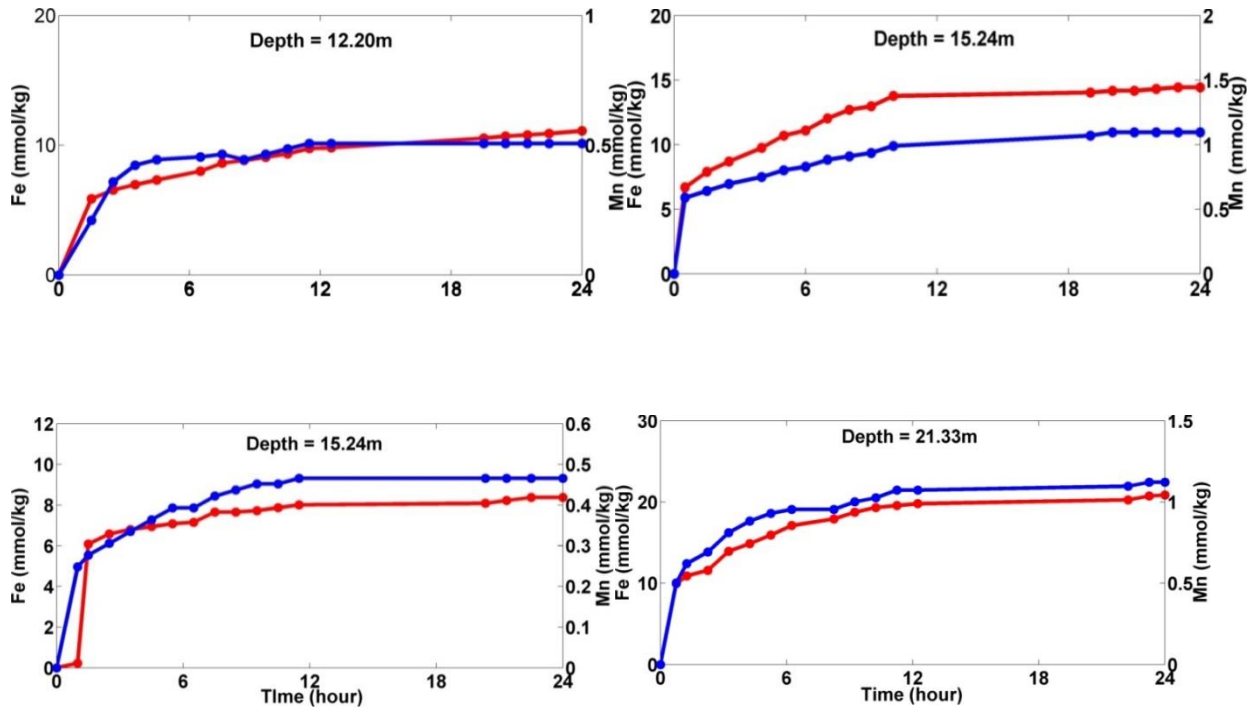


Figure 4.16: Dissolution of iron and manganese oxides from the sediments at the Kidd 2 site as a function of time, driven by ascorbate-citrate solution buffered at pH=7.5 for 24 hours. See text for complete description and discussion.

The concentrations of the total ascorbate-citrate extractable iron and manganese are presented in Table 4.6. The data for the time-dependent release of iron and manganese to solution was fitted to the modified rate law (Larsen & Postma, 2001), as shown in Equation 4.6:

$$\frac{m}{m(0)} = [-k'(1 - Y)t + 1]^{\frac{1}{1-Y}} \quad (\text{Equation 4.6})$$

Where m is the residual crystal mass in sediments (mol), $m(0)$ is the total crystal mass (mol), k' is the rate constant (S^{-1}), Y is the reaction exponent, and t is the time (s).

Optimized values for the parameters $m(0)$, k' , and γ were determined by fitting the time-dependent dissolution data to Equation 4.6, using the Matlab Curve-Fitting Toolbox 3.3.1. The reactive continuum model provided a relatively good fit to the dissolution data. In addition to the optimized parameter values, lower and upper limits were obtained for the 95% confidence intervals. However, for the shallowest sample (at depth of 7.83m) which the constant value was not achieved at the end of extraction, the confidence intervals only reached 92%, indicating the limitation of the reactive continuum model. The corresponding fitted model parameters are given in Table 5.2, including $m(0)$, k' and γ . The assigned value of $m(0)$ is critical, because the continuum model is a function of the change in crystal mass ($\frac{m}{m_0}$). In this study, $m(0)$ is defined as the maximum ascorbate-citrate extractable iron and manganese. The total ascorbate-citrate extractable iron and manganese at the end of the extractions agreed well with the $m(0)$ for most of samples, which was estimated by the reactive continuum curve (Tables 4.6 and 4.7), indicating buffered ascorbate-citrate solution is effective to dissolve reactive iron and manganese oxides.

Table 4.6: Total iron and manganese concentrations dissolved from the Kidd 2 site sediments in the ascorbate-citrate chemical extractions after 24 h.

Depth (m)	Extractable reactive Fe (mmol/kg)	Extractable reactive Fe (ppm)	Extractable reactive Mn (mmol/kg)	Extractable reactive Mn (ppm)
7.8	36.0	2009	2.30	126
10.9	19.1	1066	1.10	60.4
12.2	11.1	619	0.51	28.0
15.5	14.4	804	1.10	60.4
15.8	13.1	731	0.99	54.4
19.3	8.4	469	0.47	25.8
21.3	20.8	1161	1.10	60.4

Table 4.7: Kinetic extraction was conducted under ascorbate-citrate solution buffered at pH=7.5 for 24 hours, and initial mass (mo), kinetic rate constant (K') and reaction exponent (Y) are estimated by Matlab curve fitting.

Sediment sample	Initial Mass (mo)		Kinetic rate constant (k')		Y (reaction exponent)	
	reactive Fe (mmol/kg)	reactive Mn (mmol/kg)	Fe (s^{-1})	Mn (s^{-1})	Fe	Mn
7.8	34.8	2.2	1.60×10^{-4}	1.44×10^{-4}	2.34	1.89
10.9	18.2	1.1	1.25×10^{-4}	1.14×10^{-4}	1.88	1.13
12.2	10.9	0.50	1.34×10^{-4}	1.41×10^{-4}	1.88	1.24
15.5	13.4	1.1	1.81×10^{-4}	3.57×10^{-4}	1.89	2.43
15.8	12.4	0.96	1.85×10^{-4}	3.45×10^{-4}	2.19	2.46
19.3	9.0	0.45	1.87×10^{-4}	3.31×10^{-4}	1.56	2.09
21.3	20.1	1.11	1.92×10^{-4}	2.31×10^{-4}	1.91	1.90

The results show that the rate constants for iron and manganese oxides are within the same order of magnitude. Reactivity of iron oxides ranged from $1.25 \times 10^{-4} s^{-1}$ to $1.92 \times 10^{-4} s^{-1}$, and the values for manganese oxide ranged from $1.14 \times 10^{-4} s^{-1}$ to $3.57 \times 10^{-4} s^{-1}$ (Table 4.7). Manganese oxide showed more variability in reactivities (Figure 4.17), especially at depths from 15.8 m to 19.3 m. The slightly higher reactivities may have partially led to the elevated dissolved manganese in deeper water. Nevertheless, the small difference in rate constants along the depth profile suggests that the reactivities of iron and manganese oxides were practically the same and cannot explain the enormous difference of iron and manganese concentrations in solution.

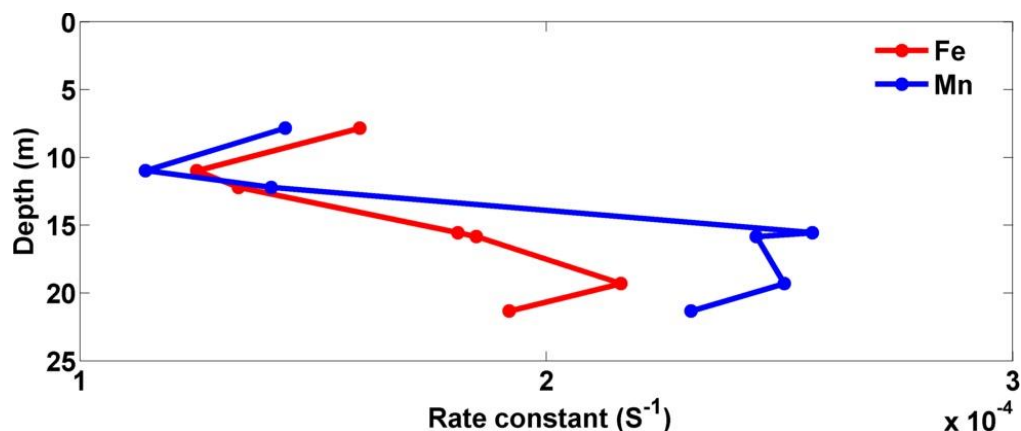


Figure 4.17: Rate constant (k') for iron and manganese oxides along the depth profile.

Postma (2001) determined that the rate constant for most reactive synthetic 2-line ferrihydrites ranges from $7.6-6.6 \times 10^{-4} \text{ s}^{-1}$, whereas, the initial rate for poorly crystalline goethite drops down to $5.4 \times 10^{-6} \text{ s}^{-1}$, which is two orders of magnitude smaller than for the ferrihydrites. The rate constant of lepidocorcite is in between, ranges from $3.2 - 8.1 \times 10^{-5} \text{ s}^{-1}$. Figure 4.18 shows a logarithmic plot of the undissolved mineral fraction: $-\log(m/m_0)$ versus the logarithm of the normalized initial dissolution rate to initial mass: $-\log(J/m_0)$ (Eq. 4.7).

$$\frac{J}{m_0} = k' \left(\frac{m}{m_0} \right)^\gamma \quad (\text{Equation 4.7}) \quad (\text{Larsen \& Postma, 2001})$$

Where k' is the rate constant, J is the overall rate of dissolution (mol/s), $m(0)$ is the initial mass of crystals (mol), m is the remaining crystal mass (mol), γ is the reaction exponent, and t is the time (s).

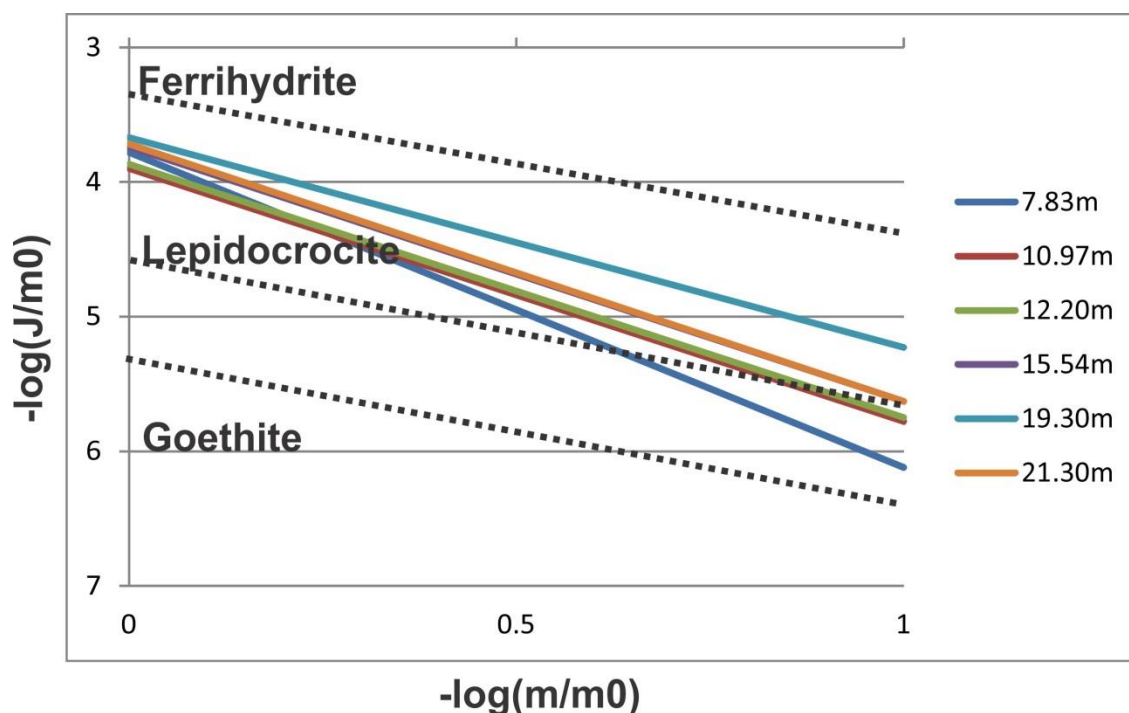


Figure 4.18: Comparison of reactivities of iron oxide to well-defined ferrihydrite, lepidocrocite, and goethite (from Larsen & Postma 2001). The x-axis is normalized over initial mass (J/m_0), and the y-axis is the fraction (m/m_0) remaining in the solid phase.

The upper and lower black dashed lines represent ferrihydrite and goethite, respectively. Lines for all sediments at the Kidd 2 site fall between the two lines (ferrihydrite and poorly crystalline goethite). The initial rate constants of samples approach to the upper bound of ferrihydrite, and gradually move toward to the lower bounds of lepidocrocite and goethite with time. In addition, it is noted that rate constants for samples at depths of 7.83m, 10.97m and 12.20m are representative of slightly more crystalline materials, which fall between lepidocrocite and goethite. The reactivities of iron oxides demonstrate the presence of reactive iron oxides in the sediments. Moreover, the crystal structure parameter γ for iron and manganese oxide, found in the Kidd 2 site, range from 1.56 to 2.34, and from 1.13 to 2.36, respectively. Crystal distribution tends to be homogeneous as γ approaches 1. Therefore, the small values of γ indicate that the crystal structure of iron and manganese oxides are nearly invariable, which is consistent with the constant k' along the depth profile.

4.3.1.2 Parameter Comparison

Table 4.8 compares kinetic reaction parameters (m_0 , k' , and γ) at the Kidd 2 site with other studies. Comparable parameters confirm the reliability of results.

Table 4.8: Comparison of kinetic parameters, including m_0 (initial mass of extractable iron), k' (rate constant), and γ (reaction exponent).

	Kidd 2 site		Scheldt estuary (Hyacinthe, 2006)		Island of Romo (Postma, 1993)	Bight of Aarhus (Postma, 1993)
Sediment type	Homogeneous medium sand, interbedded with silt and clay		Microtidal zone, surfacial brackish/freshwater marsh material, fine grain		Oxidized sandy aquifer	Marine oxidized mud
Reagent	Buffered ascorbate-citrate solution at pH=7.5		Buffered ascorbate-citrate solution at pH=7.5		Ascorbate at pH 3.0	
parameter	min	max	min	max	average	average
m_0 (mM/kg)	9.0	34.8	17.2	109.0	12.9*	94.0*
k'	1.25×10^{-4}	1.92×10^{-4}	4.6×10^{-4}	1.68×10^{-3}	5.30×10^{-5}	7.40×10^{-3}
γ	1.56	2.34	1.30	4.90	2.75	4.70
Aqueous Fe^{2+} (mg/L)	10	306	NA	NA	NA	NA

Note: *iron oxides (m_0) were extracted directly from the dithionite solution

The quantity of reactive iron oxide is related to the grain size. Small grain sizes like clay and silt tend to be associated with high iron (Table 4.8). In the Scheldt estuary and the Bight of Aarhus, where sediments are fine grained, the highest reactive iron concentration reached 109.0 mM/kg and 94.0 mM/kg, respectively. Nevertheless, in sandy aquifers like the Island of Romo, the iron content is only 12.9 mM/kg. At the Kidd 2 site, the iron content ranges from 9.0 to 34.8 mM/kg. The maximum concentration of reactive iron oxide is found at a depth of 7.83 m, where sand is interbedded with clay and silt. γ represents the heterogeneity of the iron pool. The small range of γ (1.56-2.34) indicates that iron oxides at the Kidd 2 site are more homogenous than at other sites,

which is consistent with the relatively constant k' (1.25×10^{-4} to $1.92 \times 10^{-4} \text{ s}^{-1}$). Postma (1993) presented a dissolution rate for synthetic ferrihydrite, with $k' = 4 \times 10^{-4} \text{ s}^{-1}$ and $\Upsilon = 1.10$. Therefore, the reactive iron oxides at the Kidd 2 site have properties that are between ferrihydrite and goethite, and more closer to lepidocrocite. Moreover, the homogenous sand and reducing condition lead to the relatively uniform iron pools and limits the re-oxidization of ferrous iron. At the Kidd 2 site, we expect the iron oxides to have been deposited along with the sedimentation process, resulting in a relatively homogenous pool of iron oxides with high reactivity.

4.3.2 Sequential Extraction

The sequential extraction procedure (SEP) in this study was specifically designed to characterize the pools of iron and manganese oxides based on their reactivities. To assess the variability and uncertainties, each sediment sample was split and duplicate analyses performed. Five out of forty sample pairs with a greater than 15% discrepancy were removed from the results. We also performed a single-step extraction to determine acid volatile sulfides (AVS). Solid organic matter content (Om%) was determined by the loss on ignition test, with duplicate sample sets.

Table 4.9 presents the results of the sequential extractions of iron and manganese oxides at the Kidd 2 site. In addition, single step extraction AVS and solid organic matter content in dry weight percentage (Om%) in the sediments are included. For reactive Fe oxide which was extracted by step 2 using the 0.5 M HCl, Fe(III) and Fe(II) has been differentiated. Figure 4.19 plots the results of the reactive Fe oxide, reactive Mn oxide, reactive Fe(II), reactive Fe(III), AVS and Om% depth profile at the Kidd 2 site.

Table 4.9: solid phase sequential extractions of iron and manganese oxides at the Kidd 2 site

		Sample	70% to	50% to	30% to	10% to	30	32	33	35	36	37	38	40
		ID	30	30	30	30								
		Depth(m)	6.10	6.97	7.84	8.71	9.14	9.75	10.06	10.67	10.97	11.28	11.58	12.19
parameter	Target phase	units												
Fe														
Step1 ^a	Absorbed/exchangeable fraction	mM/kg	3.35	0.27	0.65	5.87	0.29	0.55	0.36	0.17	1.33	1.03	1.81	0.72
Step2 ^b	Reactive iron oxides	mM/kg	106.73	122.37	129.57	170.27	123.42	114.66	99.00	93.78	89.27	89.48	87.52	75.30
	Fe(III)	mM/kg	25.33	30.93	29.58	43.95	28.24	26.12	20.23	20.21	18.74	17.39	17.71	19.10
	Fe(II)	mM/kg	81.40	91.44	99.99	126.32	95.17	88.55	78.77	72.56	75.05	71.88	71.77	68.42
Step3 ^c	Crystalline iron oxides	mM/kg	78.42	65.17	85.21	88.41	60.95	77.22	54.77	56.44	56.55	65.60	57.08	59.92
Step4 ^d	Residual non-reactive iron oxides	mM/kg	748.82	758.05	760.82	845.96	659.30	768.50	728.76	675.32	566.30	549.63	666.91	685.61
Total		mM/kg	937.32	945.86	976.24	1110.5	843.96	960.93	882.89	825.72	713.45	705.74	813.33	821.55
Mn														
Step1 ^a	Absorbed/exchangeable fraction	mM/kg	0.74	0.45	0.47	0.42	0.27	0.34	0.13	0.15	0.63	0.90	0.73	0.14
Step2 ^b	Reactive manganese oxides	mM/kg	2.10	3.02	4.58	5.01	2.94	3.14	3.03	2.91	3.06	2.96	3.12	2.15
Step3 ^c	Crystalline manganese oxides	mM/kg	1.05	0.92	1.12	1.15	1.29	1.25	0.94	0.91	0.85	1.02	0.89	1.01
Step4 ^d	Residual non-reactive manganese	mM/kg	7.82	8.84	7.20	8.46	10.89	10.34	10.39	9.78	7.24	7.56	8.75	10.36
Total		mM/kg	11.70	13.23	13.37	15.04	15.39	15.06	14.49	13.76	11.78	12.43	13.48	13.66
AVS^e		mM/kg	0.13	0.14	0.27	1.34	0.47	0.32	0.40	0.05	0.00	0.00	0.00	0.00
Om%^f			NA	1.57	1.51	1.71	1.97	1.39	0.76	0.78	0.91	0.88	0.82	0.75

		Sample	57	59	60	60 2nd	61	63	64	65	67	68	69	70
		Depth	17.63	18.07	18.29	18.80	19.05	19.56	19.81	20.07	20.57	20.83	21.08	21.34
parameter	Target phase	units												
Fe														
Step1 ^a	Absorbed/exchangeable fraction	mM/kg	0.01	0.15	0.02	0.03	0.00	0.00	0.00	0.00	0.01	0.00	0.00	0.01
Step2 ^b	Reactive iron oxides	mM/kg	99.50	95.14	76.49	102.59	93.30	83.66	68.31	86.37	88.84	97.40	79.34	95.78
	Fe(III)	mM/kg	21.42	18.72	18.25	25.14	18.91	17.16	18.31	15.48	19.00	15.55	19.59	22.30
	Fe(II)	mM/kg	78.08	76.42	58.24	77.45	74.38	68.55	65.35	52.83	67.37	63.12	69.25	75.09
Step3 ^c	Crystalline iron oxides	mM/kg	73.37	82.51	73.78	56.35	56.53	73.21	63.63	79.42	68.14	69.31	61.74	82.26
Step4 ^d	Residual non-reactive iron oxides	mM/kg	691.89	597.59	650.13	578.01	503.58	779.67	684.39	763.33	722.91	655.67	616.53	670.06
Total		mM/kg	864.77	775.39	800.43	736.97	653.35	936.48	816.34	929.06	879.91	822.36	757.60	848.12
Mn														
Step1 ^a	Absorbed/exchangeable fraction	mM/kg	0.26	0.26	0.20	0.17	0.20	0.15	0.08	0.15	0.28	0.09	0.11	0.11
Step2 ^b	Reactive manganese oxides	mM/kg	4.27	3.84	2.81	3.43	3.15	3.16	2.34	3.57	3.13	3.66	3.15	3.79
Step3 ^c	Crystalline manganese oxides	mM/kg	1.10	1.27	1.12	0.87	0.91	1.17	1.03	1.28	1.07	1.11	0.98	1.29
Step4 ^d	Residual non-reactive manganese	mM/kg	9.14	8.10	9.09	7.78	7.35	10.98	9.66	10.99	10.05	9.34	8.73	9.44
Total		mM/kg	14.78	13.48	13.22	12.24	11.60	15.46	13.10	15.99	14.53	14.21	12.97	14.63
AVS^e		mM/kg	0.01	0.03	0.04	0.08	0.09	0.17	0.21	0.17	0.06	0.24	0.12	0.08
Om%^f			0.92	NA	0.85	NA	NA	0.81	NA	0.83	NA	0.87	NA	0.90

		Sample	57	59	60	60 2nd	61	63	64	65	67	68	69	70
		Depth	17.63	18.07	18.29	18.80	19.05	19.56	19.81	20.07	20.57	20.83	21.08	21.34
parameter	Target phase	units												
Fe														
Step1 ^a	Absorbed/exchangeable fraction	mM/kg	0.01	0.15	0.02	0.03	0.00	0.00	0.00	0.00	0.01	0.00	0.00	0.01
Step2 ^b	Reactive iron oxides	mM/kg	99.50	95.14	76.49	102.59	93.30	83.66	68.31	86.37	88.84	97.40	79.34	95.78
	Fe(III)	mM/kg	21.42	18.72	18.25	25.14	18.91	17.16	18.31	15.48	19.00	15.55	19.59	22.30
	Fe(II)	mM/kg	78.08	76.42	58.24	77.45	74.38	68.55	65.35	52.83	67.37	63.12	69.25	75.09
Step3 ^c	Crystalline iron oxides	mM/kg	73.37	82.51	73.78	56.35	56.53	73.21	63.63	79.42	68.14	69.31	61.74	82.26
Step4 ^d	Residual non-reactive iron oxides	mM/kg	691.89	597.59	650.13	578.01	503.58	779.67	684.39	763.33	722.91	655.67	616.53	670.06
Total		mM/kg	864.77	775.39	800.43	736.97	653.35	936.48	816.34	929.06	879.91	822.36	757.60	848.12
Mn														
Step1 ^a	Absorbed/exchangeable fraction	mM/kg	0.26	0.26	0.20	0.17	0.20	0.15	0.08	0.15	0.28	0.09	0.11	0.11
Step2 ^b	Reactive manganese oxides	mM/kg	4.27	3.84	2.81	3.43	3.15	3.16	2.34	3.57	3.13	3.66	3.15	3.79
Step3 ^c	Crystalline manganese oxides	mM/kg	1.10	1.27	1.12	0.87	0.91	1.17	1.03	1.28	1.07	1.11	0.98	1.29
Step4 ^d	Residual non-reactive manganese	mM/kg	9.14	8.10	9.09	7.78	7.35	10.98	9.66	10.99	10.05	9.34	8.73	9.44
Total		mM/kg	14.78	13.48	13.22	12.24	11.60	15.46	13.10	15.99	14.53	14.21	12.97	14.63
AVS^e		mM/kg	0.01	0.03	0.04	0.08	0.09	0.17	0.21	0.17	0.06	0.24	0.12	0.08
Om%^f			0.92	NA	0.85	NA	NA	0.81	NA	0.83	NA	0.87	NA	0.90

Notes:

^a extracted by 1M CaCl₂, room temperature, 24 h rotation

^b extracted by 0.5 M HCl, room temperature, 24 h rotation

^c extracted by 1.0 M NH₂OH.HCl in 25% CH₃COOH, water bath at 90°C for 3 h, 2 times with 25% CH₃COOH rinse at end

^d extracted by Aqua Regia (1:1 full strength HCl-nitric acid solution, water bath at 80°C for 5h

^e extracted by 1M HCl, and released H₂S was trapped by zinc acetate solution

^f analyzed by loss on ignition at temperature of 550°C

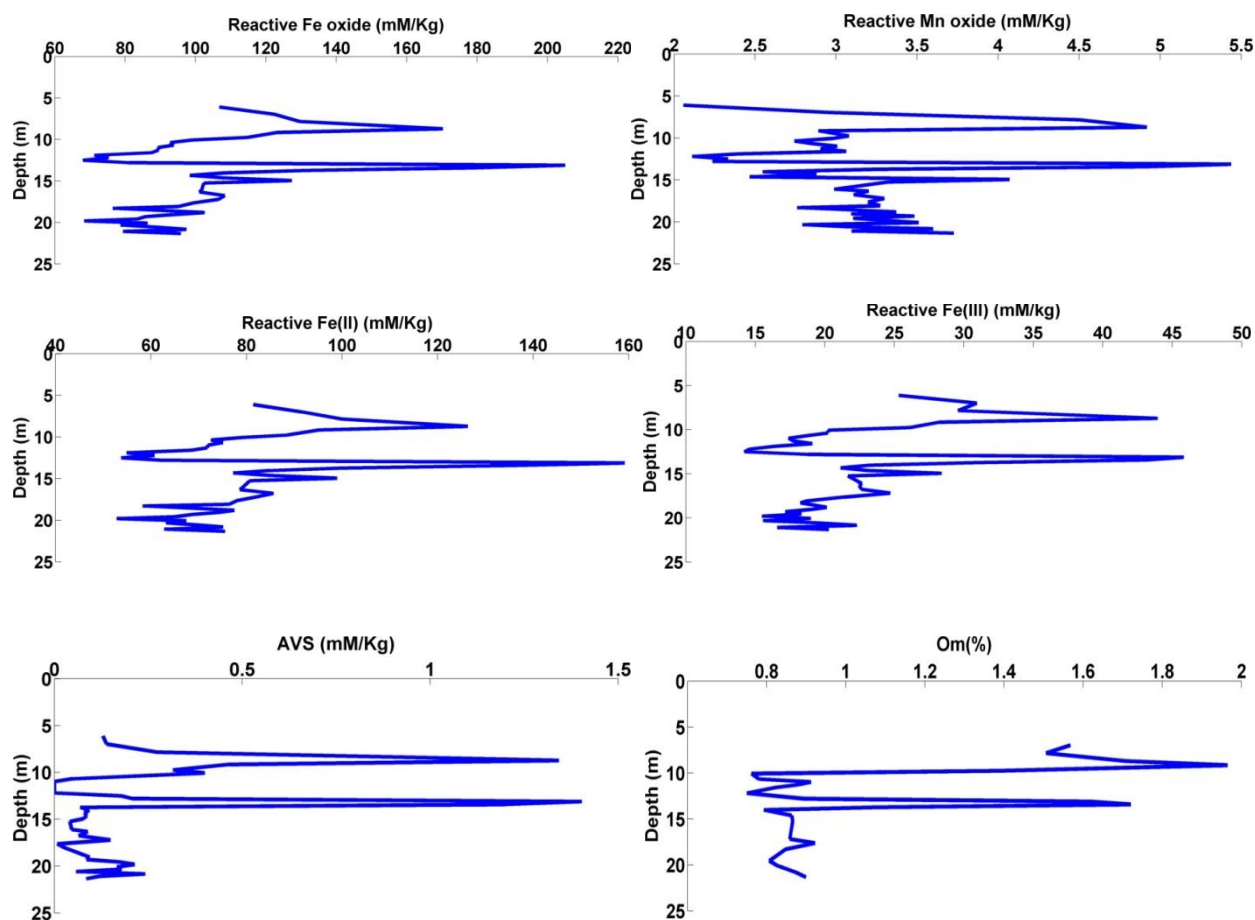


Figure 4.19: solid sediment depth profiles for a) 0.5 M HCl extractable - reactive - Fe oxide, b) 0.5 M HCl extractable - reactive Mn oxide, c) reactive Fe(II), d) reactive Fe(III), e) AVS, f) Om%

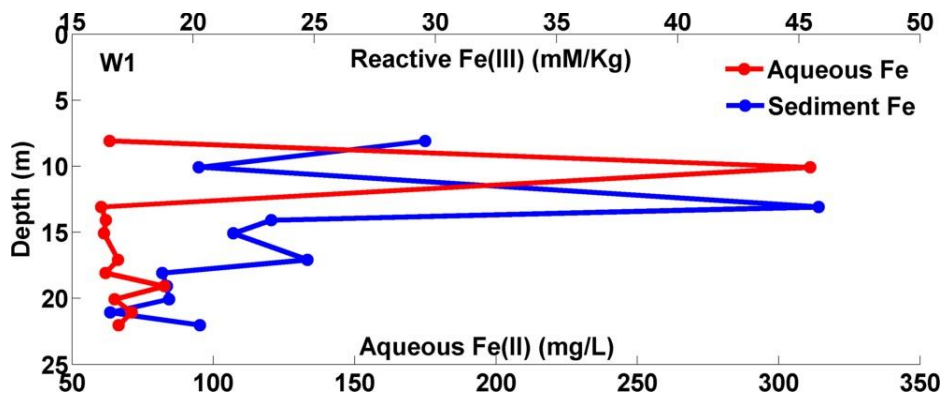
4.3.2.1 Fe(II) and Fe(III) Speciation

Results of the reactive iron speciation analysis showed that 75% to 80% of dissolved iron in 0.5M HCl extractant is Fe(II), and Fe(III) only makes up 20%-25% of total reactive Fe oxide. This finding is consistent with the field observation, which all sediment cores were exhibited grey color and no brown staining were visible. Figure 4.19 shows that both reactive Fe(II) and Fe(III) correspond well with the reactive Fe along the depth profile. Two-peaks of reactive Fe(III) and Fe(II) are observed at a depth of 8.71 m and 13.11 m respectively.

4.3.2.2 Reactive Fe(III) and Mn Oxides

Table 4.9 shows the concentration of reactive iron and manganese oxides ranging from 15.48 to 43.95 mM/kg, and from 2.1 to 5.01mM/Kg, respectively. The concentration of reactive iron oxide is approximately 8 to 20 times greater than manganese oxide, which is consistent with their aqueous concentrations. Moreover, the presence of reactive iron oxide supports the idea that iron reduction is the primary pathway for organic matter oxidation. It is shown that iron and manganese oxides appear to correlate well with each other and both have a two-peak pattern at depths of 8.7 m and 13.1 m, respectively (Figure. 4.19). Between depths of 8.7 and 13.1 m, both reactive iron and manganese oxides reached their minimum values, indicating the either the loss of reactive solid phases or source of heterogeneity. At depths deeper than the second peak, both iron and manganese remain at a more or less constant value, but manganese oxide tends to increase in concentration and forms a spike at depths of 16-18 m.

Figure 4.20 and 4.21 plot the concentrations of aqueous and solid phases for iron and manganese, respectively. The boundary line (depth=13.1 m) which is located at the lower boundary of upper mixing zone can be used to describe the relationship between aqueous and solid phase patterns.



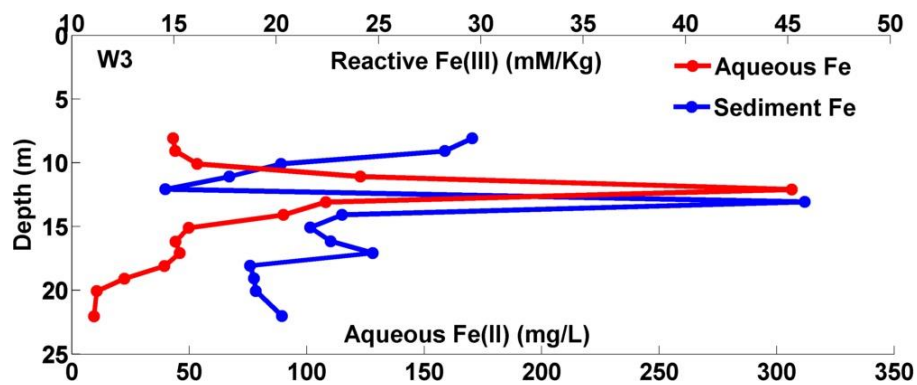


Figure 4.20: Comparison between aqueous Fe(II) and reactive Fe(III) along the depth profile in a) W1 and b) W3.

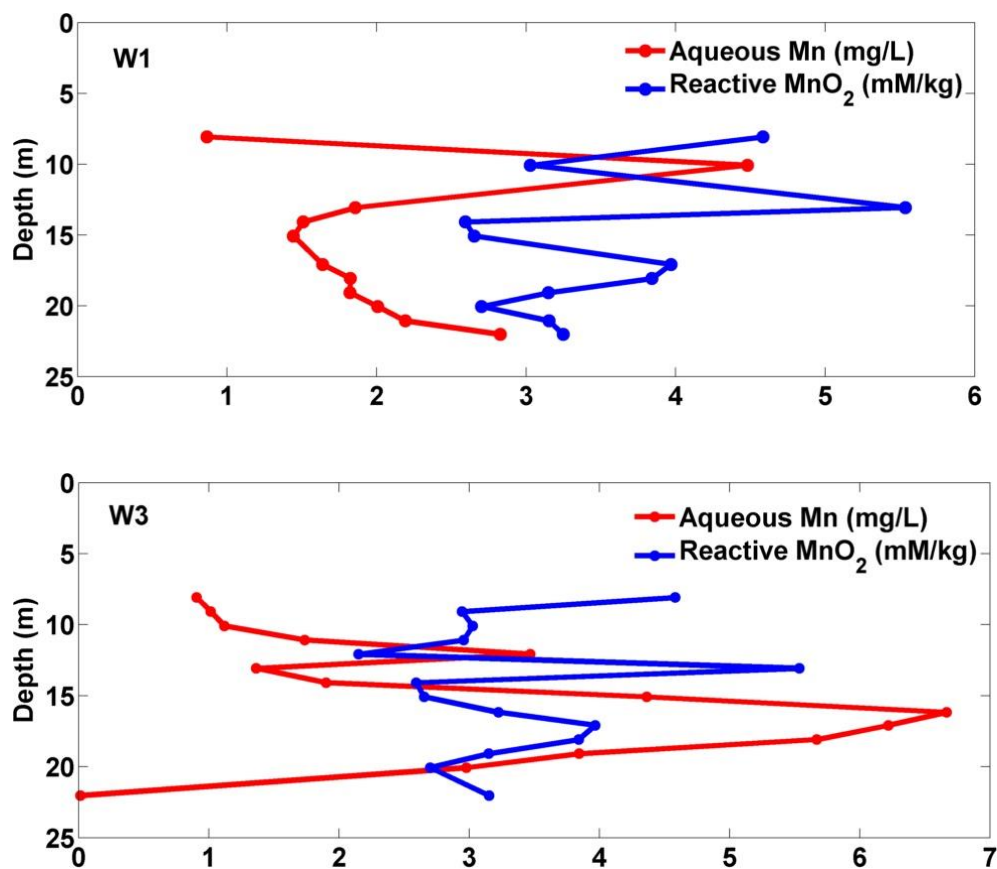


Figure 4.21: Comparison between aqueous and reactive manganese along the depth profile in a) W1 and b) W3.

In W1 (Figure. 4.20), a strong inverse relationship is seen between aqueous and solid iron above the boundary line. The peak of the aqueous iron was at a depth of 10.08 m, where the sediment-extracted reactive iron oxide was at a minimum. At a depth of 13.07 m, aqueous iron dramatically decreased from 311 mg/L to 60 mg/L, but reactive iron oxide reached its first peak of 45.8 mM/kg. Below 13.1 m; however, the inverse relationship cannot be defined. Both aqueous and solid iron remained relatively constant, with small fluctuations in their values. The same inverse relationship was present in W3 (Figure 4.20). Above 13.1 m, the aqueous iron concentration increased with depth, reaching its maximum value at a depth of 12.08 m, whereas, reactive iron oxide continuously decreased from 8 m to 12 m. At a depth of 13.1 m, the reactive iron oxide peaked. Below 13.1 m, both aqueous and reactive iron oxide gradually decreased. Aqueous iron presented a more pronounced decreasing trend.

The plots of manganese present a more complex relationship, especially in the deep saline water zone (Figure. 4.21). Above 13.1 m, the inverse relationship between aqueous and solid manganese can be established. In both W1 and W3, reactive manganese oxide reached minimum values when the aqueous concentrations encountered peaks at the upper mixing zone. Below 13.1 m, the aqueous manganese concentration in W1 decreased rapidly from 4.5 mg/L to 1.9 mg/L, and then showed an increasing trend from a depth of 17 m to 22 m. Nevertheless, reactive manganese oxide did not follow its aqueous pattern, instead forming a second peak at a depth of 17.08 m. In W3; however, the second peak of reactive manganese oxide correlated with the maximum concentration of aqueous manganese in deep saline water zone.

4.3.2.3 Sedimentary Organic Carbon

Organic matter content (Om wt. %) in sediment ranges from 0.75-1.97%, which is equivalent to 625 – 1641 mmol C/kg (Figure. 4.19). As iron reduction is the major pathway for organic matter degradation in sediments, and both iron oxides and organic matter are reactants, a consistency of these two reactants is expected. From Figure 4.22, Om% is seen to correspond well with reactive iron oxide Fe(III) along the depth profile, with $R^2=0.62$. The largest deviation occurs at

the high Om% interval (1.8-2.0%), which is associated with the peaks of reactive iron oxide at depths of 9.1 m and 13.1 m. Between these two peaks, both reactive iron oxide and Om% reach their minimum values. Below the boundary line (at 13.1 m), both of these drop off rapidly, and have relatively constant low values between depths of 14-22 m. The continuously low Om% and the reactive iron oxide in the deep saline water sediments suggest that iron reduction is not occurring as intensively as it does in the shallower groundwater.

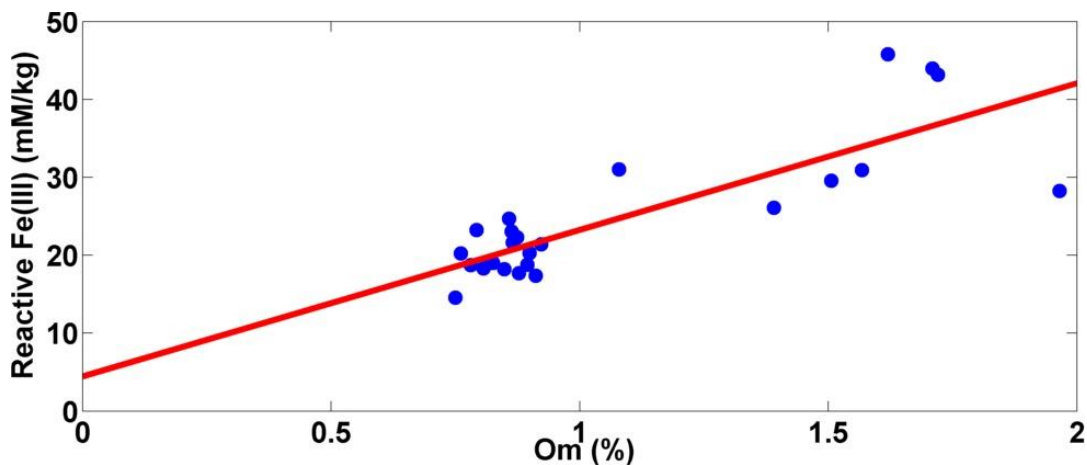


Figure 4.22: Highly correlated relationship between reactive iron oxide and organic matter content, with $R^2 = 0.62$

4.3.2.4 Acid Volatile Sulfide (AVS) and Sulfate Reduction

The presence of FeS in iron-rich aquifers is an indicator of sulfate reduction, since sulfate-reducing environments are commonly found near equilibrium with FeS (Cook, 1984; Wersin et al., 1991; Postma & Jakobsen, 1996). As seawater brings significant SO_4^{2-} into the aquifer, the elevated SO_4^{2-} could enhance the sulfate reduction if the aquifer is reduced and not limited in organic matter (Slomp & Van Cappellen, 2004). Given the abundant dissolved iron in the groundwater and the low solubility of FeS, all of the acid volatile sulphide from sulfate reduction is assumed to be incorporated with iron, and to precipitate as FeS. Table 4.9 shows that the concentrations of FeS range from 0 - 1.4 mM/kg, which are an order of magnitude smaller than the reactive iron oxide Fe(III) concentrations. The results corresponded well with the total extractable sulfur from the first two steps of the SEP, indicating the reliability of the

AVS extraction method. The small amount of FeS indicates that sulfate reduction is occurring at the Kidd 2 site, though its intensity is not comparable to that of the iron reduction.

Similar to the pattern for reactive iron oxide, the two-peak pattern of FeS occurred at depths of 8.7 m and 13.1 m (Figure 4.19). Between the two peaks, both FeS and reactive iron oxide drop to their minimum values, and even the concentration of FeS reaches zero at depths of 10.9-12.2 m (Figure. 4.19). Because FeS is undetectable, iron reduction is likely the dominant process at the upper mixing zone and sulfate reduction is strongly inhibited and only a limited amount of HS^- would be expected to be produced. Therefore, FeS is not a detectable major secondary mineral in sediments. Below 13.1 m, FeS rapidly drops from 1.4 mM/kg to 0.1 mM/kg and remains at low constant values from depths of 13.1 m to 22.0 m. The low content of FeS indicates that the sulfate reduction does not overwhelm iron reduction; even the aqueous iron concentration remains low at deeper groundwater. Overall, the low AVS content suggests that sulfate reduction is relatively minor compared to available sulfate concentration, which is consistent with mixing line of sulfate along chlorite concentration (Figure 4.2).

4.3.3 SEM Analysis

Table 4.10 lists the mineralogical descriptions for 8 samples, consisting of grain size, elements distribution and interpreted mineral phases. Figure 4.23 to Figure 4.31 presents the high resolution backscattered electron (BSE) images for sediment surfaces at each sample. Since iron and manganese would generate brighter color than surrounding silicate minerals when observed by BSE images, we focus on performing qualitative EDS analyses for interesting white spots. However, if the white spot is absent in samples, the bulk grey surface was analyzed. Keeping in mind that SEM may not be able to resolve mineral compositions if the phase concentrations are too low. As the extraction data show limited sulfide in the sediments, it is unlikely that FeS can be detected by SEM.

Concomitant “Fe” and “O” peaks were found only in samples at depths of 7.8m (Figure 4.23), 8.7 m (Figure 4.24) and 13.1 m (Figure 4.27), indicating the “Fe” and “O” are major elements of

these white spots, and the possible mineral is iron oxide. At other depths, samples generally show grey color under SEM, indicating the low concentration of iron in sediments, possibly lower the SEM detection limit. This is consistent with the “two - peak” pattern of reactive iron oxide (Figure 4.19), where reactive iron oxide is more abundant at above and below the upper mixing zone, but much less right at the mixing zone. It is noted that iron oxide forms bright surfaces or agglomerates associated with Al- and Si- rich minerals, like quartz and chlorite. As quartz and chlorite have negatively charged surfaces under neutral pH (Stumm 1992), it would absorb positively charged iron oxide colloids on to their surfaces. However, the iron oxide colloids are not observed on mineral phases. Rather, it looks like iron oxide is embedded within these Al- and Si- minerals. Therefore we believe that iron oxide was formed during the sedimentation rather than the transport of iron oxide colloids by groundwater flow. At depths of 7.8m, 8.7m, and 13.1m, sediments are dominantly composed of finer material like clay and silt, which suggests linkage between iron pool and the grain size distributions. In sample collected at depth of 7.8m (Figure 4.23) and 17.1m (Figure 4.28), siderite may also be precipitated on mineral surfaces as the presence of “C” and “O” peak under EDS analysis. This is consistent with the slow precipitation kinetics of siderite in supersaturated solutions. On the upper saline wedge around 10-12m, the sub-angular shape of grains suggest the sediment is textually immature, which is consistent with the abundant silicate minerals. Moreover, samples showed a uniform grey color and no Fe/Mn peak was observed (Figure 4.25, and Figure 4.26), indicating iron and manganese oxides are below the SEM detection limit. The lack of Fe/Mn peaks at saline wedge agrees with extraction results. Below 13.1m, major Fe and Mn peaks were still absent, indicating the low iron oxide content at deep sediments. In sample collected at depth of 17.1m, coincident Ti and Fe peaks possibly indicate the presence of $\text{Fe}_2\text{TiO}_4 - \text{FeOx}$. In sample collected at depth of 8.7m, we captured black organic matter (Figure.4.24), which shown unique “C” peak under EDS analysis. Furthermore, “Mn” peaks in all of samples are small, suggesting the low concentration of manganese. “S” peaks are even lower, or absent in some samples.

Table 4.10: Mineralogical analysis by SEM at the Kidd 2 site

Depth(m)	Grain size	EDS analysis	Major mineral phases
7.8	Silt and clay	Major peaks: Fe, O, Si	Iron oxide (FeOx), siderite (FeCO ₃), quartz(SiO ₂),
8.7	Silt and clay	Minor peaks: K, C Major peaks: Fe, O, Si	Iron oxide (FeOx), manganese oxide (MnO ₂), quartz(SiO ₂)
11.9	Medium sand	Minor Peaks: Al, K, Ti, Mn Major peaks: Si	No iron bearing mineral is detected.
12.2	Medium sand	Minor Peaks: O, Mg, Al, Ca, Fe Major peaks: Ca, P, O	No iron bearing mineral is detected.
13.1	Silty sand	Minor peaks: C, Na, Mg, Al, Si, Fe Major Peaks: Fe, O	Iron oxide (FeOx)
17.1	Medium sand	No minor peaks Major Peaks: Ti, Fe, O	Titanomagnetites(Fe ₂ TiO ₄), iron oxide (FeOx), Minor Siderite(FeCO ₃), manganese oxide(MnO ₂)
20.1	Medium sand	Minor Peaks: K, C, Si, V, Mn Major Peaks: Si, O, Al	No iron-bearing mineral is detected.
21.3	Medium sand	Minor Peaks: Na, V, Ti, C Major Peaks: Si,	Small amount of iron oxide(FeOx) is detected
		Minor Peaks: O, Mg, Na, Al, Fe	

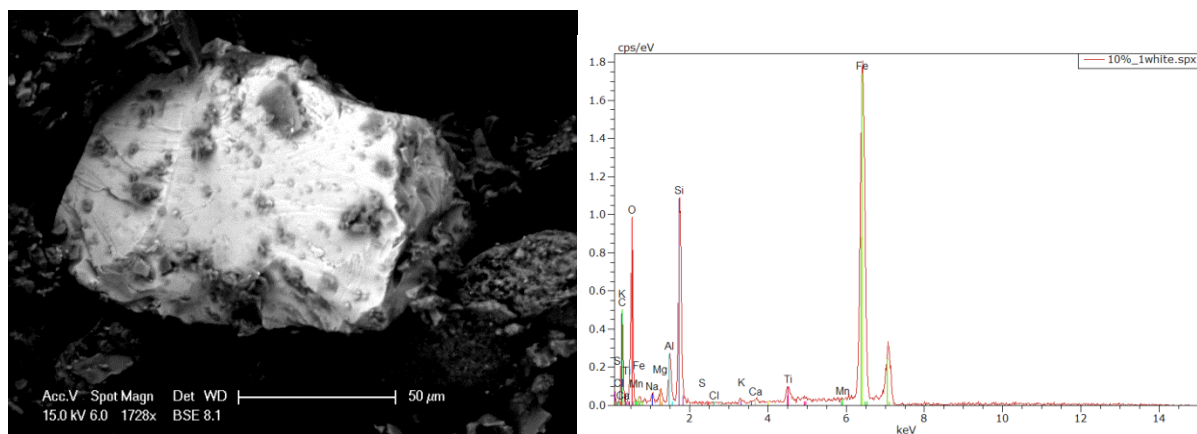


Figure 4.23: Backscattered electron image of minerals with bright surfaces (depth=7.8m). EDS analyses of white surface indicates the presence of iron oxide.

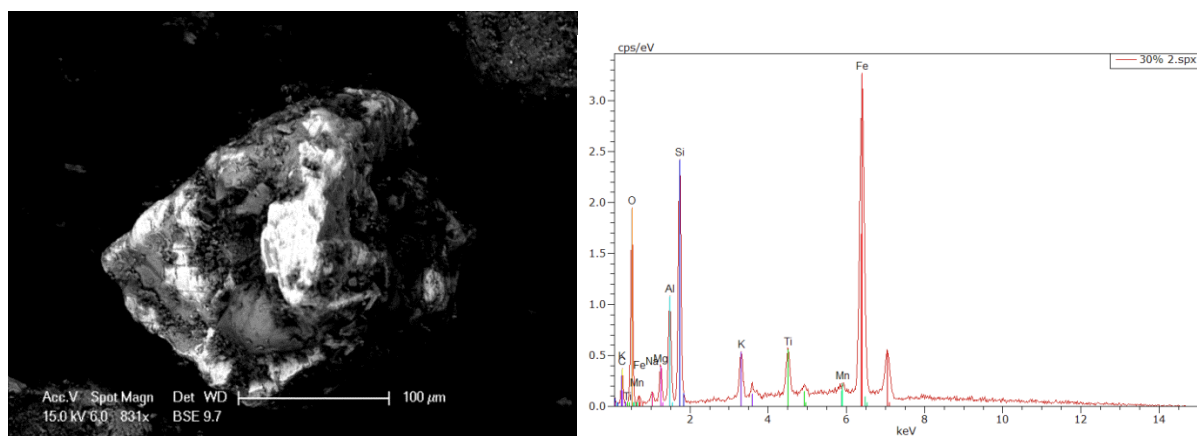


Figure 4.24: Backscattered electron image of minerals with bright agglomerates embedded into the sediment (depth=8.7m). The EDS analysis indicates the presence of iron oxide, with Al- and Si minerals, possibly quartz (SiO_2) and chlorite $(\text{Mg}, \text{Fe}^{2+})_5\text{Al}(\text{Si}_3\text{Al})\text{O}_{10}(\text{OH})_8$.

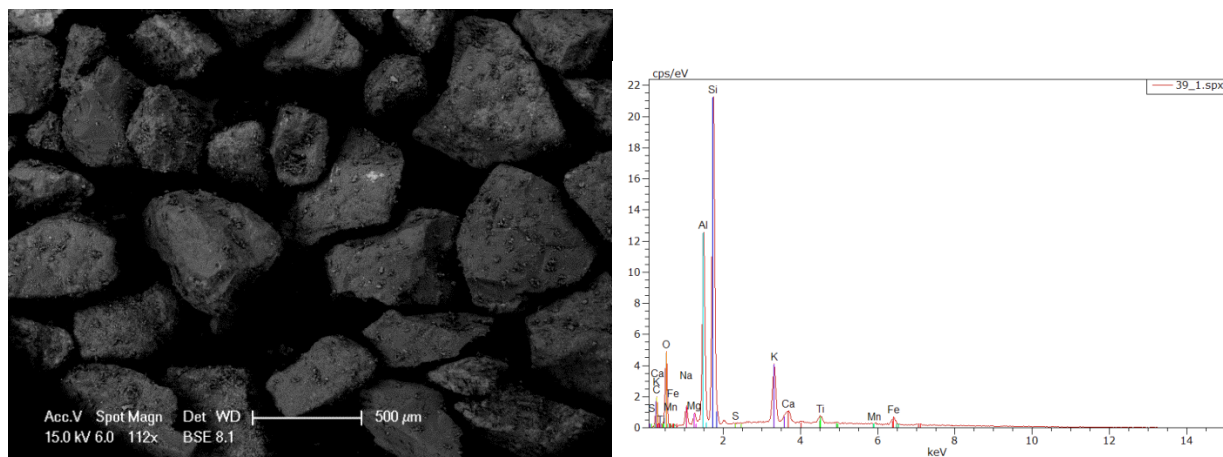


Figure 4.25: Backscattered electron image of sub-angular sediment (depth=11.9m). The absence of white spot suggests little iron or manganese in sediment. The EDS analysis indicates sediment is dominantly composed of silicate minerals: including quartz (SiO_2), plagioclase ($\text{CaAlSi}_2\text{O}_8$), chlorite $(\text{Mg,Fe}^{2+})_5\text{Al}(\text{Si}_3\text{Al})\text{O}_{10}(\text{OH})_8$.

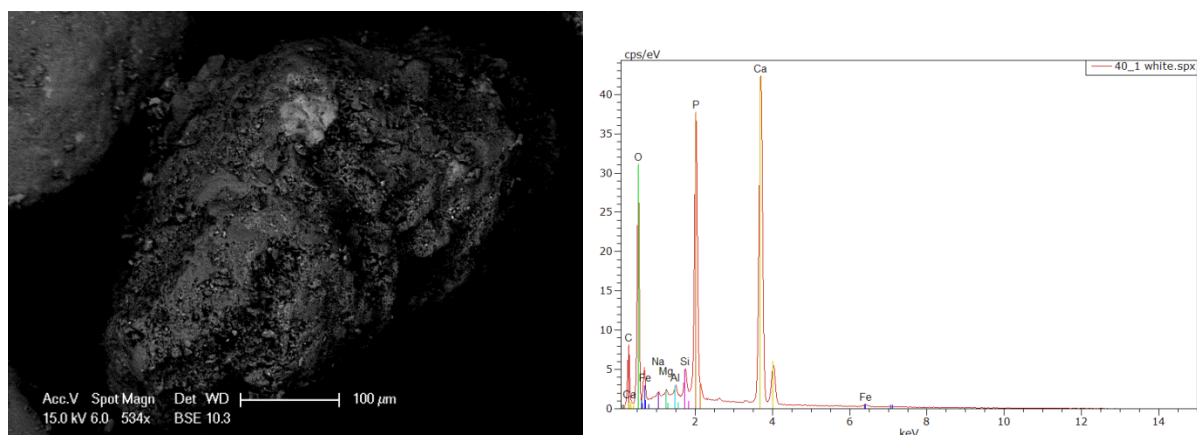


Figure 4.26: Backscattered electron image of minerals with grey color, indicates the absence of iron oxide (depth=12.2m). The EDS analysis indicates the absence of iron oxide. The high Ca, P, O peaks suggest the possible mineral phases are apatite $(\text{Ca}_5(\text{PO}_4)_3(\text{OH,F,Cl}))$ and calcite (CaCO_3).

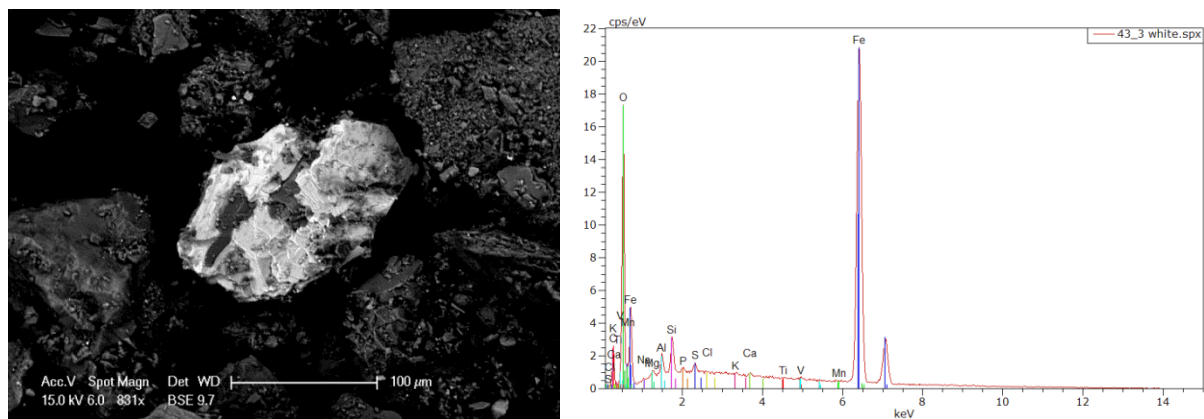


Figure 4.27: Backscattered electron image of minerals with bright agglomerates/surfaces, which embedded into the sediment (depth=13.1m). The EDS analysis indicates the presence of iron oxide as distinct “Fe” and “O” peaks.

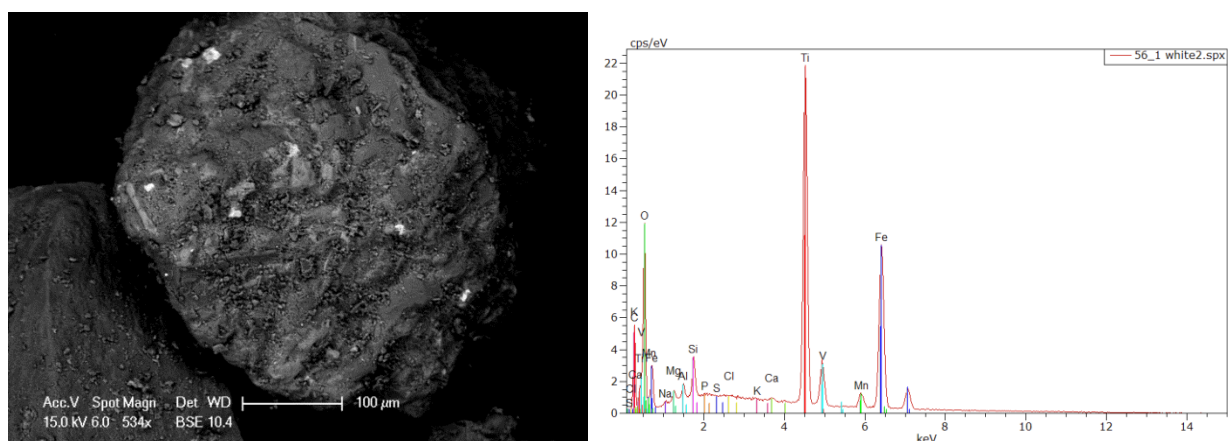


Figure 4.28: Appearance of an isolated insulating white spots ($\text{Fe}_2\text{TiO}_4 - \text{FeOx}$ inclusion) in a sediment (depth of 17.1m).

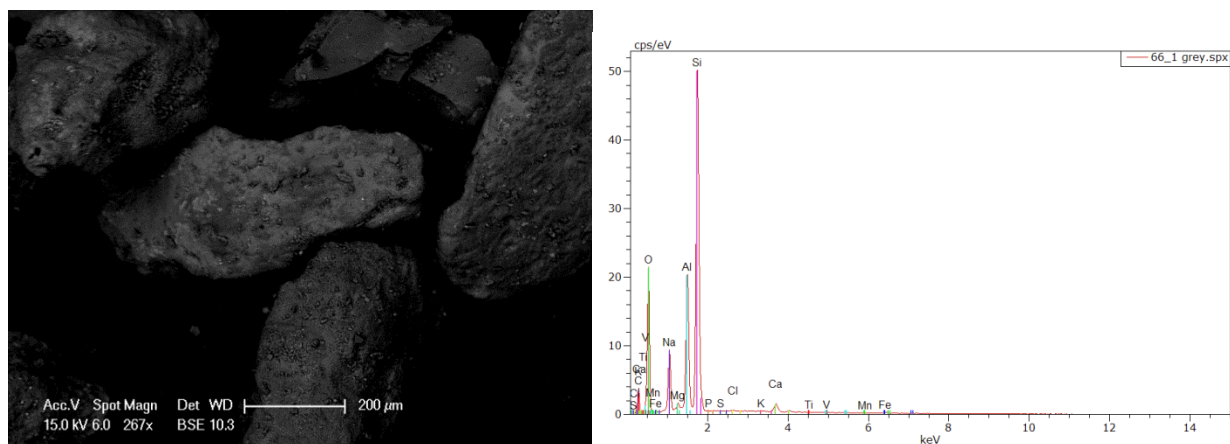


Figure 4.29: Backscattered electron image of sub-angular sediment (depth=20.1m). The absence of white spots suggests little iron or manganese in sediment. The EDS analysis indicates sediment is dominantly composed of silicate minerals: including quartz (SiO_2), plagioclase ($\text{CaAlSi}_2\text{O}_8$) and chlorite $(\text{Mg,Fe}^{2+})_5\text{Al}(\text{Si}_3\text{Al})\text{O}_{10}(\text{OH})_8$.

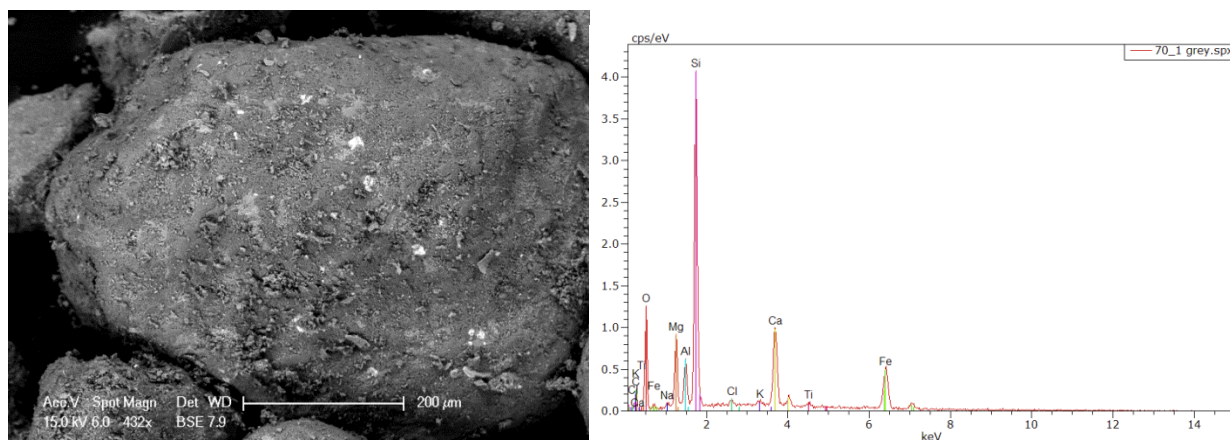


Figure 4.30: Appearance of an isolated insulating white spots (FeOx inclusion) in a sediment (depth of 21.3m). EDS analysis for white spot suggest possible iron bearing mineral phases are iron oxide (FeOx) and siderite (FeCO_3).

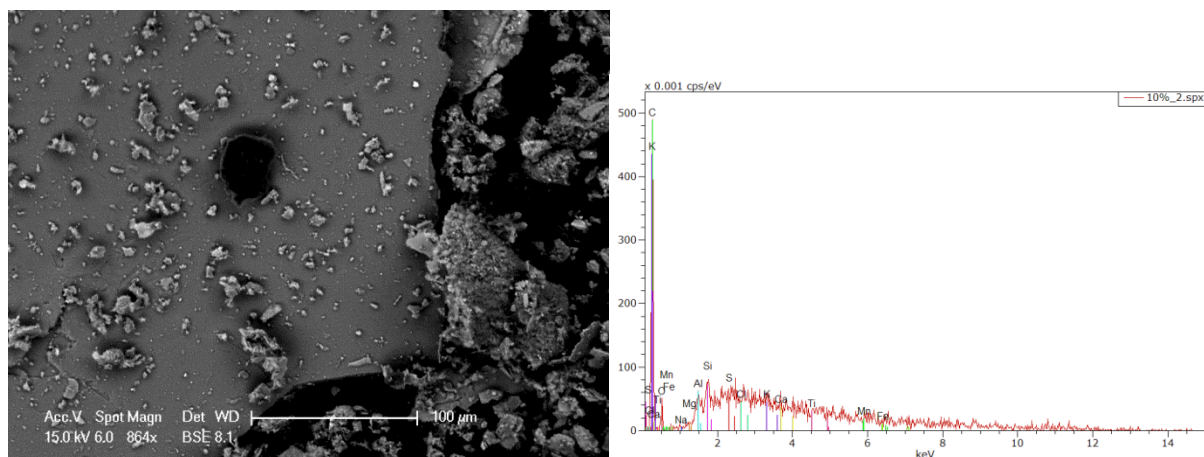


Figure 4.31: Backscattered electron image of black fragment on the mineral surface (depth of 8.7m). The EDS analysis indicates the presence of organic matter as the distinct “C” peak.

4.4 Spectroscopic Properties of Dissolved Organic Matter

Although iron is a source of interference in fluorescence properties of DOM, the iron quenching experiment have demonstrated the validation of using fluorescence indices (i.e. FI and RI) and PRRAFAC model to qualify the DOM properties and compositions.

4.4.1 Source of Organic Matter

Various indices derived from EEMs can quantify the fluorescence properties of organic matter. The fluorescence index (FI) is the most widely used index that provides information about the source of organic matter. High values of FI (approximately 1.80) indicate that DOM is derived from extracellular microbial activity, whereas low values of FI (approximately 1.20) suggest that DOM comes from terrestrial plant and soil organic matter (Cory & McKnight, 2005). The value of FI is calculated to (emission at 470 nm) / (emission at 520 nm) at excitation of 370 nm (McKnight et al. 2001).

In both W1 and W3, FI ranges from 1.59 to 1.80 (Figure 4.32), indicating that DOM is predominantly derived from microbial activity. In an anaerobic environment, the solid organic

matter must be fermented by bacteria prior to oxidation by iron/manganese reducing bacteria (Lovley & Phillips, 1986). Previous studies have also shown that microbial decomposition contributes the most DOC in aquifers (McDowell & Likens, 1988; Schiff et al., 1990).

In W1(Figure. 4.32), FI reached the minimum value at the upper mixing zone, keeping in mind that the deepest sampling port in W1 did not reach the lower mixing zone. In W3, a clear decreasing trend was seen at both the upper and lower mixing zones. Once across the lower mixing zone, FI drops rapidly, reaching the minimum value (1.59) at a depth of 22 m.

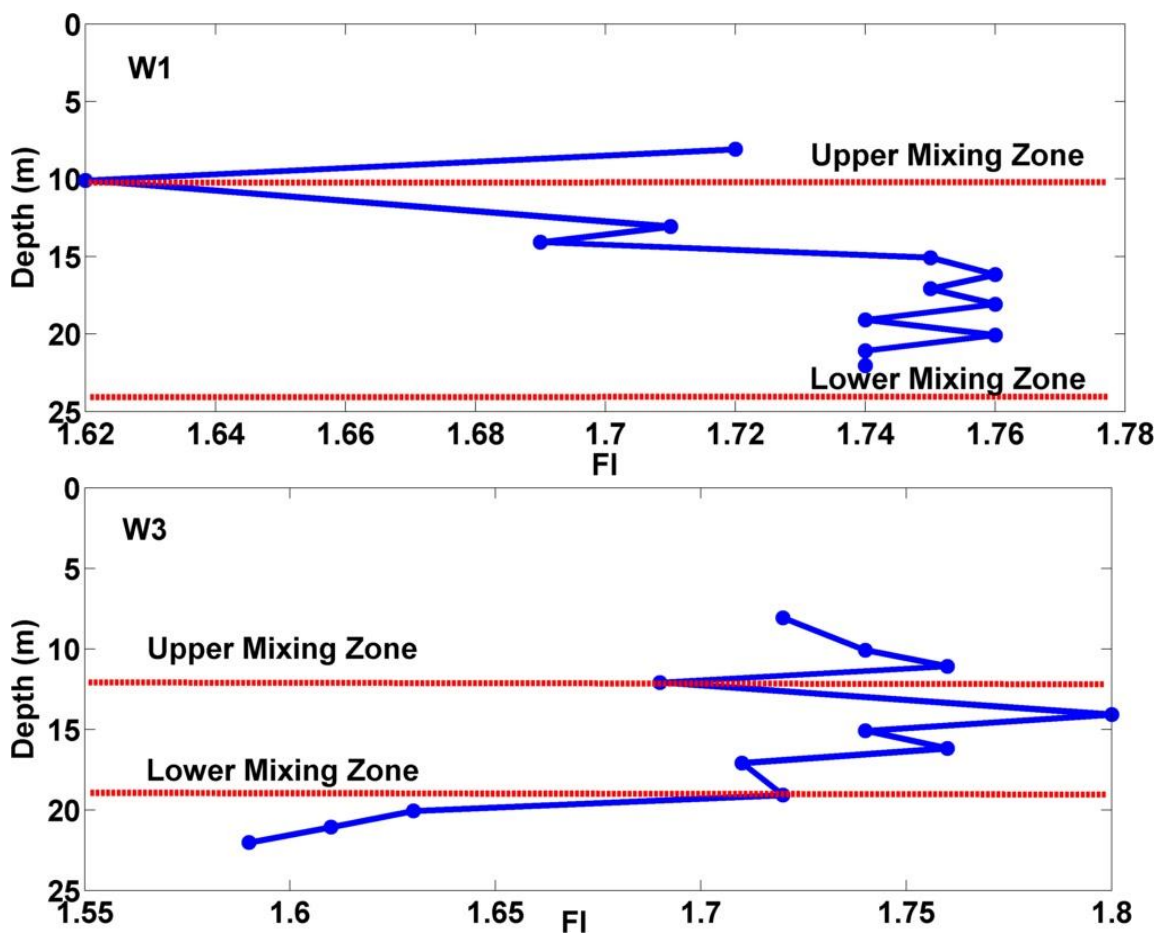


Figure 4.32: Florescence index (FI) calculated for W1 and W3; the red lines indicate the saline wedge.

4.4.2 PARAFAC Analysis

EEM data were fitted to a previously established PARAFAC model, where a multivariate modeling technique decomposes the fluorescence information into 13 components (Cory and McKnight 2005). Of the 13 components, 7 components (including three oxidized quinones Q1, Q2, and Q3 and four reduced quinones SQ1, SQ2, SQ3, HQ) were identified as quinone-like organic components, based on the similarity between their numbers, positions, and relative intensities of the component excitation peaks with the absorbance and excitation peaks of model quinones (Cory & McKnight, 2005). The 7 quinone-like components accounted for 55-68% of the total fluorescence of all samples. Quinone-like moieties can shuttle electrons by cycling between oxidized and reduced states (Scott et al., 1998; Nurmi & Tratnyek, 2002). Of the other 6 components, 2 resemble amino acid (C8 tryptophan, and C13 tyrosine) fluorophores, accounting for 4-7% of the total fluorescence, and the remaining 4 (C1, C3, C6, and C10) have not yet been associated with any class of molecules. Therefore, they are classified as unknown species, and contribute 25-41% of the total fluorescence.

The redox index (RI) is calculated as the sum of reduced quinone-like components over the total quinone-like components. It characterizes the oxidation state of the DOC and their redox reactivities (Miller et al., 2006; Mladenov et al., 2008). The RI can be used to determine whether the quinone-like components within the DOM are more reduced (closer to 1) or more oxidized (closer to 0). A shift in the RI usually indicates changes in the redox status. Miller et al. (2006) successfully used a transport model to demonstrate that the rate of oxidation of the reduced quinones was consistent with electron-transfer reactions in a wetland-stream environment, further supporting the use of RI in providing information about redox conditions and biogeochemical transformations in ecosystems.

Figure 4.33 plots the RI and DOC variation along depth profile in W3. The RI ranges from 0.3 to 0.4 along the depth profile. The smaller RI value suggests that a more intensive electron-shuttling process occurs between the reduced and oxidized quinones. Once the reduced quinones transfer electrons to outside electron acceptors, such as ferric iron, more oxidized

quinones are produced, and the RI tends to shift to a smaller value. Therefore, it is expected that shifting in RI correlates to the flux of electrons (i.e. the changing in DOC concentrations). It is shown that two obvious shifts of RI occur at the upper and lower mixing zones (Figure 4.33). The RI reaches its minimum value at the upper mixing zone, which coincides with the highest ferrous iron concentration. This intensive electron-shuttling process can be further supported by the rapidly decreasing in DOC concentrations, which decreased from initial 22 mg/L to 10 mg/L at upper mixing zone. At the lower mixing zone, the shift towards the oxidation state for the RI is less obvious, indicating that electron transfer process is less intensive than at the upper mixing zone. Similar to RI, the DOC concentration at lower mixing zone exhibited only a slightly increasing pattern, indicating a weaker electron shuttling process by DOC. In the internal zone of saline circulation, DOC maintains constant (5 - 8 mg/L) and RI values are relatively high, which implies the weakest electron transfer process and more reduced environment.

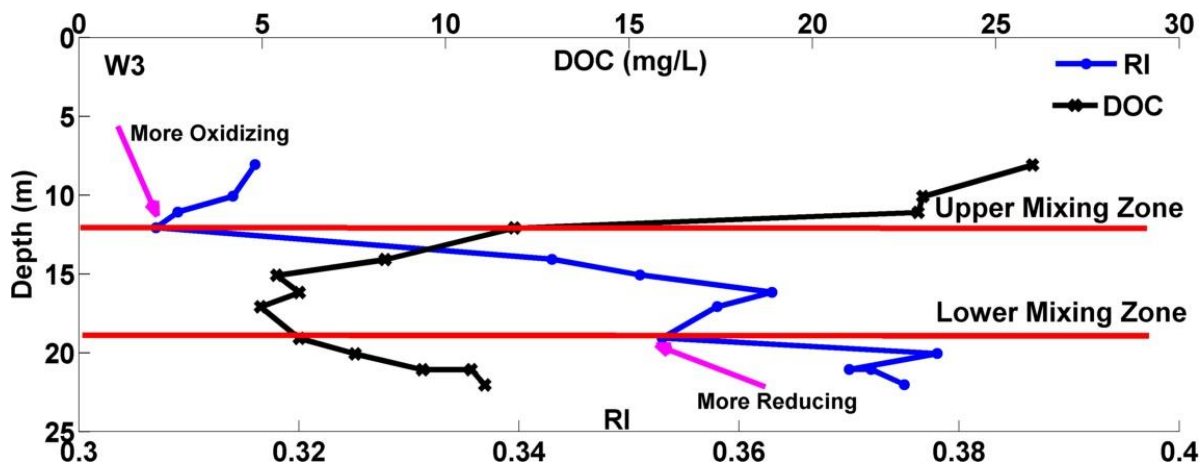


Figure 4.33: Redox index (RI) in W3, the red lines represent the upper and lower mixing zone.

In W3, the reduced component HQ exhibited the most pronounced changes along the depth profile, while SQ1, SQ2, and SQ3 are relatively constant. The ratios HQ/Q1, HQ/Q2, and HQ/Q3 can explain most of the shift in RI (Figure. 4.34) while other reduced quinones, like SQ1, SQ2, and SQ3 are less important. Since iron reduction is the primary pathway for electron transfers,

the consistent relationship between HQ and RI indicates that HQ is the dominant promoter of the electron shuttling process for iron reduction.

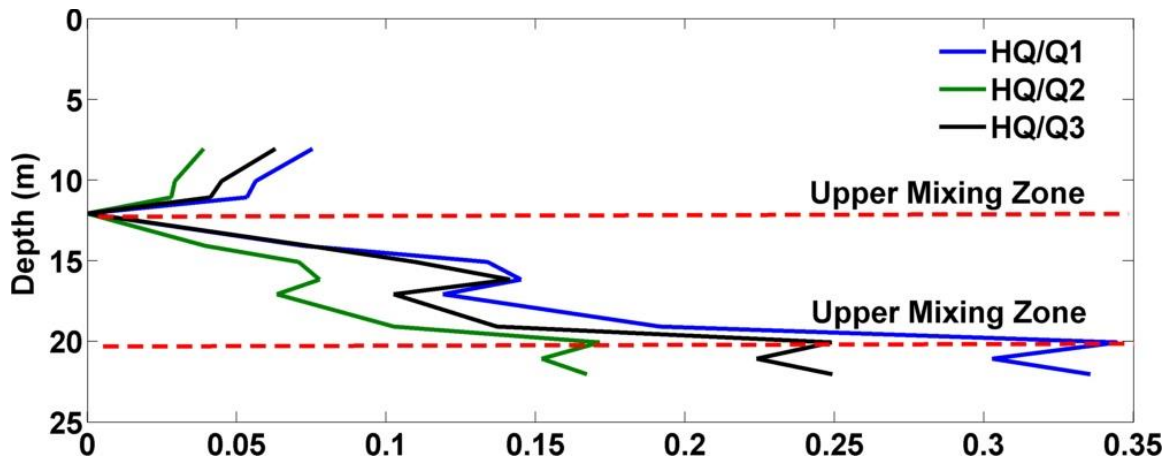


Figure 4.34: Depth profile of quinone-like ratios of HQ/Q1, HQ/Q2, and HQ/Q3 in W3.

Terrestrially-derived HQ is linked to the ferrous iron concentrations. Figure 4.35 shows that HQ is inversely related to the ferrous iron concentration. In both W1 and W3, as HQ approaches its minimum value, the ferrous iron concentrations tend to reach their maximum values at the upper mixing zone. Nevertheless, after crossing into the saline wedge, HQ increases rapidly, accompanied with decreasing ferrous iron concentrations. The negative relationship between HQ and ferrous iron suggests that the reduced quinone-like HQ is responsible for electron transfers between iron reducing microorganisms and reactive iron oxide. As reduced HQ transfers electrons to ferric iron, it turns into the oxidized state. The rapid consumption of HQ at the upper mixing zone further supports the increasing rate of both iron reduction and organic matter oxidation. Cory and McKnight (2005) also reported a similar relationship between HQ and the ratio of ferrous to ferric iron in Nymph Lake.

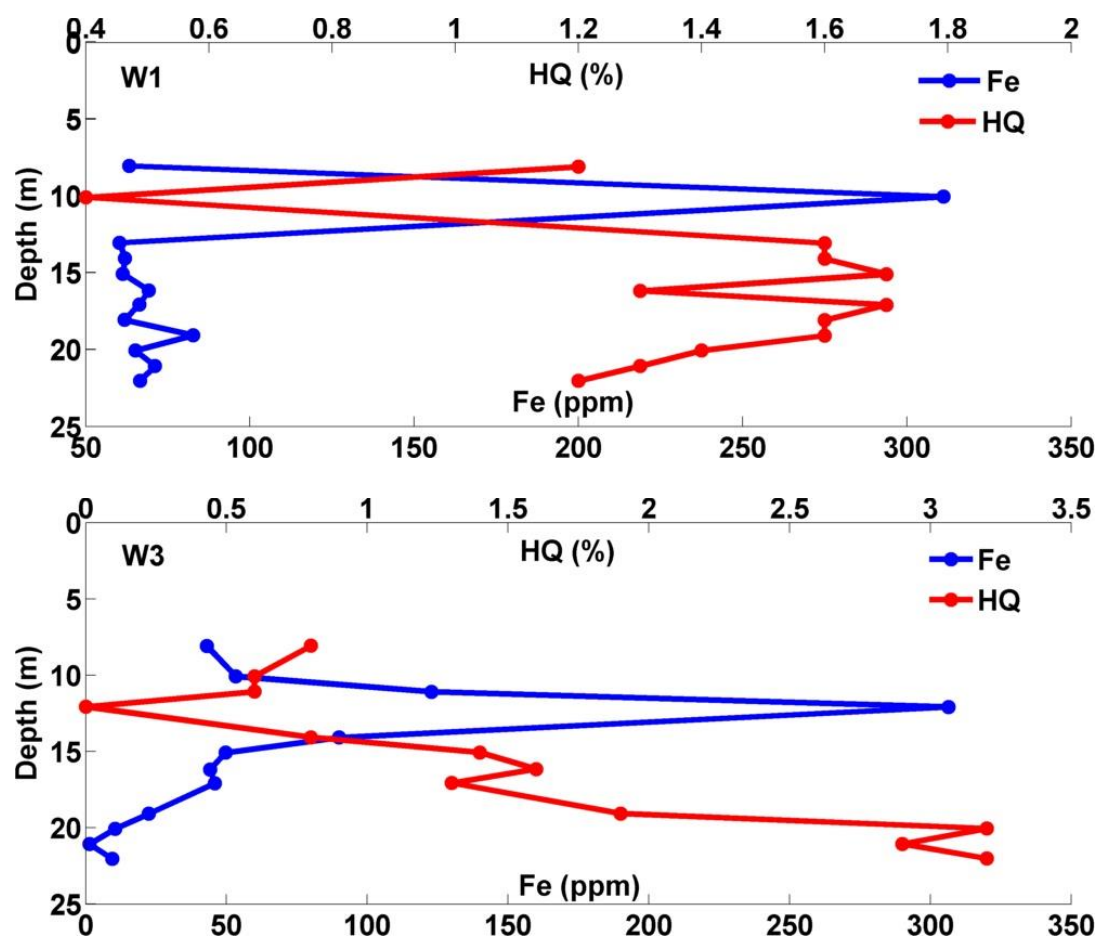


Figure 4.35: HQ versus ferrous iron concentration in W1 and W3.

4.4.3 Visual Fluorescence Peaks

Coble (1990, 1996) identified five primary peaks for visualized inspection of EEMs, including humic-like peaks A, C, and M; and protein-like peaks B and T (Coble, 1996; Coble et al., 1990). These peaks are believed to be linked to the organic matter properties and communities, and have been used for fluorescence comparisons in numerous studies.

Two humic-like fluorescence peaks were distinguished in the EEMs from the Kidd 2 site. Peak A is in the UV region at excitation wavelength = 260 nm, and Peak C is in the visible region at excitation = 300-370 nm (Coble, 1996). Both Peak A and C have broad emission maxima (approximately 450 to 500 nm), suggesting that the DOM pool contains many conjugated fluorescence molecules, that may be derived from terrestrial sources (Coble, 1998).

Figure 4.36 shows the EEMs of four water samples collected from different zones, including the shallow water zone, the upper mixing zone, the deep saline zone, and the lower mixing zone. Table 4.11 lists the classification of these four zones and the excitation/emission properties of the associated peaks. While Peak A was present in all of the four water samples, Peak C was only seen in water samples from the upper mixing zone, which coincides with the highest iron concentration (Figure. 4.36). Both pH variation and metal quenching could result in the change in fluorophores. Nevertheless, the slight in situ pH variation (pH 6.5-7.5) and an experiment that tested the effect of iron quenching suggest that pH and high iron cannot explain Peak C. Therefore, we conclude that at least one unique fluorophore is present at the upper mixing zone. Coble (1996) also suggested that Peaks A and C were independent of each other. The evidence shows that Peak C resulted from the mixture of fluorophores, whereas Peak A may have been due to a single fluorophore (Coble, 1996).

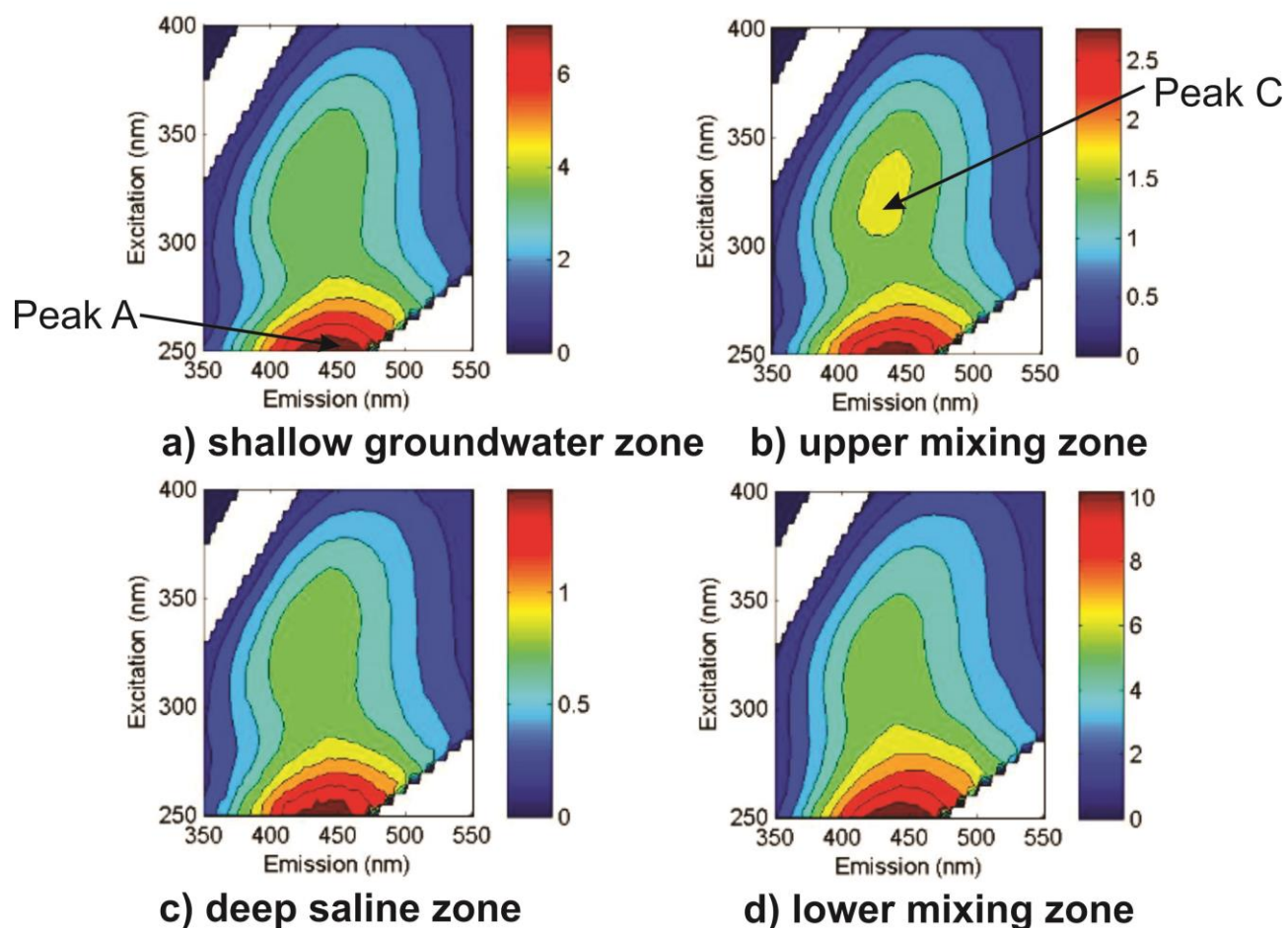


Figure 4.36: EEMs showing positions of the two fluorescence peaks: a) shallow groundwater zone (8.08 m), where only Peak A is seen; B) upper mixing zone (12.08 m), where both Peak A and C are seen; c) deep saline zone, where only Peak A is seen; and d) lower mixing zone, where only Peak A is seen. Note the different color scales on each plot.

Table 4.11: Excitation and emission wavelengths of Peak A and Peak C for water samples at different depths. Peak C is only seen at the upper mixing zone, where the iron concentration reaches its maximum.

Depth (m)	Location	Iron concentration (mg/L)	Peak A (ex/em)	Peak C (ex/em)
8.08	Shallow groundwater zone	43.0	250/450	NA
12.08	Upper mixing zone	306.5	250/444	333/441
15.08	Deep saline zone	49.7	250/444	NA
20.06	Lower mixing zone	10.5	250/441	NA

Based on the classification of the 13 components, C1 (ex/em = 340/450 nm) and C2 (Q2) (ex/em = 250/458 nm) correspond to Peaks C and A, respectively. Figure 4.37 shows the excitation-emission curves for C1 and C2. The peak with longer wavelength excitation for C1 occurs at 340 nm; whereas, the excitation maximum for C2 (Q2) occurs at wavelength 250 nm. Table 4.12 presents the properties of the C1 and C2 components. Cory and McKnight (2005) reported that C1 is positively correlated to the amount of anomeric, acetal, and ketal carbon. Although C1 is classified as an unknown species, it may be a quinone derivative (Cory & McKnight, 2005). Both C1 and C2 are humic-like components, derived from a terrestrial source (Cory & McKnight, 2005; Fellman, Hood, & Spencer, 2010), and tend to generate smaller FI values, compared to the microbial-derived organic matter. Thus, the presence of Peak “C” at the upper mixing zone further supports the idea that iron reduction is strongly related to a terrestrial source.

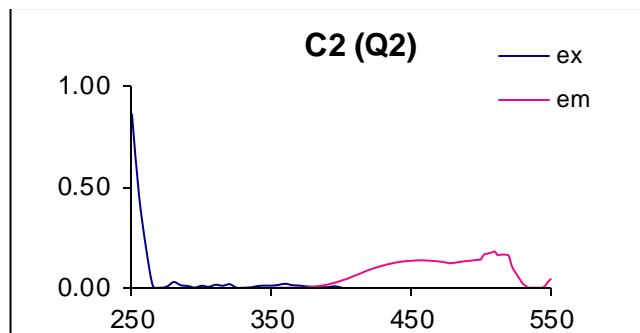
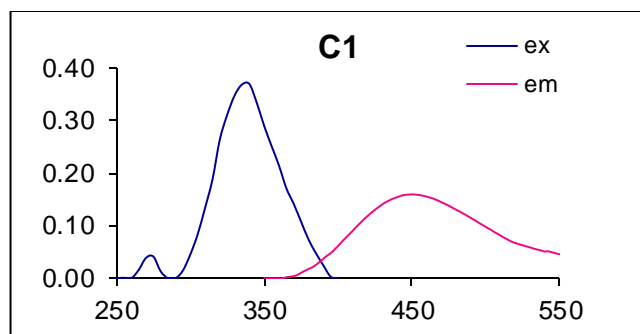


Figure 4.37: Excitation and emission curves for the C1 and C2 components.

Table 4.12: Summary of fluorescence PARAFAC components C1 and C2 and their corresponding peaks.

Cory & McKnight component	Area of EEM (Ex/Em)	Visual peak	Source ^c	Comments ^c
C1 ^a	340ex/ 450em	C ^b	Terrestrial	High-molecular-weight humic-like, widespread, but highest in wetlands and forested environments. Maybe quinone derivative, specifically a ketal, formed by the reaction of a quinone with an alcohol
C2 ^a	250ex/ 450em	A ^b	Terrestrial	High-molecular weight and aromatic humic-like, widespread, but highest in wetlands and forested environments. Oxidized quinone-like fluorophores, and correlated with the concentration of lignin-derived organic matter.

Notes: ^a Cory and McKnight (2005)

^b Coble et al. (1990); Coble (1996)

^c Cory and McKnight (2005); Fellman, Hood, and Spencer (2010)

Chapter 5: Discussion

5.1 Iron and Manganese Oxides Reduction

Fe(II) and Fe(III) speciation results showed that Fe(II) is the dominant species contributing to the 0.5 HCl extractable iron. The high content of Fe(II) in sediment further supports the reduced environment for iron reduction. Heron (1994) determined Fe(II)/Fe(III) of seven sediments with various redox degrees in the Contaminated Vejen Aquifer. Results showed that iron distribution varies significantly in samples from the different environments, which Fe(III) is dominantly present in the oxidized environment (>90%) and only small fraction (3-15%) in reduced environment (Heron et al. 1994). This result is consistent with our observations, which sediment only contains approximately 20-25% of reactive Fe(III) in the reducing environment.

The inverse relationship between solid-phase iron and manganese oxides and their reduced aqueous phases suggests that iron and manganese reduction are the predominant redox reactions at the Kidd 2 site, where Fe(II) and Mn (II) concentrations are up to 300 mg/L and 3.5 mg/L, respectively. The reducible concentrations on the sediment in the upper mixing zone were approximately 1100 mg (solid/solid) iron and 170 mg (solid/solid) manganese. If the dissolved iron and manganese were conservative species, and their current concentrations were maintained at the upper mixing zone, it would take at least 916 years and 12,000 years to flush the reactive iron and manganese oxides out of the aquifer, respectively.

We first discuss the zone above 13.1 m depth, where there is an inverse relationship between solid and aqueous phases and then the zone below 13.1 m with a poorly defined relationship.

Above 13.1 m: In this study, we only focused on the 5,000-6,000 year old defluvial silt and sand topset unit (Clague et al., 1991) from the surface down to a depth of 20 m. The relatively homogeneous and highly reactive distribution of iron and manganese oxides suggests that they were formed by diagenetic processes during sediment deposition. Therefore, the original iron and manganese oxide distribution in the sediment along the depth profile would not be

expected to vary greatly, which agrees with the relatively constant reactivities. The present variations along the depth profile are likely related to the rate of iron and manganese dissolution. The inverse relationship between the aqueous and solid reactive phases at the upper mixing zone suggests that iron and manganese reduction proceed more intensively there than at other depths. In other words, the greater iron and manganese reduction releases more iron and manganese into groundwater, leaving less solid phases in the sediment.

The sediment analyses show that there is a high correlation between the reactive Fe oxide and Om% (Figure 4.22), and both reactive Fe oxide and Om% reached to their minimum values at upper mixing zone. This information, combined with the inverse relationship between DOC and $\text{Fe}^{2+}/\text{Mn}^{2+}$ at upper mixing zone (Figure 4.5), further supports the notion that iron and manganese reduction takes place intensively at upper mixing zone. The consistent correlations between solid/aqueous phases of organic matter and iron/manganese suggest that the availability of organic matter at upper mixing zone probably produces a condition which prefers redox reactions.

In addition, it is expected that the astonishingly high concentration of dissolved iron at the upper mixing zone cannot come completely from the iron reduction without accumulation along a flow line. In the conceptual flow model, saline water enters the aquifer and migrates along the base of the sandy aquifer to a maximum 500 m inland, where it overturns and flows back towards the Fraser River at the top of the saline wedge (Neilson-Welch & Smith, 2001). The saline circulation provides a flow pathway so that the produced dissolved iron can accumulate continuously and be transported along the saline wedge to the top mixing zone. This hypothesis is demonstrated in the PHREEQC 1-D reactive transport model in Section 5.5.

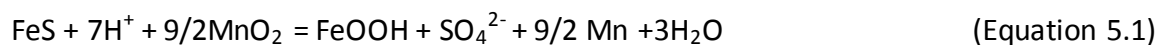
Below 13.1 m: Below 13.1 m, no correlation exists between the aqueous and reactive solid phases. Both the aqueous phase and the solid-phase of iron are seen to gradually decrease with depth, but a relationship between the two is not obvious. Even if enough reactive iron oxide is present in sediments, much less ferrous iron is produced in the groundwater. Unlike iron, the aqueous manganese concentration tends to increase with depth, with a distinct peak

occurring at a depth of 17.08 m (Figure 4.5). The disagreement of aqueous Fe and Mn in the deep saline zone can possibly be explained by different distributions of Fe and Mn oxides or different reaction processes, or both. Since manganese oxide has higher energy yields, which is more favorable for microorganism respiration, manganese reduction tends to proceed in advance of iron reduction, and produce the distinct peak at the deep saline zone. Or other chemical processes may be involved in Mn. The relative low concentration of Mn is influenced by the secondary reaction processes, such as adsorption and secondary mineral precipitation. Combinations of chemical redox reactions and secondary mineral precipitation and adsorption processes need to be further evaluated. The detailed discussion will be provided in Section 5.3.

5.2 Sulfate Reduction

The low sulfur content (0-1.4mM/kg) in AVS extraction suggests that sulfate reduction is modest. Although more stable sulfide minerals like pyrite (FeS_2) and elemental sulfur (S^0) were not quantitatively measured, sequential extractions showed that the total extracted sulfur ranged from 3.0-8.5 mM/kg (Table.4.9), which is still one order of magnitude lower than the reactive iron oxide. Both AVS and the sequential extractions demonstrate that sulfate reduction is not comparable with iron reduction.

The most likely explanation is the overall organic matter fermentation rate is lower at deeper depths, resulting in less sulfate and iron reduction. The lack of FeS in deep sediments may also be caused by chemical oxidation, with the continuous loss of FeS. Aller and Rude (1988) presented results that freshly precipitated FeS can be oxidized by manganese oxides in sediment, as expressed by Equation 5.1:



Postma (1993) also reported that FeS cannot accumulate in sediments until the manganese oxide has been exhausted. As FeS is produced by sulfate reduction, it may react immediately with the reactive manganese oxide, and release manganese into groundwater, consistent with the increasing trend of aqueous manganese in deep groundwater (Figure. 4.4 and 4.5).

It is difficult to estimate the sulfate reduction rate using AVS, since it is discontinuously distributed along the depth profile and may be altered by secondary chemical reactions. The sulfate reduction rate can be alternatively estimated from the concentration profile and the horizontal groundwater flow rate along the saline wedge.

At the upper and lower mixing zones, the sulfate concentration continuously decreases along the saline wedge. The decline in the sulfate concentration is mainly due to dilution and sulfate reduction. Dilution can be accounted for using Cl^- and isotopes (Section 4.2.2) and the sulfate-reduction rate can be obtained from the rate of depletion of sulfate along the flow path connecting the three observation wells W1, W2, and W3. Since these mass balance calculations are associated with the well distance and groundwater flow rate, the calculated rates are averaged over space and time. The sulfate reduction rates at the upper and lower mixing zones are estimated to be $0.016 \text{ mmol}\cdot\text{L}^{-1}\cdot\text{yr}^{-1}$ and $0.036 \text{ mmol}\cdot\text{L}^{-1}\cdot\text{yr}^{-1}$, respectively (See Appendix G for sample calculation).

Table 5.1 lists quantitative measurements of sulfate reduction in pristine aquifers, deposited from the Cretaceous to the Holocene. At these sites, sulfate reduction rates are derived from the depletion of sulfate concentration along flow lines or along depth profiles in combination with groundwater flow rates, which is the same method as applied at our site. Nevertheless, no or limited dilution processes are present in these aquifers, and therefore sulfate loss is attributed to sulfate reduction.

Table 5.1: Rates of sulfate reduction in different aquifers

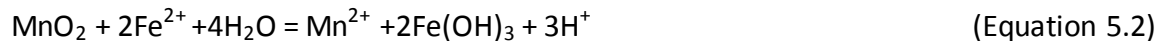
Aquifer	Sulfate concentration (mmol/L)	Sulfate reduction rate (mmol·L⁻¹·yr⁻¹)	Aquifer age	Reference
Fox Hills, USA	0.2-2.7	2.0×10^{-4}	Cretaceous	Thorstenson, Fisher, and Croft, 1979
Florida, USA	1.6-3.6	1.0×10^{-4}	Tertiary	Plummer, 1977
Fuhrberg, Germany	1.1-1.8	1.4×10^{-2}	Pleistocene	Bottcher and Strebel, 1989
Rama, Denmark	0.2-0.8	$3.1 - 9.3 \times 10^{-1}$	Holocene	Jakobsen and Postma, 1999
Kidd 2 site, Canada	3.82-7.07	$1.6 - 3.6 \times 10^{-2}$	Holocene	This study

Field studies show that rates of sulfate reduction range over several magnitudes, from 10^{-1} to 10^{-4} mmol·L⁻¹·yr⁻¹. The sulfate reduction rate also increases with the geological sequences. The rate yield from the youngest Holocene depositions at Rama, Denmark is three orders of magnitude higher than that in the oldest Cretaceous sediments, supporting the idea that bioavailability of organic matter in sediment is an important controlling factor.

The calculated sulfate reduction rates at the Kidd 2 site are comparable with those derived from aquifers deposited during the Quaternary period (Table 5.1). Even the sulfate concentrations at the Kidd 2 site are much higher than those in the Quaternary aquifers. Because no obvious relationship is seen between the sulfate concentration and the reduction rate, the iron reduction and organic matter reactivities appear to be more important in controlling the sulfate reduction. Berner (1980) also pointed out that the sulfate reduction rate relies more on the accessibility of organic matter by fermenting bacteria than on the sulfate concentration in marine sediments.

5.3 Secondary Mineral Precipitation

Iron and manganese can be incorporated with HCO_3^- to form siderite (FeCO_3) and rhodochrosite (MnCO_3), respectively. SI calculations show that pore water at all depths is supersaturated with respect to siderite (Figure. 4.10). The iron speciation from the extractions shows that reactive Fe(II) is composed of approximately 75% to 80% of total reactive iron. The possible phase of the Fe(II) bearing mineral is siderite. However, although siderite was detected by SEM in the sediments, it was found in relatively small quantities, which does not support the iron extraction result. In field studies, supersaturation with respect to siderite and rhodochrosite, has often been observed in anaerobic groundwater environments (Jensen et al. 2002) and this is particularly true for siderite. Jensen (2002); however, found that both siderite and rhodochrosite have slow precipitation kinetics in supersaturated solutions and have much faster dissolution rates in re-suspensions of precipitated crystals. This may partly explain why only a few FeCO_3 and MnCO_3 cements were found in the sediment. But still, the secondary mineral phase of Fe(II) is not fully understood. Besides carbonate mineral precipitation, part of the manganese reduction and liberation may have been cycled with ferrous iron (Equation 5.2) and dissolved sulfide (Equation 5.3), which act as two potential reductants. With the presence of a relatively high concentration of ferrous iron in groundwater, the dissolved sulfide should be very low and the manganese reduction by sulfide (Equation 5.3) would be negligible.



In addition, the reduced Mn^{2+} can be re-absorbed onto sediment and removed from groundwater. Based on an adsorption experiment conducted by Murray et al. (1984), fully oxidized Mn oxides apparently contain surface sites with very high affinity for Mn^{2+} . Therefore, Mn^{2+} can accumulate into solution only after the sites have been saturated and occupied (Canfield, Thamdrup, & Hansen, 1993). We speculate that the adsorption behavior provides a cap that limits the escape of Mn from sediments as long as the surface oxides are fully oxidized.

Since the Mn^{2+} can be easily removed by adsorption onto mineral surfaces, this eventuality cannot be neglected. Moreover, the concentration of manganese oxide is relatively low compared to the other two electron acceptors, iron oxides and sulfate. Therefore, the small amount of Mn^{2+} that is produced or removed can significantly affect the Mn geochemistry in solution, resulting in the inconsistent and complex trend along the depth profile.

5.4 Bioavailability of Dissolved Organic Matter

Both Om% and reactive iron oxide are lowest at the upper mixing zone (between 10-12 m), which is in contrast to the aqueous iron concentration. This inverse relationship between aqueous and solid phases strongly suggests that iron and manganese reduction are accompanied by organic matter oxidation. If iron and manganese reduction inherently resulted from the interaction of fresher and saline-groundwater, one would expect the same pattern in the lower mixing zone, but this is not observed. In addition, if aqueous iron accumulates as it is transported along the saline wedge it can only reach 150 mg/L at the upper mixing zone if the iron reduction rate is assumed to be constant. Therefore, the total iron concentration (300 mg/L) at the upper mixing zone must be partially due to a high rate of iron production, coupled with organic matter degradation. As the kinetic and sequential extractions show that both the quality and quantity of the solid phases are not the dominant controlling factors for the iron and manganese reduction, we expect the bioavailability of organic matter (i.e., accessibility for fermenting bacteria to use the solid organic matter and release more labile DOC for iron/manganese reducing bacteria) to be more critical in understanding the fate of metals in groundwater, especially at the upper mixing zone. We expect that the organic matter at upper mixing zone is easier to breakdown and result in a higher-energy gain for bacteria. As the result, organic matter is preferentially degraded and depleted at upper mixing zone.

Two factors could explain the high bioavailability of organic matter at the upper mixing zone. 1) Interactions between saline and freshwater may increase the rate of organic matter fermentation 2) Organic matter at the upper part (above 13.1 m) is more reactive and accessible for bacterial utilization.

Fluorescence results show that the C peak is only present at the upper mixing zone, suggesting a distinct organic matter composition there. We can use the results of Coble (1996) (see Table 5.2 below) who compared mean values for wavelength-independent fluorescence properties of waters to gain insights into the origin of DOC at the upper mixing zone.

The mean positions of excitation and emission maximum and the A:C ratios suggested that water can be grouped by the fluorescence properties, especially in terms of the intensities of humic peaks. Coble classified water samples as porewater, river water, marine transitional water, and coastal water based on salinities. Based on the salinity and hydrogeological condition, water collected from the upper mixing zone at the Kidd 2 site can be defined as coastal water.

Table 5.2: Comparison of wavelength-independent fluorescence properties (excitation maximum, emission maximum, and A:C ratio) between upper mixing zone water at the Kidd 2 site and other water types.

	Salinity	Em max (nm)	Ex max (nm)	A:C*	Reference
Porewater ^a	0	440	355	0.68	(Coble 1996)
River water ^b	2	439	345	0.80	(Coble 1996)
Marine water, transitional ^c	29.90	420	315	1.60	(Coble 1996)
Coastal water ^d	18.47	443	335	1.92	(Coble 1996)
Kidd 2 site mixture water	13.39	441	333	1.87	This study

Notes: * A:C is the ratio of fluorescence intensity of Peak A to Peak C

^a Porewater sample was collected from a single sediment core at depth of 12.50 m, located at west coast of Mexico (Lambourn et al., 1991)

^b River water sample was collected from Mississippi River, head of passes, at depth of 0.2 m

^c Marine transitional water was collected from Puget Sound, Dabob Bay

^d Coastal water was collected from Black Sea at depth of 25 m

The differences in maximum excitation wavelength between porewater, river water, marine transitional water, and coastal water are usually over 10 nm, and they do not overlap with other water groups. Nevertheless, the maximum emissions wavelengths of porewater, river

water, and coastal water are very similar and only marine transitional water shows a significantly lower value. Therefore, water types cannot be easily distinguished on the basis of maximum excitation and emission wavelengths on their own. Also, the intensity of Peak C decreases as salinity increases (Table 5.2), which can be used to further distinguish the different water origins.

At the Kidd 2 site, the fluorescence properties of water at the upper mixing zone are consistent with coastal water, suggesting that the Peak C is probably related to the saline intrusion, rather than fresh groundwater on its own. Furthermore, the absence of C Peak at other depths, including the shallowest zone, supports the idea that Peak C is not derived from the freshwater zone. We speculate that the mixing process between saline and freshwater may produce certain fluorophores that generate Peak C. Still, it is unclear why Peak C is only present at the upper mixing zone and not at the lower mixing zone.

The FI and RI are another two important parameters to examine the organic matter properties. Both of these indices show distinct shifts at upper mixing zone. The smallest RI indicates the most intensive electron shuttling process, and provides evidence for the most intensive iron and manganese reduction at upper mixing zone. The low values of FI suggests the presence of some terrestrial-derived organic matter, compared to other places.

At the lower mixing zone, organic matter is probably derived from the lower silt layer, which is enriched in organic matter. At the upper mixing zone, it may come directly from the sediment, since it contains 0.75-1.97% solid organic matter (Om%), and it is mostly enriched in the soils above 13 m. In addition, terrestrial organic matter may also be transported along with surface recharge, and mixed with saline water at the upper mixing zone. In both cases, they may introduce freshly produced organic matter into system. As these more accessible organic matter pools are not yet fully used by fermenting bacteria, they are associated with relatively low FI values.

The fluorescence index (FI) has been shown to be inversely related to the relative contribution of microbial versus higher plant organic matter (Cory & McKnight, 2005). The ratio of SQ1, divided by the sum of SQ1 and SQ2, explained the variation of FI ($R^2 = 0.95$) in W3 (Figure. 5.1), where SQ1 is a terrestrial-derived component and SQ2 is produced by microbial activity. The smaller portion of the terrestrial-derived organic matter ($SQ1/(SQ1+SQ2)$), the higher value of FI. FI can be separated into two portions, comprised of the upper portion (where FI ranges from 1.70-1.80), and the lower portion (where FI ranges from 1.59-1.63). The points in the upper portion represent samples collected in the saline wedge (at depths from 13-20 m). The points in the lower portion are represented by samples collected at the mixing zones (at depths from 10-12 m and 20-22 m). The separation of the FI supports the idea that the composition of the organic matter at the mixing zones differs from that in the saline intrusion, and that the terrestrial source of organic matter at the mixing zones is larger. At the upper mixing zone, FI reaches its smallest value, indicating that most of the terrestrial organic matter is being produced there for further bacteria utilization. Therefore, anomalies in the organic matter are probably a key factor giving rise to the high iron concentration in groundwater. This abnormal property of organic matter at the upper mixing zone probably relates to the terrestrially derived organic matter.

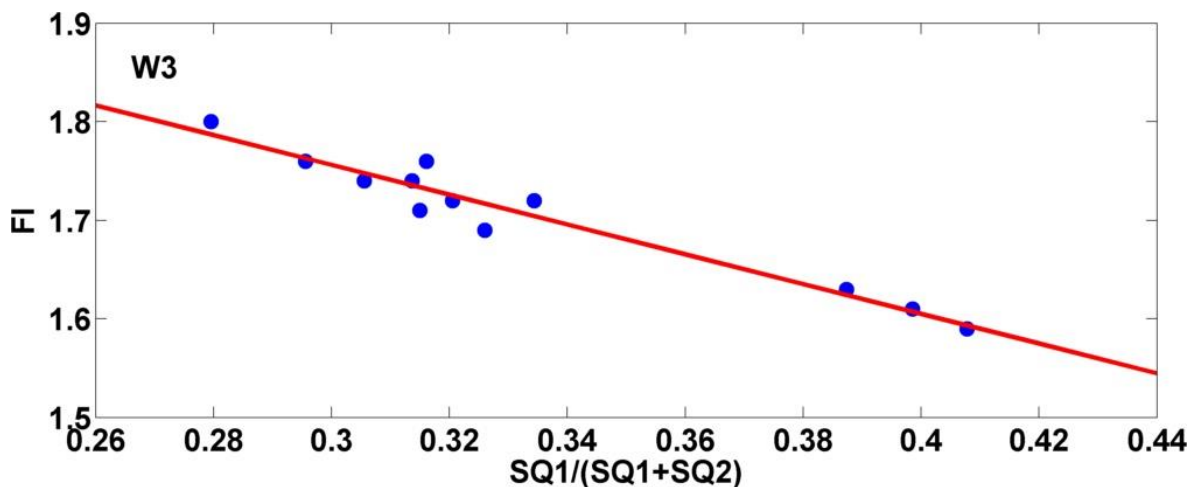


Figure 5.1: Explanation of the variation in the fluorescence index (FI) by SQ1 and SQ2.

5.5 PHREEQC 1-D Kinetic Reactive-Transport Modeling

We can test our conceptual model of the site through one-dimensional kinetic reactive-transport models that include primary mineral redox reactions and secondary mineral precipitation. The models were developed to: 1) evaluate the fate and transport of iron and manganese along the saline circulation; 2) interpret the field data to constrain the reduction-rate parameters, including the oxidation rate of organic matter by iron and manganese oxides, the importance of sulfate reduction and methanogenesis; 3) understand how other secondary minerals control aqueous ferrous iron and manganese concentrations through processes of mineral precipitation/dissolution; and 4) gain insight into the long-term evolution of the geochemistry at the site.

Sorption of iron and manganese is negligible and was not considered in the transport model. Indeed, based on extraction results, adsorbed iron and manganese accounted for 0.01%-0.79% and 0.26%-7.25% of total extractable iron and manganese, respectively. Both absorbed iron and manganese are one order of magnitude smaller than their reactive mineral phase. This result is comparable with analysis conducted by (Hall et al. 1996), in which absorbed iron and manganese accounted for only 0.48%-1.13%, and 3% -13% of total extractable iron and manganese, respectively.

Moreover, the heterogeneity of iron oxides is not considered in this model; the kinetic extractions show that the rate constants for iron and manganese oxides are similar along depth profile. However, for the purpose of long-term prediction, the heterogeneity of iron and manganese oxides should be considered as the most reactive iron and manganese oxides are continuously lost and subsequently reaction rates tend to decrease with time.

5.5.1 Model Setup

5.5.1.1 Model Domain and Physical Transport

One-dimensional PHREEQC (Parkhurst & Appelo, 1999) reactive-transport models were constructed to follow a flow line determined by Neilson-Welch and Smith (2001). Figure 5.1 shows the flow field and the 1,000 m flow line used. The flow line travels along the boundary of the saline mixing zone as water enters from the river, overturns approximately 500 m from the shore and flows back to discharge in the river. The 1000m flow line is divided into two parts: the first 500m represents the lower mixing zone and second 500m represents the upper mixing zone.

The composition of the waters used in the simulations is given in Table 5.3. All cells initially contained groundwater representative of the shallow water zone. The geochemistry of water inflowing at the river (boundary condition) was taken as water collected by Bianchin (2010) a few meters below the sediment-water interface of the Fraser River at the Kidd 2 site. The model also allowed for water from the lower silt and shallow recharge to mix along the flow path (Figure 5.2). Based on the calculations in Section 4.2.2, 25% fresh groundwater from the confining silt layer was specified to continuously mix with 75% domain water at the lower saline mixing zone. In the upper saline mixing zone, 65% of the recharge water is mixed with 35% of the domain water. To achieve the mixing, the specific amount of the water was continuously added into the flow domain by using the “REACTION” data block. Please see Appendix H for the input code. Water compositions measured in W1, W2 and W3 at the lower (distance = 300, 415, 465 m) and upper (distance = 535, 585 and 700 m) saline mixing zones are used for model calibration as they are the only sampling locations that capture both the upper and lower mixing zones.

All physical transport parameters (Table 5.4) were taken from Neilson-Welch and Smith (2001). The transport time from inflow to discharge is 250 years and the total simulation time is 5,000 years, consistent with the age of the Fraser River delta (John J. Clague et al. 1991).

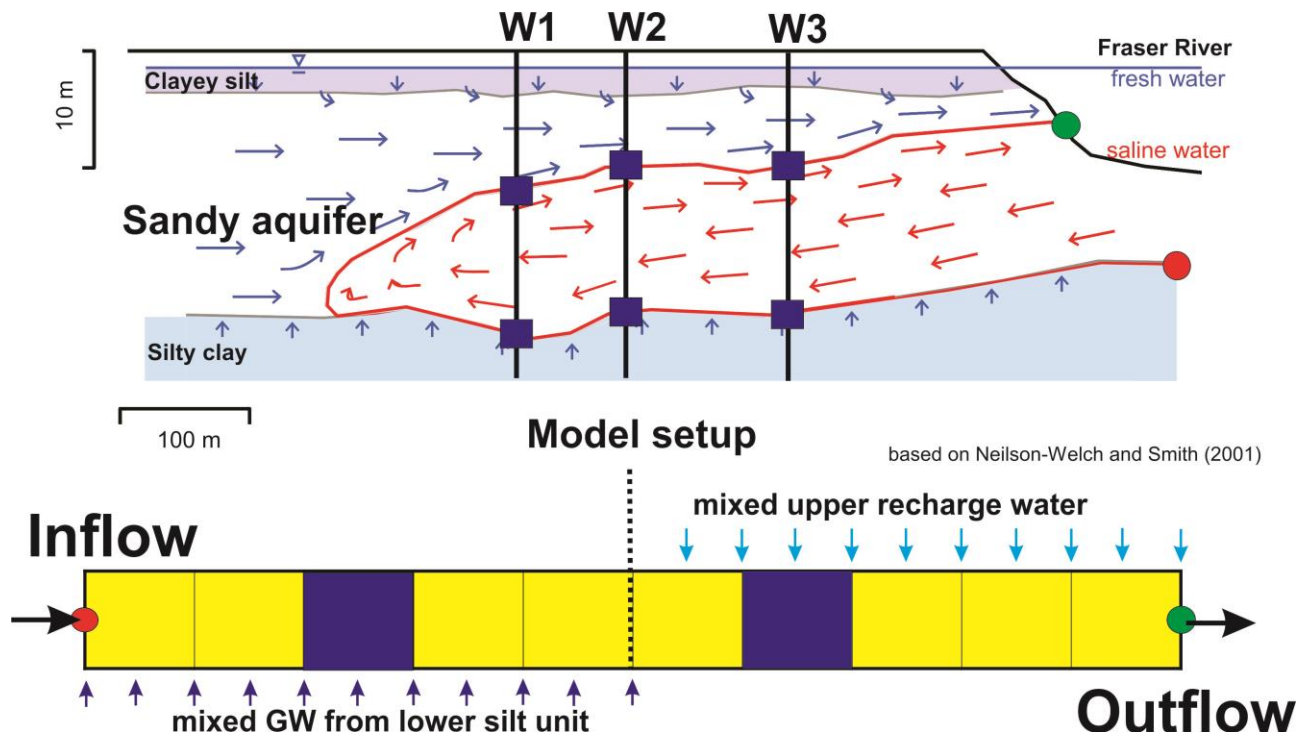


Figure 5.2: The one-dimensional reactive-transport model follows the flow line (L. Neilson-Welch and Smith 2001) indicated in red that starts at the red dot at the base of the river, flows 500 m inland, overturns and flows back to the river at the green dot.

Table 5.3: Water composition of initial and boundary conditions and neighboring units in phreeqc model

Parameter	Units	Inflowing water	Initial condition	Confining silt layer freshwater (lower mixing zone)	Recharge water (upper mixing zone)
pH		7.15	6.56	8.61	6.39
Na	mg/L	4850	139	291	23.1
Cl	mg/L	10100	121	92.6	51.8
Ca	mg/L	247	33	8.90	24.4
Mg	mg/L	630	40	11.5	48.7
K	mg/L	155	4.4	1.09	0.25
Fe	mg/L	7.43	63.2	10.9	26.1
Mn	mg/L	3.20	0.86	0.05	0.42
HCO ₃ ⁻	mg/L	86.0	469	685	272
SO ₄ ²⁻	mg/L	1310	33.4	29.5	32.3
Si	mg/L	5.49	33.8	22.3	77.0

Table 5.4: Physical parameters for the PHREEQC 1-D transport model.

Model setup parameters	Value	Comments
Model domain	1,000 m	Divided into 100 cells of 10 m
Pore-water velocity	4 m/year	Calculation based on hydraulic gradient and hydraulic conductivity (L. Neilson-Welch and Smith 2001)
Residence time	250 years	Calculation based on hydraulic gradient and hydraulic conductivity (L. Neilson-Welch and Smith 2001)
Boundary conditions	Flux/Flux	Steady-state flow
Time step	78840000s	2.5 years
Pore volume	20	5,000 years

5.5.1.2 Geochemical Processes and Reaction Network

Geochemical processes are described by both primary redox reactions involving organic matter fermentation, iron reduction, manganese reduction, sulfate reduction and methanogenesis under anaerobic conditions, and secondary reactions involving secondary mineral precipitation. The redox reactions are controlled by the external organic matter substrates and the terminal electron acceptors (TEAs) (K. S. Hunter, Wang, and Van Cappellen 1998). In most cases, however, natural organic matter is not readily metabolized directly by microorganisms, and therefore must be further broken down to smaller organic molecules like acetate, formate, as well as H_2 through a fermentation step (Lovley and Chapelle 1995). Fermentation comprises complex chain reactions and electron transfers are involved in each step. The most important stage is the final electron transfer to outside TEAs. Therefore, fermentation of organic matter is the key factor controlling the TEAs. Zero- or first- order rate expressions with respect to the concentration of organic matter substrate usually are applied in the biodegradation models (e.g., V. A. Fry 1993). In absence of evidence to choose a first order model, in this study we use a zero-order rate equation to express the fermentation of solid organic matter to labile DOM. The solid organic matter was defined as “foc” by using “PHASE” keyword. Once fermented, foc

was transferred into aqueous Om, which represented the labile DOM. The fermentation step is assumed to include all complex internal electron transfer processes of organic matter such that the labile DOM can be directly utilized by electron acceptor microorganisms and the microbial lag time is negligible. The terminal electron accepting processes examined are iron reduction, manganese reduction, sulfate reduction, and methanogenesis. In PHREEQC, these rate-limited primary redox reactions are described by a series of parallel first-order kinetic equations. These kinetic rate equations are expressed by using the “KINETIC” keywords, which enables all primary redox reactions to take place simultaneously. Table 5.5 summarizes the primary redox reactions and their kinetic parameters. The secondary non-redox mineral precipitation/dissolution reactions are described by the equilibrium conditions, and all mineral and aqueous phases are contained within the PHREEQC database (water4q.dat).

Table 5.5: Chemical reactions included in the PHREEQC simulations, with using database of water4q.dat

Primary redox reactions	Kinetic parameters	Description
Foc = Om	R_0, k_{foc}	Fermentation step, solid organic matter (Foc) is transformed to Om, which can be directly utilized for sequential electron acceptor microorganism
$Om + 4Fe(OH)_3 + 7H^+ = 4Fe^{2+} + HCO_3^- + 10H_2O$	R_1, k_{Fe}	Iron reduction
$Om + 2MnO_2 + 3H^+ = 2Mn^{2+} + HCO_3^- + 2H_2O$	R_2, k_{Mn}	Manganese reduction
$Om + \frac{1}{2} SO_4^{2-} = \frac{1}{2} HS^- + HCO_3^- + \frac{1}{2} H^+$	R_3, k_{SO4}	Sulfate reduction
$Om + \frac{1}{2} H_2O = \frac{1}{2} CH_{4(aq)} + \frac{1}{2} HCO_3^- + \frac{1}{2} H^+$	R_4, k_{CH4}	Methanogenesis

The following list shows the kinetic rate formulations for all primary redox reactions used in the PHREEQC simulations:

Zero order rate law:

$$R_0 = k_{\text{foc}}$$

First order rate law:

$$R_1 = k_{\text{Fe}} \times \text{mol ("Om")}$$

$$R_2 = k_{\text{Mn}} \times \text{mol ("Om")}$$

$$R_3 = k_{\text{SO}_4} \times \text{mol ("Om")}$$

$$R_4 = k_{\text{CH}_4} \times \text{mol ("Om")}$$

To further constrain the parameters, the reduction rates for iron, manganese, and sulfate were estimated from Kidd 2 field data. Their reduction rates were obtained from the concept of mass balance, which assumed that iron and manganese are continuously produced and transported along the flow path, whereas sulfate is depleted along the flow line. Therefore, the reduction rates can be calculated based on the concentration gradient along the flow line and the groundwater velocity, expressed as equation 5.4. It should be noticed that these calculations only provide approximately reduction rates, which are averaged over space and time. Table 5.6 lists values of various parameters used in the PHREEQC simulations and literature values to show their ranges. All assigned rate constants are within the range of literature values. The field measurement of the rate of organic matter fermentation is excluded as it is difficult to measure under in-situ conditions.

$$\text{Reduction rate} = \frac{\Delta \text{concentration over certain distance along flow line}}{\Delta \text{travel time over certain distance along flow line}} [\text{M/T}] \quad (\text{Equation 5.4})$$

Table 5.6: Parameter values in the PHREEQC simulations.

Parameter	Values used in simulations	Values calculated from in-situ measurements ^a	Values reported in literature	References
$K_{foc} (S^{-1})$	$1.5 \times 10^{-12} - 8.5 \times 10^{-11}$	NA	$9.5 \times 10^{-13} - 9.5 \times 10^{-7}$	(K. S. Hunter, Wang, and Van Cappellen 1998)
$R_{Fe} (mM/yr)$	$2.4 \times 10^{-2} - 2.7 \times 10^{-1}$	$5.0 \times 10^{-2} - 1.7 \times 10^{-1}$	$5.2 \times 10^{-1} - 1.33^b$	(Jakobsen 1999)
$R_{Mn} (mM/yr)$	$2.7 \times 10^{-4} - 3.1 \times 10^{-3}$	$8.9 \times 10^{-5} - 1.2 \times 10^{-3}$		
$R_{SO_4} (mM/yr)$	$8.7 \times 10^{-3} - 9.8 \times 10^{-2}$	$5.0 - 9.0 \times 10^{-2}$	$5 \times 10^{-2} - 4.5^c$	(Jakobsen and Postma 1994a)
$R_{CH_4} (mM/yr)$	$4.4 \times 10^{-3} - 4.9 \times 10^{-2}$	$7.6 \times 10^{-3} - 1.4 \times 10^{-2}$	$2 \times 10^{-2} - 3.2^d$	(Jakobsen and Postma 1999; Postma and Jakobsen 1996)

Notes: ^a: Maximum rates at the Kidd 2 site were directly derived from the concentration gradient along the flow line and groundwater velocity

^b: Maximum rates calculated from concentration gradient in the profile and vertical groundwater velocity

^c: Directly measured in-situ maximum rates by using radiotracer $^{35}SO_4^{2-}$

^d: Fermentation rate was directly measured in-situ by using radiotracer $^{14}CH_3COONa$

Seven scenarios were simulated for the various organic matter degradation pathways. In the baseline scenario, iron and manganese reduction are the primary pathways for organic matter oxidation. Furthermore, field evidence suggests the presence of sulfate reduction, methanogenesis, and high bioavailability of organic matter at the upper saline mixing zone. Therefore, these electron accepting processes were also evaluated. Rate constants for primary redox reactions were assigned in each scenario to match the observed Fe(II) concentration ($5.0 - 5.5 \times 10^{-3} M$) at a distance of 700 m and the value of pH used as an indicator of the quality of the model. The summary of the seven scenarios are presented below:

- Scenario 1: Iron and manganese reduction only, minerals are not allowed to precipitate;
- Scenario 2: iron and manganese reduction + secondary minerals ($FeCO_3$ and $MnCO_3$) precipitation, $SI_{FeCO_3}=1.5$, $SI_{MnCO_3}=0.5$;
- Scenario 3: iron and manganese reduction + secondary minerals ($FeCO_3$ and $MnCO_3$) precipitation, $SI_{FeCO_3}=0$, $SI_{MnCO_3}=0$;

- Scenario 4: iron reduction + sulfate reduction, without secondary mineral precipitation;
- Scenario 5: iron reduction + sulfate reduction + secondary mineral (FeS) precipitation, $SI_{FeS} = 0$;
- Scenario 6: iron reduction + sulfate reduction + methanogenesis, without secondary mineral precipitation;
- Scenario 7: Scenario 5 with different fermentation rates for the upper and lower mixing zones + secondary minerals ($FeCO_3$ and $MnCO_3$) precipitation, $SI_{FeCO_3}=2.2$, $SI_{MnCO_3}=1.0$.

5.5.2 Model Simulation

For scenario 1, 4, 5, 6 and 7, reaction-rate constants and saturation indices were adjusted to best fit the observed Fe(II) and Mn(II) concentrations at upper mixing zone. For scenario 1, 2 and 3, all reaction-rate constants are the same to evaluate the effect of siderite and rhodochrosite precipitation as both of them have slow kinetics. For scenario 5, all reaction-rate constants are the same with scenario 4, but allow FeS to precipitate. For all simulations, reaction rates are within the range of literature values (Table 5.6). Table 5.7 lists the rate constant values assigned for each scenario.

Table 5.7: Rate-constant values assigned in Scenario 1-7

	$K_{foc} (S^{-1})$	$K_{Fe} (S^{-1})$	$K_{Mn} (S^{-1})$	$K_{SO4} (S^{-1})$	$K_{CH4} (S^{-1})$	SI_{FeCO3}	SI_{MnCO3}	SI_{FeS}
Scenario 1	2.0×10^{-12}	5.5×10^{-10}	1.0×10^{-11}					
Scenario 2	2.0×10^{-12}	5.5×10^{-10}	1.0×10^{-11}			1.5	0.5	
Scenario 3	2.0×10^{-12}	5.5×10^{-10}	1.0×10^{-11}			0.0	0.0	
Scenario 4	3.0×10^{-12}	8.5×10^{-10}	1.0×10^{-11}	4.5×10^{-10}				
Scenario 5	3.0×10^{-12}	8.5×10^{-10}	1.0×10^{-11}	3.0×10^{-10}				0.0
Scenario 6	3.0×10^{-12}	8.5×10^{-10}	1.0×10^{-11}	4.5×10^{-10}	5.0×10^{-9}			
Scenario 7	upper:	2.2×10^{-9}	3.0×10^{-11}	8.5×10^{-10}	2.0×10^{-9}	2.2	1.0	0.0
	1.5×10^{-12}							
	Lower: 8.5×10^{-12}							

5.5.2.1 Scenario 1: Iron and Manganese Reduction

Based on the reduction rate obtained from the flow-line calculation, the rate constant for manganese reduction is one to two orders of magnitude smaller than the rate constant for iron reduction (Table 5.7). Even though kinetic extractions showed that the reactivities for these two electron acceptors are similar; the higher observed iron concentrations could only be reproduced with a higher rate constant. This may be associated with relative abundance of iron on the solid phase.

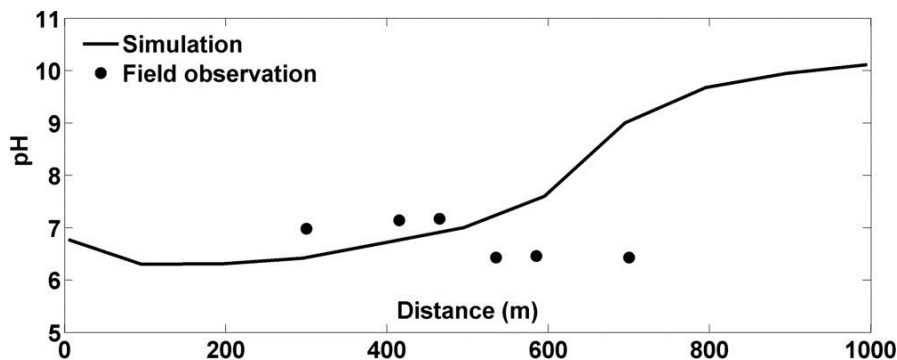
Iron and manganese concentrations along the flow line at 5,000 years simulation time are presented in Figure 5.3. Under the assigned rate constants, Fe(II) and Mn(II) continuously increase along the flow line. At the distance of 700 m, Fe(II) and Mn(II) reach to 5.3×10^{-3} M and 9.3×10^{-3} M, respectively. It is shown that modeled Fe(II) fits well with field measurements. Nevertheless, Mn(II) is not well fit by the model as measured Mn(II) concentrations were relatively constant along the flow path. There is no clear explanation for the relatively constant Mn concentrations on the flow path. Heterogeneity of the manganese oxide is another possibility that results in a higher reaction rate of manganese in the lower mixing zone. Due to the inconsistency between model and field measurements, we conclude that the homogeneous distribution of manganese oxide and primary manganese reduction are not appropriate to represent the Mn(II) distribution in solution.

Modeled pH is well controlled over the first 500m, where it ranges from 6.3 to 7.0, but from 500 to 1000m it dramatically increases from 7.0 to 10.1, due to rapid iron and manganese reduction. At a distance of 700 m, the model pH rises up to 9.0 as compared to field circumneutral pH (6.4 – 7.1) (Figure 5.3). At a distance of 1,000 m, the highest model pH (10.1) is coincident with the peaks of Fe(II) and Mn(II). It is noted that pH first drops over the first 100 m, from 6.8 to 6.3. This is because the effect of dilution from the lower confining silt layer overwhelms iron reduction, so that the Fe(II) concentration is even lower than that in initial solution. The high alkalinity in the lower silt layer successfully increases the buffer capacity and inhibits the increases of pH by iron reduction. From 200 to 1000m, the iron produced by

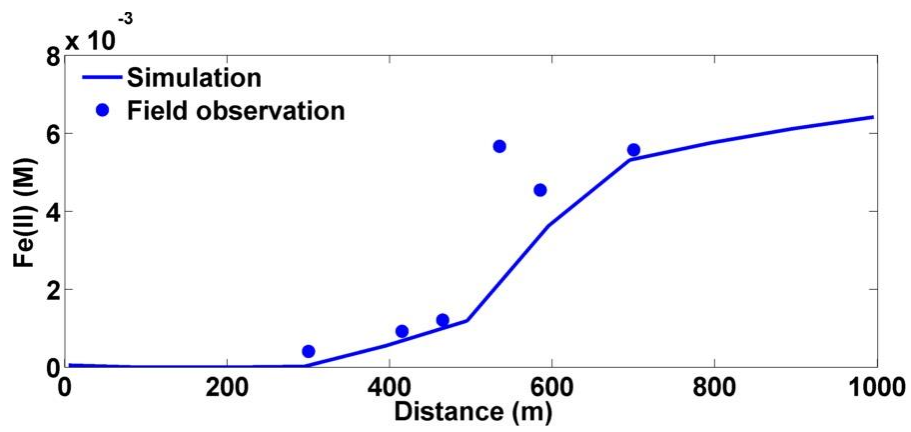
reduction overwhelms the dilution by mixing, and results in the increase of Fe(II) and subsequently pH in solution. The increase in pH is predominantly caused by the consumption of H^+ and production of HCO_3^- from iron and manganese reduction; these pathways generate the highest amounts of alkalinity per unit carbon oxidized (Van Cappellen et al. 1998).

In this scenario, secondary minerals like siderite and rhodochrosite are not allowed to precipitate, and all produced Fe(II) and Mn(II) are in the aqueous phase. It is shown that the SI for siderite and rhodochrosite continuously increase along the flow path, reaching to 3.10 and 1.66, respectively. As iron reduction produces a large amount of HCO_3^- , it is not possible to match the pH and the iron concentration simultaneously. To evaluate the effect of mineral precipitation, siderite and rhodochrosite are allowed to precipitate in scenario 2 and 3 at various SI values.

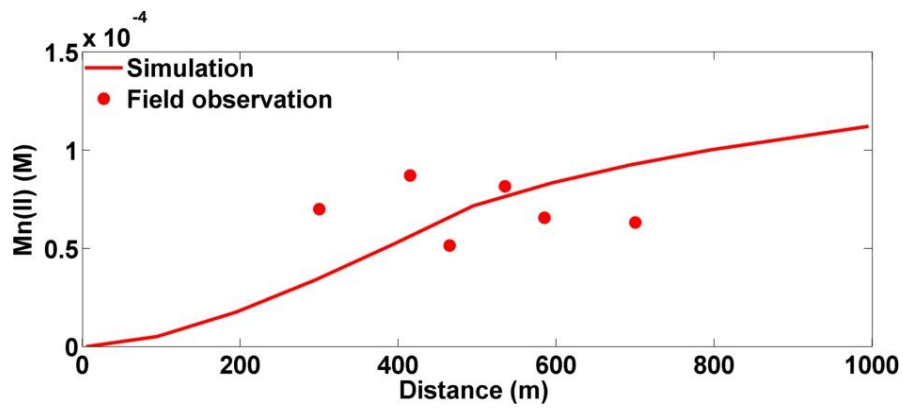
a)



b)



c)



d)

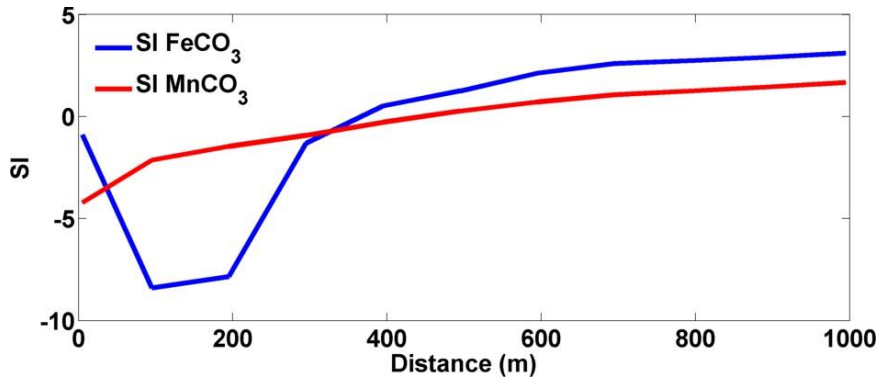


Figure 5.3: Scenario 1 baseline, $T = 5,000$ years; advective flow is from left to right; distance = 0 m corresponds to saline intrusion inflow point, distance = 1,000 m corresponds to outflow point. The dots correspond to field values and the lines correspond to model simulations. a) pH; b) Aqueous concentrations of Fe(II); c) Aqueous concentrations of Mn(II); d) Saturation indices for siderite and rhodochrosite. See text for discussion.

5.5.2.2 Scenario 2: Secondary Mineral Precipitation ($SI_{FeCO_3}=1.5$, $SI_{MnCO_3}=0.5$)

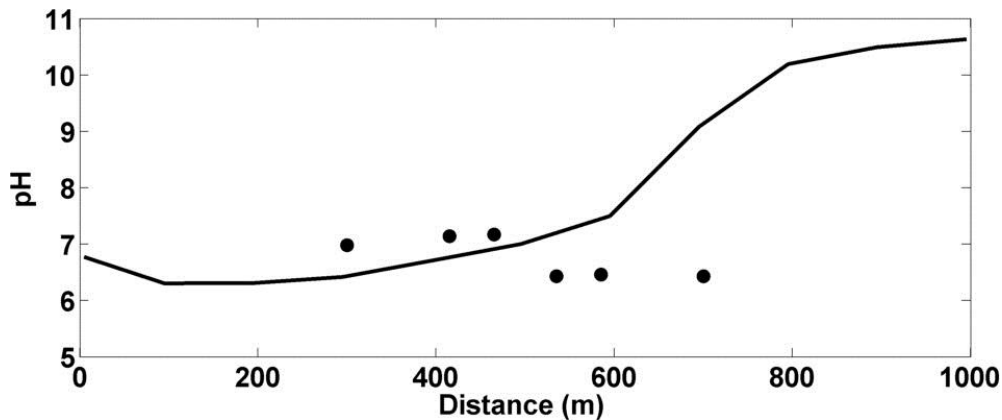
In this scenario, SI_{FeCO_3} and SI_{MnCO_3} are assigned to 1.5 and 0.5, respectively. These SI values are derived from averaging individual SI values of water samples located at mixing zones. All other parameters were assigned as the same as scenario 1 to isolate the effect of secondary mineral precipitation.

Iron and manganese concentrations and saturation indices along the flow line at 5,000 years simulation time are presented in Figure 5.4. Siderite is undersaturated and the SI is below zero until 600m, where it starts to precipitate out of the solution (Figure 5.4). As a result, modeled Fe(II) concentrations are far below measured at upper mixing zone and modeled Fe(II) only reaches to $8.76 \times 10^{-4} M$ at distance of 700m. It is noted that Fe(II) first drops over the distance 500 to 700m as it precipitates out of solution to reach saturation, and then gradually increases from 700 to 1,000m where the iron production rate exceeds the precipitation rate. However, the rate of Fe(II) increase is much slower than in Scenario 1.

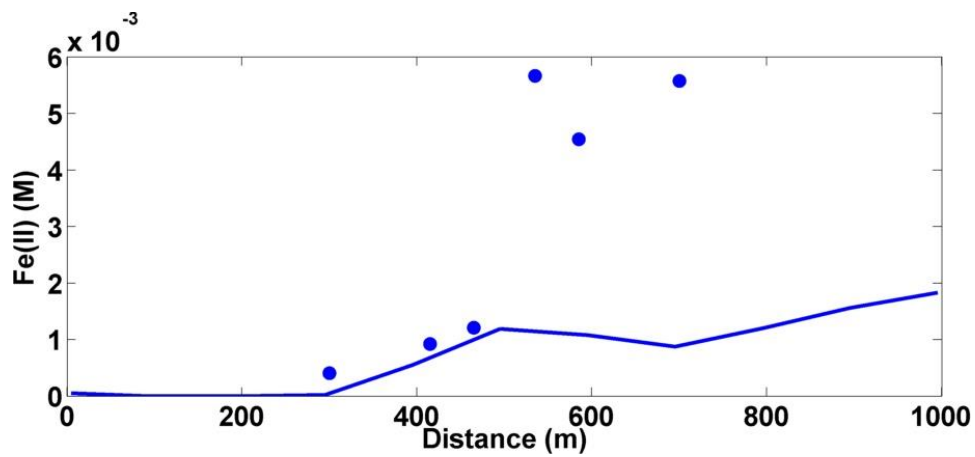
A comparison of Scenario 1 and 2 indicates that the Fe(II) distribution can be intensively modified by precipitation. Based on the simulation, a total of $4.58 \times 10^{-3} \text{ M}$ of Fe(II) is lost from the solution. Similar to Fe(II), Mn(II) begins to decrease as SI_{MnCO_3} reaches 0.5 at distance of 600m. Nevertheless, Mn(II) continuously decreases thereafter, driven by the continuous production of HCO_3^- along the flow path. In this scenario, a total of $7.20 \times 10^{-5} \text{ M}$ of Mn(II) was lost to secondary minerals.

Alkalinity also decreases as siderite and rhodochrosite precipitate. In total, $1.22 \times 10^{-3} \text{ M}$ HCO_3^- is lost, which comprises 27% of total alkalinity. Remarkably, the loss of alkalinity does not decrease pH. It is shown that pH in Scenario 2 increases up to 10.62, which is even higher than that in Scenario 1 (pH = 10.1).

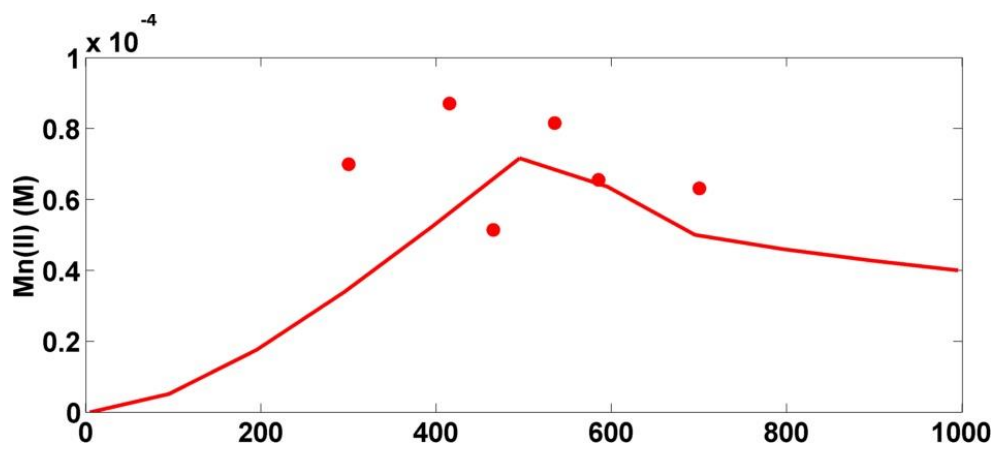
a)



b)



c)



d)

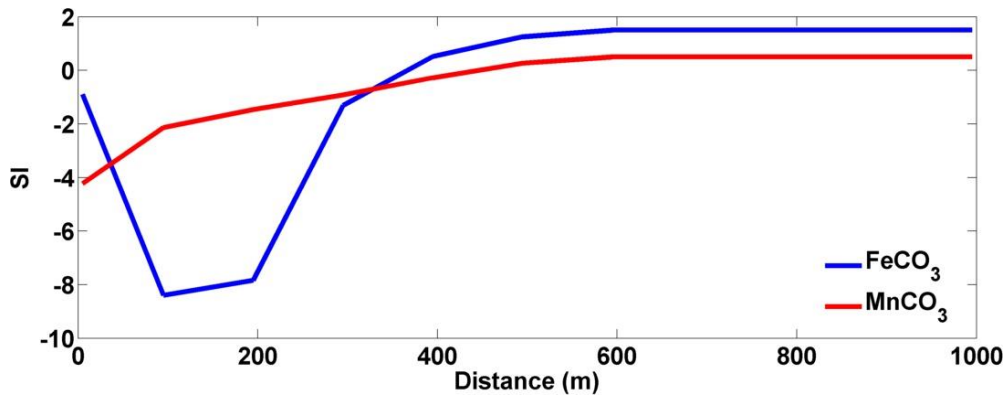


Figure 5.4: Scenario 2, effect of siderite and rhodochrosite precipitation, $SI_{FeCO_3}=1.5$, $SI_{MnCO_3}=0.5$; $T = 5,000$ years; advective flow is from left to right; distance = 0 m corresponds to saline intrusion inflow point, distance = 1,000 m corresponds to outflow point. The dots correspond to field values and the lines correspond to model simulations. a) pH; b) Aqueous concentrations of Fe(II); c) Aqueous concentrations of Mn(II); d) Saturation indices for siderite and rhodochrosite. See text for discussion.

5.5.2.3 Scenario 3: Secondary Mineral Precipitation ($SI_{FeCO_3}=0$, $SI_{MnCO_3}=0$)

In this scenario, SI_{FeCO_3} and SI_{MnCO_3} are both assigned to 0, indicating secondary minerals more readily reach saturation. All other parameters are kept the same as scenario 2.

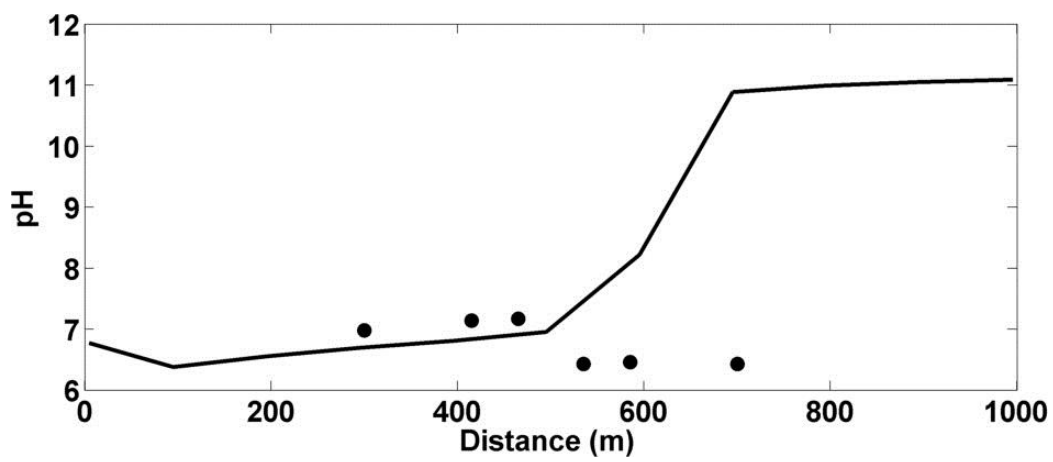
In this scenario modeled Fe(II) is lower than the field observations. Siderite remains undersaturated from 0-400 m and starts to precipitate thereafter (Figure 5.5). At distance of 700m, Fe(II) only reaches to $3.0 \times 10^{-4} M$, which is approximately 17 times smaller than that in the field, and 3 times smaller than that in scenario 2. Compared to scenario 2, an additional $1.2 \times 10^{-3} M$ of Fe(II) is lost in this scenario. Unlike Fe(II), all Mn(II) minerals are undersaturated except at distance of 700m. As the result, a sharp drop of Mn(II) is observed, where Mn(II) decreases from 8.33×10^{-5} to $1.71 \times 10^{-5} M$. From 700 to 1000m, Mn(II) remains undersaturated, and gradually increases to $5.46 \times 10^{-5} M$.

Alkalinity decreases coincident with siderite precipitation. A comparison between Scenario 2 and 3 indicates that an additional $1.1 \times 10^{-3} \text{ M}$ of HCO_3^- is lost in upper mixing zone (cell 51- 100) in Scenario 3. The loss of alkalinity further decreases the buffer capacity, and therefore pH increases up to 10.9.

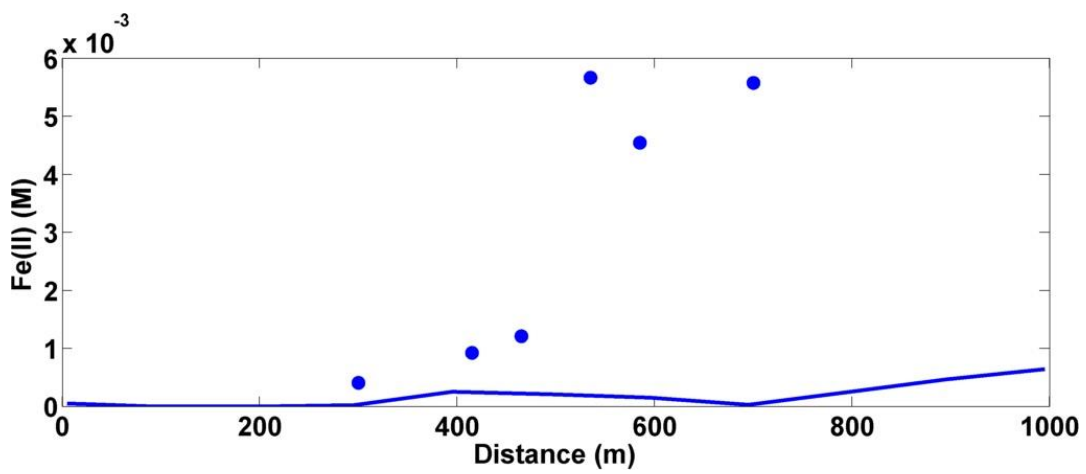
Scenario 2 and 3 have clearly shown that mineral precipitation would significantly inhibit Fe(II) and Mn(II) accumulating in solution. In field studies, supersaturation with respect to siderite and rhodochrosite, has often been observed in anaerobic groundwater environments (Jensen et al. 2002) and this is particularly true for siderite. Jensen et al (2002), however, found that both siderite and rhodochrosite have slow precipitation kinetics in supersaturated solutions and have much faster dissolution rates in re-suspensions of precipitated crystals. Nevertheless, the calculations of SI with Phreeqc are based on equilibrium conditions, and kinetic simulation is not considered. Moreover, Fe(II) and Mn(II) concentrations are highly sensitive to the specified SI values of siderite and rhodochrosite. In Scenario 2 and 3, over 70 - 90% of Fe(II) and 50 - 65% of Mn(II) are lost from solution, depending on assigned SI values. Therefore, mineral precipitation should be considered carefully in the model, as it can significantly redistribute Fe(II) and Mn(II) concentrations.

In addition, mineral precipitation further increases the pH of the solution. Therefore, we conclude that to mimic field conditions, in our model iron and manganese reduction must be augmented by other acid-producing reactions to further buffer the pH.

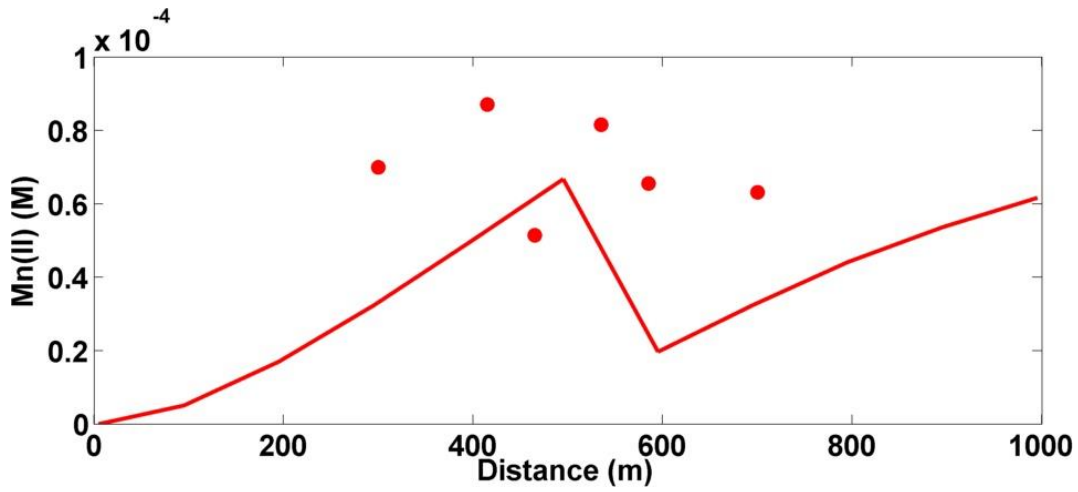
a)



b)



c)



d)

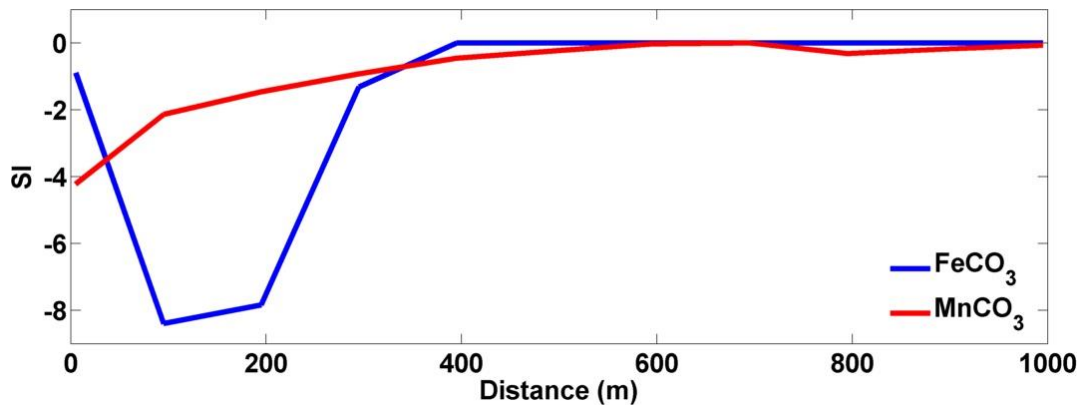


Figure 5.5: Scenario 3, effect of siderite and rhodochrosite precipitation, $SI_{FeCO_3}=0$, $SI_{MnCO_3}=0$; $T = 5,000$ years; advective flow is from left to right; distance = 0 m corresponds to saline intrusion inflow point, distance = 1,000 m corresponds to outflow point. The dots correspond to field values and the lines correspond to model simulations. a) pH; b) Aqueous concentrations of Fe(II); c) Aqueous concentrations of Mn(II); d) Saturation indices for siderite and rhodochrosite. See text for discussion.

5.5.2.4 Scenario 4: Sulfate Reduction

Sulfate reduction and methanogenesis are two alternative microbial degradation pathways, which could generate H^+ and control pH. Indeed, Simpson and Hutcheon (1995) used isotopes to document microbial sulfate reduction in the Fraser River delta sediments. In Scenario 4, sulfate reduction is considered in the simulation, to show its influence on water geochemistry. To isolate the effect of sulfate reduction, the secondary mineral precipitation is not considered in this scenario. However, sulfate reduction would produce HS^- , which can incorporate with Fe(II) readily and precipitate as FeS. In scenario 5, secondary mineral FeS is allowed to precipitate, and the impact of FeS precipitation on Fe(II) distribution can be evaluated.

Table 5.7 presents the assigned rate constants for kinetic reactions in Scenario 4. As sulfate reduction competes with iron reduction, organic matter fermentation rate and iron reduction rate must increase accordingly in order to force Fe(II) concentrations match to field measurements at upper mixing zone. The rate for sulfate reduction is adjusted to best fit field measurements. It is noted that the rate constant of sulfate reduction is lower than that for iron reduction, suggesting that iron reduction is the primary pathway for organic matter degradation.

The influence of sulfate reduction can be seen clearly in the behavior of the pH. The simulation results for the pH at 5,000 years simulation time is presented in Figure 5.6. The pH is well controlled along the saline mixing zone. Unlike the rapidly rising pH in Scenario 1, pH slowly increases from 6.6 to 7.2 over 1,000 m (Figure 5.6). However, modeled pH values are still slightly higher than field measurements at upper mixing zone where pH maintained around 6.5. Fe(II) and Mn(II) have similar patterns as those in Scenario 1. The highest pH coincides with the peak iron ($5.7 \times 10^{-3} M$) and manganese concentration ($6.4 \times 10^{-5} M$) at a distance of 1,000 m, as a result of iron and manganese reduction. At a distance of 700 m, Fe(II) and Mn(II) reach $5.2 \times 10^{-3} M$ and $5.8 \times 10^{-5} M$ at pH = 7.05, which agrees well with field measurements.

The concentration of SO_4^{2-} continuously decreases from the initial $1.38 \times 10^{-2} M$ to $2.56 \times 10^{-3} M$ at distance of 1,000 m, due to dilution and sulfate reduction. Based on the model simulations,

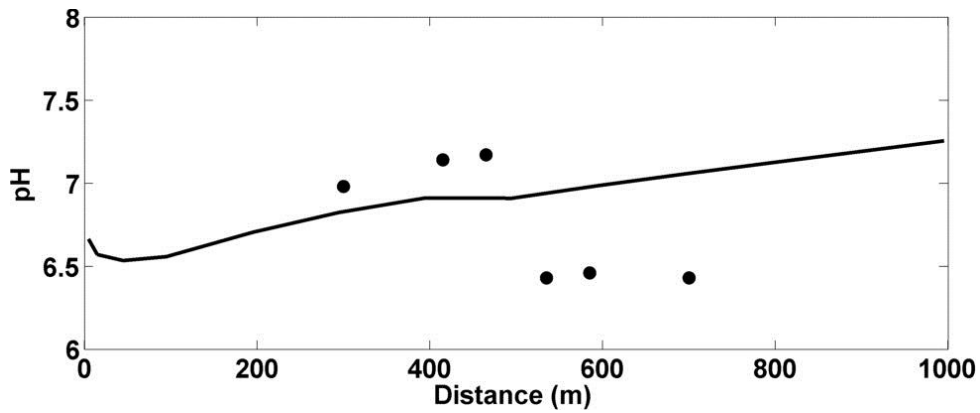
SO_4^{2-} concentrations decline by $1.12 \times 10^{-2} \text{M}$, with reduction comprising only 25% of the total loss. Therefore, dilution is the dominant process, which is consistent with the plot of SO_4^{2-} versus Cl^- (Figure 4.2 d)). A total of $2.7 \times 10^{-3} \text{M}$ of SO_4^{2-} is lost by sulfate reduction. The sulfide (HS^-) produced by reduction is a significant pH buffer (Christensen et al. 1994).

Moreover, the consistent two-peak pattern for AVS and reactive iron oxide above 13.1 m indicates that sulfate and iron reduction are occurring simultaneously. Jakobsen and Postma (1999) demonstrated that segregation of different terminal electron-accepting reactions in separate zones is, at least for iron and sulfate reduction, less strict than the energy yield of the TEAP process. Field studies have shown that the interface between zones of iron and sulfate reduction is rather poorly defined, and sulfate reduction also occurs in Fe(II) rich environments (Canfield, Thamdrup, & Hansen, 1993; Jakobsen & Postma, 1994). Also, Koretsky et al. (2003) reported that in organic-rich sediments, sulfate reduction can even overcome reactive Fe(III) oxides. Jakobsen and Postma (1999) demonstrated that iron reduction is energetically favored over sulfate reduction only in the presence of amorphous Fe oxides. As the stability of iron oxides increases, sulfate reduction becomes increasingly favored (Postma & Jakobsen, 1996). The kinetic extraction results show that the reactivity of the iron oxides is between that of ferrihydrite and goethite. Therefore, as the most reactive amorphous iron oxide is consumed, bacteria tend to use the more stable reactive iron oxide. In addition, pH also has an impact on the overlapping between iron and sulfate reduction. Under normal pH conditions, the presence of the less reactive Fe oxides, such as lepidocrocite, could be reduced simultaneously with sulfate reduction. In acidic environments; however, where iron reduction is favored over sulfate reduction, sulfate reduction could occur simultaneously, even with more stable Fe oxides such as goethite and hematite (Postma & Jakobsen, 1996). The pH at the Kidd 2 site ranges from 6.5-7.6, which is suitable for sulfate reduction. Therefore, it is possible that more crystalline ferrihydrite and sulfate reduction can be reduced simultaneously under field conditions.

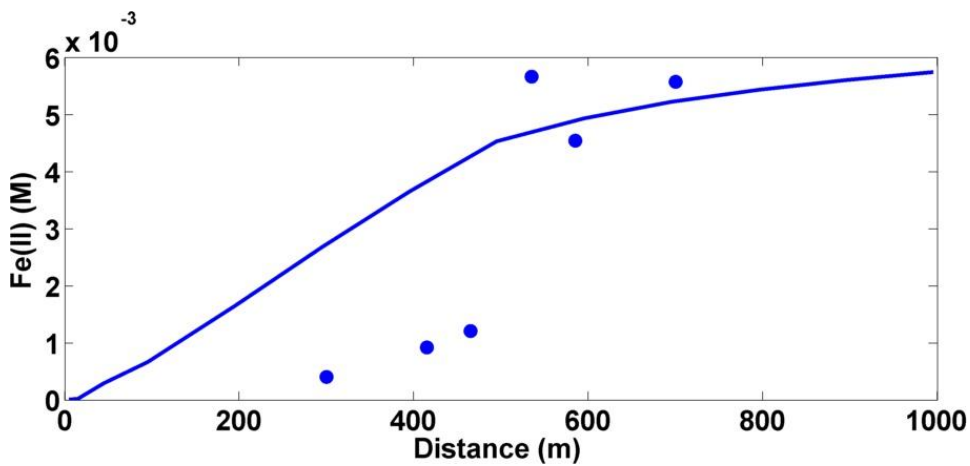
In Scenario 4, pH is maintained at a circumneutral level, while the modeled Fe(II) and Mn(II) match well with field observations at the upper mixing zone (distance = 700 m). Based on the

model simulation and laboratory/field observation, we conclude that sulfate reduction has an important role in controlling pH, and cannot be excluded from the transport process.

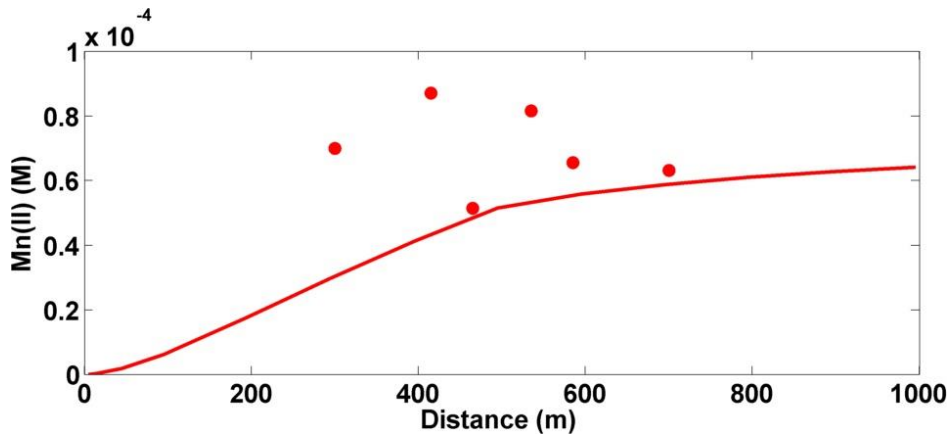
a)



b)



c)



d)

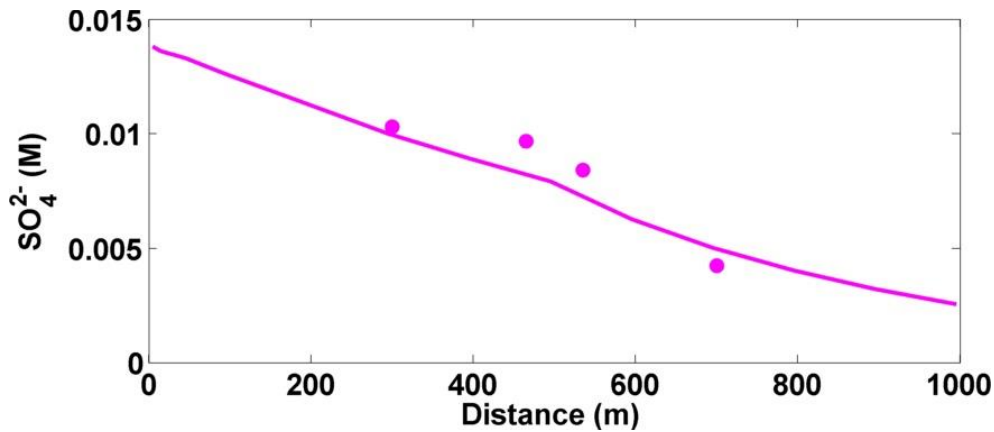


Figure 5.6: Scenario 4, effect of sulfate reduction; $T = 5,000$ years; advective flow is from left to right; distance = 0 m corresponds to saline intrusion inflow point, distance = 1,000 m corresponds to outflow point. The dots correspond to field values and the lines correspond to model simulations. a) pH; b) Aqueous concentrations of Fe(II); c) Aqueous concentrations of Mn(II); d) Aqueous concentrations of SO_4^{2-} . See text for discussion.

5.5.2.5 Scenario 5: Sulfate Reduction + Secondary Mineral (FeS) Precipitation

In this scenario, SI_{FeS} is assigned to 0 because precipitation of FeS is a relatively fast geochemical process. To compare the quantity of lost Fe(II) by FeS precipitation, the rate of

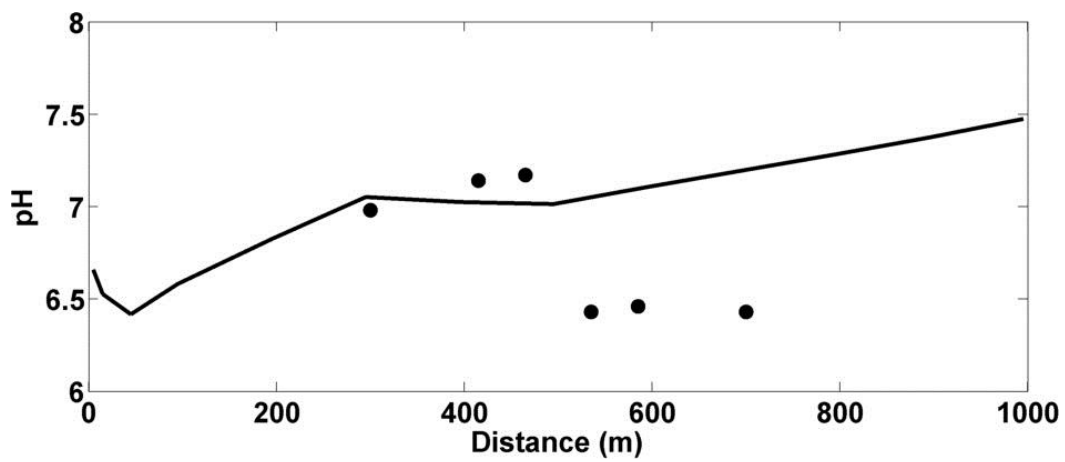
iron reduction remains the same as scenario 4. The rate of sulfate reduction has been adjusted until pH remains in a reasonable range.

FeS reaches saturation at 100 m and starts to precipitate thereafter (Figure 5.7). At 700m, Fe(II) reaches $4.27 \times 10^{-4} \text{ M}$. From 700 to 1000m, Fe(II) is relatively constant, indicating the balance of iron production and precipitation. A comparison between scenario 4 and 5 indicates that $9.5 \times 10^{-4} \text{ M}$ of Fe(II) is lost to FeS precipitation. Based on the AVS extraction results, the extractable AVS at mixing zones ranged from 1-4 $\mu\text{g/g}$. By assuming the porosity (n) of 0.3 and soil density (ρ_s) of 2840 kg/m^3 , this amount of extractable AVS is equivalent to $2 \times 10^{-4} \text{ M}$ to $8 \times 10^{-4} \text{ M}$ of sulfide (HS^-) derived from sulfate reduction, which is comparable with the model result. The consistency of the laboratory extraction and model simulation supports that sulfate reduction and sulfide mineral precipitation are occurring.

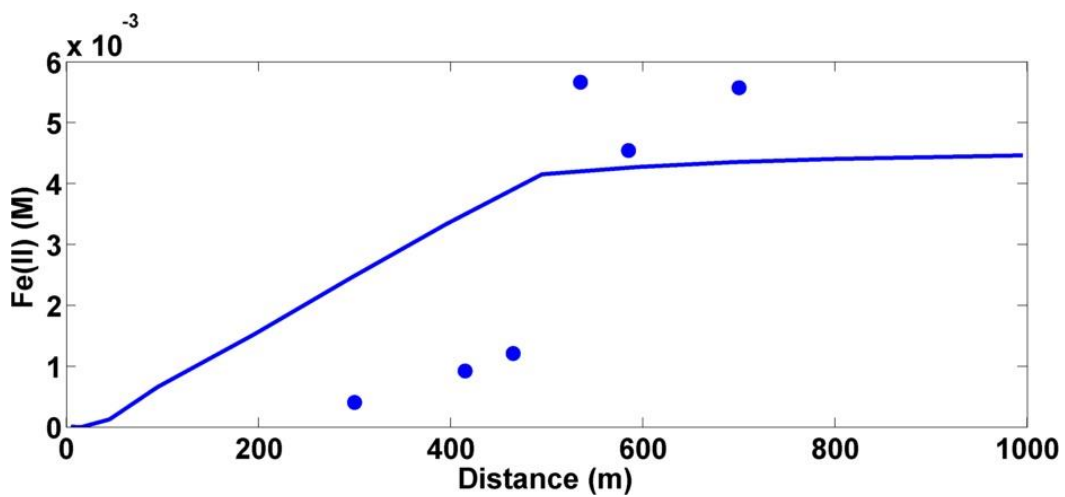


Moreover, precipitation of FeS is an important process to lower the pH, as presented by equation 5.4. By including the FeS precipitation, the rate of sulfate reduction in this scenario can be decreased from $4.5 \times 10^{-4} \text{ M}$ (in scenario 4) to $3.0 \times 10^{-4} \text{ M}$ while maintaining the same rate of iron reduction. Compared to scenario 4, although less SO_4^{2-} ($4.8 \times 10^{-4} \text{ M}$) is reduced, the pH in scenario 5 still maintains circumneutral.

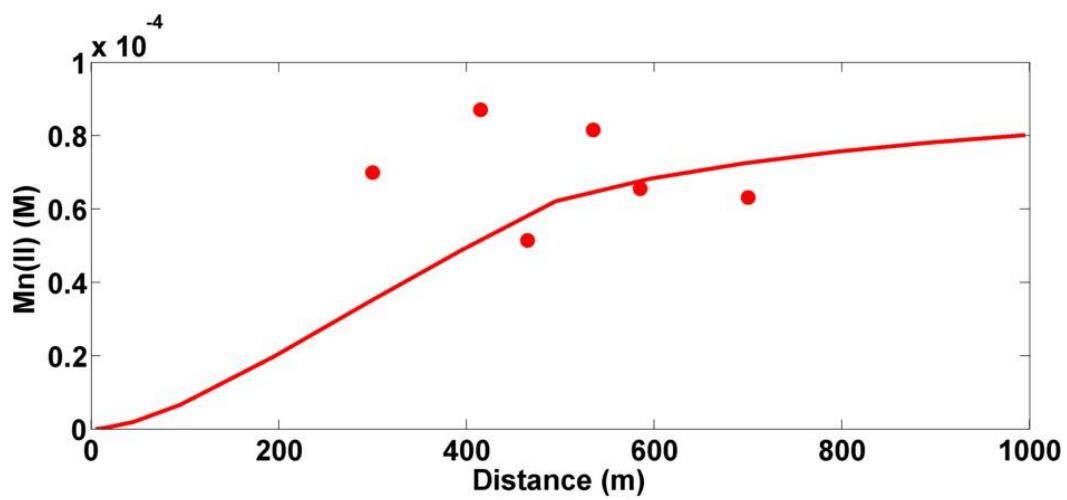
a)



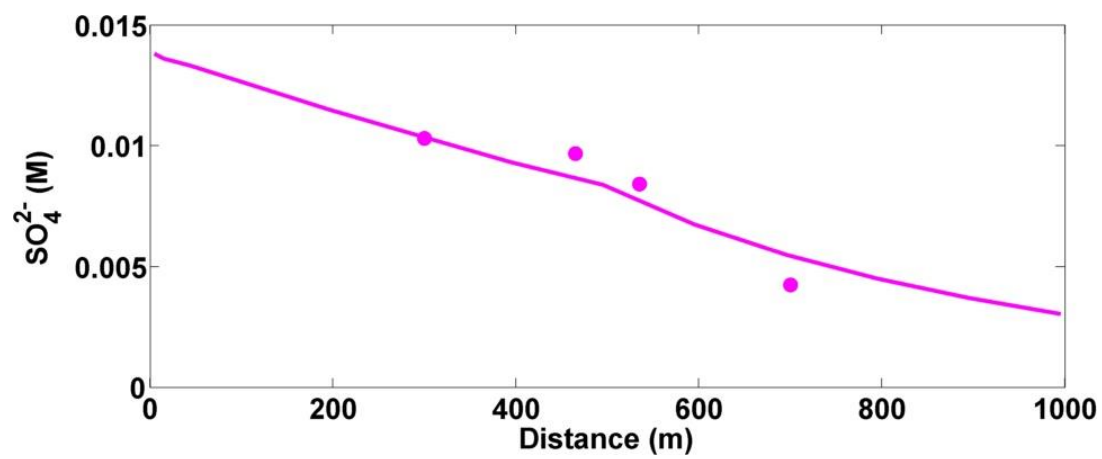
b)



c)



d)



e)

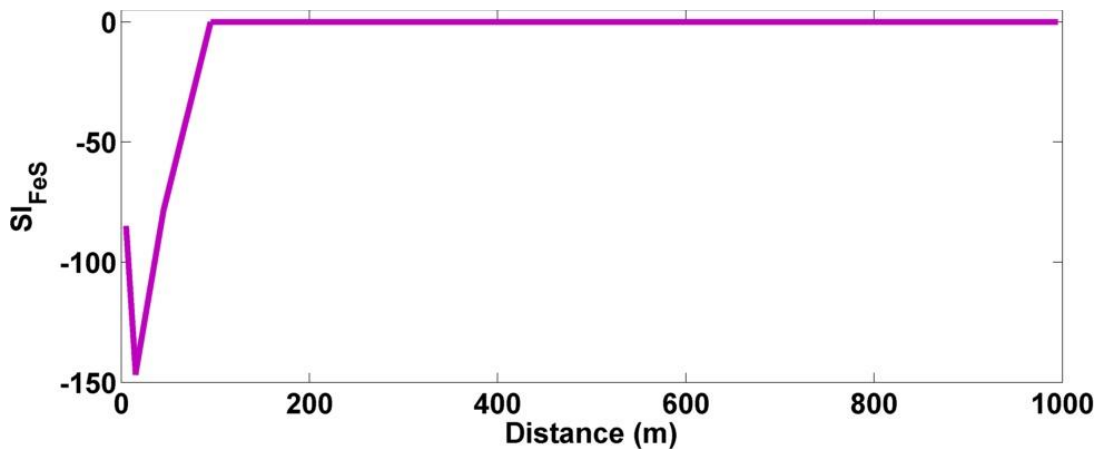


Figure 5.7: Scenario 5, effect of secondary mineral (FeS) precipitation; $T = 5,000$ years; advective flow is from left to right; distance = 0 m corresponds to saline intrusion inflow point, distance = 1,000 m corresponds to outflow point. The dots correspond to field values and the lines correspond to model simulations. a) pH; b) Aqueous concentration of Fe(II); c) Aqueous concentration of Mn(II); d) Aqueous concentration of SO_4^{2-} ; e) Saturation index of FeS. See text for discussion.

5.5.2.5 Scenario 6: Methanogenesis

Besides sulfate reduction, we also detected methane (CH_4) in the aquifer, especially in the deep groundwater. The presence of CH_4 indicates methanogenesis from the fermentation of the organic matter. To understand the impact of methanogenesis on the other redox reactions and pH, methanogenesis is included in the simulation in Scenario 6. Moreover, to isolate the effects of methanogenesis, secondary mineral precipitation is excluded in this scenario and then considered in scenario 7.

In Scenario 6, a series of parallel reactions, consisting of iron reduction, manganese reduction, sulfate reduction, and methanogenesis are simulated simultaneously along the saline edge. Because only W3 was sampled to measure methane, the distribution of methane is not well

understood along the flow path. Unlike iron and manganese reduction, methanogenesis is not likely occurring all along the flow path. The field sampling results showed that methane concentrations increased with depth, reaching a maximum in the lower confining silt layer. This may be because the organic matter-enriched silt layer is more energetically favorable for methanogenesis or does not contain iron and manganese oxides. In the sand unit, the methane production is likely inhibited, especially at the upper saline mixing zone where intensive iron reduction occurs. Therefore, uniform rate constant of methanogenesis is not expected to represent the complex methane distribution in aquifer. To simplify the problem, methanogenesis is only allowed to occur at lower mixing zone (0-500m). The rate constant of methanogenesis is assigned to best fit with the field measurement at lower mixing zone. Rate constants for other redox reactions are assigned as the same as the scenario 4 (Table 5.7), in order to evaluate the effect of methanogenesis.

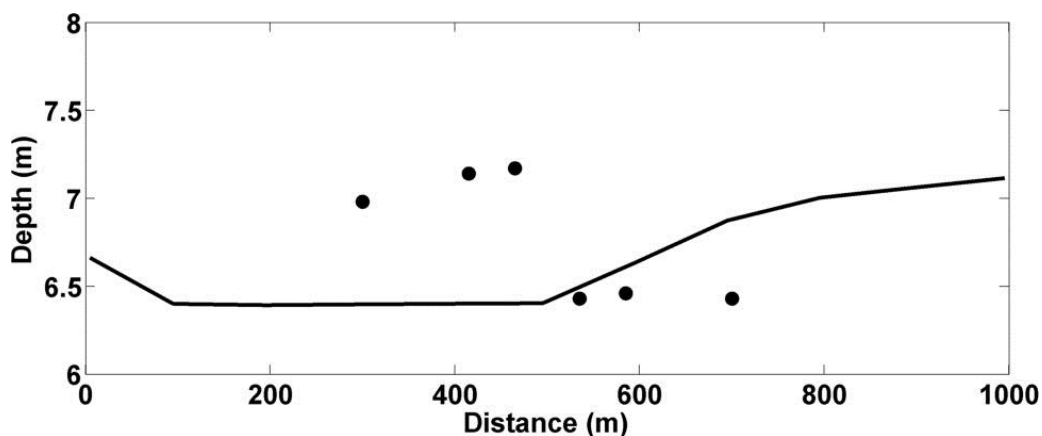
The simulation results for the pH at 5,000 years simulation time is presented in Figure 5.8. It is shown that the methane concentration continuously increases from zero to $1.61 \times 10^{-3} \text{M}$ along the lower mixing zone, then it slowly decreases to $9.21 \times 10^{-4} \text{M}$ at upper mixing zone due to dilution process (Figure 5.8). Although methanogenesis is not allowed to occur at upper mixing zone, the simulated result is still two times higher than measured value.

Besides being transported from the deep groundwater, methane also can be involved in secondary redox reactions. For example, methane can be re-oxidized by iron oxide, or by sulfate. These mechanisms could further remove methane in groundwater. In addition, the heterogeneity of methane production in sediments may also result in the apparent discrepancy. Hansen and Jakobsen (2001) first used radiotracer to measure methane production rate in shallow sandy aquifer. They found that a high concentration of methane does not necessarily indicate the high methanogenesis rate, because methane may be produced in one part of sediment where organic matter activity is high, and subsequently transported to zones with a low organic matter activity (Hansen, Jakobsen, and Postma 2001). The small-scale variability in methane production rates could further increase the uncertainty of the spatial methane distribution in aquifer.

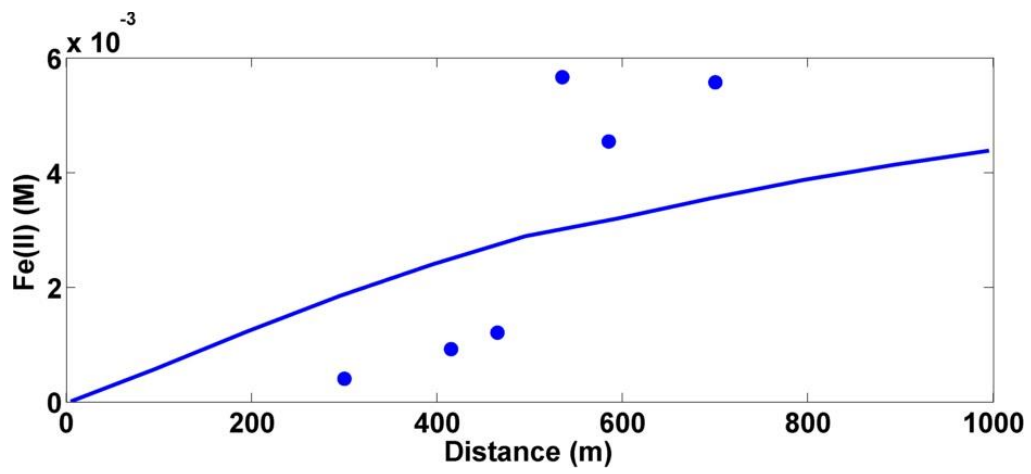
Although Scenario 6 may not represent the complex methane dynamics in solution, it still provides insights into how methanogenesis influences the pH of the system. The pH at 5,000 years of simulation time is shown in Figure 5.8. Along the 1,000 m flow path, pH increases even more gradually, from 6.6 to 7.1 (Figure 5.8). A comparison of pH in scenario 5 and 6 indicates methanogenesis further decreases pH, though the acid buffering effect of methanogenesis is much weaker than that of sulfate reduction. It is shown that pH maintains constant value (6.4) along lower mixing zone because of methanogenesis. The pH decreases by 0.5 units as compared to scenario 5. At upper mixing zone, pH starts increasing and reaches maximum value of 7.1 at distance of 1,000m. Unlike the additional HS^- produced by sulfate reduction, methanogenesis generates the same amount of both H^+ and HCO_3^- , and the HCO_3^- can compensate with its acid-buffering effect. Furthermore, since methanogenesis is likely only significant in the underlying silt, its effect on pH is slight.

As methanogenesis competes with iron and manganese reduction to consume organic matter, Fe(II) and Mn(II) production in scenario 5 are lower than in those in scenario 4. At distance of 700m, Fe(II) and Mn(II) only reach to 3.9×10^{-3} M and 3.6×10^{-5} M at pH = 6.87, which are approximately 30% lower than field measurements (Figure. 5.7).

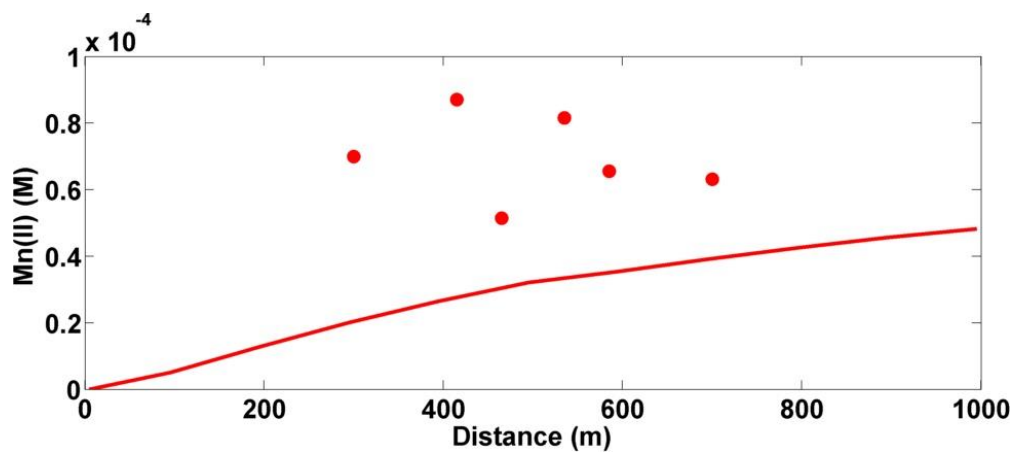
a)



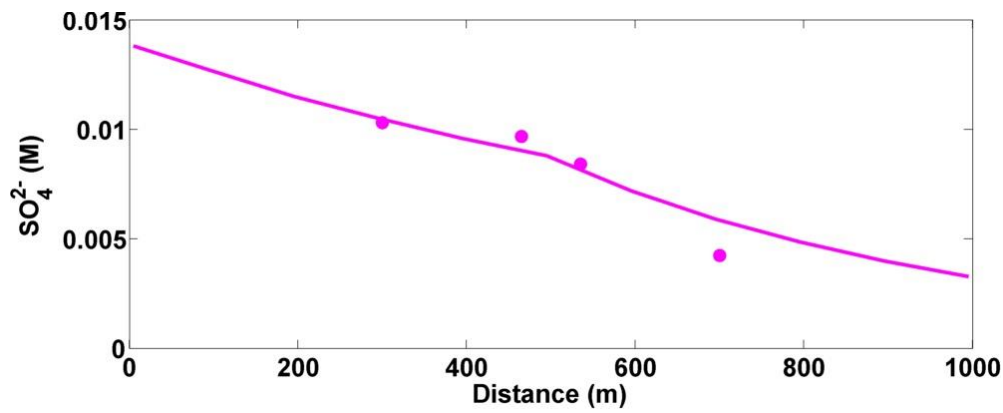
b)



c)



d)



e)

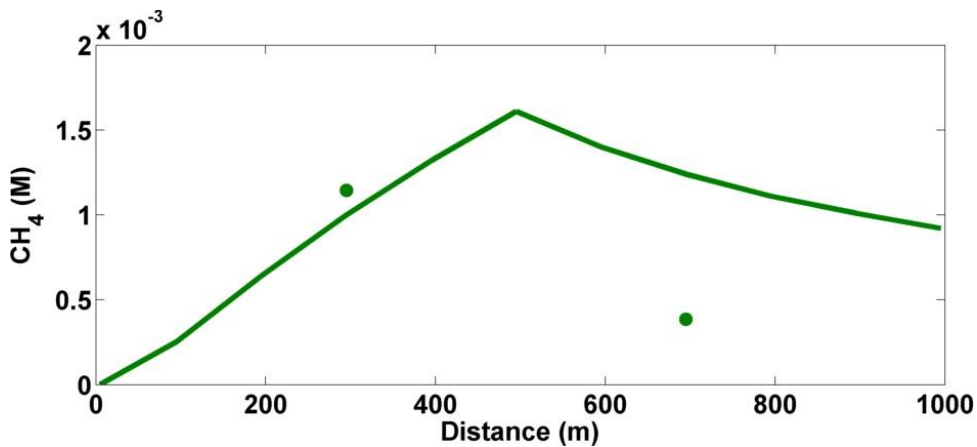


Figure 5.8: Scenario 6, effect of methanogenesis; $T = 5,000$ years; advective flow is from left to right; distance = 0 m corresponds to saline intrusion inflow point, distance = 1,000 m corresponds to outflow point. The dots correspond to field values and the lines correspond to model simulations. a) pH; b) Aqueous concentration of Fe(II); c) Aqueous concentration of Mn(II); d) Aqueous concentration of SO_4^{2-} ; e) Aqueous concentration of methane. See text for discussion.

Based on the above scenarios, an immediate conclusion from these observations is that sulfate reduction and methanogenesis accompany iron and manganese reduction, and sulfate

reduction can effectively control the pH of solution with high Fe(II) production. Nevertheless, it is noted that modeled Fe(II) at lower mixing zone and at upper mixing zone are not consistent with field measurements at the same time, even including secondary precipitation. For example, to achieve at least 5.35×10^{-3} M of Fe(II) at distance of 700m, the Fe(II) at distance of 300m must reach $2.19 - 2.26 \times 10^{-3}$ M under the current model set-up. Nevertheless, the measured Fe(II) only ranges from 3.57 to 8.92×10^{-4} M, which is 5-times lower than the modeled results. This model assumes a constant iron reduction rate so that Fe(II) accumulates linearly and proportional to the distance and travel time. Hence, a uniform iron reduction rate cannot satisfy the Fe(II) concentration simultaneously at the lower and upper saline mixing zones.

As discussed in Sections 5.4, we speculate that the bioavailability of organic matter at the upper mixing zone is much higher than at any other place, resulting in intensive iron reduction. The bioavailability of organic matter is a difficult property to parameterize, as it is determined by various factors, including organic matter reactivities, microorganism activities, and possible interactions between saline and freshwater. In Scenario 7, we assume that the various biogeochemical factors are reflected by the fermentation rate of sediment organic matter. In this way, a high fermentation rate represents the organic matter that is more easily utilized by bacteria and tends to release more labile DOM for electron acceptors. Conversely, a low fermentation rate suggests that the slow depletion of solid organic matter and less labile DOM is available for sequential redox reactions.

5.5.2.7 Scenario 7: Bioavailability of Organic Matter

In Scenario 7, the model is set up with different fermentation rates at the upper and lower saline mixing zones. At the lower saline mixing zone (cell 1-50), the fermentation rate of organic matter is changed to 1.5×10^{-12} , to limit the overall redox reactions. At the upper saline mixing zone (cell 51-100), the fermentation rate increases to 8.5×10^{-11} , which is approximately six times higher than that at the lower saline mixing zone (Table 5.7). The saturation indices with respect to siderite and rhodochrosite are assigned to 2.4 and 1.0, respectively, which

comparable to the actual values of 1.5 and 0.8. The higher saturation index of siderite is to prevent unrealistically high Fe(II) in solution. FeS is allowed to precipitate at equilibrium. The rate constants for electron acceptors are uniform along the flow line, thus isolating the effect of fermentation.

The simulated aqueous concentration profiles are presented in Figure 5.9, and differ markedly from previous uniform fermentation cases. Under the low fermentation rate at the lower saline mixing zone, though iron reduction rates for iron and manganese are high, both Fe(II) and Mn(II) increase slowly and are maintained at low levels. pH stays around 6.5, which is approximately 0.5 unit lower than measured values. At a distance of 300 m, Fe(II) at 1.19×10^{-3} M is similar to observed. Still, modeled Mn(II) under a uniform reaction rate cannot fit the observed elevated Mn(II) at lower mixing zone. As water turns over to the upper saline mixing zone, the high fermentation rate allowed the rapid production of Fe(II) and Mn(II), accompanied with rising in pH. At the upper mixing zone, pH increases from 6.5 to 7.5. At a distance of 700 m, Fe(II) and Mn(II) reached 5.16×10^{-3} M and 6.28×10^{-5} M, respectively, which agree with field measurements. SI, with respect to FeCO_3 and MnCO_3 , also reflect the rapid accumulation of Fe(II) and Mn(II) along the flow line. Along the lower mixing zone, both FeCO_3 and MnCO_3 remain undersaturated, suggesting low production of Fe(II) and Mn(II). Once water moves to the upper mixing zone, which is associated with a higher fermentation rate, both FeCO_3 and MnCO_3 begin to precipitate out of solution at 700m. From 800 to 1000m, both Fe(II) and Mn(II) show a sharp decreasing trend, due to the secondary mineral precipitation. However, the amount of precipitation under the assigned SI in this model is not representative of the real value, since kinetics of these secondary minerals is extremely slow. The reason for applying SI in this scenario is to prevent too much Fe(II) and Mn(II) from accumulating in the solution under such a high fermentation rate. For example, Fe(II) would increase to 1.05×10^{-2} M at the end of flow path if siderite were not allowed to precipitate. The distance between W1 and W3 is approximately 150 m. The measured Fe(II) concentration difference between W1 and W3 is maintained at $5.35\text{-}5.53 \times 10^{-3}$ M. Therefore, it is likely that Fe(II) has reached a steady state, in which the rate of production equals rate of the precipitation. Although the field data beyond W3 (700 -1000m) is not available, the Fe(II) concentration at the end of flow path does

not likely increase linearly. This assumption can be supported by the circumneutral pH and relatively high sulfate concentration at the Kidd 2 site. No evidence indicates fast sulfate reduction from 700 to 1000m to maintain the circumneutral pH.

Similar to iron and manganese reduction, removing SO_4^{2-} by sulfate reduction is shown at two different stages. At the lower saline mixing zone, sulfate reduction is strongly inhibited by a low fermentation rate. Hence, the loss of SO_4^{2-} at the lower saline mixing zone is mainly attributed to dilution. At the upper saline mixing zone however, approximately 1.96×10^{-3} M of SO_4^{2-} is lost due to more rapid sulfate reduction. In this scenario, secondary mineral FeS is allowed to precipitate, resulting in a further decrease in pH and loss of Fe(II). Model results show that FeS starts to precipitate at distance of 100m and is at saturation along the rest of flow path.

Methanogenesis is only applied at lower mixing zone. It is shown that the methane concentration increases up to 1.16×10^{-3} M at distance of 500m, and slowly decreases at the lower mixing zone due to dilution. It is likely that the high concentration of methane at the lower mixing zone is mainly derived from the lower silt by diffusion and groundwater leakage. Moreover, methane is also possibly involved in secondary re-oxidation reactions. Again, due to the qualitative field measurement and low resolution of the methane along the saline mixing zone, it is difficult to fully understand methanogenesis at the Kidd 2 site.

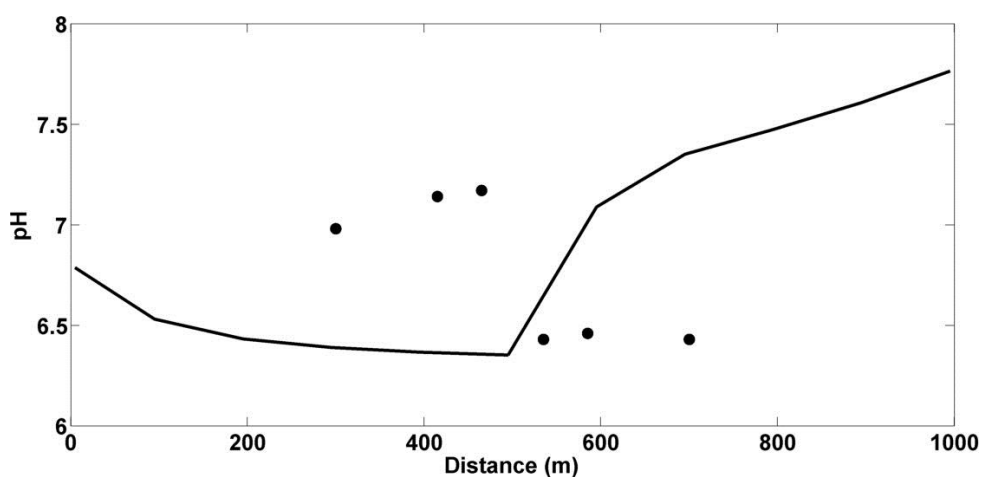
The “two fermentation rates” scenario provides insight into the importance of the bioavailability of organic matter in the system. This simulation successfully reproduces the accumulation of Fe(II) along the saline mixing zone, and describes the geochemical evolution during transport. Simulation results show the distinctly different aqueous patterns as the two fermentation rates are applied. That is, the bioavailability of organic matter is critical in determining the biogeochemical processes in the groundwater system.

Still, it remains unclear which process is driving the high bioavailability of organic matter at the upper saline mixing zone. Possible situations include:

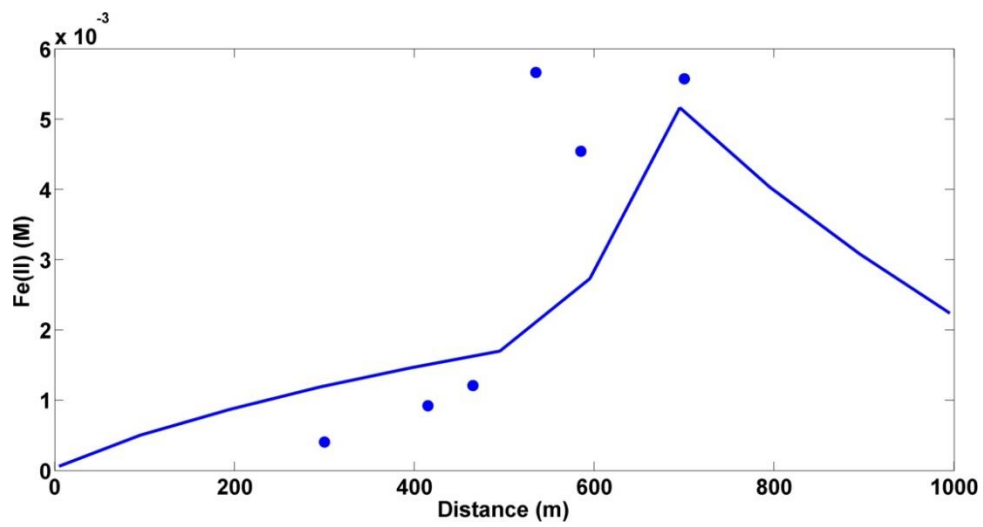
- High organic matter reactivities at the upper saline mixing zone can be continuous or heterogeneous (i.e., patches of reactive organic matter),
- Additional organic matter may be transported by recharge water,
- Additional organic matter may be released from the surficial silt layer,
- Interactions may be occurring between saline and fresh groundwater

These uncertainties make the kinetic processes and mechanisms difficult to elucidate. To better understand the geochemical evolution and the reactive transport processes at the Kidd 2 site, more widely distributed spatial data needs to be collected, particularly along the saline mixing zone. For example, in situ aqueous concentration profiles should be measured at the overturn and at the end of the saline circulation, to further calibrate the model and constrain the reaction rate. Furthermore, kinetic rate expressions are critical in producing meaningful simulation results. Hence, they should be carefully generated, especially when considering secondary mineral precipitation.

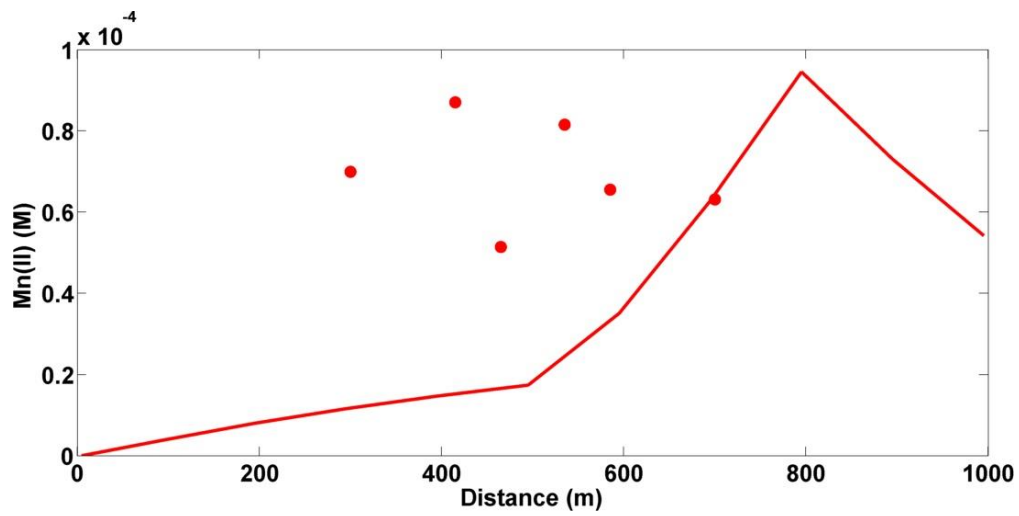
a)



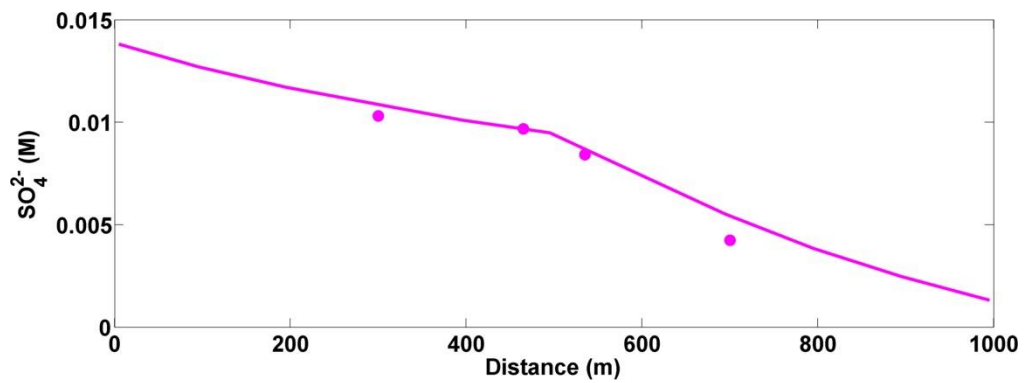
b)



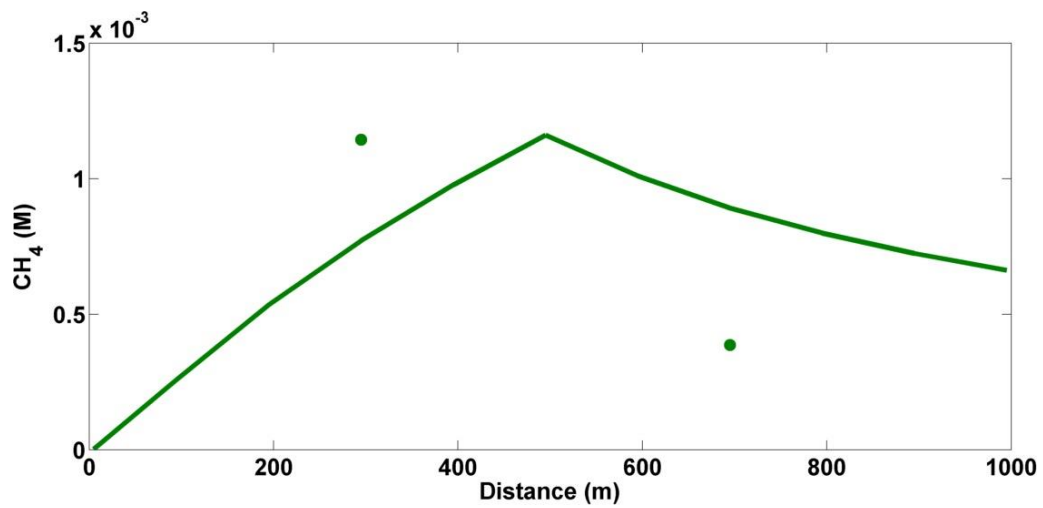
c)



d)



e)



f)

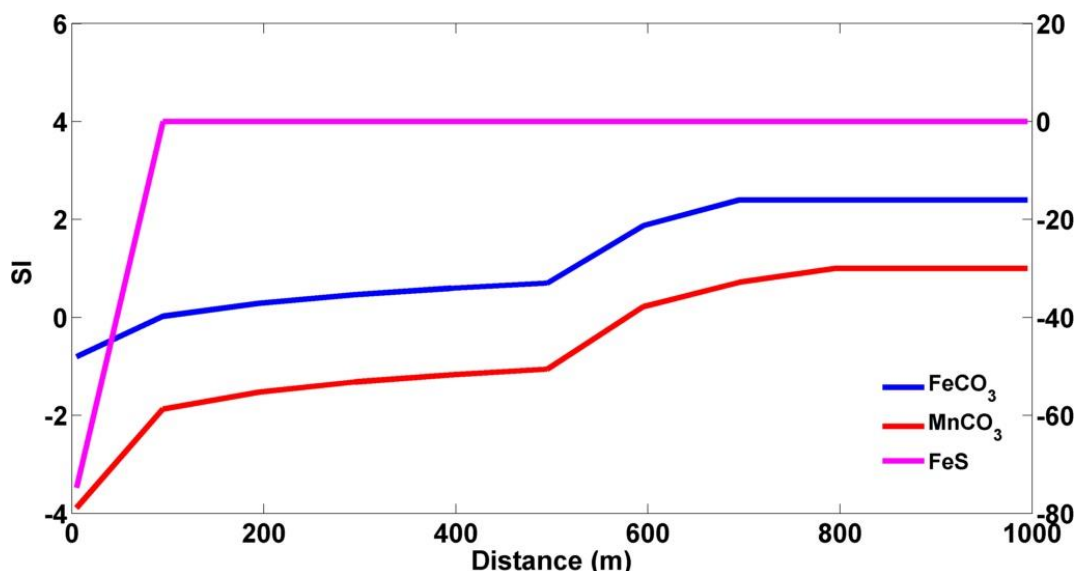


Figure 5.9: Scenario 7, effect of bioavailability; T = 5,000 years; advective flow is from left to right; distance = 0 m corresponds to saline intrusion inflow point, distance = 1,000 m corresponds to outflow point. The dots correspond to field values and the lines correspond to model simulations. a) pH; b) Aqueous concentrations of Fe(II); c) Aqueous concentrations of Mn(II); d) Aqueous concentrations of SO_4^{2-} ; e) Aqueous concentrations of methane; f) Saturation indices for siderite, rhodochrosite and iron sulfide. See text for discussion.

5.5.3 Long-term Evolution of the Geochemistry

As discussed above, scenario 7 is likely the most representative simulation for the geochemical processes along the flow path, and thus can be applied to evaluate the long-term evolution of geochemistry at the Kidd 2 site.

Based on the model results, approximately 0.1 and 1.36 moles of iron oxide have been consumed in the lower and upper mixing zone, respectively, during the 5,000 years simulation. Sequential extractions showed that reactive iron oxide in the mixing zones ranged from 14.2 to 25.1mM/kg, with mean of 18.1mM/kg. By assuming the porosity of 0.3 and soil density of 2,840kg/m³, 1 liter of water is in contact with approximately 6.62 kg of solid. If the current reaction rates are maintained and assuming organic matter is unlimited, an additional 6,033

and 450 years is needed to exhaust the reactive iron oxide at lower and upper mixing zone, respectively. The lower concentration of iron oxide at the upper mixing zone also supports the faster consumption rate at upper mixing zone. However, as discussed above, the most reactive iron oxides are expected to be preferentially consumed initially and the reduction rate will tends to slow down as remaining iron oxides are more stable. As a result, it is expected that iron reduction should last longer than the model estimation. Meanwhile, as most reactive iron oxides exhausted, sulfate reduction may progressively overwhelm iron reduction since the saline circulation during the medium-high tide continuously bringing SO_4^{2-} and circulating along the saline mixing zone. As discussed above, sulfate reduction would significantly lower the pH. Therefore, it is expected more acidic water would develop. In addition, the produced H_2S is a dangerous toxin that will impart a taste and odor to the water. The overall reaction rate and iron reduction are controlled by fermentation of organic matter. During the 5,000 years simulation, approximately 0.24 and 1.34 mole of organic matter has been consumed on lower and upper mixing zone, respectively. The loss of ignition results showed that organic matter in sediments ranged from 0.75 to 1.07%, with the mean of 0.86%. By assuming all organic matter can be utilized for fermentation step, the consumption of total organic matter needs approximately additional 38,900 and 7,000 years at lower and upper mixing zone, respectively. As a result, it is clearly shown that iron oxide will be exhausted first at the Kidd 2 site.

Chapter 6: Conclusions and Recommendations

6.1 Conclusions

This thesis presents the analysis of the astonishing concentrations of dissolved iron and manganese in the upper mixing zone of groundwater-saline water in the deltaic sediments of the Fraser River delta in Vancouver, Canada. Both laboratory analysis and model simulation were performed to better understand the biogeochemical redox reactions and transport processes involved in this reduced, circumneutral groundwater system.

The following conclusions are drawn with respect to the thesis objectives:

- *To understand the primary and secondary redox reactions in the aquifer system:* iron and manganese reduction are the primary redox reactions which result in the elevated iron and manganese concentrations, accompanying the oxidation of organic matter. The presence of the secondary minerals (siderite and rhodochrosite) further supports the mechanism of iron and manganese reduction. Sulfate reduction occurs simultaneously with iron/manganese reduction. However, both groundwater geochemistry and AVS extraction suggest that sulfate reduction is relatively slow and strongly inhibited by iron reduction, especially at the upper mixing zone. The presence of methane indicates the occurrence of methanogenesis. The increasing pattern of methane along depth profile provides evidence that methane probably comes from the deep confining silt layer and transport along the saline circulation.
- *To determine iron and manganese oxide reactivities:* A kinetic method was used to describe the composition of the iron and manganese oxide pools at the Kidd 2 site, which allows a quantification of iron and manganese oxide reactivity in sediments. The reactivity of reactive iron and manganese oxides ranged from $1.25\text{--}1.92 \times 10^{-4} \text{ s}^{-1}$ and $1.14\text{--}3.57 \times 10^{-4} \text{ s}^{-1}$, respectively. Overall, the small difference in rate constants along the depth profile suggests that the reactivities of iron and manganese oxides were

practically the same and cannot explain the enormous difference of iron and manganese concentrations in solution. However, the depletion of iron and manganese oxides at the upper mixing zone indicates the intensive redox reduction and thereby, it is expected that the significant high concentration of iron at upper mixing zone is probably derived from the bioavailability of organic matter and the transport process along saline circulation.

- *To identify the source of dissolved organic matter and de-component organic matter complex:* The relatively high FI values (1.59 to 1.80) indicate that DOM is predominantly derived from extracellular microbial activity. The unique C peak (excitation = 300-370 nm, emission = 450-500 nm) at the upper mixing zone suggests the abnormal property of the dissolved organic matter. A comparison of fluorescence property between DOM at the upper mixing zone and other depths indicate that the C peak is probably related to the saline intrusion, rather than freshwater on its own. This information, combining with the minimum RI provides evidence that DOM at the upper mixing zone is more accessible to bacteria fermentation, and subsequently creates a preferential pathway for iron and manganese reduction.
- *To develop one-dimensional kinetic reactive-transport model:* The one - dimensional kinetic reaction–transport model presents seven quantitative scenarios to simulate the biogeochemical reactions and multi-components transport along flow paths in reduced groundwater systems. Simulation demonstrates that iron reduction, manganese reduction, sulfate reduction, and methanogenesis occur concomitantly at the Kidd 2 site. Although certain assumptions were made to simplify the complex environment (i.e. density dependent groundwater flow, bioavailability of organic matter), the model results provide insight on the groundwater geochemistry and its long term evolution in Fraser River sandy aquifer.

6.2 Recommendations

- *DOM bioavailability:* Based on our findings, DOM bioavailability is an important factor which drives the intensive iron and manganese reduction at the upper mixing zone. However, the reason which causes the high liability of organic matter is still not fully understood, which includes organic matter reactivity, the interaction of the mixing of fresh-saline water, or the both. To identify the efficiency of organic matter utilization, a laboratory incubation experiment could be conducted by inoculating groundwater with microbial inocula collected from different saline intrusion zones based on salinities. In addition, the groundwater collected outside the saline circulation (undisturbed water) should also be examined, to further understand the role of the salinity.
- *Groundwater sampling resolution at the upper mixing zone:* As the upper mixing zone only extents 1-2 m in depth, multilevel wells with interval of 1m are not sufficient to capture the geochemical features at the upper mixing zone. Due to the low resolution, it is still not clear how iron concentration changes within the mixing zone and how salinity related to the rate of iron reduction. Moreover, an additional groundwater monitoring well could be drilled further downstream along a north-south cross section at the Kidd site (at the exit of the saline water). Analysis of the groundwater at this location could further constrain the iron reduction rate applied in the model, and confirm the steady state or the transit condition of the iron dissolution/precipitation along the saline transport pathway.
- *Sediment analysis:* Extent of sediment analysis should be expanded, because the single location of the sediment profile may not be sufficient to capture the heterogeneity of the sediment properties, including the reactivity of iron/manganese oxide and the patchiness of organic matter with relatively high reactivity at upper mixing zone. Similar to groundwater monitoring well, sediment samples at an undisturbed area should be collected to validate the current transport model.

- *Fe(II) and Fe(III) speciation*: The iron speciation from the extractions shows that reactive Fe(II) is the majority iron oxide phase, which is composed of approximately 75% to 80% of total reactive iron. The high content of Fe(II) further supports the reducing condition of the aquifer, and indicates the secondary mineral reactions. However, possible mineral phases are not defined by SEM. This discrepancy between extraction and SEM mineralogy should be noticed and need further characterize.
- *Methanogenesis*: The presence of methane provides evidence of methanogenesis at the Kidd 2 site. However, due to the slow gas diffusion process (over 30 minutes), equilibrium between aqueous and vapor was not achieved and only qualitative gas measurements were obtained in this study. The slow equilibrium process suggests the kinetic limitation of the methanogenesis, and the reaction rate applied in the transport model may not be representative. To obtain the quantitative methane production rate in the field, radiotracer method and stable methane isotope analysis could be applied in the future study.
- *Model simulation*: Future research with reactive transport model will include expanding the code to two and three dimensions in order to address the density-dependent groundwater flow and mixing process, considering additional biogeochemical reaction processes like metabolic activity and sorption of iron and manganese. By incorporating a more complete description of the chemical and microbial kinetics, the reactive transport model can provide more realistic representations of the field-derived data and predict the fate of iron and manganese under various field scales.

References

- Aller, Robert C., and Peter D. Rude. 1988. "Complete Oxidation of Solid Phase Sulfides by Manganese and Bacteria in Anoxic Marine Sediments." *Geochimica et Cosmochimica Acta* 52 (3): 751–65. doi:10.1016/0016-7037(88)90335-3.
- Appelo, C. A. J., and Dieke Postma. 2005. *Geochemistry, Groundwater and Pollution, Second Edition*. CRC Press.
- Berner, Robert A. 1980. *Early Diagenesis: A Theoretical Approach*. Princeton University Press.
- Bianchin, M. 2010. "A Field Investigation Characterizing the Hyporheic Zone of a Tidally-Influenced River." Vancouver: University of British Columbia, Earth and Ocean Sciences.
- Bolton, Mark, and Roger Beckie. 2011. "Aqueous and Mineralogical Analysis of Arsenic in the Reduced, Circumneutral Groundwater and Sediments of the Lower Fraser River Delta, British Columbia, Canada." *Applied Geochemistry*, Arsenic and other toxic elements in global groundwater systems, 26 (4): 458–69. doi:10.1016/j.apgeochem.2011.01.005.
- Boudreau, B. P., and B. R. Ruddick. 1991. "On a Reactive Continuum Representation of Organic Matter Diagenesis." <http://Dalspace.library.dal.ca/handle/10222/26293>.
- Canfield, D. E., B. Thamdrup, and J. W. Hansen. 1993. "The Anaerobic Degradation of Organic Matter in Danish Coastal Sediments: Iron Reduction, Manganese Reduction, and Sulfate Reduction." *Geochimica Et Cosmochimica Acta* 57 (16): 3867–83.
- Chao, T. T., and P. K. Theobald. 1976. "The Significance of Secondary Iron and Manganese Oxides in Geochemical Exploration." *Economic Geology* 71 (8): 1560–69. doi:10.2113/gsecongeo.71.8.1560.
- Chao, T. T., and Liyi Zhou. 1983. "Extraction Techniques for Selective Dissolution of Amorphous Iron Oxides from Soils and Sediments1." *Soil Science Society of America Journal* 47 (2): 225. doi:10.2136/sssaj1983.03615995004700020010x.
- Christensen, Thomas H., Peter Kjeldsen, Hans-Jørgen Albrechtsen, Gorm Heron, Per H. Nielsen, Poul L. Bjerg, and Peter E. Holm. 1994. "Attenuation of Landfill Leachate Pollutants in Aquifers." *Critical Reviews in Environmental Science and Technology* 24 (2): 119–202. doi:10.1080/10643389409388463.
- Christoffersen, Jørgen, and Margaret R. Christoffersen. 1976. "The Kinetics of Dissolution of Calcium Sulphate Dihydrate in Water." *Journal of Crystal Growth* 35 (1): 79–88. doi:10.1016/0022-0248(76)90247-5.
- Clague, J.J. 1998. "Geological Setting of the Fraser River Delta." Edited by J.L. Luternauer and D.C. Mosher, 7–16.
- Clague, J.J., J.L. Luternauer, S.E. Pullan, and J.A. Hunter. 1991. "Postglacial Deltaic Sediments, Southern Fraser-River Delta, British-Columbia." *Canadian Journal Of Earth Sciences* 28 (9): 1386–93.
- Clague, John J., J. L. Luternauer, S. E. Pullan, and J. A. Hunter. 1991. "Postglacial Deltaic Sediments, Southern Fraser River Delta, British Columbia." *Canadian Journal of Earth Sciences* 28 (9): 1386–93. doi:10.1139/e91-122.
- Coble, Paula G. 1996. "Characterization of Marine and Terrestrial DOM in Seawater Using Excitation-Emission Matrix Spectroscopy." *Marine Chemistry* 51 (4): 325–46. doi:10.1016/0304-4203(95)00062-3.

- . 1998. "Distribution and Optical Properties of CDOM in the Arabian Sea during the 1995 Southwest Monsoon." *Deep Sea Research Part II: Topical Studies in Oceanography* 45 (10–11): 2195–2223. doi:10.1016/S0967-0645(98)00068-X.
- Coble, Paula G., Sarah A. Green, Neil V. Blough, and Robert B. Gagosian. 1990. "Characterization of Dissolved Organic Matter in the Black Sea by Fluorescence Spectroscopy." *Nature* 348 (6300): 432–35. doi:10.1038/348432a0.
- Coffin, D. E. 1963. "A METHOD FOR THE DETERMINATION OF FREE IRON IN SOILS AND CLAYS." *Canadian Journal of Soil Science* 43 (1): 7–17. doi:10.4141/cjss63-002.
- Cook, Robert B. 1984. "Distributions of Ferrous Iron and Sulfide in an Anoxic Hypolimnion." *Canadian Journal of Fisheries and Aquatic Sciences* 41 (2): 286–93. doi:10.1139/f84-033.
- Cory, Rose M., and Diane M. McKnight. 2005. "Fluorescence Spectroscopy Reveals Ubiquitous Presence of Oxidized and Reduced Quinones in Dissolved Organic Matter." *Environmental Science & Technology* 39 (21): 8142–49. doi:10.1021/es0506962.
- Douglas, Mitchell Wells. 2011. "Laser Spectroscopic Analysis of Stable Water Isotopes in Coastal Aquifer Groundwater: Fraser River Delta, British Columbia, Canada." Thesis Dissertation, University of British Columbia.
- Fellman, Jason B., Eran Hood, and Robert G. M. Spencer. 2010. "Fluorescence Spectroscopy Opens New Windows into Dissolved Organic Matter Dynamics in Freshwater Ecosystems: A Review." *Limnology and Oceanography* 55 (6): 2452–62. doi:10.4319/lo.2010.55.6.2452.
- Hall, G. E. M., J. E. Vaive, R. Beer, and M. Hoashi. 1996. "Selective Leaches Revisited, with Emphasis on the Amorphous Fe Oxyhydroxide Phase Extraction." *Journal of Geochemical Exploration* 56 (1): 59–78. doi:10.1016/0375-6742(95)00050-X.
- Hansen, Lars Kyhnau, Rasmus Jakobsen, and Dieke Postma. 2001. "Methanogenesis in a Shallow Sandy Aquifer, Rømø, Denmark." *Geochimica et Cosmochimica Acta* 65 (17): 2925–35. doi:10.1016/S0016-7037(01)00653-6.
- Heron, Gorm., Catherine. Crouzet, Alain C. M. Bourg, and Thomas H. Christensen. 1994. "Speciation of Fe(II) and Fe(III) in Contaminated Aquifer Sediments Using Chemical Extraction Techniques." *Environmental Science & Technology* 28 (9): 1698–1705. doi:10.1021/es00058a023.
- Horneman, A., A. Van Geen, D.V. Kent, P.E. Mathe, Y. Zheng, R.K. Dhar, S. O'Connell, et al. 2004. "Decoupling of As and Fe Release to Bangladesh Groundwater under Reducing Conditions. Part 1: Evidence from Sediment Profiles." *Geochimica Et Cosmochimica Acta* 68 (17): 3459–73.
- Horneman, A., A. van Geen, D.V. Kent, P.E. Mathe, Y. Zheng, R.K. Dhar, S. O'Connell, et al. 2004. "Decoupling of As and Fe Release to Bangladesh Groundwater under Reducing Conditions. Part I: Evidence from Sediment Profiles." *Geochimica et Cosmochimica Acta* 68 (17): 3459–73. doi:10.1016/j.gca.2004.01.026.
- Hunter, J. A. 1994. "Borehole Geophysics Logs, Fraser River Delta (92G), British Columbia." *Geological Survey of Canada Open File* 2841.
- Hunter, Kimberley S., Yifeng Wang, and Philippe Van Cappellen. 1998. "Kinetic Modeling of Microbially-Driven Redox Chemistry of Subsurface Environments: Coupling Transport, Microbial Metabolism and Geochemistry." *Journal of Hydrology* 209 (1–4): 53–80. doi:10.1016/S0022-1694(98)00157-7.

- Hyacinthe, C. 2006. "Reactive iron(III) in Sediments: Chemical versus Microbial Extractions." *Geochimica et Cosmochimica Acta* 70 (16): 4166–80. doi:10.1016/j.gca.2006.05.018.
- Hyacinthe, C., and P. Van Cappellen. 2004. "An Authigenic Iron Phosphate Phase in Estuarine Sediments: Composition, Formation and Chemical Reactivity." *Marine Chemistry* 91 (1–4): 227–51. doi:10.1016/j.marchem.2004.04.006.
- Jakobsen, Rasmus. 1999. "Redox Zoning, Rates of Sulfate Reduction and Interactions with Fe-Reduction and Methanogenesis in a Shallow Sandy Aquifer, Rømø, Denmark." *Geochimica et Cosmochimica Acta* 63 (1): 137–51. doi:10.1016/S0016-7037(98)00272-5.
- Jakobsen, Rasmus, and Dieke Postma. 1994a. "In Situ Rates of Sulfate Reduction in an Aquifer (Rømø, Denmark) and Implications for the Reactivity of Organic Matter." *Geology* 22 (12): 1101–6. doi:10.1130/0091-7613(1994)022<1103:ISROSR>2.3.CO;2.
- . 1994b. "In Situ Rates of Sulfate Reduction in an Aquifer (Rømø, Denmark) and Implications for the Reactivity of Organic Matter." *Geology* 22 (12): 1101–6. doi:10.1130/0091-7613(1994)022<1103:ISROSR>2.3.CO;2.
- . 1999. "Redox Zoning, Rates of Sulfate Reduction and Interactions with Fe-Reduction and Methanogenesis in a Shallow Sandy Aquifer, Rømø, Denmark." *Geochimica et Cosmochimica Acta* 63 (1): 137–51. doi:10.1016/S0016-7037(98)00272-5.
- Jensen, Dorthe L, Jens K Boddum, Jens Christian Tjell, and Thomas H Christensen. 2002. "The Solubility of Rhodochrosite (MnCO₃) and Siderite (FeCO₃) in Anaerobic Aquatic Environments." *Applied Geochemistry* 17 (4): 503–11. doi:10.1016/S0883-2927(01)00118-4.
- Kampbell, Don, and Daniel M. McInnes. 2003. "Bubble Stripping To Determine Hydrogen Concentrations in Ground Water: A Practical Application of Henry's Law." *Journal of Chemical Education* 80 (5): 516. doi:10.1021/ed080p516.
- Keon, N.E., C.H. Swartz, D.J. Brabander, C. Harvey, and H.F. Hemond. 2001. "Validation of an Arsenic Sequential Extraction Method for Evaluating Mobility in Sediments." *Environmental Science & Technology* 35 (13): 2778–84.
- Koretsky, Carla M., Charles M. Moore, Kristine L. Lowe, Christof Meile, Thomas J. DiChristina, and Philippe Van Cappellen. 2003. "Seasonal Oscillation of Microbial Iron and Sulfate Reduction in Saltmarsh Sediments (Sapelo Island, GA, USA)." *Biogeochemistry* 64 (2): 179–203. doi:10.1023/A:1024940132078.
- Larsen, Ole, and Dieke Postma. 2001. "Kinetics of Reductive Bulk Dissolution of Lepidocrocite, Ferrihydrite, and Goethite." *Geochimica et Cosmochimica Acta* 65 (9): 1367–79. doi:10.1016/S0016-7037(00)00623-2.
- Lawaetz, Anders Juul, and Colin A. Stedmon. 2009. "Fluorescence Intensity Calibration Using the Raman Scatter Peak of Water." *Applied Spectroscopy* 63 (8): 936–40.
- Lovley, Derek R., and Francis H. Chapelle. 1995. "Deep Subsurface Microbial Processes." *Reviews of Geophysics* 33 (3): 365. doi:10.1029/95RG01305.
- Lovley, Derek R., and Elizabeth J. P. Phillips. 1986a. "Organic Matter Mineralization with Reduction of Ferric Iron in Anaerobic Sediments." *Applied and Environmental Microbiology* 51 (4): 683–89.
- . 1986b. "Organic Matter Mineralization with Reduction of Ferric Iron in Anaerobic Sediments." *Applied and Environmental Microbiology* 51 (4): 683–89.

- McDowell, William H., and Gene E. Likens. 1988. "Origin, Composition, and Flux of Dissolved Organic Carbon in the Hubbard Brook Valley." *Ecological Monographs* 58 (3): 177–95. doi:10.2307/2937024.
- McKnight, Diane M., Elizabeth W. Boyer, Paul K. Westerhoff, Peter T. Doran, Thomas Kulbe, and Dale T. Andersen. 2001. "Spectrofluorometric Characterization of Dissolved Organic Matter for Indication of Precursor Organic Material and Aromaticity." *Limnology and Oceanography* 46 (1): 38–48.
- Miller, Matthew P., Diane M. McKnight, Rose M. Cory, Mark W. Williams, and Robert L. Runkel. 2006. "Hyporheic Exchange and Fulvic Acid Redox Reactions in an Alpine Stream/Wetland Ecosystem, Colorado Front Range." *Environmental Science & Technology* 40 (19): 5943–49. doi:10.1021/es060635j.
- Mladenov, Natalie, Philippa Huntsman-Mapila, Piotr Wolski, Wellington R. L. Masamba, and Diane M. McKnight. 2008. "Dissolved Organic Matter Accumulation, Reactivity, and Redox State in Ground Water of a Recharge Wetland." *Wetlands* 28 (3): 747–59. doi:10.1672/07-140.1.
- Neilson-Welch, Laurie A. 1999. "Saline Water Intrusion from the Fraser River Estuary a Hydrogeological Investigation Using Field Chemical Data and a Density-Dependent Groundwater Flow Model." M.Sc., Vancouver: University of British Columbia. <http://resolve.library.ubc.ca/cgi-bin/catsearch?bid=2208224>.
- Neilson-Welch, Laurie, and Leslie Smith. 2001. "Saline Water Intrusion Adjacent to the Fraser River, Richmond, British Columbia." *Canadian Geotechnical Journal* 38 (1): 67–82. doi:10.1139/t00-075.
- N.E.Keon, C.H.Swartz. 2001. "Validation of an Arsenic Sequential Extraction Method for Evaluating Mobility in Sediments." *Environ. Sci. Technol* 35: 2778–84.
- Nurmi, James T., and Paul G. Tratnyek. 2002. "Electrochemical Properties of Natural Organic Matter (NOM), Fractions of NOM, and Model Biogeochemical Electron Shuttles." *Environmental Science & Technology* 36 (4): 617–24. doi:10.1021/es0110731.
- Oliver, Barry G., Earl M. Thurman, and Ronald L. Malcolm. 1983. "The Contribution of Humic Substances to the Acidity of Colored Natural Waters." *Geochimica et Cosmochimica Acta* 47 (11): 2031–35. doi:10.1016/0016-7037(83)90218-1.
- Plummer, L. N. 1977. "Defining Reactions and Mass Transfer in Part of the Floridan Aquifer." *Water Resources Research* 13 (5): 801–12. doi:10.1029/WR013i005p00801.
- Postma, Dieke. 1993. "The Reactivity of Iron Oxides in Sediments: A Kinetic Approach." *Geochimica et Cosmochimica Acta* 57 (21–22): 5027–34. doi:10.1016/S0016-7037(05)80015-8.
- Postma, Dieke, and Rasmus Jakobsen. 1996. "Redox Zonation: Equilibrium Constraints on the Fe(III)/SO₄-Reduction Interface." *Geochimica et Cosmochimica Acta* 60 (17): 3169–75. doi:10.1016/0016-7037(96)00156-1.
- Prommer, H, D. A Barry, and G. B Davis. 2002. "Modelling of Physical and Reactive Processes during Biodegradation of a Hydrocarbon Plume under Transient Groundwater Flow Conditions." *Journal of Contaminant Hydrology*, The 2000 Contaminated Site Remediation Conference: From Source Zones to Ecosystems, 59 (1–2): 113–31. doi:10.1016/S0169-7722(02)00078-5.

- Ricketts, B.D. 1998. "Groundwater Flow beneath the Fraser River Delta, British Columbia; a Preliminary Model." Edited by J.L. Luternauer and D.C. Mosher, 241–55.
- Schiff, S. L., R. Aravena, S. E. Trumbore, and P. J. Dillon. 1990. "Dissolved Organic Carbon Cycling in Forested Watersheds: A Carbon Isotope Approach." *Water Resources Research* 26 (12): 2949–57. doi:10.1029/WR026i012p02949.
- Scott, Durelle T., Diane M. McKnight, Elizabeth L. Blunt-Harris, Sarah E. Kolesar, and Derek R. Lovley. 1998. "Quinone Moieties Act as Electron Acceptors in the Reduction of Humic Substances by Humics-Reducing Microorganisms." *Environmental Science & Technology* 32 (19): 2984–89. doi:10.1021/es980272q.
- Simpson, G., and I. Hutcheon. 1995. "Pore-Water Chemistry And Diagenesis Of The Modern Fraser-River Delta." *Journal Of Sedimentary Research Section A-Sedimentary Petrology And Processes* 65 (4): 648–55.
- Simpson, Graham, and Ian Hutcheon. 1995. "Pore-Water Chemistry and Diagenesis of the Modern Fraser River Delta." *Journal of Sedimentary Research* 65 (4a): 648–55. doi:10.1306/D426818A-2B26-11D7-8648000102C1865D.
- Slomp, Caroline P., and Philippe Van Cappellen. 2004. "Nutrient Inputs to the Coastal Ocean through Submarine Groundwater Discharge: Controls and Potential Impact." *Journal of Hydrology* 295 (1–4): 64–86. doi:10.1016/j.jhydrol.2004.02.018.
- Sondag, F. 1981. "Selective Extraction Procedures Applied To Geochemical Prospecting in An Area Contaminated By Old Mine Workings." *Journal of Geochemical Exploration* 15 (1–3): 645–52. doi:10.1016/0375-6742(81)90094-7.
- Spencer, Robert G. M., Lucy Bolton, and Andy Baker. 2007. "Freeze/thaw and pH Effects on Freshwater Dissolved Organic Matter Fluorescence and Absorbance Properties from a Number of UK Locations." *Water Research* 41 (13): 2941–50. doi:10.1016/j.watres.2007.04.012.
- Stumm, Werner. 1992. *Chemistry of the Solid-Water Interface: Processes at the Mineral-Water and Particle-Water Interface in Natural Systems*. New York: Wiley.
- Tessier, A., P. G. C. Campbell, and M. Bisson. 1979. "Sequential Extraction Procedure for the Speciation of Particulate Trace Metals." *Analytical Chemistry* 51 (7): 844–51. doi:10.1021/ac50043a017.
- Thorstenson, Donald C., Donald W. Fisher, and Mack G. Croft. 1979. "The Geochemistry of the Fox Hills-Basal Hell Creek Aquifer in Southwestern North Dakota and Northwestern South Dakota." *Water Resources Research* 15 (6): 1479–98. doi:10.1029/WR015i006p01479.
- V. A. Fry, J. D. Istok. 1993. "An Analytical Solution to the Solute Transport Equation with Rate-Limited Desorption and Decay." *Water Resources Research - WATER RESOUR RES* 29 (9). doi:10.1029/93WR01394.
- Van Cappellen, Philippe, Eric Viollier, Alakendra Roychoudhury, Lauren Clark, Ellery Ingall, Kristine Lowe, and Thomas Dichristina. 1998. "Biogeochemical Cycles of Manganese and Iron at the Oxic–Anoxic Transition of a Stratified Marine Basin (Orca Basin, Gulf of Mexico)." *Environmental Science & Technology* 32 (19): 2931–39. doi:10.1021/es980307m.

- Wersin, Paul, Patrick Höhener, Rudolf Giovanoli, and Werner Stumm. 1991. "Early Diagenetic Influences on Iron Transformations in a Freshwater Lake Sediment." *Chemical Geology* 90 (3–4): 233–52. doi:10.1016/0009-2541(91)90102-W.
- Williams, H.F.L., and M.C. Roberts. 1989. "Holocene Sea-Level Change And Delta Growth - Fraser-River Delta, British-Columbia." *Canadian Journal Of Earth Sciences* 26 (9): 1657–66.

Appendices

Appendix A: Flow Time Calculation at the Kidd 2 site

The distance (D) of the saline circulation = 1000m

The groundwater velocity is defined as:

$$v = \frac{q}{n} = \frac{K \times i}{n}$$

q = the Darcy's flux (m/s)

n = porosity

K = hydraulic conductivity (m/s)

i = hydraulic gradient

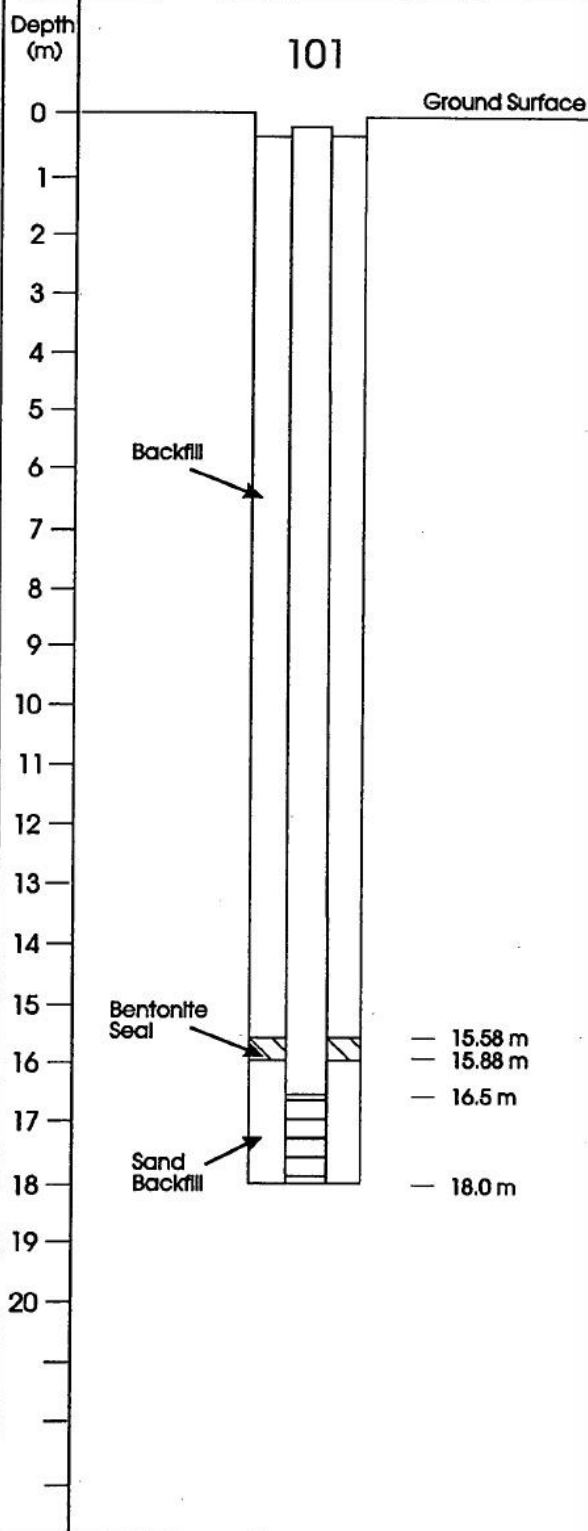
$$v = \frac{k \times i}{n} = \frac{4 \times 10^{-4} \text{ m/s} \times 0.0001}{0.3} = 1.3 \times 10^{-7} \text{ m/s} = 4.2 \text{ m/y}$$

$$\text{The flow time (T)} = \frac{D}{v} = \frac{1000 \text{ m}}{4.2 \text{ m/y}} = 238 \text{ y}$$

Appendix B: Piezometer and Well Logs for the Kidd 2 site(L. A. Neilson-Welch 1999)

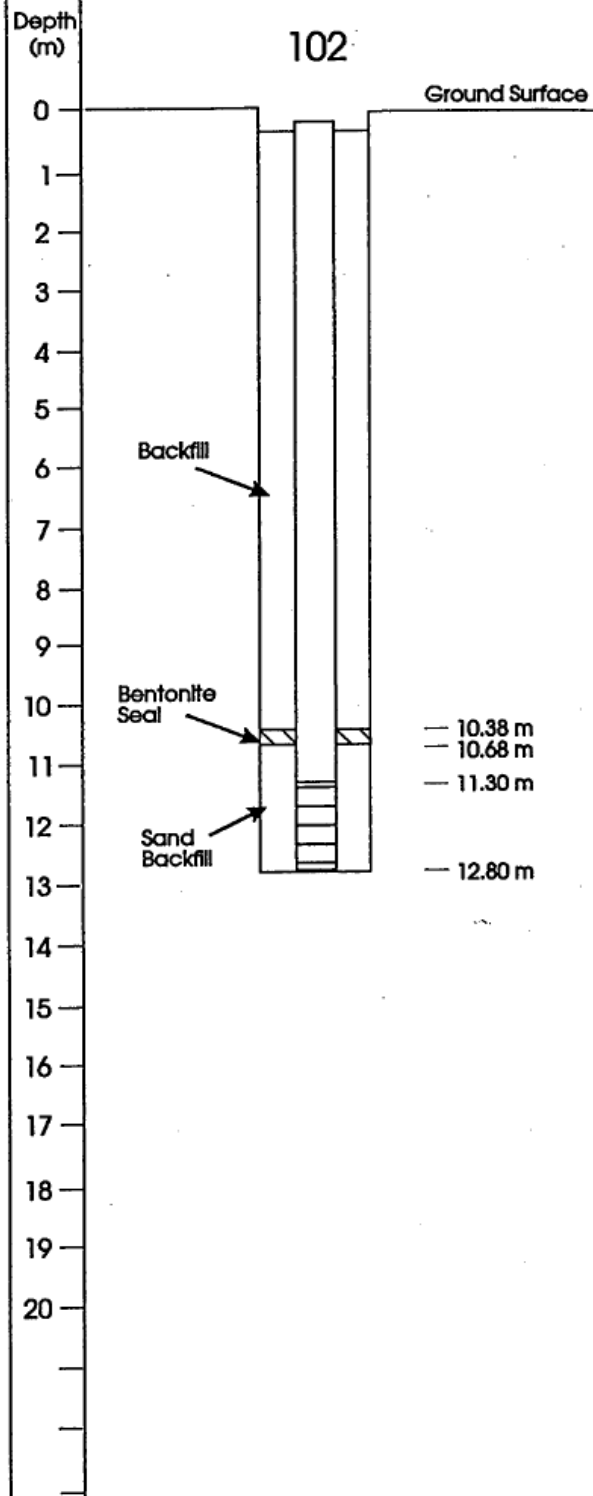
PIEZOMETER 101

Site Location: UBC Field Site, Richmond, BC
 Drilling Date: 1995
 Borehole Diameter: 0.17 m
 Borehole Depth: 18.0 m
 Well Material: PVC
 Well Diameter: 0.05 m
 Well Screen Length: 1.5 m
 Well Depth (below grade): 18.0 m
 Top of Well Elevation: 1.370 m



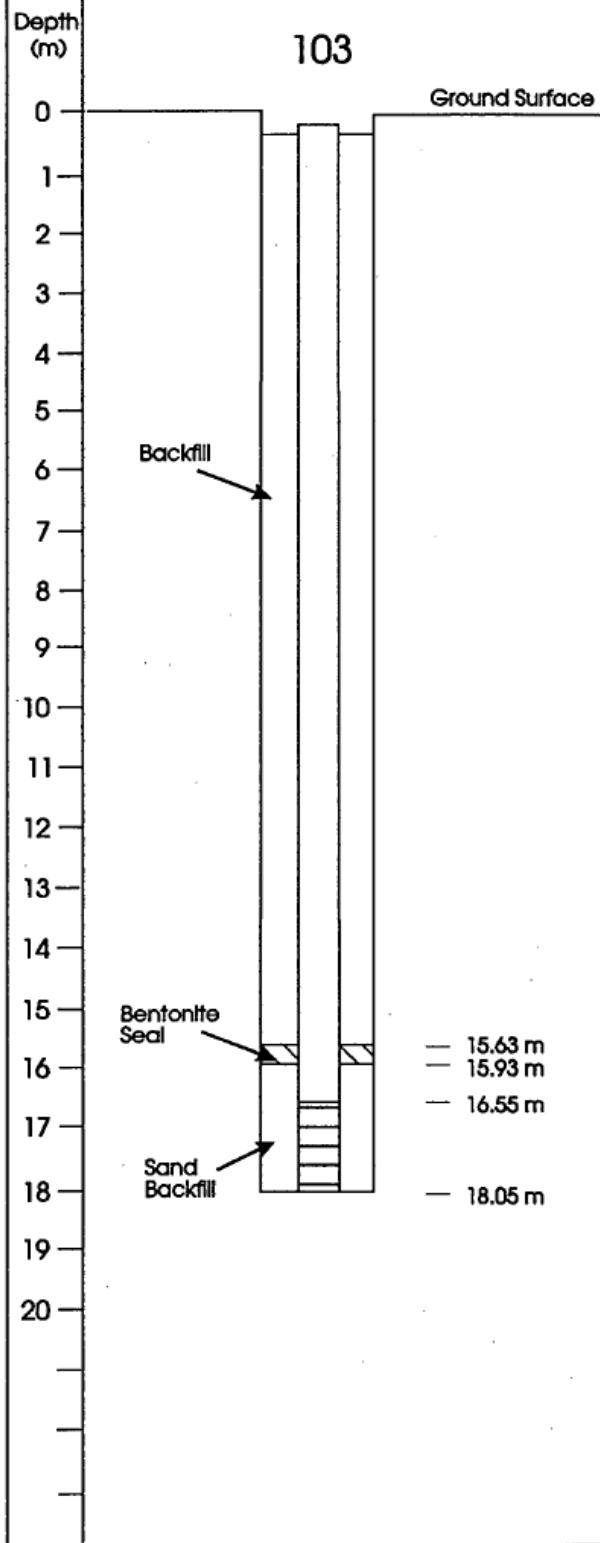
PIEZOMETER 102

Site Location: UBC Field Site, Richmond, BC
 Drilling Date: 1995
 Borehole Diameter: 0.17 m
 Borehole Depth: 12.80 m
 Well Material: PVC
 Well Diameter: 0.05 m
 Well Screen Length: 1.5 m
 Well Depth (below grade): 12.80 m
 Top of Well Elevation: 1.371 m



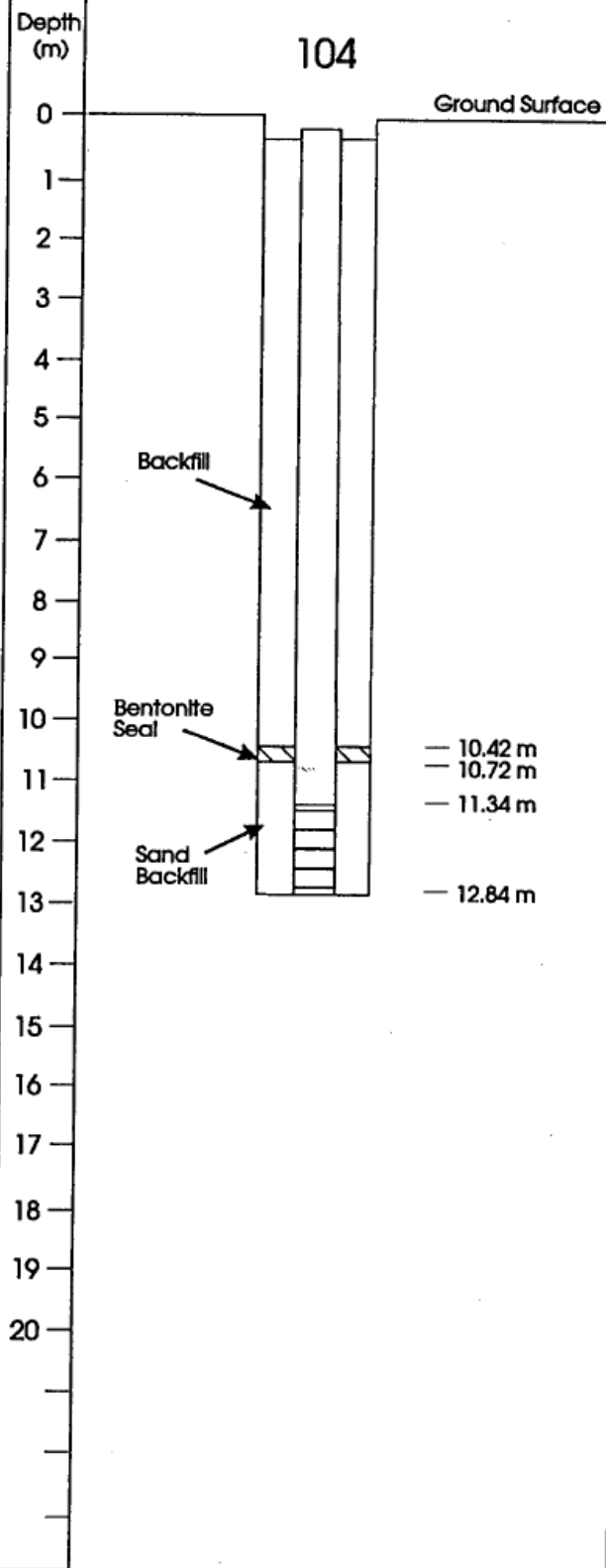
PIEZOMETER 103

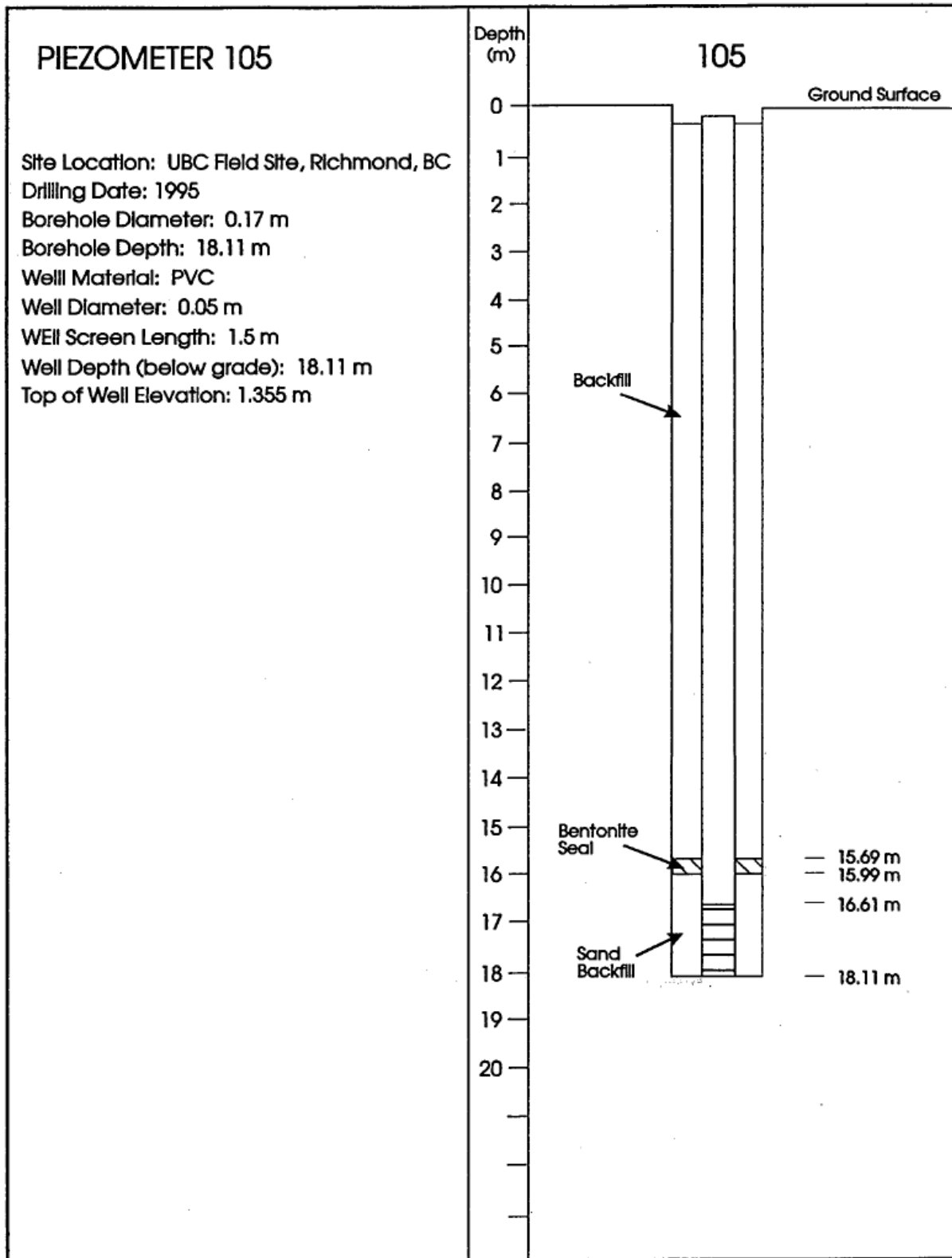
Site Location: UBC Field Site, Richmond, BC
 Drilling Date: 1995
 Borehole Diameter: 0.17 m
 Borehole Depth: 18.05 m
 Well Material: PVC
 Well Diameter: 0.05 m
 Well Screen Length: 1.5 m
 Well Depth (below grade): 18.05 m
 Top of Well Elevation: 1.366 m



PIEZOMETER 104

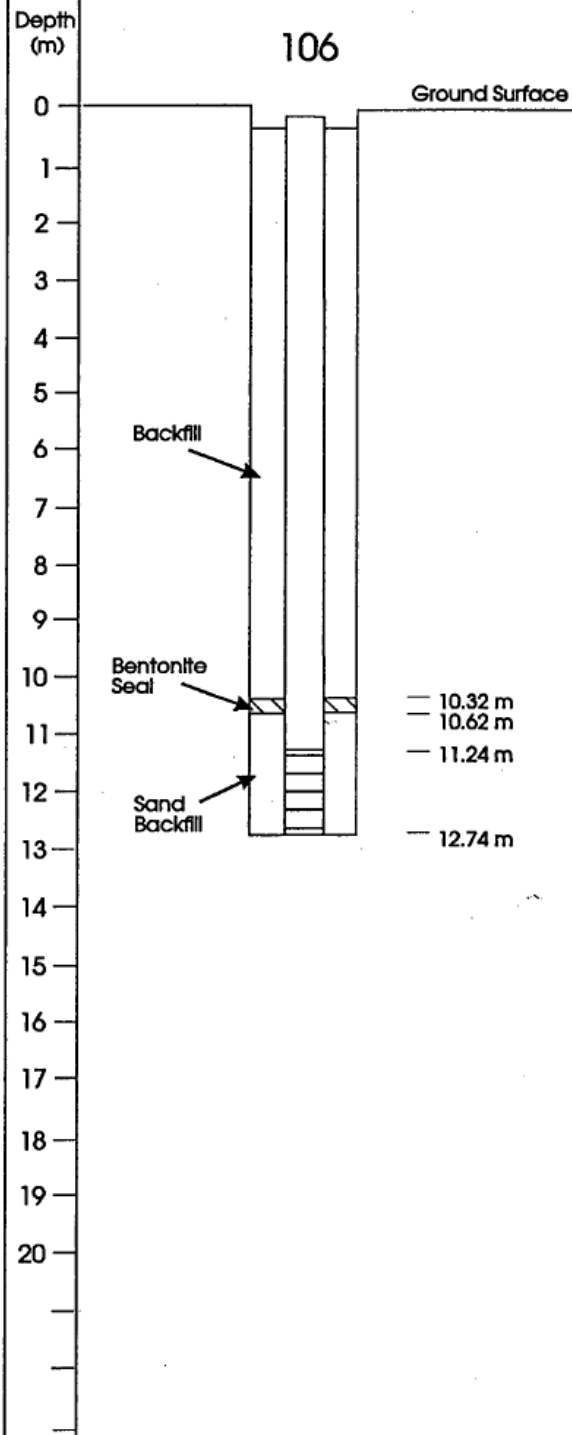
Site Location: UBC Field Site, Richmond, BC
 Drilling Date: 1995
 Borehole Diameter: 0.17 m
 Borehole Depth: 12.84 m
 Well Material: PVC
 Well Diameter: 0.05 m
 Well Screen Length: 1.5 m
 Well Depth (below grade): 12.84 m
 Top of Well Elevation: 1.362 m





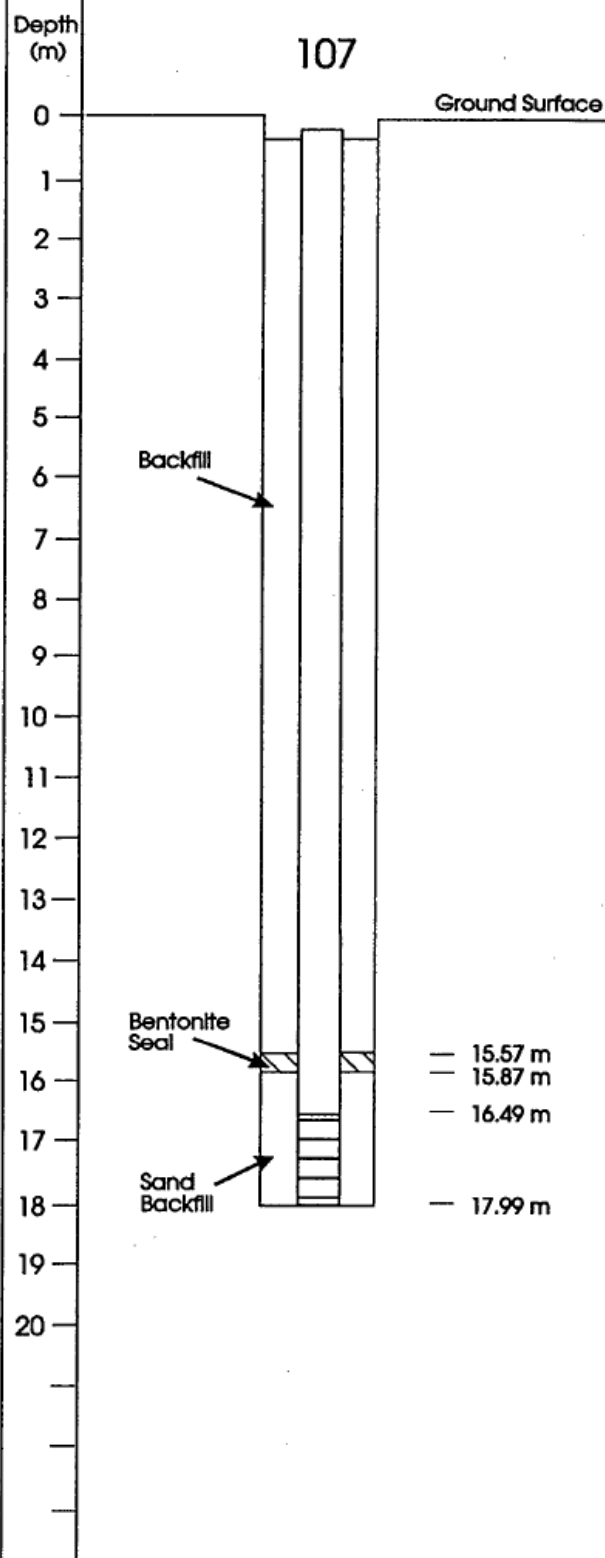
PIEZOMETER 106

Site Location: UBC Field Site, Richmond, BC
Drilling Date: 1995
Borehole Diameter: 0.17 m
Borehole Depth: 12.74 m
Well Material: PVC
Well Diameter: 0.05 m
Well Screen Length: 1.5 m
Well Depth (below grade): 12.74 m
Top of Well Elevation: 1.368 m



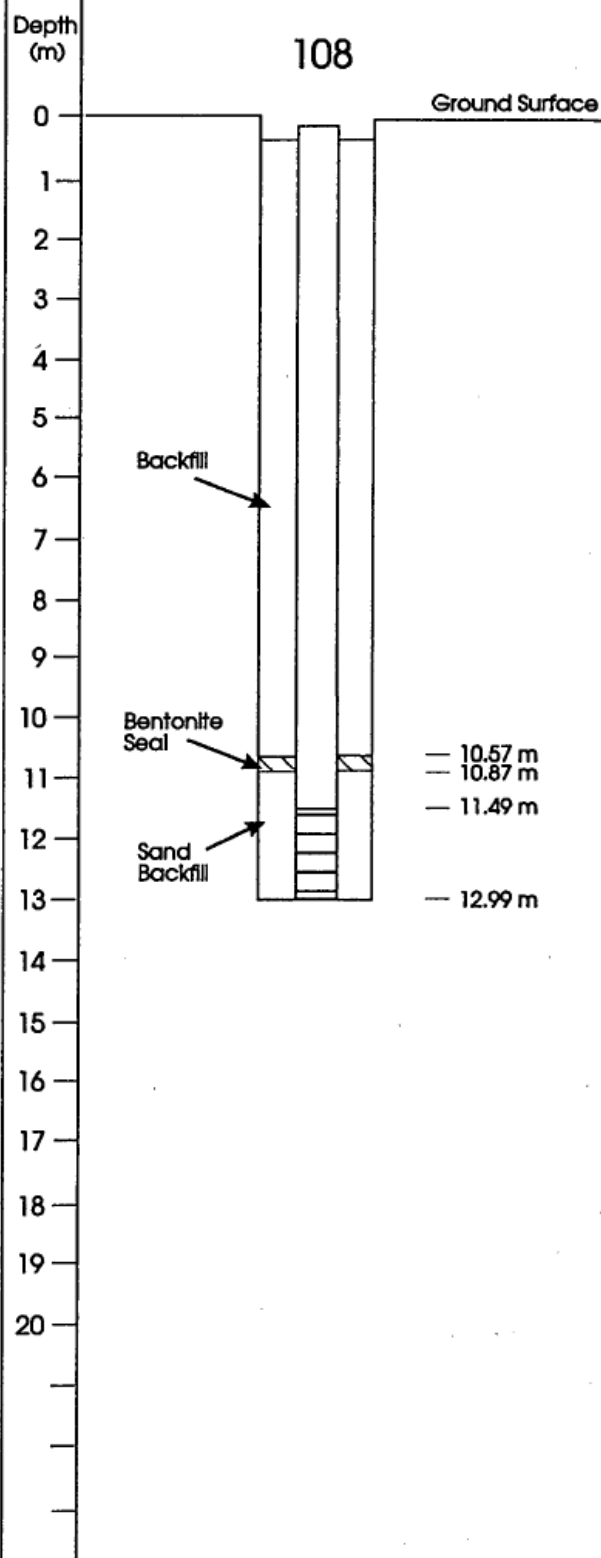
PIEZOMETER 107

Site Location: UBC Field Site, Richmond, BC
 Drilling Date: 1995
 Borehole Diameter: 0.17 m
 Borehole Depth: 17.99 m
 Well Material: PVC
 Well Diameter: 0.05 m
 Well Screen Length: 1.5 m
 Well Depth (below grade): 17.99 m
 Top of Well Elevation: 1.486 m



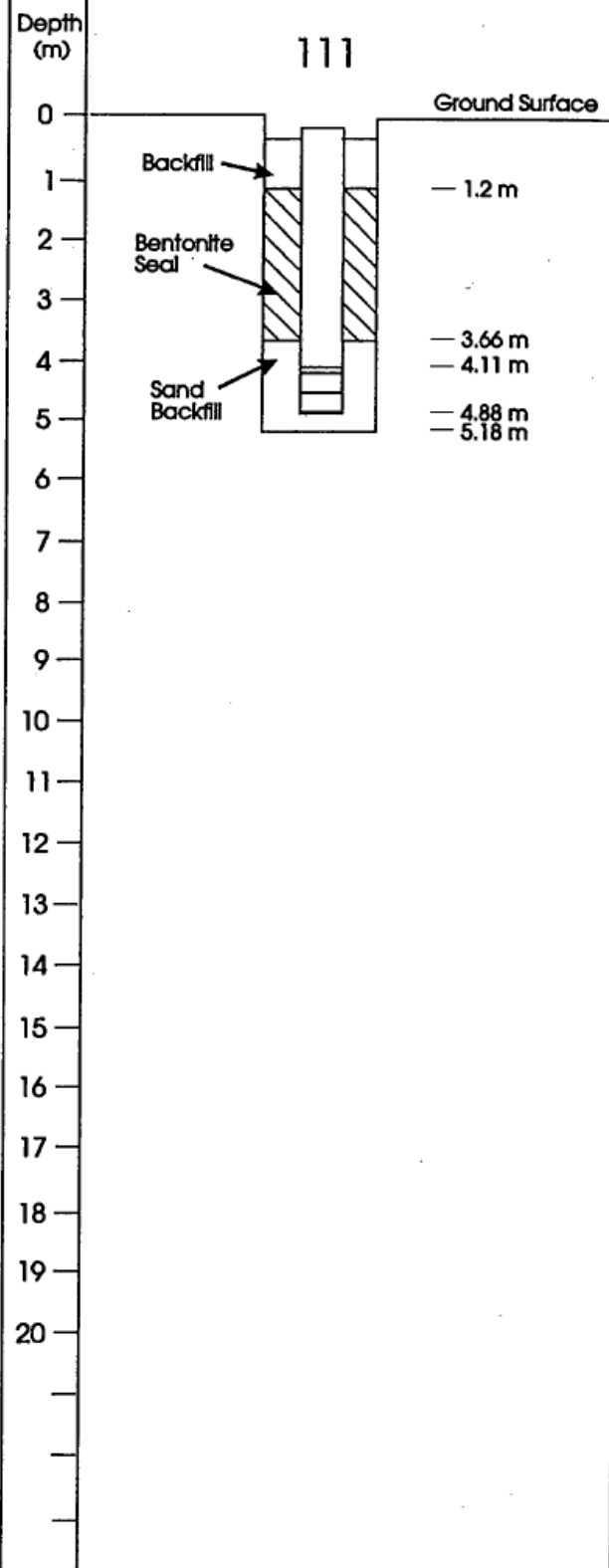
PIEZOMETER 108

Site Location: UBC Field Site, Richmond, BC
 Drilling Date: 1995
 Borehole Diameter: 0.17 m
 Borehole Depth: 12.99 m
 Well Material: PVC
 Well Diameter: 0.05 m
 Well Screen Length: 1.5 m
 Well Depth (below grade): 12.99 m
 Top of Well Elevation: 1.486 m



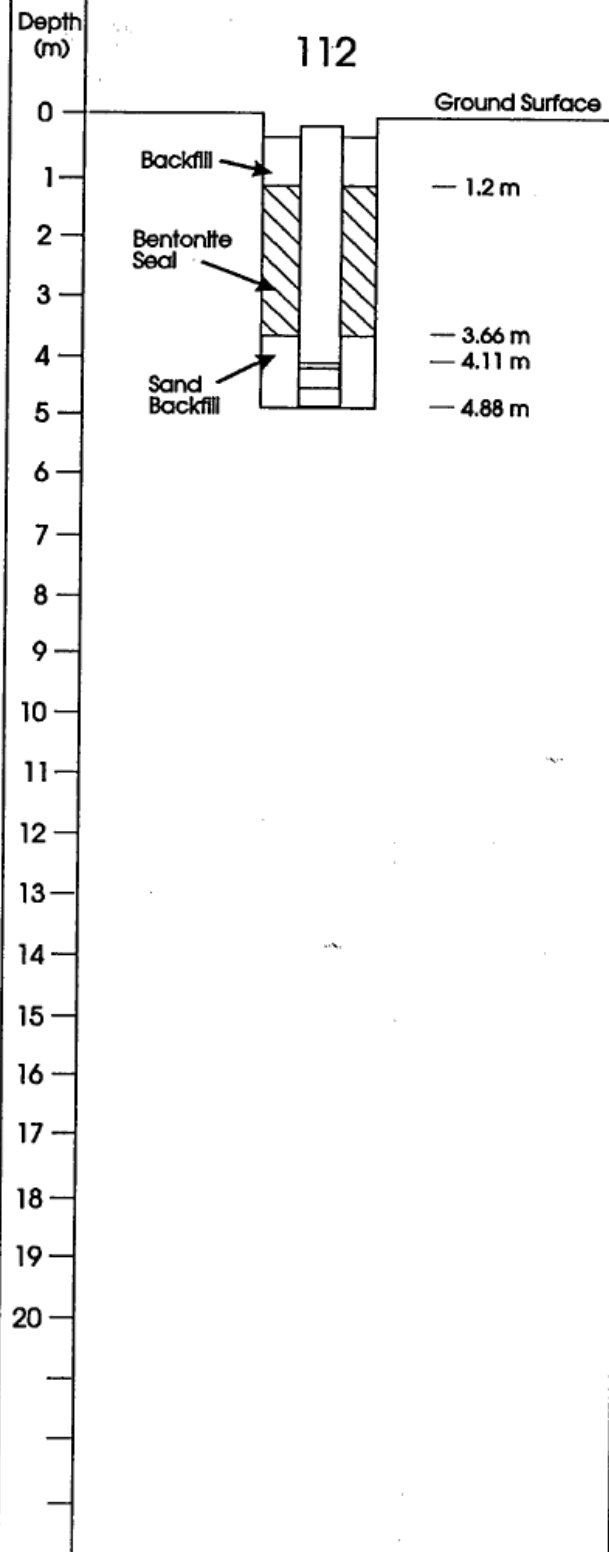
PIEZOMETER 111

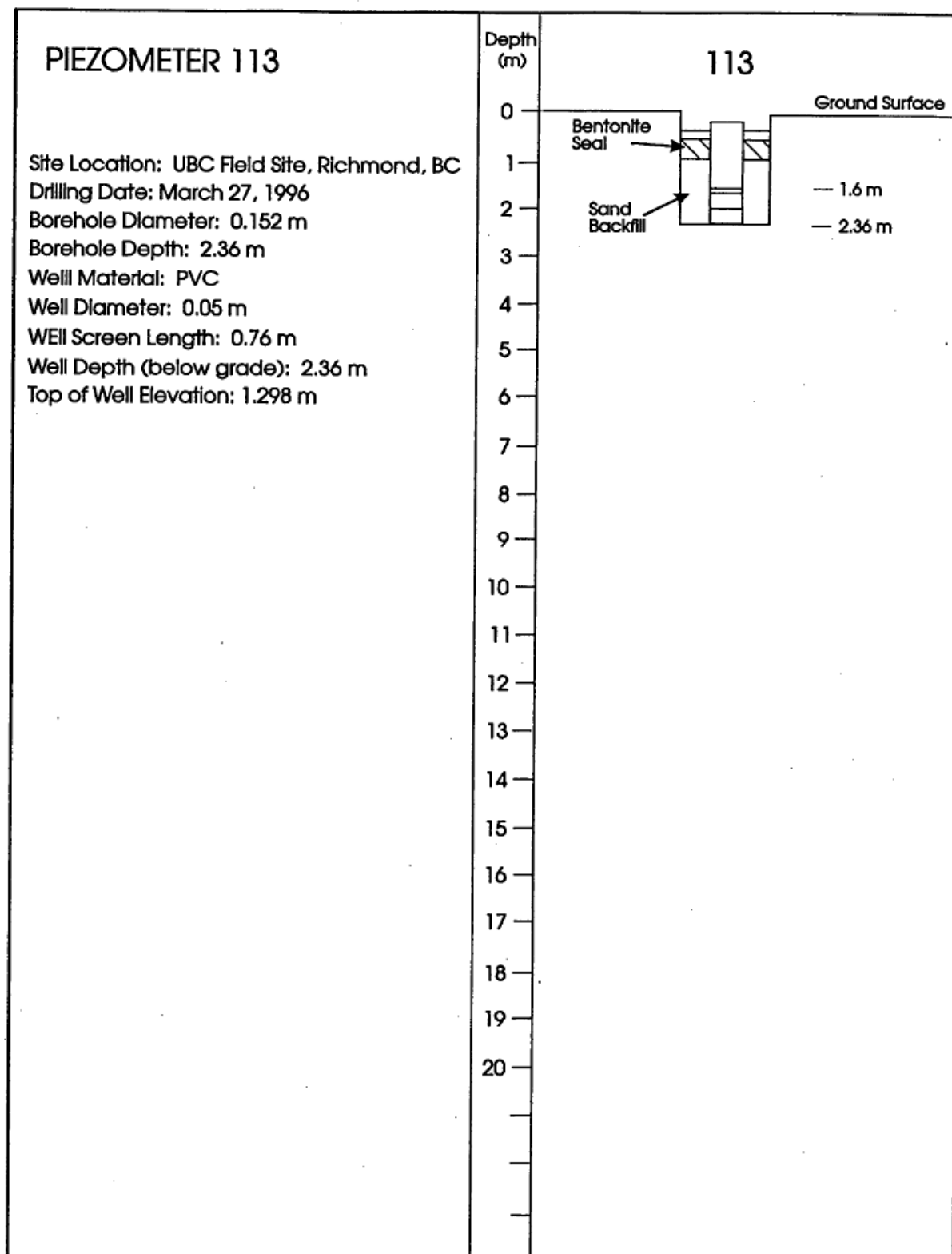
Site Location: UBC Field Site, Richmond, BC
 Drilling Date: March 27, 1996
 Borehole Diameter: 0.152 m
 Borehole Depth: 5.18 m
 Well Material: PVC
 Well Diameter: 0.05 m
 Well Screen Length: 0.76 m
 Well Depth (below grade): 4.88 m
 Top of Well Elevation: 1.286 m



PIEZOMETER 112

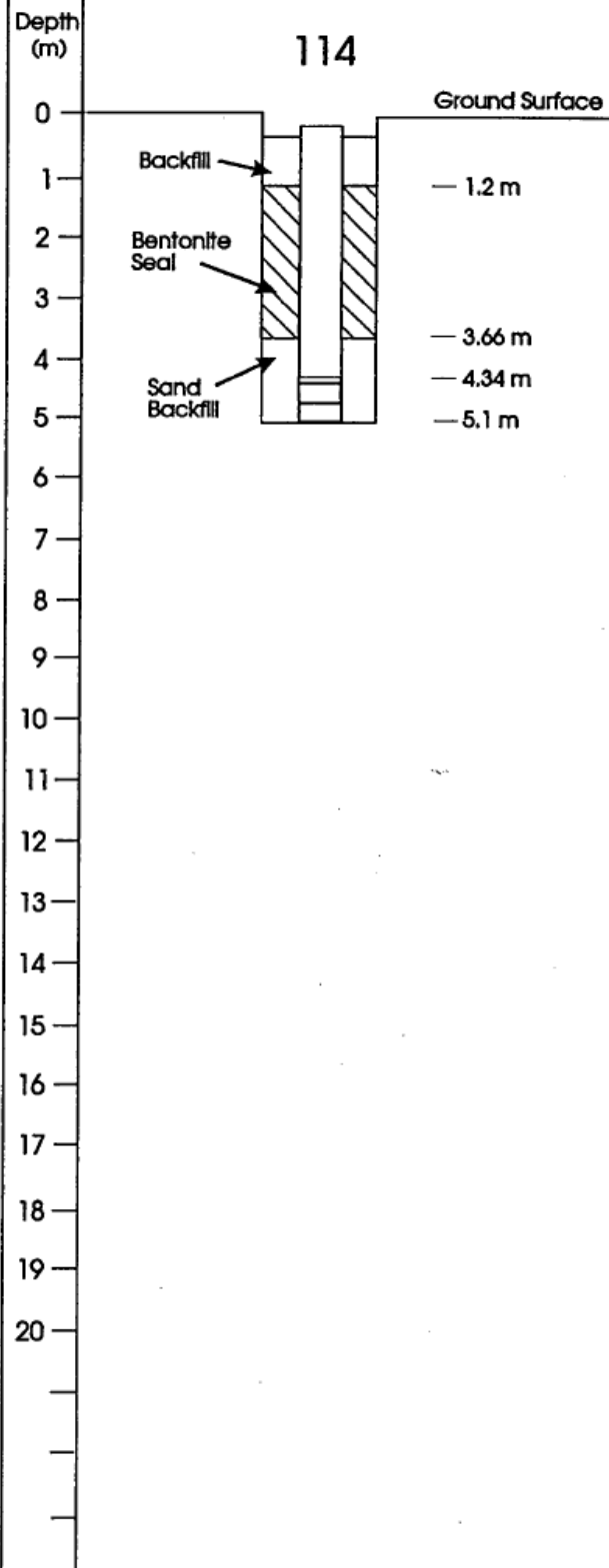
Site Location: UBC Field Site, Richmond, BC
 Drilling Date: March 27, 1996
 Borehole Diameter: 0.152 m
 Borehole Depth: 4.88 m
 Well Material: PVC
 Well Diameter: 0.05 m
 Well Screen Length: 0.76 m
 Well Depth (below grade): 4.88 m
 Top of Well Elevation: 1.326 m





PIEZOMETER 114

Site Location: UBC Field Site, Richmond, BC
 Drilling Date: March 27, 1996
 Borehole Diameter: 0.152 m
 Borehole Depth: 5.1 m
 Well Material: PVC
 Well Diameter: 0.05 m
 Well Screen Length: 0.76 m
 Well Depth (below grade): 5.1 m
 Top of Well Elevation: 1.343 m



PUMPING WELL

Site Location: UBC Field Site, Richmond, BC

Borehole Diameter: 0.25 m

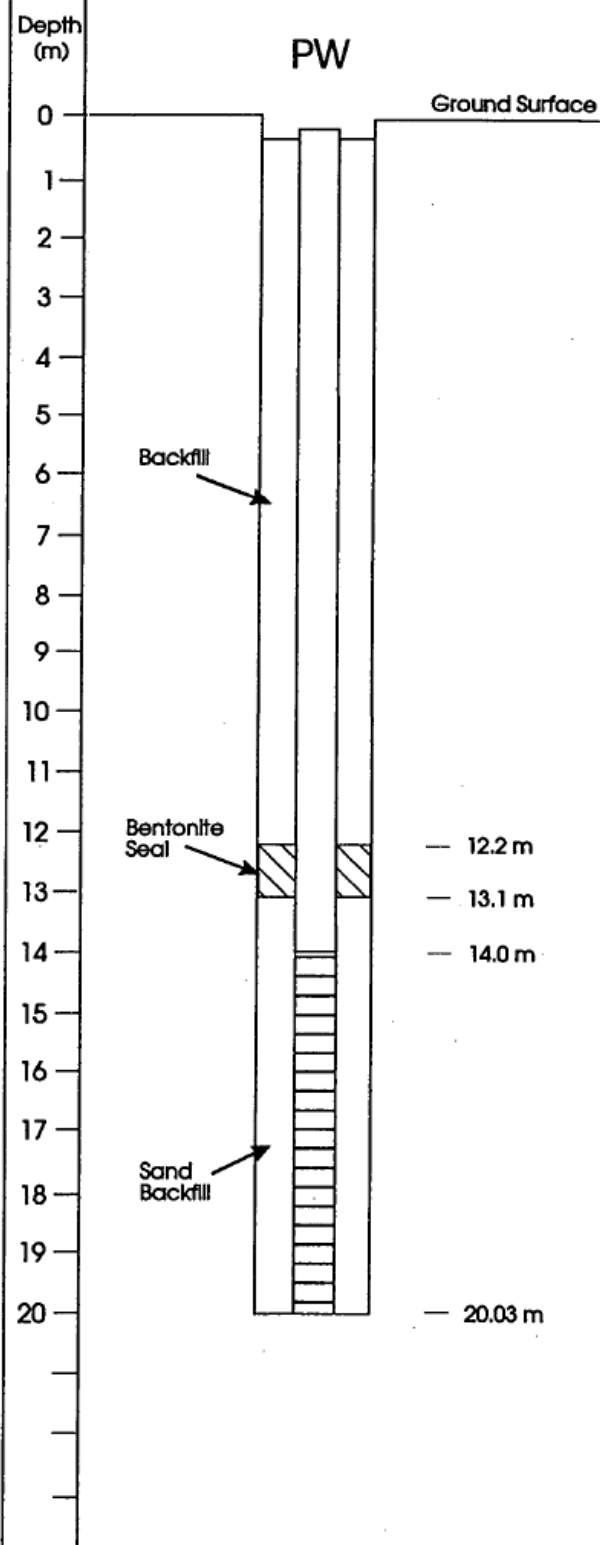
Borehole Depth: 20.03 m

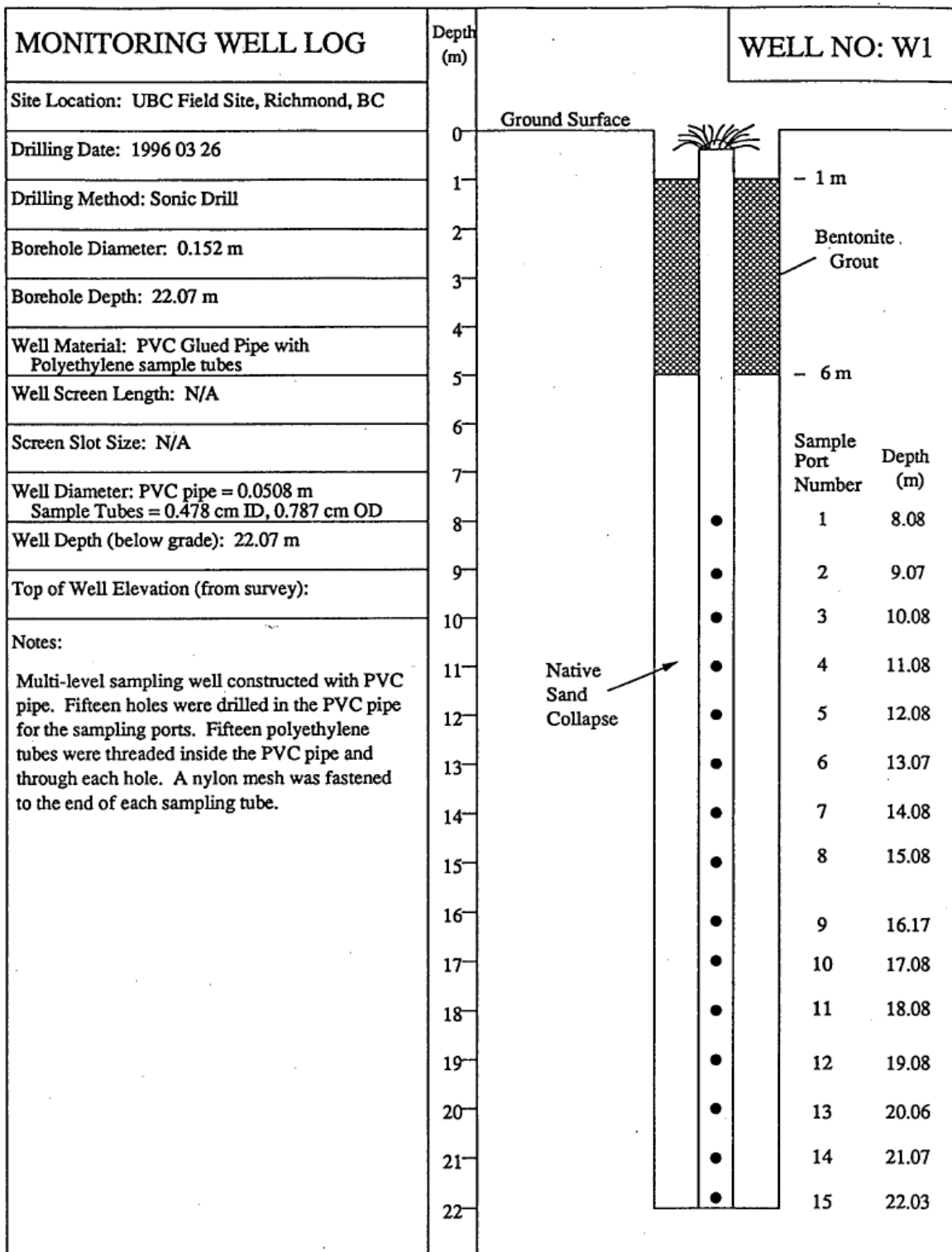
Well Material: PVC

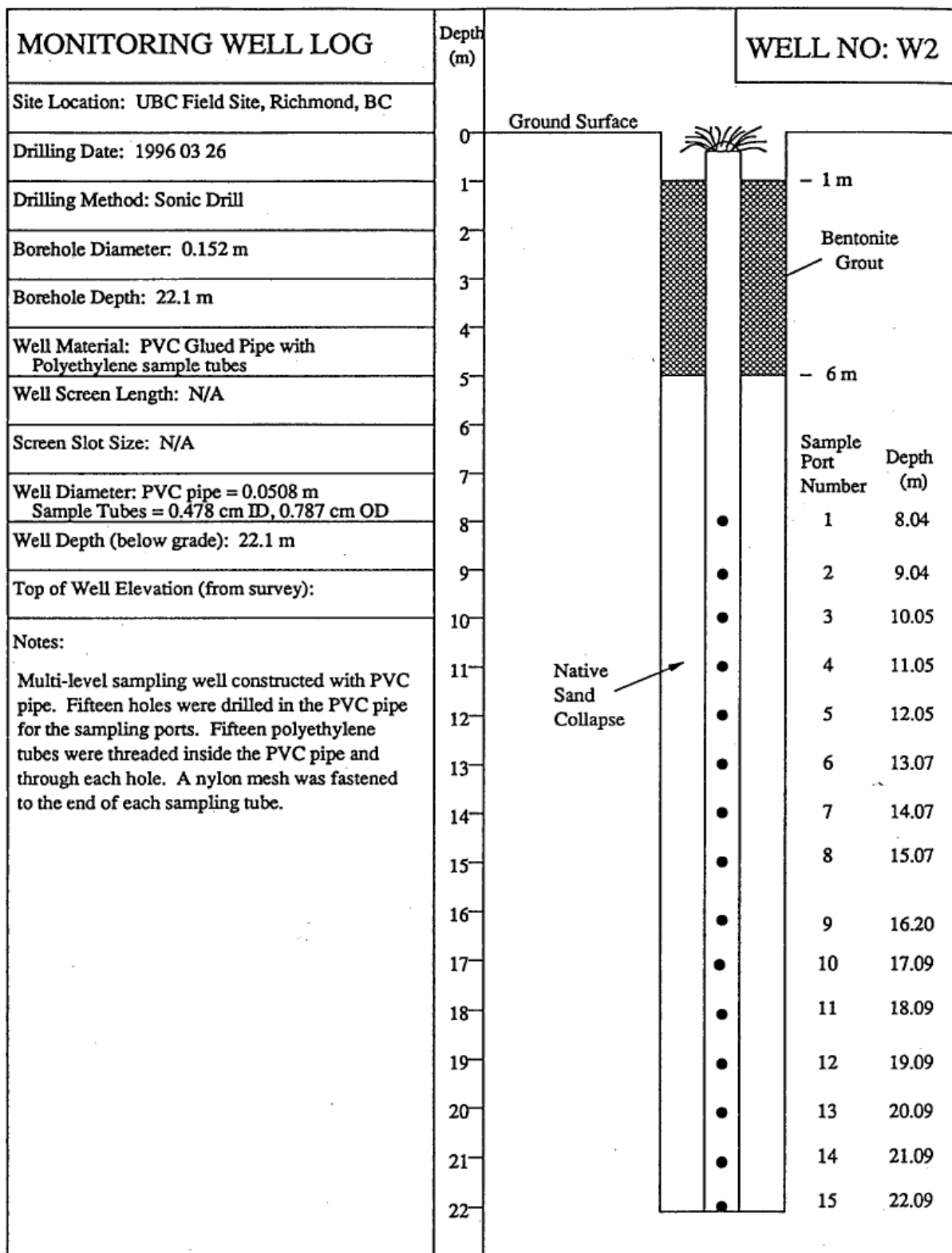
Well Diameter: 0.15 m

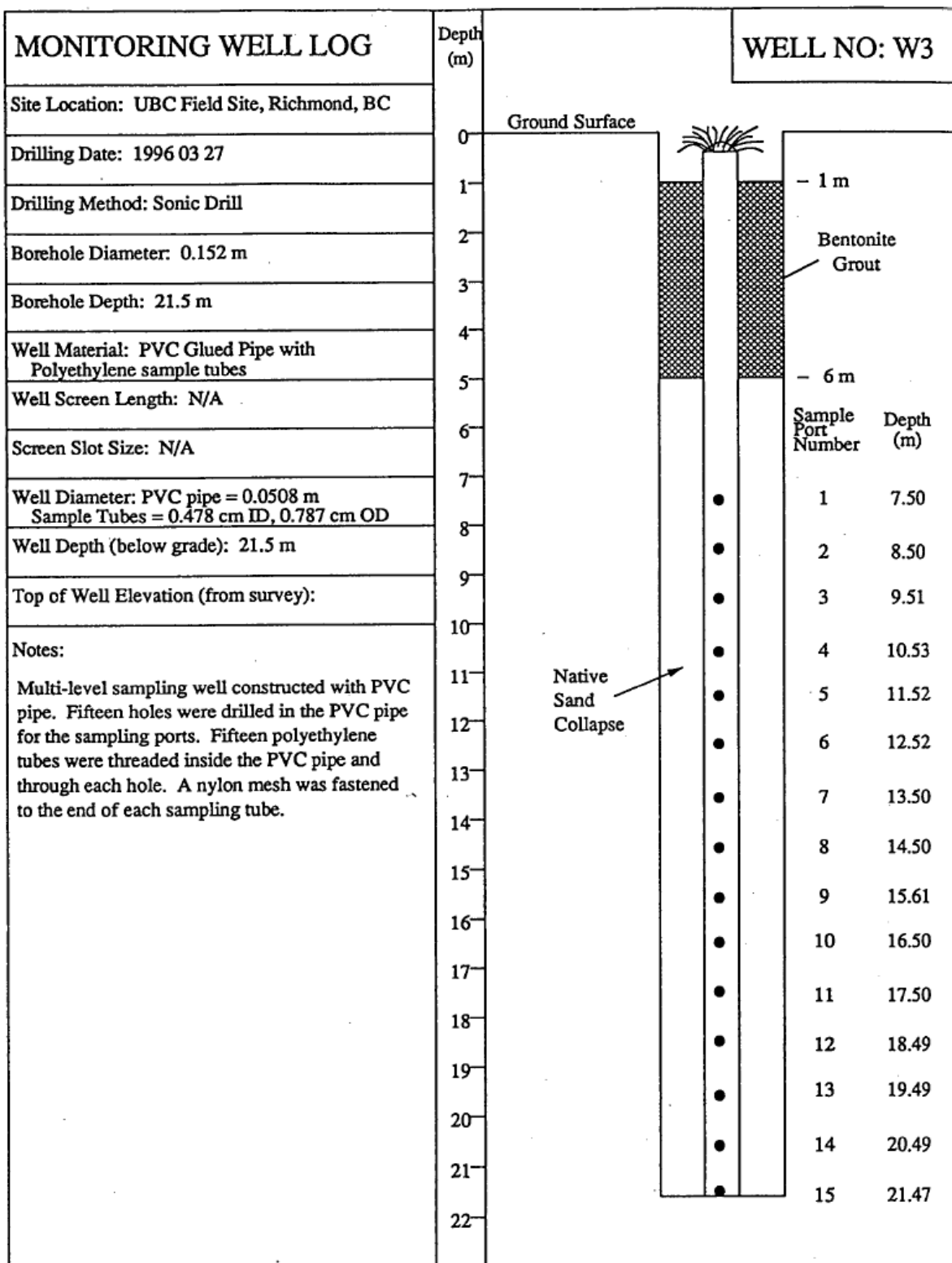
Well Screen Length: 6.03 m

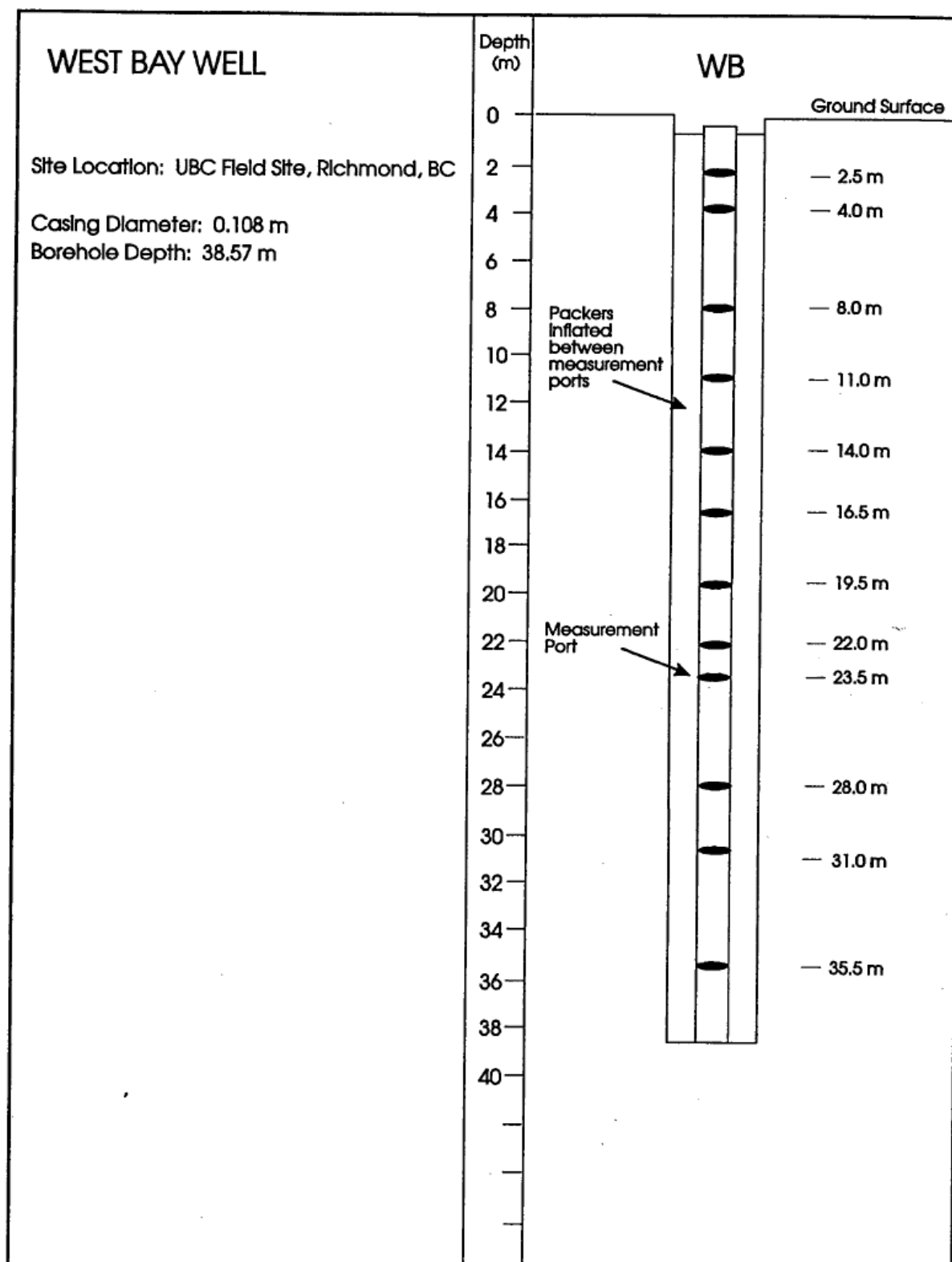
Well Depth (below grade): 20.03 m











Appendix C: Sampling Wells and Collection Date

First Sampling Date	Sampling Wells	Second Sampling Date	Sampling Wells
04/27/2012	BH101	09/27/2012	W1-1
	BH102		W1-3
	BH103		W1-6
	BH104		W1-7
	BH105		W1-8
	BH106		W1-9
	BH107		W1-10
	BH108		W1-11
	BH111		W1-12
	BH112		W1-13
	BH114		W1-14
	W1-1		W1-15
	W1-3		W2-1
	W1-6		W2-3
	W1-7		W2-10
	W1-8		W2-11
	W1-9		W2-13
	W1-10		W2-14
	W1-11		W3-1
	W1-12		W3-2
	W1-13		W3-3
	W1-14		W3-4
	W1-15		W3-5
	W2-1		W3-6
	W2-3		W3-7
	W2-10		W3-8
	W2-11		W3-9
	W2-13		W3-10
	W2-14		W3-11
	W3-1		W3-12
	W3-2		W3-13
	W3-6		W3-14
	W3-7		W3-15
	W3-12		
	W3-15		
	WB-3		
	WB-4		
	WB-5		
	WB-6		
	WB-11		
	WB-12		

Appendix D: Selected Photographs



Photo1: Vinyl glove box. SEPs were performed in vinyl glove box under anaerobic condition. To create anaerobic condition, the glove box was purged with a mixture of pure N_2 and N_2/H_2 until O_2 was below 2% in the chamber.

Appendix E: Sample Calculations for Alkalinity Titration Analysis

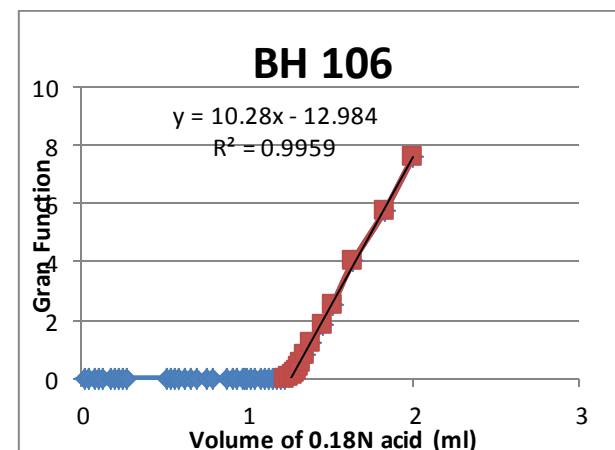
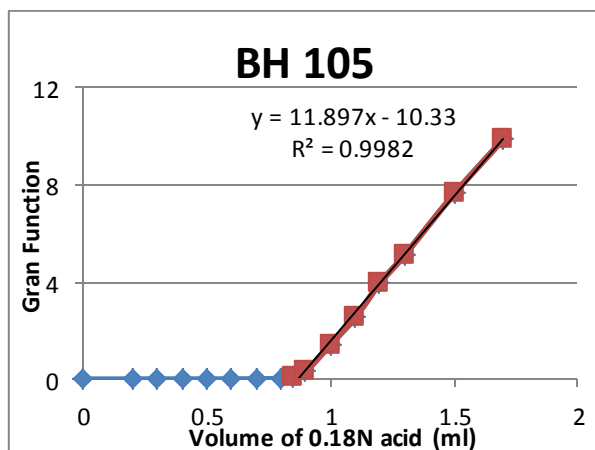
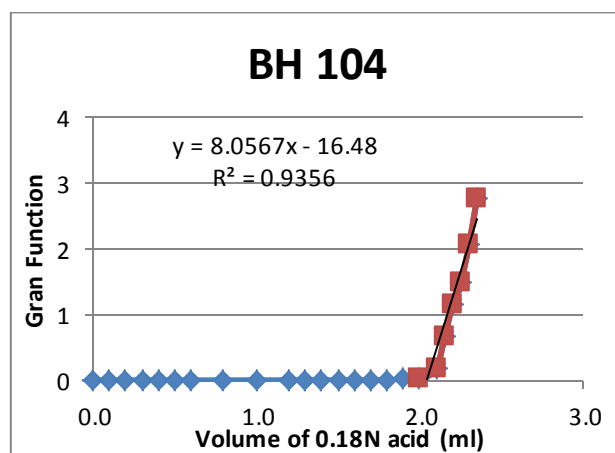
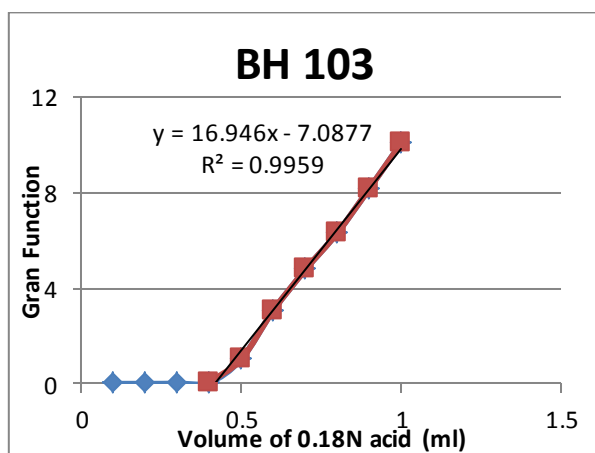
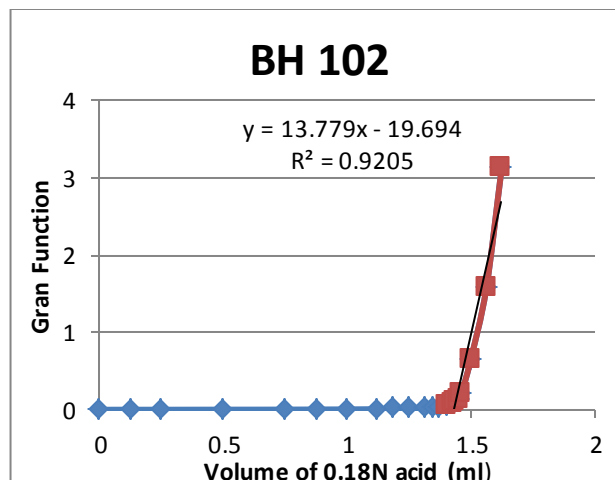
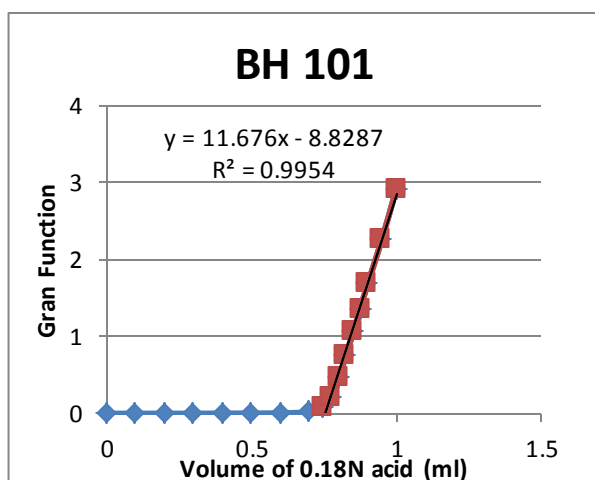
Sample ID: BH101

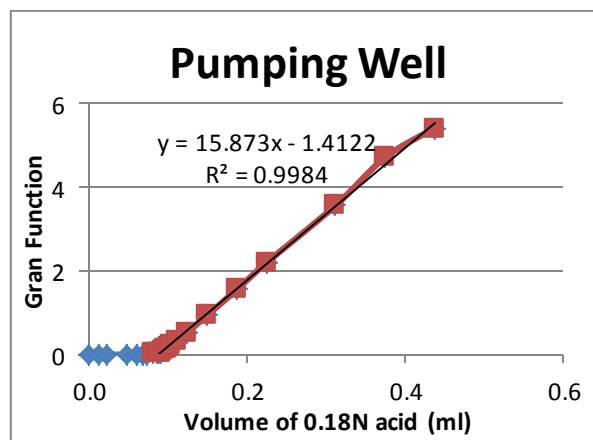
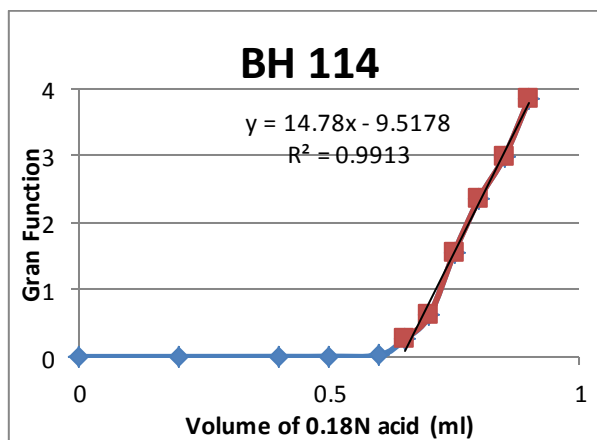
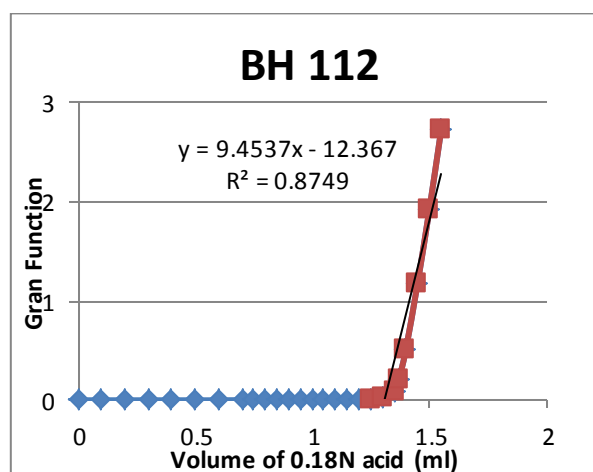
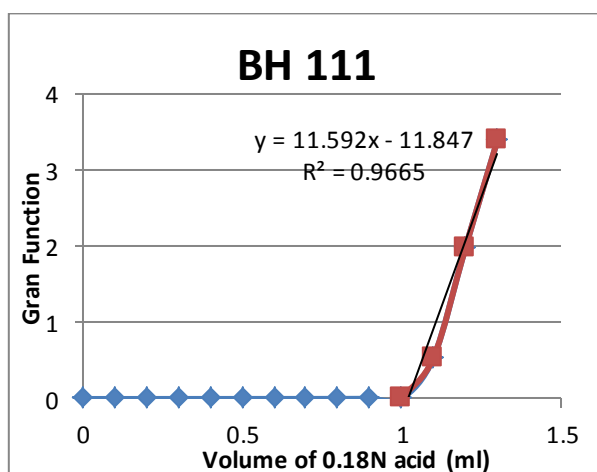
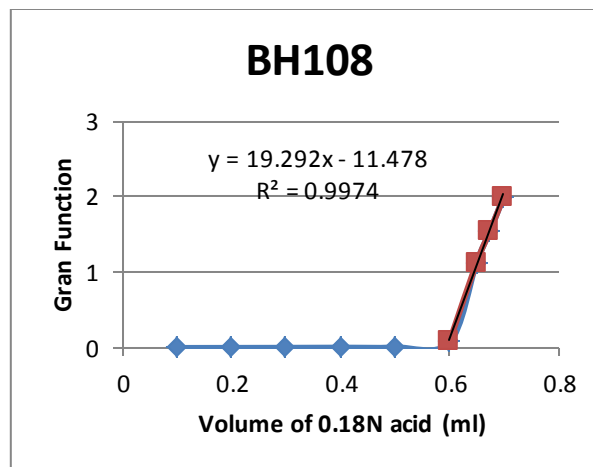
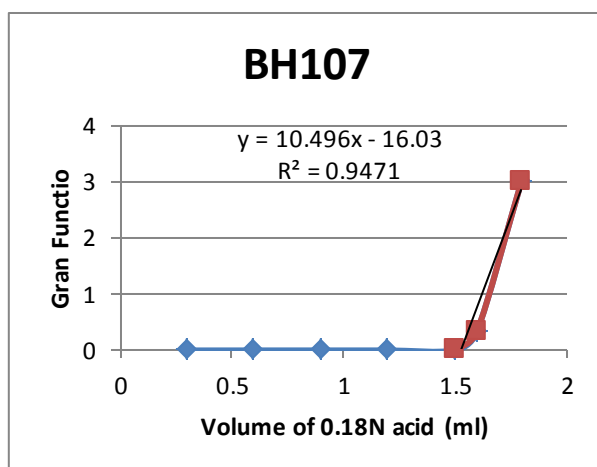
Collection date: April 27, 2012	Temperature: 12.9°C	Initial titration volume: 25ml
Equation: $y = 11.676x - 8.8287$	Interception point: 0.76ml	Molarity of H_2SO_4 : 0.1782N

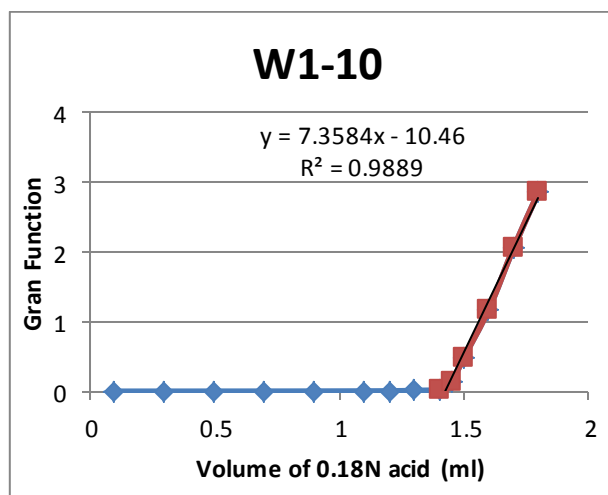
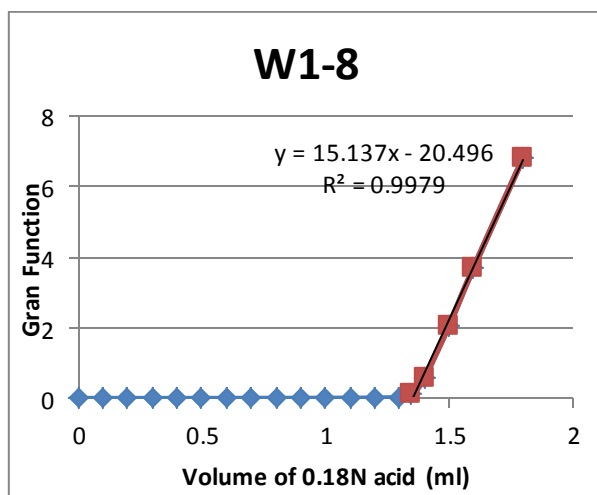
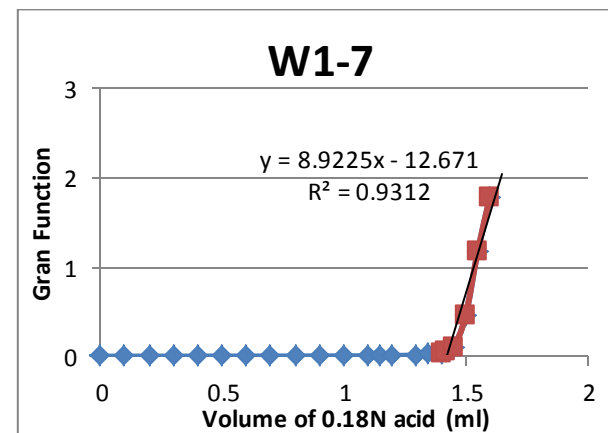
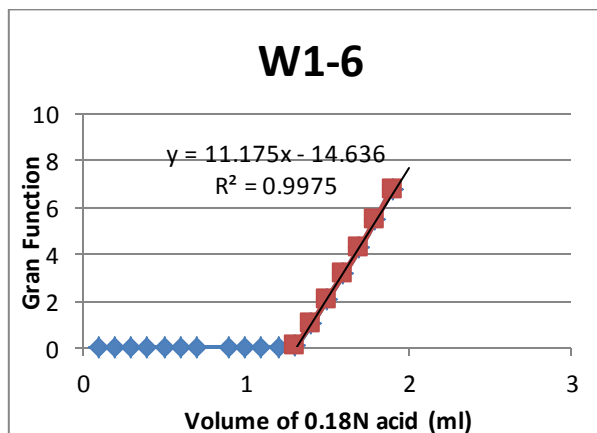
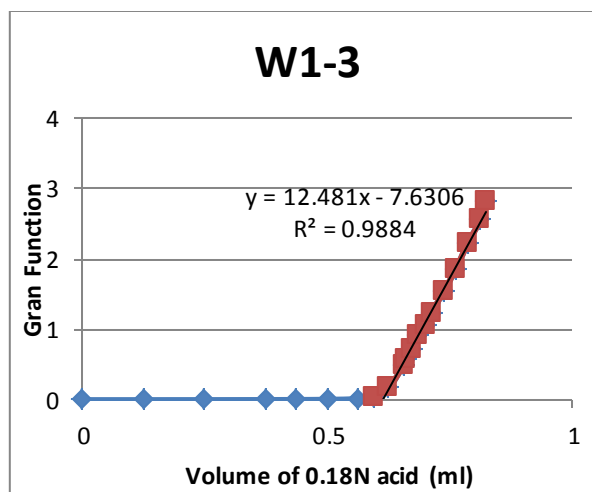
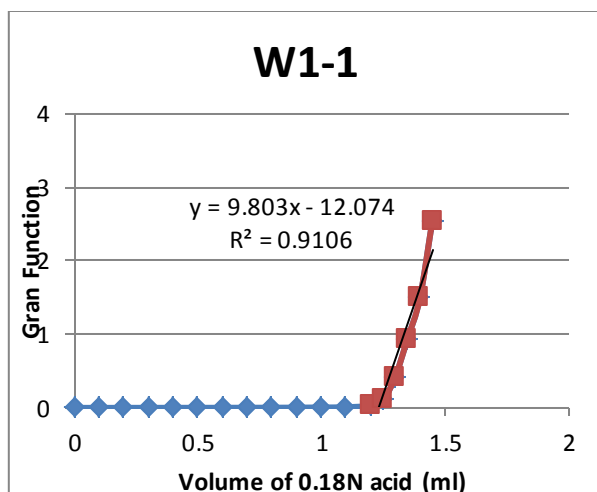
$$\text{Alkalinity} = \frac{1000 \times \text{volume at interception point} \times \text{molarity of acid}}{\text{initial volume of titration}} = \frac{1000 \times 0.76 \text{ ml} \times 0.1782 \text{ N}}{25 \text{ ml}} = 5.42 \text{ meq/L}$$

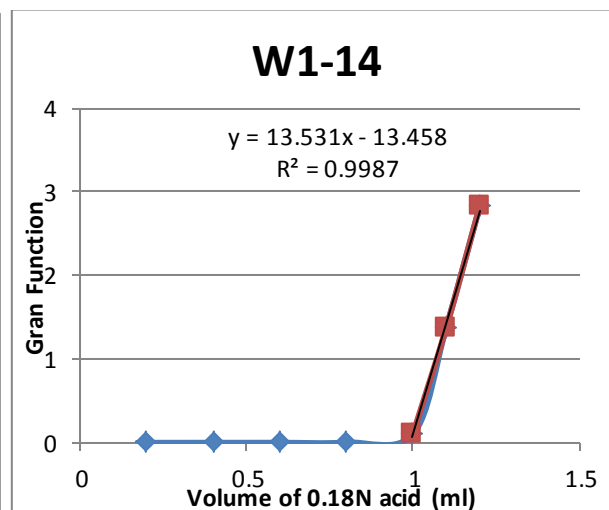
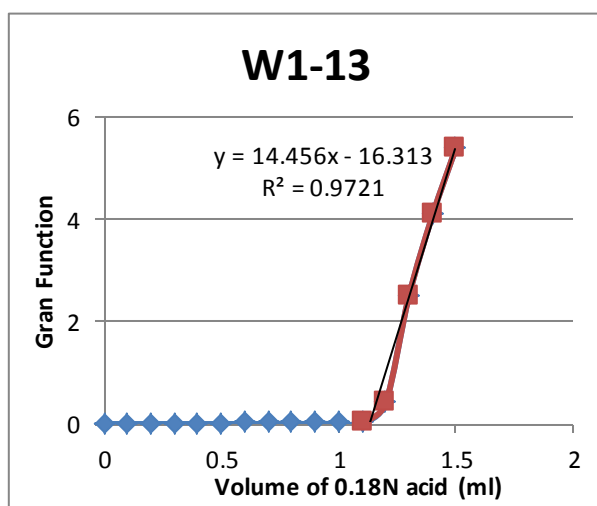
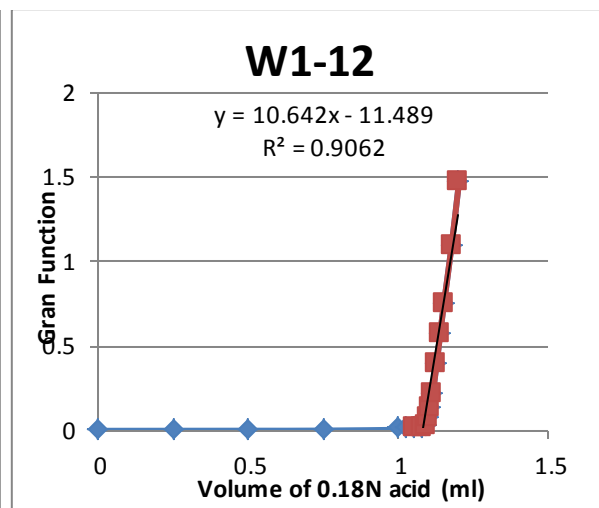
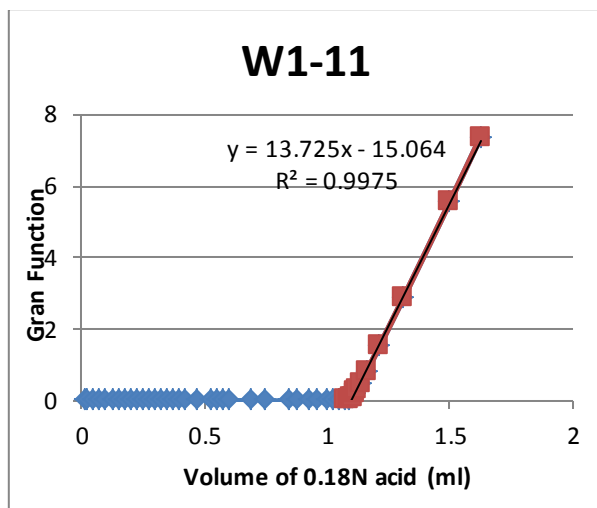
$$\text{Alkalinity as } HCO_3 = \frac{5.42 \text{ meq/L} \times 61 \text{ mg/mmol}}{1 \text{ valence}} = 331 \text{ mg/L}$$

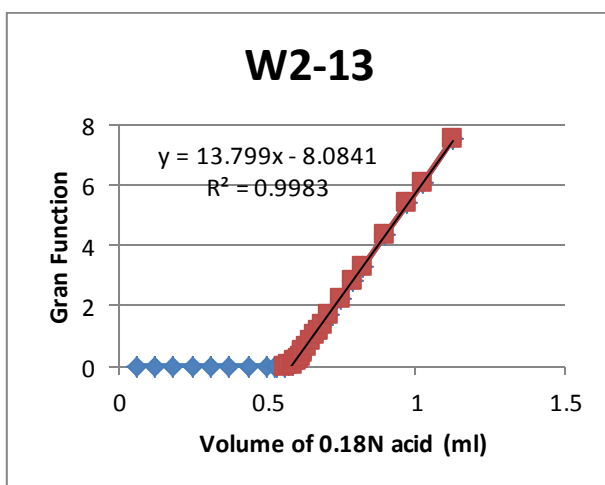
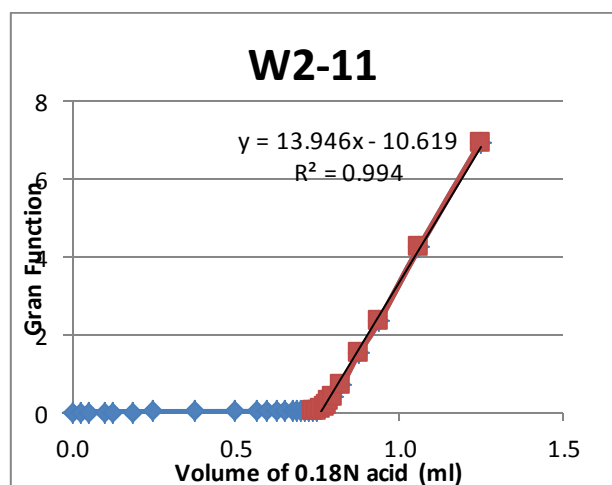
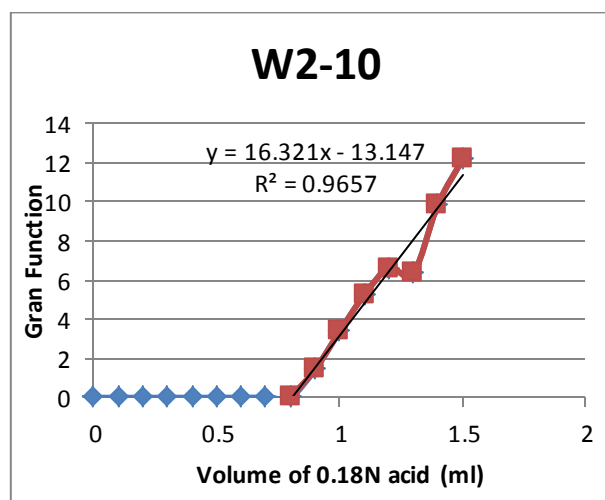
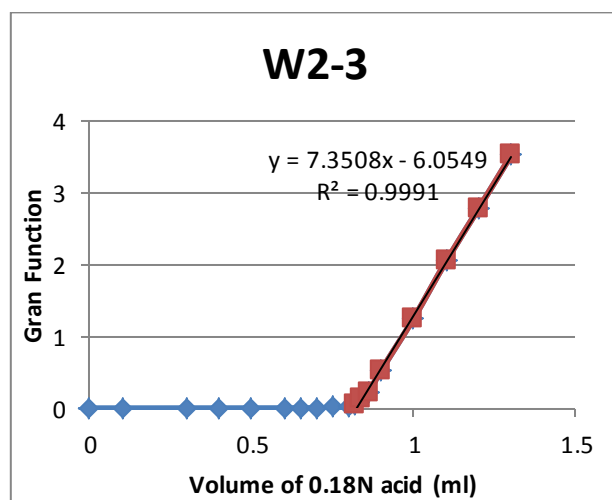
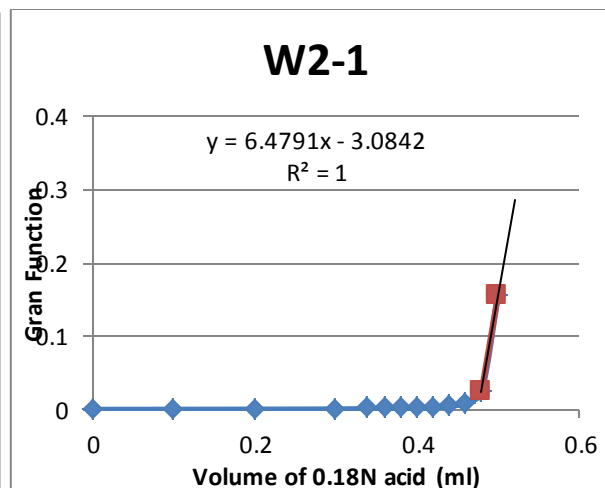
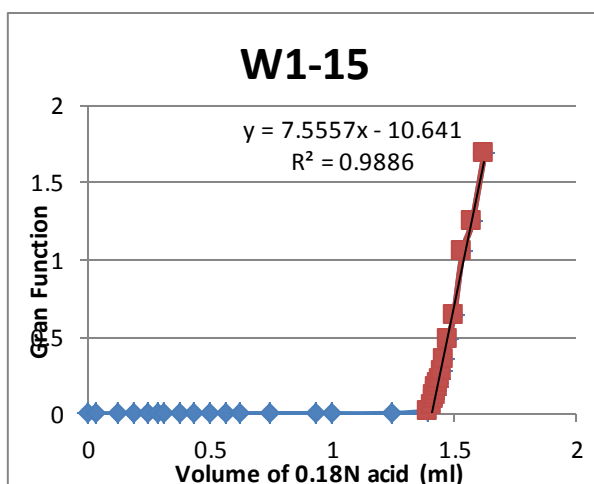
pH	Volume of acid added (mL)	Gran Function
6.92	0	0.000300566
6.62	0.1	0.000602107
6.51	0.2	0.000778754
6.39	0.3	0.001030672
6.08	0.4	0.00211268
5.88	0.5	0.003361555
5.62	0.6	0.006141012
5.12	0.7	0.019495444
4.58	0.75	0.067729401
4.09	0.775	0.209507066
3.75	0.8	0.458796088
3.54	0.825	0.744801136
3.39	0.85	1.053078018
3.28	0.875	1.357939303
3.19	0.9	1.672244453
3.06	0.95	2.260150516
2.95	1	2.917247981

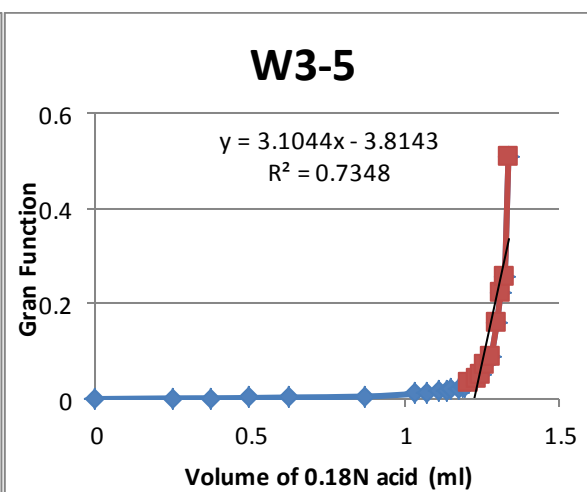
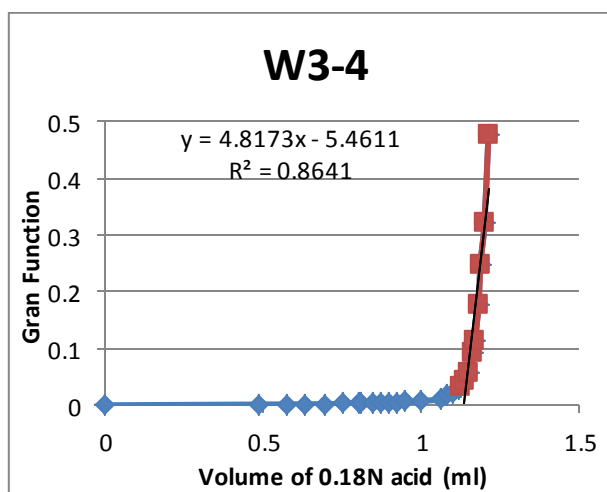
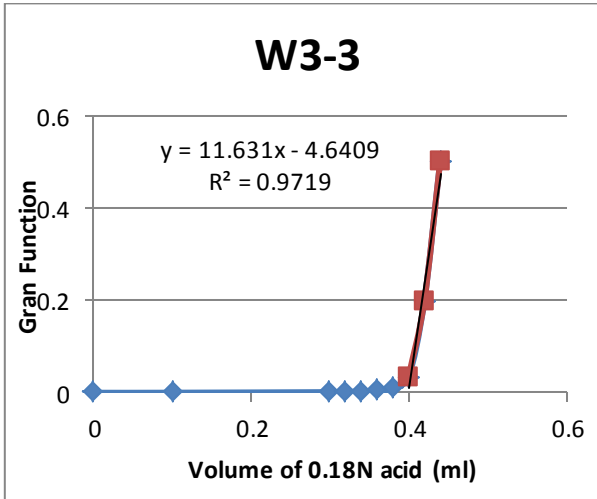
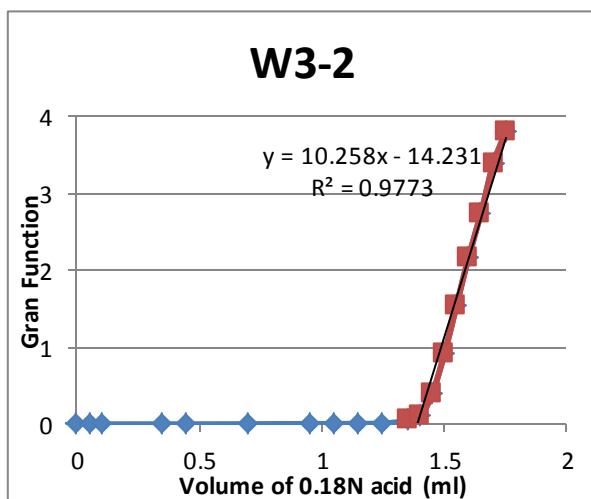
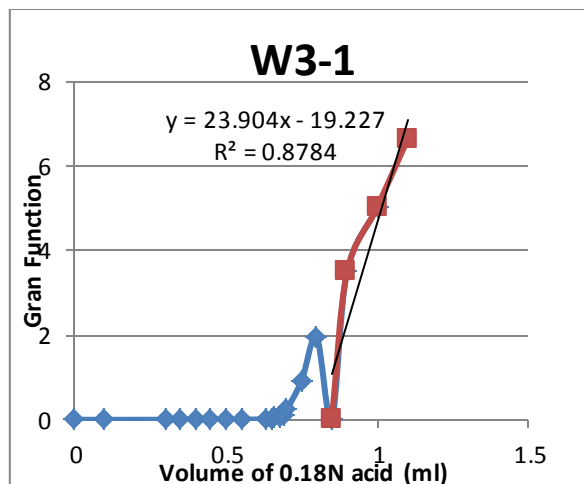
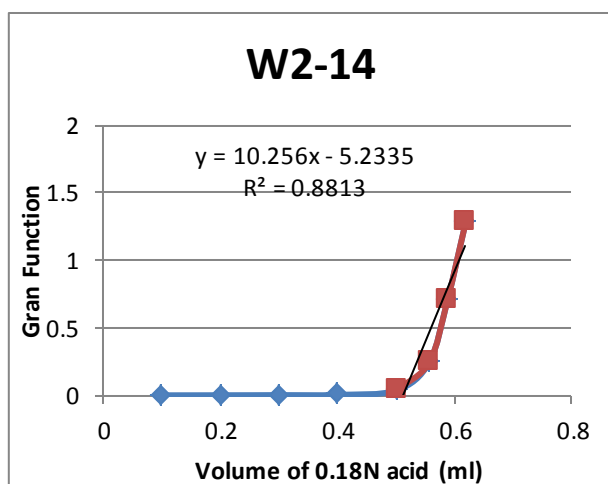


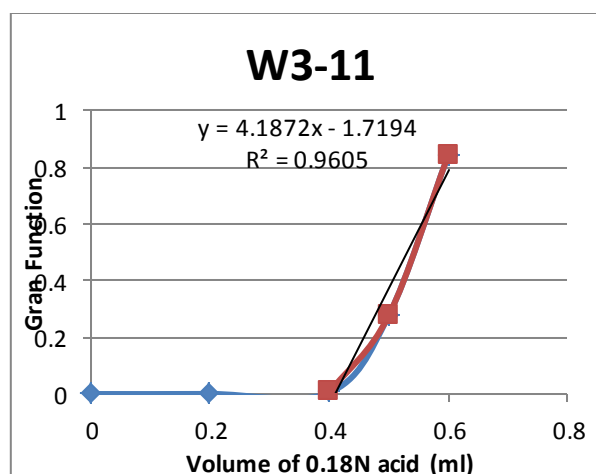
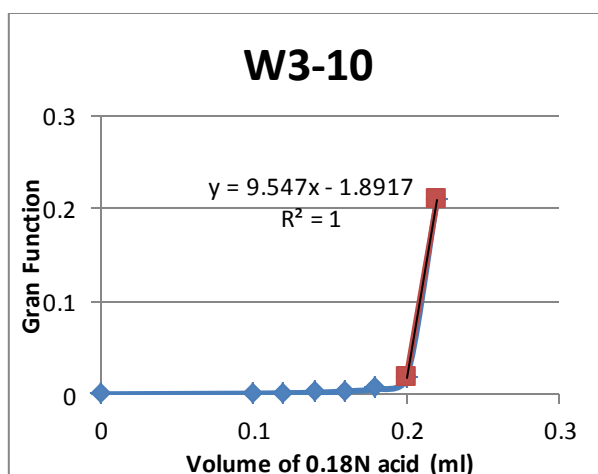
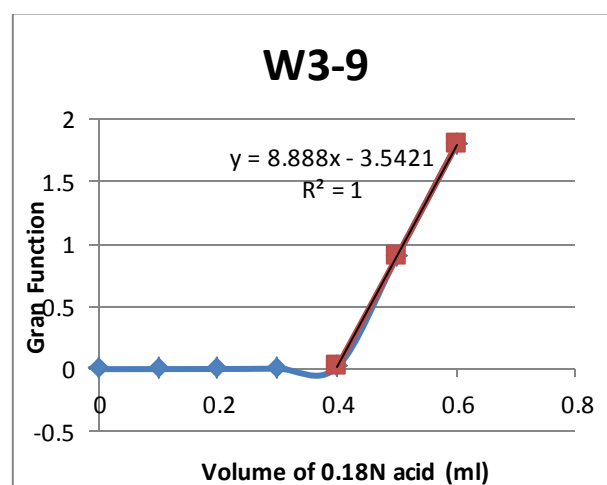
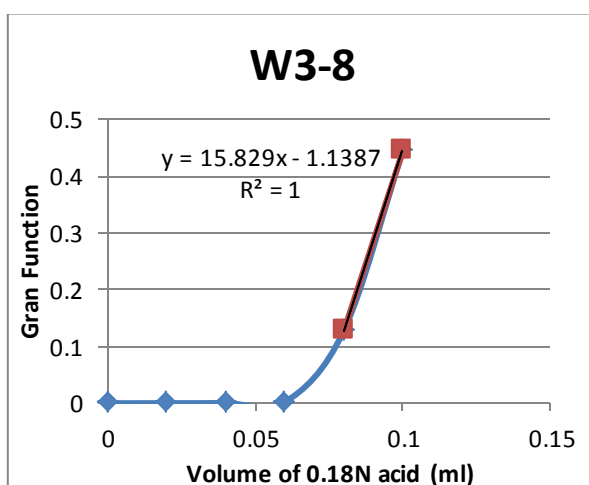
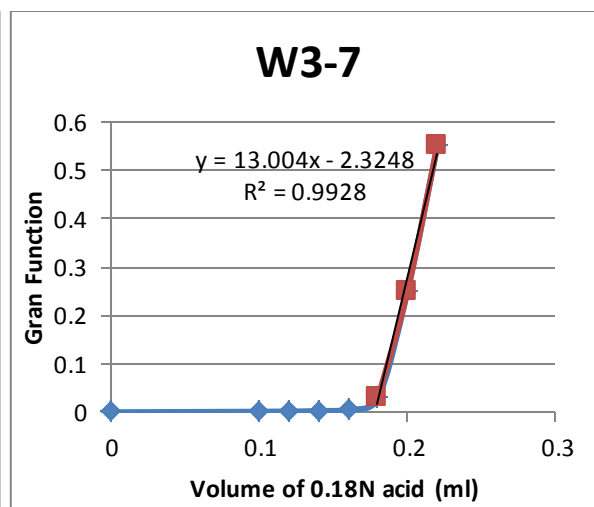
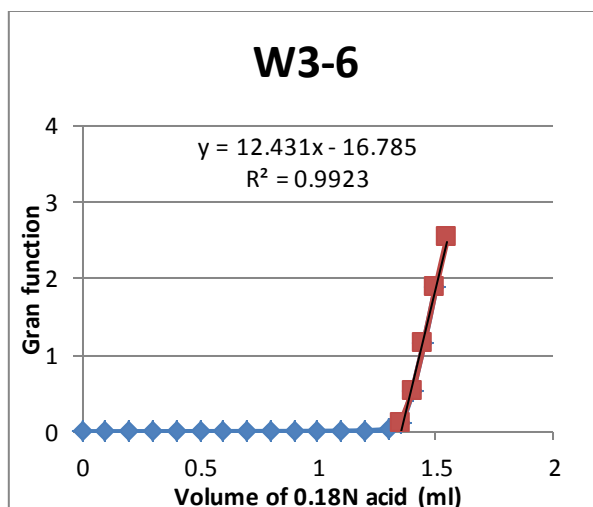


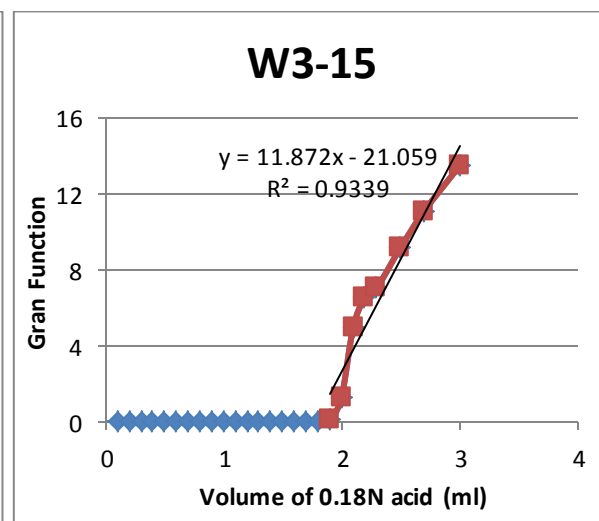
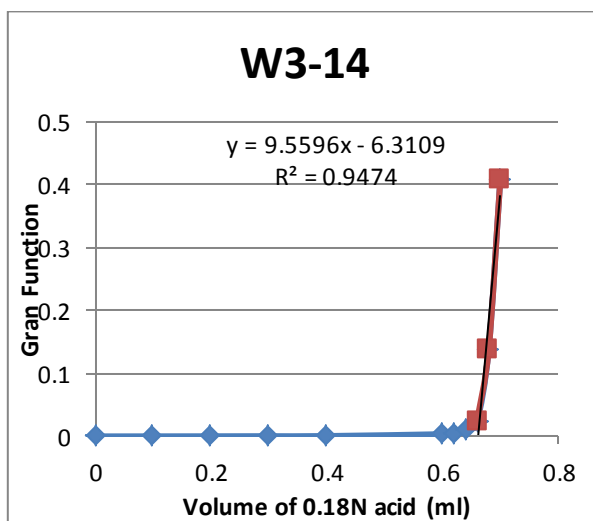
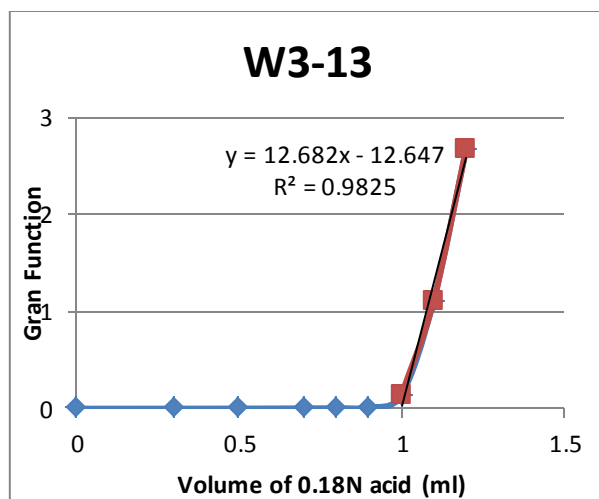
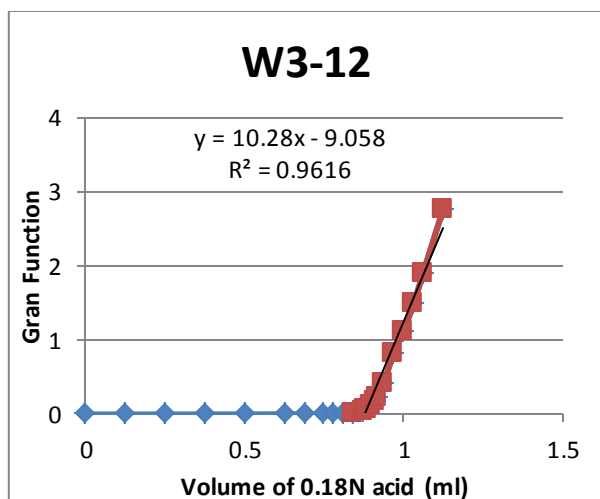












Summary of Alkalinity Result

Well No.	Alkalinity (meq/L)	Alkalinity as HCO ₃ (mg/L)
BH101	5.42	330.62
BH102	10.19	621.59
BH103	2.79	170.19
BH104	14.3	872.3
BH105	5.91	360.51
BH106	10.1	616.1
BH107	10.89	664.29
BH108	4.24	258.64
BH111	8.84	539.24
BH112	9.32	568.52
BH114	4.45	271.45
W1-1	0.59	35.99
W1-3	8.78	535.58
W1-6	3.76	229.36
W1-7	8.95	545.95
W1-8	10.07	614.27
W1-9	10.27	626.47
W1-10	10.44	636.84
W1-11	10.37	632.57
W1-12	8.78	535.58
W1-13	8.64	527.04
W1-14	9.02	550.22
W1-15	6.37	388.57
W2-1	9.01	549.61
W2-3	7.12	434.32
W2-10	5.17	315.37
W2-11	4.95	301.95
W2-13	4.74	289.14
W2-14	4.69	286.09
W3-1	7.17	437.37
W3-2	8.11	494.71
W3-3	7.01	427.61
W3-4	6.93	422.73
W3-5	8.16	497.76
W3-6	9.62	586.82
W3-7	3.91	238.51
W3-8	10.27	626.47
W3-9	3.50	213.5
W3-10	3.48	212.28
W3-11	7.21	439.81
W3-12	5.20	317.2
W3-13	8.76	534.36
W3-14	11.59	706.99
W3-15	14.57	888.77

Appendix F: Sample Calculation for Methane Concentration Conversion

Based on Henry's law:

$$C_{aq} = \frac{C_{gas}}{KH}$$

Where C_{gas} is the vapor concentration (ppm) present in the headspace, C_{aq} is the aqueous phase concentration of methane in solution (ppm) and H is Henry's law constant at a particular temperature (dimensionless).

$K_H(T) = K_H^\circ \exp\left(\frac{d(\ln(KH))}{d(1/T)} \times \left(\frac{1}{T} - \frac{1}{298.15K}\right)\right)$, K_H is calculated based on the literature method (Lide and Frederikse, 1995)

Where K_H° is Henry's Law constant at 298.15K ((mol/kg*bar), and $K_H^\circ = 0.0014$ (mol/kg*bar); $d(\ln(KH))/d(1/T)$ is temperature dependence constant (K), and $d(\ln(KH))/d(1/T) = 1600$

By assuming groundwater temperature of 10°C, and groundwater density is 1g/cm³,

$$\begin{aligned} K_H^\circ (10^\circ\text{C}) &= 0.0014 \text{ mol/kg*bar} \times \exp\left(\frac{d(\ln(KH))}{d(1/T)} \times \left(\frac{1}{T} - \frac{1}{298.15K}\right)\right) \\ &= 0.0014 \text{ mol/kg} * \text{bar} \times \exp\left(1600 \times \left(\frac{1}{283.15} - \frac{1}{298.15}\right)\right) \\ &= 0.00186 \text{ mol/kg*bar} \\ &= 0.00186 \text{ mol/kg*bar} \times \frac{1 \text{ bar}}{0.9869 \text{ atm}} \\ &= 0.00188 \text{ mol/kg*atm} \\ &= 530.49 \text{ kg*atm/mol} \end{aligned}$$

$$= \frac{530.49 \text{ kg} \cdot \text{atm} / \text{mol}}{0.08205 \text{ atm} \cdot \text{L} / (\text{mol} \cdot \text{K}) \times 283.15 \text{ K}} = 22.83$$

For example, if the gas concentration of methane at headspace is 600 ppm, its equilibrium aqueous concentration at a temperature of 10°C can be calculated as:

$$C_{\text{aq}} = \frac{C_{\text{gas}}}{KH} = \frac{600}{22.83} = 26.27 \text{ ppm}$$

Appendix G: Sulfate Reduction Rate

Based on the mass balance, sulfate-reduction rate can be obtained from the rate of depletion of sulfate along the flow path connecting the two observation wells W1 and W3. Since sulfate concentration is decreased also by dilution at both upper and lower mixing zones, the amount of dilution were calculated by PHREEQC simulation.

	Lower mixing zone			Upper mixing zone		
	Distance (m)	Modeled SO_4^{2-} (mg/L)	Measured SO_4^{2-} (mg/L)	Distance (m)	Modeled SO_4^{2-} (mg/L)	Measured SO_4^{2-} (mg/L)
W1	465	927	410	535	877	504
W3	300	1056	678	700	720	407

Sulfate reduction at lower mixing zone:

Δ distance between W1 and W3 = 465m – 300m =165m

$$\text{Travel time} = \frac{165\text{m}}{4.2\text{m/y}} = 39.2 \text{ y}$$

ΔSO_4 concentration by dilution = 1056 – 927 = 129 mg/L

Δ measured SO_4 concentration (dilution + sulfate reduction) = 678 – 410 = 268mg/L

ΔSO_4 (sulfate reduction) = 268 – 129 = 139mg/L = 1.45 mmol/L

$$\text{Sulfate reduction rate (K}_{\text{lower}}) = \frac{1.45\text{mmol/L}}{39.2\text{y}} = 0.036 \text{ mmol/L}\cdot\text{yr}$$

Sulfate reduction at upper mixing zone:

Δ distance between W1 and W3 = 700m – 535m = 165m

Travel time = $\frac{165m}{4.2m/y} = 39.2 \text{ y}$

ΔSO_4 concentration by dilution = 877 – 720 = 157 mg/L

Δ measured SO_4 concentration (dilution + sulfate reduction) = 504 – 407 = 97mg/L

ΔSO_4 (sulfate reduction) = 157 – 97 = 60mg/L = 0.62 mmol/L

Sulfate reduction rate (K_{upper}) = $\frac{0.62mmol/L}{39.2y} = 0.016 \text{ mmol/L}\cdot\text{yr}$

Appendix H: Phreeqc Simulation Input

Scenario 1: Iron and Manganese Reduction

SOLUTION 0 mario's water boundary condition

temp 10
pH 7.15
pe -4
redox pe
units mg/l
density 1
Ca 247
K 155
Mg 630
Na 4850
S(6) 1310 as SO4
Cl 10100 charge
Alkalinity 86 as HCO3-
Fe 7.43
-water 1 # kg

SOLUTION 1-100 initial condition

temp 11
pH 6.56
pe -4
redox pe
units mg/l
density 1
Alkalinity 469 as HCO3-
Ca 33
Cl 121
K 4.4
Mg 40
Na 139
S(6) 33.43
Fe 63.24
Mn 0.86
-water 1 # kg

REACTION 1-50 continously adding lower fresh water WB-31m

H2O 1
HCO3 0.0002
Cl 4.7e-005
Ca 4.01e-006
Mg 8.65e-006
SO4 5.53e-006
Fe 3.5e-006
Si 1.43e-005
0.50 moles in 1 steps

REACTION 51-100 continuously adding upper fresh water BH114

H2O 1
HCO3 8.01e-005

```

Cl      2.63e-005
Ca      1.1e-005
Mg      3.65e-005
K       1.17e-007
SO4     6.06e-006
Fe      8.41e-006
Si      4.95e-005
1.20 moles in 1 steps
END

```

```

SOLUTION_MASTER_SPECIES
Om      Om      0      CH2O      30

```

```

SOLUTION_SPECIES
Om = Om
log_k    0

```

```

PHASES
foc
Om = Om
log_k    0

```

```

RATES
foc
-start
10 if (M<=0) THEN GOTO 50
20 k_foc=2.0e-12
30 rate = k_foc
40 moles = rate * time
50 SAVE moles
-end

```

```

ferrihydrite
-start
10 if (M<=0) THEN GOTO 210
20 k_ferri=5.5e-10
30 rate = k_ferri* mol("Om")
200 moles = rate * time
210 SAVE moles
-end

```

```

MnO2
-start
10 if (M<=0) THEN GOTO 50
20 k_MnO2=1.0e-11
30 rate = k_MnO2* mol("Om")
40 moles = rate * time
50 SAVE moles
-end

```

```

KINETICS 1-100
foc
-formula Om 1
-m      10
-m0     10
-tol    1e-008
ferrihydrite

```

```

    -formula  Om  -0.25 H+  -1.75 HCO3-  0.25 Fe+2  1 H2O  2.5
    -m        1
    -m0       1
    -tol      1e-008
MnO2
    -formula  Om  -0.5 H+  -1.5 Mn+2  1 H2O  1 HCO3-  0.5
    -m        1
    -m0       1
    -tol      1e-008
    -steps    1
    -step_divide 1
    -runge_kutta 3
    -bad_step_max 500

TRANSPORT
    -cells            100
    -shifts           2000
    -time_step        78840000 1 # seconds
    -lengths          100*10
    -diffusion_coefficient 7e-010
    -thermal_diffusion 2 0
    -print_cells      100
    -punch_cells      1 10 20 30 40
                     50 60 70 80 90
                     100
    -punch_frequency  100
    -multi_d          true 0 0.3 0 0

KNOBS
    -iterations       500
    -convergence_tolerance 1e-008
    -tolerance         1e-015
    -step_size         100
    -pe_step_size      10

EQUILIBRIUM_PHASES 1-100
    Calcite  0 0
    Dolomite 0 0

SELECTED_OUTPUT
    -file          selected.out
    -charge_balance true
    -percent_error true
    -totals         Mn  Na  Cl  Mg  Ca  Alkalinity  S(6)
                   Om  Fe(2)  Oc  S  S(-2)
    -saturation_indices  Siderite  Calcite  FeS(ppt)  Rhodochrosite
    -kinetic_reactants  foc  ferrihydrite  MnO2
End

```

Scenario 2: Secondary Mineral Precipitation ($SI_{FeCO_3}=1.5$, $SI_{MnCO_3}=0.5$)

SOLUTION 0 mario's water boundary condition

temp	10
pH	7.15
pe	-4
redox	pe
units	mg/l
density	1
Ca	247
K	155
Mg	630
Na	4850
S(6)	1310 as SO4
Cl	10100 charge
Alkalinity	86 as HCO3-
Fe	7.43
-water	1 # kg

SOLUTION 1-100 initial condition

temp	11
pH	6.56
pe	-4
redox	pe
units	mg/l
density	1
Alkalinity	469 as HCO3-
Ca	33
Cl	121
K	4.4
Mg	40
Na	139
S(6)	33.43
Fe	63.24
Mn	0.86
-water	1 # kg

REACTION 1-50 continuously adding lower fresh water WB-31m

H2O	1
HCO3	0.0002
Cl	4.7e-005
Ca	4.01e-006
Mg	8.65e-006
SO4	5.53e-006
Fe	3.5e-006
Si	1.43e-005
0.50 moles in 1 steps	

REACTION 51-100 continuously adding upper fresh water BH114

H2O	1
HCO3	8.01e-005
Cl	2.63e-005
Ca	1.1e-005
Mg	3.65e-005

```

      K          1.17e-007
      SO4        6.06e-006
      Fe         8.41e-006
      Si         4.95e-005
      1.20 moles in 1 steps
END

SOLUTION_MASTER_SPECIES
      Om          Om          0      CH2O          30

SOLUTION_SPECIES
      Om = Om
      log_k       0

PHASES
      foc
      Om = Om
      log_k       0

RATES
      foc
      -start
      10 if (M<=0) THEN GOTO 50
      20 k_foc=2.0e-12
      30 rate = k_foc
      40 moles = rate * time
      50 SAVE moles
      -end

      ferrihydrite
      -start
      10 if (M<=0) THEN GOTO 210
      20 k_ferri=8.5e-10
      30 rate = k_ferri* mol("Om")
      200 moles = rate * time
      210 SAVE moles
      -end

      MnO2
      -start
      10 if (M<=0) THEN GOTO 50
      20 k_MnO2=1.0e-11
      30 rate = k_MnO2* mol("Om")
      40 moles = rate * time
      50 SAVE moles
      -end

KINETICS 1-100
      foc
      -formula    Om    1
      -m          10
      -m0         10
      -tol        1e-008
      ferrihydrite
      -formula    Om    -0.25 H+   -1.75 HCO3-   0.25 Fe+2   1 H2O   2.5
      -m          1
      -m0         1

```

```

        -tol          1e-008
MnO2
    -formula  Om  -0.5 H+  -1.5 Mn+2  1 H2O  1 HCO3-  0.5
    -m        1
    -m0       1
    -tol      1e-008
    -steps    1
    -step_divide 1
    -runge_kutta 3
    -bad_step_max 500

TRANSPORT
    -cells            100
    -shifts           2000
    -time_step        78840000 1 # seconds
    -lengths          100*10
    -diffusion_coefficient 7e-010
    -thermal_diffusion 2 0
    -print_cells      100
    -punch_cells      1 10 20 30 40
                      50 60 70 80 90
                      100
    -punch_frequency  100
    -multi_d          true 0 0.3 0 0

KNOBS
    -iterations       500
    -convergence_tolerance 1e-008
    -tolerance         1e-015
    -step_size         100
    -pe_step_size      10

EQUILIBRIUM_PHASES 1-100
    Calcite  0 0
    Dolomite 0 0
    Rhodochrosite 0.5 0
    Siderite 1.5 0

SELECTED_OUTPUT
    -file          selected.out
    -charge_balance true
    -percent_error true
    -totals        Mn  Na  Cl  Mg  Ca  Alkalinity  S(6)
                  Om  Fe(2)  Oc  S  S(-2)
    -saturation_indices Siderite Calcite FeS(ppt) Rhodochrosite
    -kinetic_reactants  foc ferrihydrite MnO2
End

```

Scenario 3: Secondary Mineral Precipitation ($SI_{FeCO_3}=0$, $SI_{MnCO_3}=0$)

SOLUTION 0 mario's water boundary condition

temp	10
pH	7.15
pe	-4
redox	pe
units	mg/l
density	1
Ca	247
K	155
Mg	630
Na	4850
S(6)	1310 as SO4
Cl	10100 charge
Alkalinity	86 as HCO3-
Fe	7.43
-water	1 # kg

SOLUTION 1-100 initial condition

temp	11
pH	6.56
pe	-4
redox	pe
units	mg/l
density	1
Alkalinity	469 as HCO3-
Ca	33
Cl	121
K	4.4
Mg	40
Na	139
S(6)	33.43
Fe	63.24
Mn	0.86
-water	1 # kg

REACTION 1-50 continuously adding lower fresh water WB-31m

H2O	1
HCO3	0.0002
Cl	4.7e-005
Ca	4.01e-006
Mg	8.65e-006
SO4	5.53e-006
Fe	3.5e-006
Si	1.43e-005
0.50 moles in 1 steps	

REACTION 51-100 continuously adding upper fresh water BH114

H2O	1
HCO3	8.01e-005
Cl	2.63e-005
Ca	1.1e-005
Mg	3.65e-005


```

      K          1.17e-007
      SO4        6.06e-006
      Fe         8.41e-006
      Si         4.95e-005
      1.20 moles in 1 steps
END

SOLUTION_MASTER_SPECIES
      Om          Om          0      CH2O          30

SOLUTION_SPECIES
Om = Om
  log_k          0

PHASES
foc
  Om = Om
  log_k          0

RATES
  foc
-start
10 if (M<=0) THEN GOTO 50
20 k_foc=2.0e-12
30 rate = k_foc
40 moles = rate * time
50 SAVE moles
-end

      ferrihydrite
-start
10 if (M<=0) THEN GOTO 210
20 k_ferri=5.5e-10
30 rate = k_ferri* mol("Om")
200 moles = rate * time
210 SAVE moles
-end

      MnO2
-start
10 if (M<=0) THEN GOTO 50
20 k_MnO2=1.0e-11
30 rate = k_MnO2* mol("Om")
40 moles = rate * time
50 SAVE moles
-end

KINETICS 1-100
foc
  -formula Om 1
  -m        10
  -m0       10
  -tol      1e-008
ferrihydrite
  -formula Om -0.25 H+ -1.75 HCO3- 0.25 Fe+2 1 H2O 2.5
  -m        1
  -m0       1

```

```

        -tol          1e-008
MnO2
    -formula  Om  -0.5 H+  -1.5 Mn+2  1 H2O  1 HCO3-  0.5
    -m        1
    -m0       1
    -tol      1e-008
    -steps    1
    -step_divide 1
    -runge_kutta 3
    -bad_step_max 500

TRANSPORT
    -cells            100
    -shifts           2000
    -time_step        78840000 1 # seconds
    -lengths          100*10
    -diffusion_coefficient 7e-010
    -thermal_diffusion 2 0
    -print_cells      100
    -punch_cells      1 10 20 30 40
                     50 60 70 80 90
                     100
    -punch_frequency  100
    -multi_d          true 0 0.3 0 0

KNOBS
    -iterations       500
    -convergence_tolerance 1e-008
    -tolerance        1e-015
    -step_size        100
    -pe_step_size     10

EQUILIBRIUM_PHASES 1-100
    Calcite  0 0
    Dolomite 0 0
    Siderite 0 0
    Rhodochrosite 0 0

SELECTED_OUTPUT
    -file          selected.out
    -charge_balance true
    -percent_error true
    -totals        Mn Na Cl Mg Ca Alkalinity S(6)
                  Om Fe(2) Oc S S(-2)
    -saturation_indices Siderite Calcite FeS(ppt) Rhodochrosite
    -kinetic_reactants  foc ferrihydrite MnO2
End

```

Scenario 4: Sulfate Reduction

SOLUTION 0 mario's water boundary condition

temp	10
pH	7.15
pe	-4
redox	pe
units	mg/l
density	1
Ca	247
K	155
Mg	630
Na	4850
S(6)	1310 as SO4
Cl	10100 charge
Alkalinity	86 as HCO3-
Fe	7.43
-water	1 # kg

SOLUTION 1-100 initial condition

temp	11
pH	6.56
pe	-4
redox	pe
units	mg/l
density	1
Alkalinity	469 as HCO3-
Ca	33
Cl	121
K	4.4
Mg	40
Na	139
S(6)	33.43
Fe	63.24
Mn	0.86
-water	1 # kg

REACTION 1-50 continuously adding lower fresh water WB-31m

H2O	1
HCO3	0.0002
Cl	4.7e-005
Ca	4.01e-006
Mg	8.65e-006
SO4	5.53e-006
Fe	3.5e-006
Si	1.43e-005
0.50 moles in 1 steps	

REACTION 51-100 continuously adding upper fresh water BH114

H2O	1
HCO3	8.01e-005
Cl	2.63e-005
Ca	1.1e-005
Mg	3.65e-005

```

      K          1.17e-007
      SO4        6.06e-006
      Fe         8.41e-006
      Si         4.95e-005
      1.20 moles in 1 steps
END

```

```

SOLUTION_MASTER_SPECIES
      Om          Om          0      CH2O          30

```

```

SOLUTION_SPECIES
Om = Om
  log_k      0

```

```

PHASES
foc
  Om = Om
  log_k      0

```

```

RATES
  foc
-start
10 if (M<=0) THEN GOTO 50
20 k_foc=3.0e-12
30 rate = k_foc
40 moles = rate * time
50 SAVE moles
-end

  ferrihydrite
-start
10 if (M<=0) THEN GOTO 210
20 k_ferri=8.5e-10
30 rate = k_ferri* mol("Om")
200 moles = rate * time
210 SAVE moles
-end

  MnO2
-start
10 if (M<=0) THEN GOTO 50
20 k_MnO2=1.0e-11
30 rate = k_MnO2* mol("Om")
40 moles = rate * time
50 SAVE moles
-end

  SO4_reduction
-start
10 if (M<=0) THEN GOTO 110
20 k_SO4 = 5.5e-10
30 rate = k_SO4* mol("Om")
100 moles = rate * time
110 save moles
-end

```

```

KINETICS 1-100

```

```

foc
  -formula Om 1
  -m 10
  -m0 10
  -tol 1e-008
ferrihydrite
  -formula Om -0.25 H+ -1.75 HCO3- 0.25 Fe+2 1 H2O 2.5
  -m 1
  -m0 1
  -tol 1e-008
MnO2
  -formula Om -0.5 H+ -1.5 Mn+2 1 H2O 1 HCO3- 0.5
  -m 1
  -m0 1
  -tol 1e-008
SO4_reduction
  -formula Om -2 SO4 -1 HS- 1 HCO3- 2 H+ 1
  -m 1
  -m0 1
  -tol 1e-008
-steps 1
-step_divide 1
-runge_kutta 3
-bad_step_max 500

TRANSPORT
  -cells 100
  -shifts 2000
  -time_step 78840000 1 # seconds
  -lengths 100*10
  -diffusion_coefficient 7e-010
  -thermal_diffusion 2 0
  -print_cells 100
  -punch_cells 1-2 5 10 20 30
               40 50 60 70 80
               90 100
  -punch_frequency 50
  -multi_d true 0 0.3 0 0

KNOBS
  -iterations 300
  -convergence_tolerance 1e-008
  -tolerance 1e-015
  -step_size 100
  -pe_step_size 10

EQUILIBRIUM_PHASES 1-100
  Calcite 0 0
  Dolomite 0 0

SELECTED_OUTPUT
  -file selected.out
  -charge_balance true
  -percent_error true
  -totals Mn Na Cl Mg Ca Alkalinity S(6)

```

```

                                Om  Fe(2)  Oc
-saturation_indices  Siderite  Calcite  FeS(ppt)  Rhodochrosite
-kinetic_reactants   foc  ferrihydrite  MnO2  SO4_reduction
End

```

Scenario 5: Sulfate Reduction + Secondary Mineral (FeS) Precipitation

SOLUTION 0 mario's water boundary condition

```

temp      10
pH         7.15
pe        -4
redox     pe
units     mg/l
density   1
Ca        247
K         155
Mg        630
Na        4850
S(6)      1310 as SO4
Cl        10100 charge
Alkalinity 86 as HCO3-
Fe         7.43
-water    1 # kg

```

SOLUTION 1-100 initial condition

```

temp      11
pH         6.56
pe        -4
redox     pe
units     mg/l
density   1
Alkalinity 469 as HCO3-
Ca        33
Cl        121
K          4.4
Mg        40
Na        139
S(6)      33.43
Fe        63.24
Mn        0.86
-water    1 # kg

```

REACTION 1-50 continously adding lower fresh water WB-31m

```

H2O        1
HCO3       0.0002
Cl         4.7e-005
Ca         4.01e-006
Mg         8.65e-006
SO4        5.53e-006
Fe         3.5e-006
Si         1.43e-005
0.50 moles in 1 steps

```

REACTION 51-100 continuously adding upper fresh water BH114

H2O 1
HCO3 8.01e-005
Cl 2.63e-005
Ca 1.1e-005
Mg 3.65e-005
K 1.17e-007
SO4 6.06e-006
Fe 8.41e-006
Si 4.95e-005
1.20 moles in 1 steps

END

SOLUTION_MASTER_SPECIES

Om Om 0 CH2O 30

SOLUTION_SPECIES

Om = Om
log_k 0

PHASES

foc
Om = Om
log_k 0

RATES

foc
-start
10 if (M<=0) THEN GOTO 50
20 k_foc=3.0e-12
30 rate = k_foc
40 moles = rate * time
50 SAVE moles
-end

ferrihydrite

-start
10 if (M<=0) THEN GOTO 210
20 k_ferri=8.5e-10
30 rate = k_ferri* mol("Om")
200 moles = rate * time
210 SAVE moles
-end

MnO2

-start
10 if (M<=0) THEN GOTO 50
20 k_MnO2=1.0e-11
30 rate = k_MnO2* mol("Om")
40 moles = rate * time
50 SAVE moles
-end

SO4_reduction

-start
10 if (M<=0) THEN GOTO 110
20 k_SO4 = 3.0e-10

```

30 rate = k_SO4* mol("Om")
100 moles = rate * time
110 save moles
-end

KINETICS 1-100
foc
  -formula Om 1
  -m 10
  -m0 10
  -tol 1e-008
ferrihydrite
  -formula Om -0.25 H+ -1.75 HCO3- 0.25 Fe+2 1 H2O 2.5
  -m 1
  -m0 1
  -tol 1e-008
MnO2
  -formula Om -0.5 H+ -1.5 Mn+2 1 H2O 1 HCO3- 0.5
  -m 1
  -m0 1
  -tol 1e-008
SO4_reduction
  -formula Om -2 SO4 -1 HS- 1 HCO3- 2 H+ 1
  -m 1
  -m0 1
  -tol 1e-008
-steps 1
-step_divide 1
-runge_kutta 3
-bad_step_max 500

TRANSPORT
  -cells 100
  -shifts 2000
  -time_step 78840000 1 # seconds
  -lengths 100*10
  -diffusion_coefficient 7e-010
  -thermal_diffusion 2 0
  -print_cells 100
  -punch_cells 1-2 5 10 20 30
  40 50 60 70 80
  90 100
  -punch_frequency 50
  -multi_d true 0 0.3 0 0

KNOBS
  -iterations 300
  -convergence_tolerance 1e-008
  -tolerance 1e-015
  -step_size 100
  -pe_step_size 10

EQUILIBRIUM_PHASES 1-100
  Calcite 0 0
  Dolomite 0 0

```


Mackinawite 0 0

SELECTED_OUTPUT

```
-file                selected.out
-charge_balance      true
-percent_error        true
-totals              Mn  Na  Cl  Mg  Ca  Alkalinity  S(6)
                    Om  Fe(2)  Oc
-saturation_indices  Siderite  Calcite  FeS(ppt)  Rhodochrosite
-kinetic_reactants   foc  ferrihydrite  MnO2  SO4_reduction
```

End

Scenario 6: Methanogenesis

SOLUTION 0 mario's water boundary condition

```
temp      10
pH         7.15
pe         -4
redox      pe
units      mg/l
density    1
Ca         247
K          155
Mg         630
Na         4850
S(6)       1310 as SO4
Cl         10100 charge
Alkalinity 86 as HCO3-
Fe         7.43
-water     1 # kg
```

SOLUTION 1-100 initial condition

```
temp      11
pH         6.56
pe         -4
redox      pe
units      mg/l
density    1
Alkalinity 469 as HCO3-
Ca         33
Cl         121
K          4.4
Mg         40
Na         139
S(6)       33.43
Fe         63.24
Mn         0.86
-water     1 # kg
```

REACTION 1-50 continously adding lower fresh water WB-31m

```
H2O        1
HCO3        0.0002
Cl          4.7e-005
```

```

Ca          4.01e-006
Mg          8.65e-006
SO4         5.53e-006
Fe          3.5e-006
Si          1.43e-005
0.50 moles in 1 steps

REACTION 51-100 continuously adding upper fresh water BH114
H2O         1
HCO3        8.01e-005
Cl          2.63e-005
Ca          1.1e-005
Mg          3.65e-005
K           1.17e-007
SO4         6.06e-006
Fe          8.41e-006
Si          4.95e-005
1.20 moles in 1 steps
END

SOLUTION_MASTER_SPECIES
Om          Om          0      CH2O          30
Meth        Meth        0      CH4           16

SOLUTION_SPECIES
Om = Om
log_k       0
Meth = Meth
log_k       0

PHASES
foc
Om = Om
log_k       0

RATES
foc
-start
10 if (M<=0) THEN GOTO 50
20 k_foc=3.0e-12
30 rate = k_foc
40 moles = rate * time
50 SAVE moles
-end

ferrihydrite
-start
10 if (M<=0) THEN GOTO 210
20 k_ferri=8.5e-10
30 rate = k_ferri* mol("Om")
200 moles = rate * time
210 SAVE moles
-end
MnO2
-start
10 if (M<=0) THEN GOTO 50

```

```

20 k_MnO2=1.0e-11
30 rate = k_MnO2* mol("Om")
40 moles = rate * time
50 SAVE moles
-end
    SO4_reduction
-start
10 if (M<=0) THEN GOTO 110
20 k_SO4 = 5.5e-10
30 rate = k_SO4* mol("Om")
100 moles = rate * time
110 save moles
-end
    Methanogenesis
-start
10 if (M<=0) THEN GOTO 50
20 k_Meth=5.0e-10
30 rate = k_Meth* mol("Om")
40 moles = rate * time
50 SAVE moles
-end

KINETICS 1-50
foc
    -formula Om 1
    -m 10
    -m0 10
    -tol 1e-008
ferrihydrite
    -formula Om -0.25 H+ -1.75 HCO3- 0.25 Fe+2 1 H2O 2.5
    -m 1
    -m0 1
    -tol 1e-008
MnO2
    -formula Om -0.5 H+ -1.5 Mn+2 1 H2O 1 HCO3- 0.5
    -m 1
    -m0 1
    -tol 1e-008
SO4_reduction
    -formula Om -2 SO4 -1 HS- 1 HCO3- 2 H+ 1
    -m 1
    -m0 1
    -tol 1e-008
Methanogenesis
    -formula H2O -1 Om -2 HCO3- 1 H+ 1 Meth 1
    -m 1
    -m0 1
    -tol 1e-008
-steps 1
-step_divide 1
-runge_kutta 3
-bad_step_max 500

KINETICS 51-100
foc
    -formula Om 1
    -m 10

```

```

        -m0          10
        -tol         1e-008
ferrihydrite
        -formula     Om  -0.25 H+  -1.75 HCO3-  0.25 Fe+2  1 H2O  2.5
        -m           1
        -m0          1
        -tol         1e-008
MnO2
        -formula     Om  -0.5 H+  -1.5 Mn+2  1 H2O  1 HCO3-  0.5
        -m           1
        -m0          1
        -tol         1e-008
SO4_reduction
        -formula     Om  -2 SO4  -1 HS-  1 HCO3-  2 H+  1
        -m           1
        -m0          1
        -tol         1e-008

-steps             1
-step_divide       1
-runge_kutta       3
-bad_step_max      500

TRANSPORT
        -cells              100
        -shifts             2000
        -time_step          78840000 1 # seconds
        -lengths            100*10
        -diffusion_coefficient 7e-010
        -thermal_diffusion   2 0
        -print_cells         100
        -punch_cells         1 10 20 30 40
                             50 60 70 80 90
                             100
        -punch_frequency     50
        -multi_d             true 0 0.3 0 0

KNOBS
        -iterations         300
        -convergence_tolerance 1e-008
        -tolerance           1e-015
        -step_size           100
        -pe_step_size        10

EQUILIBRIUM_PHASES 1-100
        Calcite  0 0
        Dolomite 0 0

SELECTED_OUTPUT
        -file              selected.out
        -charge_balance    true
        -percent_error     true
        -totals             Mn  Na  Cl  Mg  Ca  Alkalinity  S(6)
                             Om  Fe(2)  Meth
        -saturation_indices  Siderite  Calcite  FeS(ppt)  Rhodochrosite

```

```

-kinetic_reactants    foc ferrihydrite MnO2 SO4_reduction
                      Methanogenesis
End

```

Scenario 7: Bioavailability of Organic Matter

SOLUTION 0 mario's water boundary condition

```

temp      10
pH        7.15
pe        -4
redox     pe
units     mg/l
density   1
Ca        247
K         155
Mg        630
Na        4850
S(6)      1310 as SO4
Cl        10100 charge
Alkalinity 86 as HCO3-
Fe        7.43
-water    1 # kg

```

SOLUTION 1-100 initial condition

```

temp      11
pH        6.56
pe        -4
redox     pe
units     mg/l
density   1
Alkalinity 469 as HCO3-
Ca        33
Cl        121
K         4.4
Mg        40
Na        139
S(6)      33.43
Fe        63.24
Mn        0.86
-water    1 # kg

```

REACTION 1-50 continously adding lower fresh water WB-31m

```

H2O       1
HCO3      0.0002
Cl        4.7e-005
Ca        4.01e-006
Mg        8.65e-006
SO4       5.53e-006

```

```

Fe          3.5e-006
Si          1.43e-005
0.50 moles in 1 steps

REACTION 51-100 continuously adding upper fresh water BH114
H2O          1
HCO3         8.01e-005
Cl           2.63e-005
Ca           1.1e-005
Mg           3.65e-005
K            1.17e-007
SO4          6.06e-006
Fe           8.41e-006
Si           4.95e-005
1.20 moles in 1 steps
END

SOLUTION_MASTER_SPECIES
Om           Om           0      CH2O           30
Oc           Oc           0      CH2O           30
Meth         Meth         0      CH4            16

SOLUTION_SPECIES
Om = Om
log_k        0
Oc = Oc
log_k        0
Meth = Meth
log_k        0

PHASES
foc
Om = Om
log_k        0
foc1
Oc = Oc
log_k        0

RATES
foc
-start
10 if (M<=0) THEN GOTO 50
20 k_foc=1.5e-12
30 rate = k_foc
40 moles = rate * time
50 SAVE moles
-end
foc1
-start
10 if (M<=0) THEN GOTO 50
20 k_foc1=8.5e-12
30 rate = k_foc1
40 moles = rate * time
50 SAVE moles
-end
ferrihydrite
-start

```

```

10 if (M<=0) THEN GOTO 210
20 k_ferri=3.0e-9
30 rate = k_ferri* mol("Om")
200 moles = rate * time
210 SAVE moles
-end
    MnO2
-start
10 if (M<=0) THEN GOTO 50
20 k_MnO2=3.0e-11
30 rate = k_MnO2* mol("Om")
40 moles = rate * time
50 SAVE moles
-end
    SO4_reduction
-start
10 if (M<=0) THEN GOTO 110
20 k_SO4 = 9.5e-10
30 rate = k_SO4* mol("Om")
100 moles = rate * time
110 save moles
-end
    Methanogenesis
-start
10 if (M<=0) THEN GOTO 50
20 k_Meth=2.0e-9
30 rate = k_Meth* mol("Om")
40 moles = rate * time
50 SAVE moles
-end
    ferrihydrite_1
-start
10 if (M<=0) THEN GOTO 50
20 k_ferri=3.0e-9
30 rate = k_ferri* mol("Oc")
40 moles = rate * time
50 SAVE moles
-end
    SO4_reduction1
-start
10 if (M<=0) THEN GOTO 50
20 k_SO4 = 9.5e-10
30 rate = k_SO4* mol("Oc")
40 moles = rate * time
50 save moles
-end
    MnO2_reduction1
-start
10 if (M<=0) THEN GOTO 50
20 k_MnO2=3.0e-11
30 rate = k_MnO2* mol("Oc")
40 moles = rate * time
50 SAVE moles
-end

KINETICS 1-50
foc

```

```

        -formula Om 1
        -m 1
        -m0 1
        -tol 1e-008
ferrihydrite
        -formula Om -0.25 H+ -1.75 HCO3- 0.25 Fe+2 1 H2O 2.5
        -m 1
        -m0 1
        -tol 1e-008
MnO2
        -formula Om -0.5 H+ -1.5 Mn+2 1 HCO3- 0.5 H2O 1
        -m 1
        -m0 1
        -tol 1e-008
SO4_reduction
        -formula Om -2 SO4 -1 HS- 1 HCO3- 2 H+ 1
        -m 1
        -m0 1
        -tol 1e-008
Methanogenesis
        -formula H2O -1 Om -2 HCO3- 1 H+ 1 Meth 1
        -m 1
        -m0 1
        -tol 1e-008
-steps 1
-step_divide 1
-runge_kutta 3
-bad_step_max 500

KINETICS 51-100
foc1
        -formula Oc 1
        -m 20
        -m0 20
        -tol 1e-008
ferrihydrite_1
        -formula Oc -0.25 H+ -1.75 HCO3- 0.25 Fe+2 1 H2O 2.5
        -m 10
        -m0 10
        -tol 1e-008
MnO2_reduction1
        -formula Oc -0.5 H+ -1.5 Mn+2 1 HCO3- 0.5 H2O 1
        -m 1
        -m0 1
        -tol 1e-008
SO4_reduction1
        -formula Oc -2 SO4 -1 HS- 1 HCO3- 2 H+ 1
        -m 1
        -m0 1
        -tol 1e-008
-steps 1
-step_divide 1
-runge_kutta 3
-bad_step_max 500

TRANSPORT
        -cells 100

```



```

-shifts                2000
-time_step              78840000 1 # seconds
-lengths                100*10
-diffusion_coefficient 7e-010
-thermal_diffusion      2    0
-print_cells            100
-punch_cells            1 10 20 30 40
                      50 60 70 80 90
                      100
-punch_frequency        50
-multi_d                true 0 0.3 0 0

KNOBS
-iterations             300
-convergence_tolerance  1e-008
-tolerance              1e-015
-step_size              100
-pe_step_size           10

EQUILIBRIUM_PHASES 1-100
  Calcite    0 0
  Dolomite   0 0
  Rhodochrosite 1.0 0
  Siderite   2.4 0
  FeS(ppt)   0 0

SELECTED_OUTPUT
-file                selected.out
-charge_balance      true
-percent_error        true
-totals              Mn Alkalinity S(6) Om Fe(2) Oc Meth
-saturation_indices  Siderite Calcite Rhodochrosite FeS(ppt)
-gases               CH4(g)
-kinetic_reactants   foc foc1 ferrihydrite ferrihydrite_1
                      MnO2 MnO2_reduction1 SO4_reduction

SO4_reduction1
Methanogenesis Methanogenesis1

End

```